

Dissertation zur Erlangung des Doktorgrades
der Fakultät für Chemie und Pharmazie
der Ludwig-Maximilians-Universität München

Coherent Control and Quantum Dynamics in Complex Chemical and Biological Environments

Daniel Keefer

aus

Schwäbisch Gmünd, Deutschland

2019

Erklärung:

Diese Dissertation wurde im Sinne von §7 der Promotionsordnung vom 28. November 2011 von Frau Prof. Dr. Regina de Vivie-Riedle betreut.

Eidesstattliche Versicherung:

Diese Dissertation wurde eigenständig und ohne unerlaubte Hilfe erarbeitet.

München, den 22.03.2019
Daniel Keefer

Dissertation eingereicht am: 22.03.2019
1. Gutachterin: Prof. Dr. Regina de Vivie-Riedle
2. Gutachter: Prof. Dr. Achim Hartschuh
Tag der mündlichen Prüfung: 09.05.2019

Contents

Abstract	v
List of publications	vii
Introduction	1
1. Methodology Outline	5
2. Quantum Control of a Methyl Transfer Reaction in Explicit Solvent Environment	13
2.1. Multi-Target Control of Several Solvent Cages by Simultaneous Vibrational Excitation	15
2.2. Including Fluctuations and Dynamics of the Solvent Environment	27
3. Photorelaxation of Uracil: Monitoring and Preparing an Elusive State Leading to Photolesions	51
3.1. Isolated uracil: Quantum Control to Accelerate and Prevent Relaxation	52
3.2. The Influence of an RNA Strand and Different Base Sequences	59
4. Implications of the Quantum Control Results for Future Studies	69
5. UV-Induced Self-Repair of a Photolesion in a DNA Strand	79
5.1. Exciplex States Between Guanine and Adenine	80
5.2. Excited State Characterization Using CASSCF and QM(CASPT2)/MM	84
6. Summary and outlook	87
A. Supporting information for chapter 3.1	91
B. Supporting information for chapter 3.2	101
List of abbreviations	121
Bibliography	123
Danksagung	131

Abstract

In ultrafast molecular sciences, short laser pulses are used to initiate and interrogate chemical and physical phenomena. This thesis presents simulations on different molecular examples within this framework, where the specific goal ranges from the design of ultrafast experiments, over their interpretation and to feasibility assessments for future applications. Additionally, simulation protocols are developed to consider the influence of complex environments on the studied processes, as this is essential for the aspired experimental connection and often very challenging.

The first topic deals with the initiation of a synthetically relevant reaction with shaped laser pulses. The model system is a methyl transfer between cyclohexanone and trimethylaluminium, which includes a carbon-carbon bond formation as the key step in many pharmaceutical syntheses. The surrounding molecules of the chemical solution are found to considerably affect the one-dimensional model reaction coordinate describing the methyl transfer. Quantum control studies are performed by optimizing laser pulses, selectively steering a nuclear wavepacket toward the methyl transfer pathway. A simulation protocol based on multi-target Optimal Control Theory is employed to overcome the environmental complexities and excite the molecules in various different static solvent cages simultaneously. In combination with statistical estimates, it is found that theoretically the population yield in the target level can be considerable. Going beyond the static inclusion of solvent cages, the temporal evolution of the environmental influence is revealed along five different classical trajectories of 2.5 picoseconds each. The affected vibrational levels of the target molecule are found to fluctuate on the femtosecond time scale, i.e. the environmental influence can switch between extreme cases several times during the time where the controlling laser pulse is active. Optimized laser pulses can also be efficient in scenarios which they were not optimized for, which has several implications for practical applications.

The second topic revolves around photoexcited phenomena in nucleic acids. The RNA-nucleobase uracil is investigated with respect to its photostability. One reason for the canonical nucleobases being extraordinarily stable towards UV absorption is their ultrafast relaxation back to the electronic ground state. Besides presenting the first full quantum dynamical simulations on this process for uracil, quantum control optimizations are used to trap the wave packet and prevent relaxation. This artificially prepares the elusive state which can be a precursor for photodamage, as delayed relaxation has been directly connected with the formation of harmful lesions before. The optimized laser pulse is surprisingly smooth and within the accessibility of modern experimental setups, which renders this study a tangible instruction for possible spectroscopic experiments. Besides the artificial trap on isolated uracil, wavepacket simulations within its natural RNA environment reveal that this influence can also lead to trapping in the photoexcited state. Sampling over 10 different neighboring base sequences and a total of 275 environmental snapshots, this mechanism is found to be base-independent.

In this connection, the third study goes from the formation of photodamage to its repair. An experimentally observed repair mechanism of the frequently occurring cyclobutane pyrimidine dimer — formed by two thymines in DNA — is investigated with quantum chemistry. The excited states of the neighboring guanine adenine sequence

are characterized to distinguish between local and charge transfer excitation, validating the initial step of the experimentally suggested mechanism.

List of publications

This thesis is based on the following publications, listed in chronological order. They are reprinted in chapters 2.1 **(1)**, 2.2 **(5)**, 3.1 **(2)**, 3.2 **(3)** and 4 **(4)**.

- 1 D. Keefer**, S. Thallmair, J. P. P. Zauleck, R. de Vivie-Riedle
A multi target approach to control chemical reactions in their inhomogeneous solvent environment.
J. Phys. B: At. Mol. Opt. Phys. **2015**, 48, 234003.
Contributions by D. Keefer: performing all calculations and analysis, writing of the manuscript.
- 2 D. Keefer**, S. Thallmair, S. Matsika, R. de Vivie-Riedle
Controlling Photorelaxation in Uracil with Shaped Laser Pulses: A Theoretical Assessment.
J. Am. Chem. Soc. **2017**, 139, 5061.
Contributions by D. Keefer: performing all calculations and analysis, writing of the manuscript.
- 3 S. Reiter, D. Keefer** and R. de Vivie-Riedle
RNA Environment is Responsible for Decreased Photostability of Uracil.
J. Am. Chem. Soc. **2018**, 140, 8714.
Contributions by D. Keefer: designing the project; supervising of calculations, analysis and manuscript preparation.
- 4 D. Keefer**, R. de Vivie-Riedle
Pathways to New Applications for Quantum Control.
Acc. Chem. Res. **2018**, 51, 2279.
Contributions by D. Keefer: developing the concept; writing of the manuscript.
- 5 D. Keefer**, R. de Vivie-Riedle
Theoretical Quantum Control of Fluctuating Molecular Energy Levels in Complex Chemical Environments.
Adv. Quantum Technol. **2019**, submitted.
Contributions by D. Keefer: designing the project, performing all calculations and analysis, writing of the manuscript.

Additional publications:

- 6** P. Zeller, A.-K. Henß, M. Weinl, L. Diehl, **D. Keefer**, J. Lippmann, A. Schulz, J. Kraus, M. Schreck, J. Wintterlin
Detachment of CVD-grown graphene from single crystalline Ni films by a pure gas phase reaction.
Surf. Sci. **2016**, 653, 143.
- 7** **D. Keefer**, S. Thallmair, J. P. P. Zauleck, R. de Vivie-Riedle
Optimal Control Theory for Molecular Reactions in Atomistic Surroundings.
in: *International Conference on Ultrafast Phenomena 2016*, OSA Technical Digest (online), paper UTh3B.5.
- 8** **D. Keefer**, S. Thallmair, S. Matsika, R. de Vivie-Riedle
How to Control the Ultrafast Dynamics of Uracil with Shaped Laser Pulses: Theoretical Insights.
in: *International Conference on Ultrafast Phenomena 2016*, OSA Technical Digest (online), paper UTh3B.2.
- 9** S. Thallmair, **D. Keefer**, F. Rott, R. de Vivie-Riedle
Simulating the control of molecular reactions via modulated light fields: from gas phase to solution.
J. Phys. B: At. Mol. Opt. Phys. **2017**, 50, 082001.
- 10** **D. Keefer**, S. Reiter, R. de Vivie-Riedle
Ultrafast Photorelaxation of Uracil Embedded in an RNA Strand.
in: *International Conference on Ultrafast Phenomena 2018*, submitted.
- 11** S. Reiter, **D. Keefer**, V. Besel, R. de Vivie-Riedle
UV-induced DNA Self-Repair Mechanism Traced With Quantum Chemistry
in: *International Conference on Ultrafast Phenomena 2018*, submitted.
- 12** S. Reiter, **D. Keefer**, R. de Vivie-Riedle
Einfluss von UV-Strahlung auf das Erbgut — RNA Strang beeinträchtigt Photo-stabilität von Uracil
GIT Labor-Fachzeitschrift **2019**, 63, 28.

Much to learn, you still have.
Yoda

Introduction

The interaction between light and molecular quantum systems is a fundamental scheme in nature. Elementary steps of photosynthesis [1–4], vision [5–7], vitamin D synthesis [8] and the formation of photolesions in the genetic code [9–13] are triggered by sunlight. In ultrafast molecular sciences, artificial light sources in the form of short laser pulses are used to initiate and interrogate these processes in a laboratory environment and on their intrinsic timescale from picoseconds to attoseconds. Groundbreaking for this approach were the works of Ahmed Zewail, pioneering the field of time-resolved femtosecond spectroscopy [14–16], which allowed to directly monitor molecular wavepackets (WPs) in real-time. Numerous experimental efforts since then have constantly increased the capabilities of pulse generation and created more sophisticated spectroscopic techniques to access ever shorter timescales and better spatial resolution, while still having the same goal: Tracing nuclear (and nowadays even electronic [17–19]) WPs to explain light-induced processes with unprecedented resolution and detail and discover new chemistry and physics. Beyond the pure observation of ultrafast phenomena, the invention of femtosecond pulse shapers [20] opened the possibility to control them. Combined with feedback-driven optimization setups, this opened the field of quantum optimal control (QOC) [21–24], where molecular WPs are specifically prepared. A multitude of impactful control aims have been reached experimentally: Bonds were cleaved selectively in two different iron complexes [25], the energy flow in the light-harvesting complex LH2 was optimized [26], the *cis-trans* photoisomerization in a solvated dye-molecule was switched on and off [27], and the primary step of vision — isomerization of retinal — was controlled in the protein bacteriorhodopsin [28], to name a few highlights.

Bond cleavage and isomerization are not only occurring naturally, but constitute common elementary steps in the preparation of organic and pharmaceutically relevant molecules. It has thus always been a highly ambitious goal of QOC to make its entry into applied chemical synthesis. With modern synthetic routes becoming increasingly complex [29–31], finding efficient shortcuts by precise steering of nuclear motion is very promising. Several light-based approaches indeed were successfully implemented in contemporary chemical laboratories, like initiating biomimetic synthesis with the irradiation of reptile lamps [32], visible light and ultraviolet (UV) organic photocatalysis [33] or the incorporation of photoswitchable units into bioactive compounds [34, 35]. Recently, infrared (IR) laser irradiation tuned to a carbonyl vibration was reported to accelerate a bimolecular ground-state reaction leading to urethane formation [36]. However, optical control in the spirit of feedback-driven pulse tailoring to coherently steer nuclear motion has not found a notable degree of application in chemical synthesis yet.

Be it WP observation or controlled preparation in different domains and varieties, theoretical studies very often accompanied, explained and inspired these experimental advances. For example, two-dimensional vibrational Raman spectroscopy [37, 38] and the pump-dump scheme for coherent control [39, 40] were first proposed theoretically and put to practice in many experiments afterwards, and theoretical assessments of the possibilities and limits in QOC [21, 41, 42] are among the most highly cited works in their community. The basis for theoretical studies of this kind

are WP simulations, i.e. molecular quantum dynamics (QD). They usually revolve around solving the time-dependent Schrödinger equation (TDSE) in some way, and interpreting the time evolution of the propagated nuclear WP to draw conclusions about the quantum behavior of the system at hand. A very general and straightforward implementation of QD simulations is the dynamic fourier method (DFM) [43–45], which uses a discretized spatial representation of nuclear WPs on ab-initio electronic potential energy surfaces (PESs). The quantum character of the nuclear motion is fully included, and describing the system as a matter wave allows for an accurate simulation of the interaction with light waves, and thus light-induced dynamics. Coherent phenomena like optical quantum control [39, 46–48] or the non-adiabatic population transfer through conical intersections (CoIns) [49–51] — a process determining the outcome of virtually all photochemistry — can be conveniently simulated. This framework is restricted to a small number of spatial degrees of freedom however, as the computational cost scales $O(n \log n)$ with the number of grid points n , which exponentially scale with the number of coordinates. For molecular systems with chemical and biological applications, the number of included degrees of freedom has to be reduced, which usually constitutes the biggest approximation in DFM simulations. Coordinate reduction can be achieved by chemical intuition [52] or automated procedures [53, 54], where usually much time and effort needs to be spent for the search and verification of coordinates.

Performing WP simulations in the DFM framework requires an ab-initio evaluation of the electronic PES in the chosen coordinate space. This is done using the methods of quantum chemistry (QC). There exist different frameworks and flavors to solve the time-independent electronic structure problem for molecular systems, mainly based on either Kohn-Sham density functional theory (DFT) [55, 56] or on wavefunction (WF) approaches [57]. Both frameworks offer the possibility to compute electronically excited states, either through the cost-efficient time-dependent density functional theory (TDDFT) [58–60] or various WF based formalisms like complete active space self consistent field (CASSCF) [61] and complete active space second-order perturbation theory (CASPT2) [62–64], second-order algebraic diagrammatic construction (ADC2) [65, 66], configuration interaction (CI) [67] or the coupled-cluster (CC) family [68–70], to name the most prominent ones. The computation of excited states is essential for photochemical and -physical processes triggered with visible and UV wavelengths, as these are usually resonant to the lowest-lying symmetry-allowed electronic transitions. Both for ground- and excited state calculations, each method combined with a chosen basis set offers a specific trade-off between computational accuracy and cost and is suitable for different molecular scenarios. Before starting QD simulations, usually a considerable amount of time is invested in benchmarking and characterizing different methods for the specific molecular problem at hand in order to optimize the accuracy to cost ratio and ensure methodological validity.

Since ultrafast processes like the ones described above, and as they will be presented within this thesis, often happen in some kind of environment. Be it the native ribonucleic acid (RNA) strand for the formation of nucleobase photolesions or the solvent environment in chemical synthesis, it is desirable to include these effects in the QD simulation. One way for environmental effects to be included is via the ab-initio PES on which the nuclear WP evolves. For all QC methods mentioned above, there exists the possibility to consider the influence of the environment on the electronic structure in different levels of sophistication, and this issue is still subject to extensive method development. The most accessible models are electrostatic continua, like the frequently used polarizable continuum model (PCM) and conductor-like screening

model (COSMO). The solute is placed in an electrostatic cavity with a dielectric constant according to the specific solvent. Continuum-type approaches were also used directly during a WP propagation. In Ref. [71], a frictional force was employed along a photochemical dissociation coordinate to slow down the WP. This represented the steric hindrance which the dissociating molecular moieties experience due to the solvent cage.

A broadly applicable explicit scheme for environmental effects was enabled with the advent of the quantum mechanics/molecular mechanics (QM/MM) method [72–75]. Here, the system is divided into two domains, which are treated on different levels of theory. The high-level unit, performing the process of interest (for example the reactant molecule(s) in a chemical reaction), is treated fully quantum mechanically, while the explicit environment is represented by point masses and charges according to the classical schemes of molecular mechanics (MM). Making the approximation of a static environment, WP simulations can be performed on QM/MM PESs to model the time-evolution of a molecular system within its native and explicitly included surrounding, being called the quantum dynamics/molecular dynamics (QD/MD) approach [76]. This approximation is especially valid for ultrafast processes, where the relevant dynamics usually happen within femtoseconds or few picoseconds, a time-scale too short for the environment to adapt. Past and recent advances also reported the implementation of a coupled QD/MD propagation, where the interaction between quantum and classical system is included in an Ehrenfest fashion and both domains are propagated simultaneously [77–81].

The overview of topics and methods given up until now sets the stage and context for the studies which are presented within this thesis. After a concise description of the simulation protocols which were used throughout this thesis in chapter 1, chapter 2 deals with the quantum control of a methyl group transfer including carbon-carbon formation in an organic molecule. This chemical reaction is representative for elementary steps in the synthesis of pharmaceutically applicable molecules. A protocol to explicitly include the effects of a solvent environment in coherent control simulations is presented. The arising complexities in the thermodynamic ensemble are explored to identify the reasons due to which quantum control has not been able to enter chemical synthesis up until now, and whether they can possibly be overcome. In chapter 3, the photostability of the RNA nucleobase uracil after UV excitation is explored. Quantum control simulations are presented which demonstrate how to efficiently trap the WP in the otherwise elusive excited state, a scenario which is often connected with the formation of photolesions [82–84]. This study closely connects to gas phase experiments in the photorelaxation of nucleobases [85], where ultrafast spectroscopy is used to investigate the excited state lifetimes and the photorelaxation pathways of nucleobases. With the possible artificial preparation of a precursor state of photolesions, the investigation of photodamage pathways in the genetic code could be pushed forward. Since uracil in its natural environment is incorporated in an RNA strand and surrounded by water, QD simulations according to the QD/MD scheme were performed and are presented in chapter 3.2. The trap of the WP which was artificially created with shaped laser pulses in chapter 3.1 now occurs due to environmental effects in some configurations. The photostability of uracil was investigated in several neighboring base configurations, aiming at obtaining a representative statistical picture on one hand and breaking down the effects to specific base sequences on the other hand.

In addition to causing photolesions, UV light was also found to initiate the repair of known photolesions like the cyclobutane pyrimidine dimer (CPD) lesion in

deoxyribonucleic acid (DNA) [86]. In this context, excited state QM/MM calculations of the experimentally used base sequence were performed and are presented in chapter 5. The goal is to identify the character of the initially addressed excited state and investigate the first step of the repair mechanism, which is assumed to be an electron transfer from the adjacent guanine adenine sequence to the CPD unit. Since all nucleobases in nucleic acids absorb UV light in the same energetic region, it is hard to experimentally disentangle the various contributions and properly characterize the electronic structure of the excited state, and excited state simulations can be a useful tool to help experiments in identifying the correct ultrafast mechanism.

Lastly, chapter 4 contains a perspective on how the presented results may influence the field of QOC and assist it in finding new powerful applications. It is mainly based on the publications presented in chapters 2.1 and 3.1, and aims at explaining them to a broader chemical and physical audience with the clear mindset on not only summarizing past or recent advances, but illustrating their implications for the future.

Chapter 1.

Methodology Outline

In chapters 2, 3 and 5, the detailed methodology used to perform the respective studies is described in the reprinted publications. While there are differences in the specific steps to include the atomistic environments, all studies take place in the same simulation framework. It is thus useful to sketch the general procedure here and state the differences in the respective chapters. The general aim is to perform QD simulations and optimal control theory (OCT) optimizations on ab-initio PESs including the atomistic environment, and a flowchart of the necessary steps to set up these simulations is given in Figure 1.1. The final goal is to solve the TDSE, which in its general form reads

$$i\hbar\frac{\partial}{\partial t}\psi = \hat{H}\psi, \quad (1.1)$$

and contains the Hamiltonian \hat{H} , the reduced Planck-constant \hbar , the system's WF ψ and the time t . In the context of this work, the TDSE with the specific terms in \hat{H} reads

$$i\hbar\frac{\partial}{\partial t}\psi^S = \left[\hat{T}_q + \hat{V}_{tot}^{ES}(R_q^S, R^E) - \varepsilon(t)\hat{\mu}_q \right] \psi^S. \quad (1.2)$$

The nuclear wave packet of the molecular system of interest is represented by ψ^S , \hat{T}_q is the kinetic energy operator in reduced dimensions q , $\varepsilon(t)$ notes the laser field and $\hat{\mu}_q$ is the dipole operator along the reduced coordinates. The operator $\hat{V}_{tot}^{ES}(R_q^S, R^E)$ is the total PES, which depends on the nuclear positions R_q^S of the system. This is also the term where the atomistic environment enters the simulation, as the potential operator also depends on the nuclear positions R^E of the atomistic environment. In the first study in chapter 2.1, the system will be propagated in frozen solvent cages, decoupling the movement of system and environment and thereby R^E being time-independent. In chapter 2.2, the atomistic environment changes during the quantum dynamical propagation, making the potential operator time-dependent and thus noting $\hat{V}_{tot}^{ES}(R_q^S, R^E(t))$. The necessary steps to obtain all terms in equation (1.2) are briefly discussed in the following.

1. Coordinate reduction

WP simulations according to the TDSE in the DFM framework are only feasible in few dimensions due to the number of grid points scaling exponentially. Synthetically or biologically relevant molecules however usually exhibit well above 10 degrees of freedom ($3N-6$ for non-linear molecules with N being the number of atoms). A full-dimensional QD simulation of the chemical reactant in chapter 2 would thus require 84 dimensions, and for uracil 27 dimensions respectively, both being way above the accessibility of modern computational architectures. Discarding all but few degrees of freedom is necessarily an approximation, and as it usually is the biggest one in DFM based simulations, significant care has to be taken. Simulating ultrafast phenomena, this approximation is often justifiable however, since the process is often completed within femto- or picoseconds, i.e. before internal vibrational relaxation to different

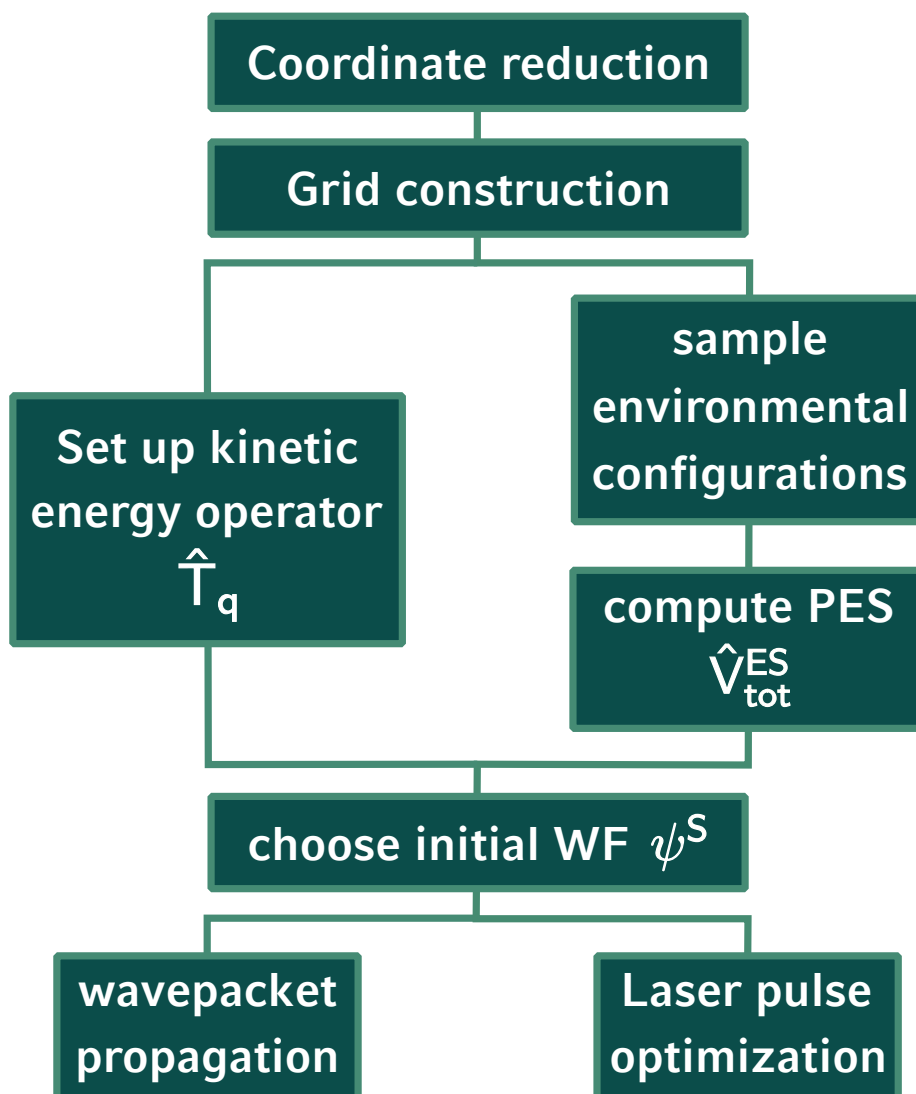


Figure 1.1.: Flowchart of the methodology used in the studies throughout this thesis, enabling to simulate WP evolution and their control in explicit chemical and biological. The QD simulations are performed on spatial grids using reduced reactive coordinates, where the environmental influence enters the Hamiltonian through the potential energy operator. Different approaches to realize this are described in the present and other chapters of this thesis.

molecular modes can take place. Thus, only few reactive modes are important for the description of a specific process. This especially holds true for laser-induced processes, as the WP is started with a specific carrier frequency and the participating degrees of freedom can be anticipated reasonably. For example, if the targeted molecule contains a carbonyl group and the wavelength of the laser pulse is resonant with it, it is mandatory to include the carbonyl vibration dimension in the QD simulation. Coherent coupling to other modes can take place in these processes, which makes it also mandatory to include the according degrees of freedom. It is also possible to combine several normal modes within a single molecular displacement vector, a concept being known as *reactive coordinates*, which have proven to be able to produce physically meaningful results [52]. As an instructive example, a reactive coordinate

can for example be represented by the intrinsic reaction coordinate (IRC) [87, 88] of a chemical reaction, which is a minimum energy path connecting the molecular structures of reactant, transition state and product. In this spirit, the first approach in coordinate reduction — manual selection — is based on chemical intuition and possible *a priori* knowledge gained through preparatory studies. Coordinate reduction for the presented studies in this thesis was performed by manual selection. The one-dimensional IRC was used for the chemical reaction in chapter 2, and uracil was reduced to a two-dimensional reactive coordinate space using molecular structures which were identified to play a major role during the photorelaxation process [89, 90]. Recent advances also devised automated procedures for coordinate reduction using more quantifiable criteria. Coordinates were generated from semiclassical trajectories [53], by dividing the IRC into two or three dimensions [53], and even through the usage of machine learning techniques [54].

Beyond the DFM, there exist more approximate approaches to solving the TDSE allowing for more degrees of freedom. A prominent and commonly used example are different formulations of the multi-configuration time-dependent Hartree (MCTDH) [91], enabling the inclusion of few dozens of degrees of freedom. It works well in cases where the system’s Hamiltonian is expandable in a normal mode fashion [92, 93], but is less applicable when the system’s PES resembles non-benign structures regarding this expansion, or if there is strong correlation between the degrees of freedom [94]. This can often be the case in laser-induced reactive processes as they are investigated within this thesis.

2. Grid construction

Once coordinates have been selected, a spatial grid is constructed by choosing the minimum and maximum values of structural displacement along the coordinate vectors, and a sufficient amount of grid points for the spatial representation of the WP. While it is desirable to keep the grid point density as low as possible for reasons of computational cost, the Nyquist-Shannon sampling theorem sets a lower bound to this [95, 96]. The maximum range in momentum space is connected to the amount of grid points in each separate dimension, so while for uracil — consisting only of relatively light atoms — 128 grid points in both dimensions were sufficient, the simulation of molecules consisting of heavier atoms requires more grid points (e.g. 1536×2048 grid points for a molecule containing bromine in Ref. [97]).

3. Kinetic energy operator

The kinetic energy operator in a full-dimensional Cartesian coordinate space x reads

$$\hat{T}_x = -\frac{\hbar}{2} \sum_{i=1}^{3N} \frac{1}{m_i} \frac{\partial^2}{\partial x_i^2}, \quad (1.3)$$

with the masses m_i of each atom i . A convenient way to transform it into arbitrary coordinates q is given by the Wilson G-Matrix formalism [98–100]. As it offers a very general transformation instruction, it is also suited for the case of reactive coordinates. The detailed implementation therefor is laid out in Refs. [101] and yields the following expression for the kinetic energy operator \hat{T}_q in reactive coordinates:

$$\hat{T}_q \simeq -\frac{\hbar}{2} \sum_{r=1}^M \sum_{s=1}^M \frac{\partial}{\partial q_r} \left[G_{rs} \frac{\partial}{\partial q_s} \right]. \quad (1.4)$$

The G-Matrix is conveniently accessible by computation of its inverse elements [102]

$$(G^{-1})_{rs} = \sum_{i=1}^{3N} m_i \frac{\partial x_i}{\partial q_r} \frac{\partial x_i}{\partial q_s}, \quad (1.5)$$

i.e. using finite differences with a displacement of the molecular structure along the coordinates q . In contrast to \hat{T}_x , \hat{T}_q contains cross partial derivatives of two coordinates r and s , originating from non-orthogonal connections of Cartesian components and representing a kinetic coupling between the coordinates r and s . In this formulation, it is mandatory to satisfy the Eckart conditions [103], which separate internal degrees of freedom from the external rotational and translational ones. This ensures that the coordinate transformation is unique and thus reversible, which keeps the G-Matrix invertible. An implementation on how to perform this separation is given in Refs. [104, 105].

For the studies on uracil presented in chapter 3, the two-dimensional coordinate space consists of two linear coordinates, which makes the computation of G_{rs} simple as the diagonal and off-diagonal entries do not change along the particular coordinates. For the non-linear IRC used in chapter 2, G_{rs} is position dependent and the inverse elements were calculated separately at each grid point.

4. Sample environmental configuration

In order to draw meaningful conclusions about ultrafast processes in environment, the effect of a thermodynamic ensemble on the quantum system has to be sampled. This means that in the framework of the QD/MD approach, where the time evolution of a molecular WP is simulated within its microscopic solvent cage, this has to be done not only for one configuration, but for an ensemble of configurations until some degree of convergence is reached. In connection with equation (1.2), multiple propagations must be performed, each one with different atomic positions R^E of the environment and thus a different potential energy operator $\hat{V}_{tot}^{ES}(R_q^S, R^E)$. The thermodynamic configuration space of the environment is sampled using classical molecular dynamics (MD) simulations, where the individual atoms are represented by point masses and charges, and the time evolution occurs according to Newton's equations of motion. The forces determining the movement are calculated using so-called force fields, which define the bonding and non-bonding interactions for each type of atom. Force fields usually apply to a rather specific type of problem, where the parameters for these classical interactions are derived e.g. from extensive QC studies. In case of the studies presented in chapter 2 the OPLS-AA force field [106] was used, which was optimized for organic solutions of typical solvents like tetrahydrofuran (THF). For the biologic RNA/water environment in chapter 3.2, a combination of two force fields was used. The AMBER14SB force field [107–110] was employed to simulate the RNA strand, while the interactions with water occurred according to TIP3P [111].

Since the quantum WP evolution of the solute will be simulated later according to the TDSE, its geometry is frozen during the classical MD propagation. This will slightly influence the interactions with the environment and affect the trajectory, but ensures comparability since all WP propagation start from the same initial state. The freeze was performed using the RATTLE algorithm [112], introducing constraints by a Lagrange multiplier formalism. RATTLE works in combination with the Velocity Verlet integrator [113] for the actual integration of the equations of motion, while there are other implementations if different integrators are used [114]. To keep the whole system at room temperature, the Berendsen thermostat [115] was used, and all MD simulations were performed with the program package GROMACS [116].

A proper sampling of the configuration and phase space necessitates the exclusion or minimization of biases. Several measures have thus been taken. After a proper equilibration time, multiple trajectories were started from different initial geometries and each with random starting velocities. From all trajectories, snapshots of the current geometries were taken at random times and from well-separated intervals to avoid unwanted correlations. In each study, the taken sample size was later checked for convergence with respect to the extracted observable quantity. At this, it should be noted that while the environmental configuration space is huge, not every individual solvent cage has its unique influence on the ultrafast process. The configuration space is thus be reduced to an effective one, spanned not by the possible environmental geometries but rather the different effects on the PES, which significantly accelerates convergence.

5. Compute potential energy surface

The PES within each individual snapshot is calculated by means of (multiscale) QC. In the original implementation of the QD/MD approach [76], the environmental influence was computed separately and beforehand. This means the potential energy operator is split into two terms

$$\hat{V}_{tot}^{ES}(R_q^S, R^E) = \hat{V}_{mol}^S(R_q^S) + \hat{V}^E(R^{SF}, R^E), \quad (1.6)$$

with $\hat{V}_{mol}^S(R_q^S)$ noting the PES of the molecular system in vacuum and in reduced coordinates, and $\hat{V}^E(R^{SF}, R^E)$ including the environmental influence. The reactant was partitioned into moieties F which do not change configuration over the course of the reaction, and for each possible orientation between a solvent molecule and a solute moiety an interaction energy $E(R^{SF}, R^E)$ was calculated. The total PES \hat{V}_{tot}^{ES} is then obtained by summation over each interaction energy according to their orientation in the current snapshot:

$$\hat{V}^E(R^{SF}, R^E) = \sum_{i=1}^{N^E} \sum_{j=1}^{N^F} E(R^{SF}, R^E). \quad (1.7)$$

This solvent potential is added to the molecular PES \hat{V}_{mol} , being computed in vacuum, to obtain the total potential operator according to equation (1.6). The intention behind this approach is a reduction of computational cost. If many single-point QC calculations have to be performed to obtain a single PES, as it can be the case for a higher-dimensional coordinate space, and if many snapshots have to be considered to sample the effective thermodynamic phase space, the net computational cost can get very high. Computing $E(R^{SF}, R^E)$ for each possible orientation beforehand and investing the time here, the actual assembly of \hat{V}^E after obtaining the snapshots is very fast. Additional to considerations of computation time this approach works well under two conditions, namely if the environment is composed of many molecules of the same type (e.g. a chemical solution), and if the reactant can be partitioned into few approximately static moieties.

Another and more direct approach, on condition of being computationally feasible, is to directly calculate \hat{V}^E or V_{tot}^{ES} within each individual snapshot. The quantum system geometry is displaced according to the vectors spanning the low-dimensional coordinate space, while satisfying the Eckart conditions [103] and keeping the environment frozen. This has been done for the RNA/water environment in chapter 3.2, as it is not possible to be separated into many small non-interacting parts of the same type. \hat{V}^E was computed using QM/MM, with the high-level region incorporating uracil and its neighboring bases along with the strand backbone on the DFT level,

and by subtracting the DFT PES of isolated uracil. This yields \hat{V}^E representing only the influence of the environment, which was added to the excited state \hat{V}_{mol}^S of uracil to obtain V_{tot}^{ES} .

For the chemical reaction in chapter 2, V_{tot}^{ES} was computed directly within each snapshot, treating the reduced microsolvation shell on the same methodical level as the reactant itself. For the microsolvation shell, a cutoff-distance r_{cutoff} was defined, which was measured between the closest two atomic centers of reactant and solvent molecule. If there is an atom of the solvent molecule which is closer to a reactant atom than r_{cutoff} , the whole solvent molecule was regarded in the microsolvation shell, while all other solvent molecules were discarded. This selection procedure is drawn in Figure 1.2 at the molecular example which was used in chapter 2. Here, a cutoff-distance of 7.5 Å was used, resulting in snapshots consisting of 200-300 atoms.

The reaction takes place in the electronic ground state and is represented by a one-dimensional reactive coordinate, rendering the computation of the total PES in each separate snapshot not too costly. The three presented possibilities of obtaining V_{tot}^{ES} — direct computation of V_{tot}^{ES} in each snapshot, direct computation of \hat{V}^E in each snapshot, and indirect computation of \hat{V}^E by summing over individual interaction energies according to equation (1.7) — constitute three different tools of incorporating the effect of an explicit environment on reactive processes, where the particular usage can be chosen according to the characteristics of the specific process and after evaluating the accuracy to cost ratio.

Lastly, it should be noted that at the computation of any PES, it is not necessary to perform a QC calculation at every point of the discretized grid being used for WP propagation in the end. The potential energy can rather be evaluated at much fewer points of the grid and interpolated afterwards using for example cubic splines [117, 118], moving least squares [119, 120] or polyharmonic splines [121]. The sampling by QC calculations is dependent on the structure of the PES, which becomes harder to evaluate in higher dimensions. Recent advances conveniently introduced an adaptive scheme being able to decide automatically how sparse the sampling can be performed for successful interpolation afterwards [122].

6. Choose initial wavepacket

The starting WP is chosen according to the process to be simulated. It is often reasonable to start from the lowest vibrational eigenfunction of the electronic ground state, as it is the most representative state for a relaxed molecule at room temperature. It can also be sensible to start from a combination of eigenfunctions, depending on the circumstances under which the process is simulated. As eigenfunctions play a major role in WP composition and their analysis, there exist several methods to calculate them, such as the Fourier grid Hamiltonian [123] or propagation in imaginary time [124].

7. Wavepacket propagation

The propagation of the WP itself is performed according to the TDSE, as it is written in equation 1.2. The setup of \hat{T}_q was discussed on page 7, and on page 9 ways to obtain V_{tot}^{ES} were laid out. The laser field $\varepsilon(t)$ is constructed according to the corresponding experiment, and μ_q are the matrix elements of the dipole operator in the reduced-dimensional coordinate space, also obtained with the means of QC. The actual solution of the TDSE is performed by using the Chebychev propagation scheme [44], expanding the time evolution operator $\hat{U}(t) = \exp(-i\hat{H}t)$ in a Chebychev poly-

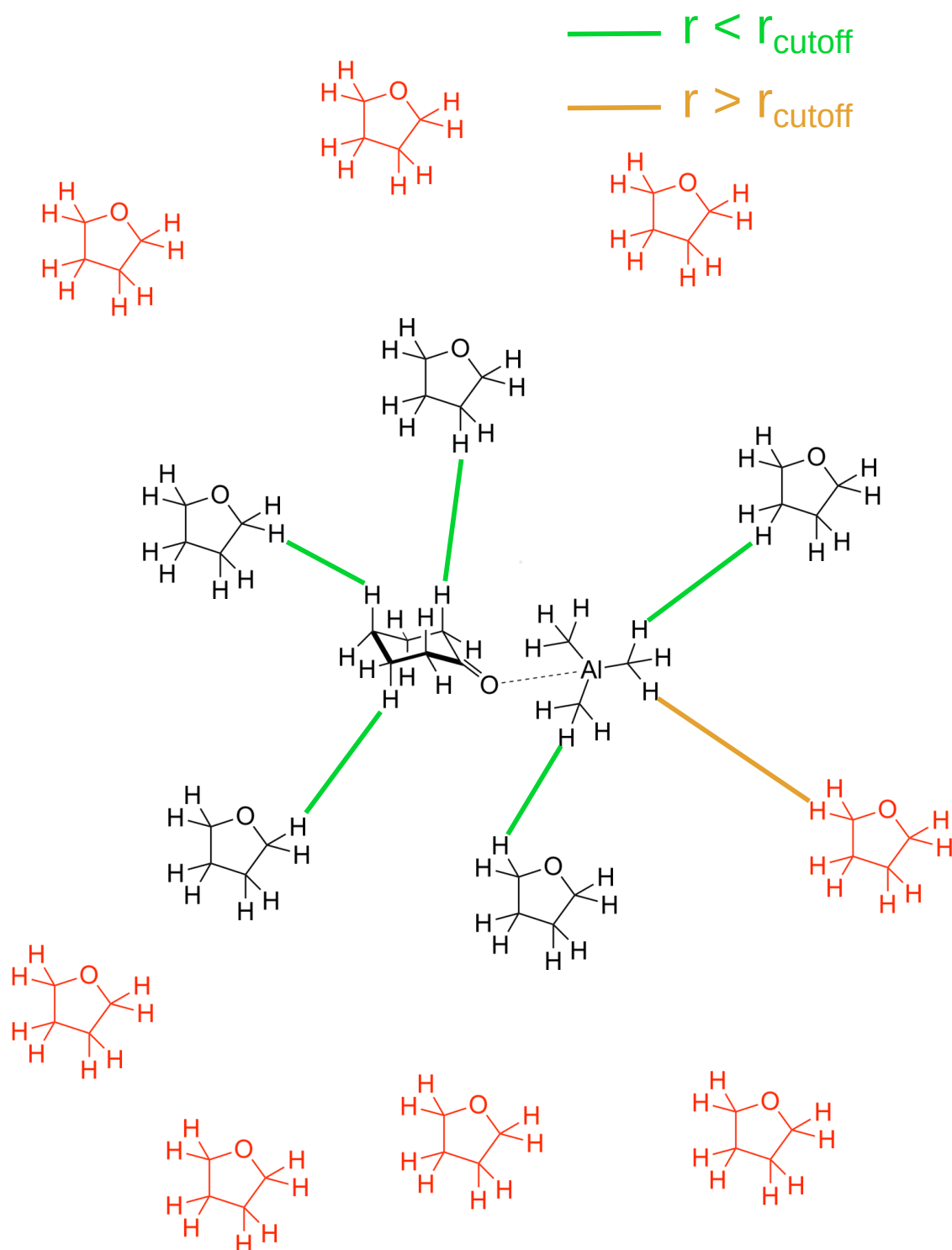


Figure 1.2.: Selection procedure to set up the microsolvation shell within which V_{tot}^{ES} is calculated directly. The reactant (cyclohexanone and trimethylaluminum) is drawn in the middle, with THF molecules surrounding it. All THF molecules which have an atomic distance closer than r_{cutoff} to any reactant atom are kept (black), while the other solvent molecules (red) are discarded.

mial series. The advantage in contrast to other common propagation schemes is that in principle arbitrarily large time steps can be chosen, limited only by the amount of Chebychev polynomials which must be employed to support it [44]. Another feature of this propagation scheme is its scaling with the minimum and maximum values in the potential operator, which can make it beneficial to introduce cutoff energies in regions which the WP does not reach.

8. Laser pulse optimization

The formalism which was used to optimize laser pulses in all studies is OCT [39, 46, 125–127]. Its application to molecular examples are reviewed extensively in Refs. [48, 128], and also discussed in the various publications reprinted in this thesis. There are several features of OCT which are beneficial to the intentions of the studies in this thesis. On one hand, the globality of the algorithm is useful for proof of principle and feasibility studies like the ones presented in chapter 2. If no laser pulse can be optimized with OCT for a specific control aim, it is likely not reachable within the given simulation framework. On the other hand, additions to OCT, like a frequency filter to restrict the pulse spectrum [48, 129] or the usage of a Gaussian shape function to keep the pulse envelope smooth [48], enable a much closer relation to experiments. As otherwise OCT is a purely mathematical procedure and does not necessarily yield experimentally feasible laser pulses, this is very beneficial in ensuring a close correlation to experiments, as it is demonstrated in chapter 3.1.

Chapter 2.

Quantum Control of a Methyl Transfer Reaction in Explicit Solvent Environment

In this chapter, two studies are presented which explore the capabilities of shaped laser pulses to control applied chemical synthesis. The prospect of reaching this aim always was one of the major driving forces in constant QOC development [21, 24]. While selective bond-dissociation [25] or isomerization [7, 27] have been achieved with laser pulses and can constitute key steps in chemical reactions, organic synthesis is often about forming new bonds — especially between carbon atoms — and about the relocation or transfer of chemical moieties. Control aims like these have not been reached to date, and QOC has not found broad application in chemical synthesis. Besides practical limitations, like an unclear and possibly high photon cost per mole of controlled matter, there exist conceptual limitations affecting the controllability. A possible source introducing complexity to the control task of a molecular system is its environment. One aspect of environmental influence can be investigated within the density matrix formalism [130–133]. Here, the quantum states of a molecular system are encoded in a density matrix, which can be coupled to an external bath. The time evolution of the density matrix and its interaction with light fields is described by the Liouville-von Neumann equation, as it is laid out e.g. in Ref. [134]. Over the course of the propagation, dissipation effects — caused by inelastic impacts with the surrounding — can constantly change the population of states within the density matrix. This adds increasing complexity to the control task, and quantum control simulations within this framework [135–137] usually ask and answer the question whether the problem of dissipative effects can be overcome [138–143].

Spectroscopically speaking, these effects correspond to a homogeneous line broadening of energetic levels. In contrast to that, the explicit QD/MD description of the environment enables for an investigation of inhomogeneous effects, as each specific molecule is considered within its own microscopic environment in a thermodynamic ensemble. Each solvent cage has its specific influence on several molecular properties, severely complicating the control task as many different cases must be controlled simultaneously for efficient quantum control. This effect is analogous what has been observed by Berens and Wilson in 1981 for rotational states in a molecular gas phase ensemble [99].

The following two studies identify the inhomogeneous solvent environment as a major complication in quantum control optimizations. Besides exploring the extend of this influence, ways to design laser pulses capable of dealing with this problem are presented. By discussing both extreme scenarios and the statistical success of optimized laser pulses in the complete thermodynamic ensemble, an assessment is made about the feasibility of quantum control applied to chemical synthesis.

The model coordinate used to investigate these features is the one-dimensional non-linear IRC of a methyl group rearrangement between cyclohexanone and trimethylaluminum. The reaction is drawn in Figure 1 in the reprinted publication **1** in chap-

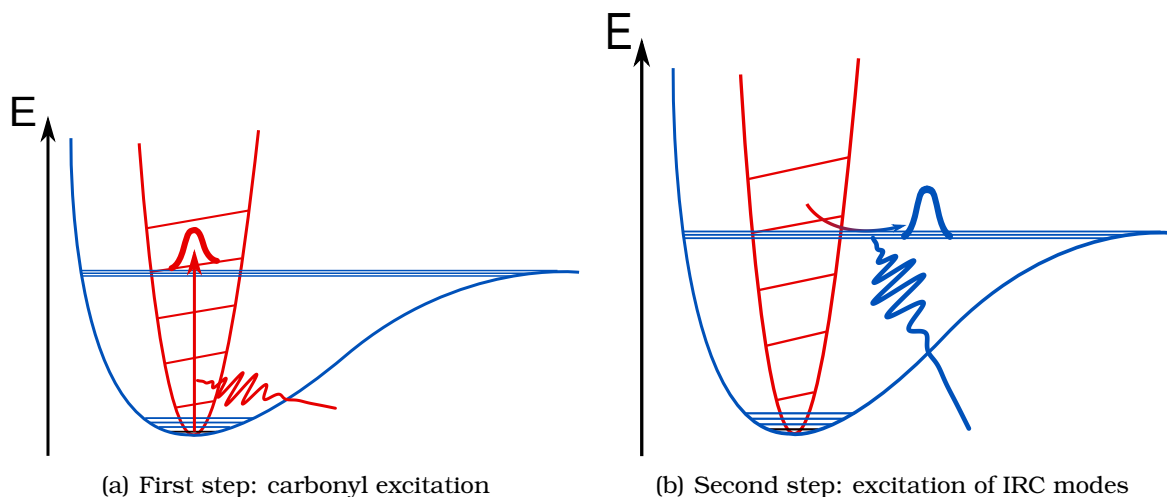


Figure 2.1.: Control scheme for the initiation of a methyl transfer reaction between cyclohexanone and trimethylaluminium. The IRC coordinate with the vibrational levels is drawn in blue, and the orthogonal carbonyl coordinate is drawn in red accordingly. The first step is vibrational ladder climbing in the carbonyl mode with an IR laser pulse up until $\nu=4$, which is sufficient to reach the transition state barrier. Step two uses a terahertz laser pulse to selectively excite the IRC modes and initiate the reaction by steering of the WP. This second step is heavily influenced by the explicit environment and is the model coordinate for the following studies investigating the feasibility of quantum control in solution.

ter 2.1. Quantum control of a bimolecular reaction is much harder to accomplish than the unimolecular examples of isomerization and bond cleavage. This is mainly due to diffusion processes in the sample, where two molecules finding each other and reacting is a rare event. In contrast to this, unimolecular reactions start from a defined ground state, which on one hand makes it easier for simulations as starting from a defined geometry is a reasonable setup, and the quantum yield in experiments is much higher because the laser pulse can be optimized for a rather fixed and representative scenario. The investigated methyl transfer between cyclohexanone and trimethylaluminium takes a step toward bimolecular reactions. The two molecules form a preallocated complex due to aluminium coordinating to the oxygen, which makes it reasonable to assume a fixed scenario for quantum control.

As the studies within the present chapter reveal, the IRC coordinate of the methyl transfer is heavily influenced by the environment, and thus well suited to investigate the environmental effects. However, being a low-frequency mode (≈ 0.02 eV), vibrational ladder climbing in the IRC is not sufficient to overcome the transition state barrier of about 0.7 eV and induce the reaction. Additional energy must be deposited to the molecule somehow, for example by exciting the easily accessible carbonyl mode as a first step, where it is sufficient to climb to $\nu=4$ to reach the transition state barrier. The carbonyl mode in this case hardly participates in the IRC and exhibits no coupling to it. It is also not affected by the explicit environment, which means this first excitation should be easily achievable experimentally in solution, and which also makes to carbonyl mode unsuitable for investigation of environmentally influenced quantum control. Nevertheless, in our proposed two-step mechanism sketched in Figure 2.1, the relevant IRC modes must be triggered after carbonyl excitation with

a second laser pulse. The environmentally influenced IRC mode is thus a well-suited model system — derived from an applied chemical process — to investigate the possibilities and limits of quantum control in these synthetically relevant systems.

2.1. Multi-Target Control of Several Solvent Cages by Simultaneous Vibrational Excitation

In the article “A multi target approach to control chemical reactions in their inhomogeneous solvent environment”, published in the *Journal of Physics B: Atomic, Molecular and Optical Physics*, the previously described methyl transfer reaction is introduced. The ground state process is represented by the one-dimensional potential along the IRC, which is recalculated for different snapshots extracted out of MD trajectories. Laser pulses are optimized to control the vibrational level population in the IRC, exploring the possibilities of selective excitation in several different snapshots simultaneously. The key points of the article are:

- The various solvent cages extracted from MD simulations can have significant effects on the reaction pathway. Spacing between vibrational levels can be doubled, and the harmonicity of the vibrational level structure is affected as well, both changing the characteristics of the control task. The environmental influence originates from solvent molecules — in this case THF moving in and out of the transfer pathway of the methyl group, leading to steric obstructions. In cases where there is no solvent molecule close to the reaction pathway, it behaves like in the isolated reactant.
- multi-target optimal control theory (MTOCT), originally developed for quantum computing applications with vibrationally excited molecules [144], proves as a valuable and fitting tool to handle the present case. The vibrational energy levels along the IRC in several different solvent cages are combined in the multi-target Hamiltonian, and laser pulses are optimized for vibrational ladder climbing in several different cases simultaneously. At this, it was possible to find laser pulses for efficient control even in the most complex cases.
- A statistical evaluation is presented to estimate the efficiency of the optimized laser pulses in the complete thermodynamic ensemble. It was found that significant population yield in the target level can already be achieved considering only few cases in the multi-target Hamiltonian. This suggests that the inhomogeneous influence of the environment can be controlled in principle with the flexibility of few-cycle terahertz pulses. Only little effort was made towards experimental accessibility of the pulses however.

Hereafter, the article “A multi target approach to control chemical reactions in their inhomogeneous solvent environment” published in the *Journal of Physics B: Atomic, Molecular and Optical Physics* is reprinted with permission from *J. Phys. B: At. Mol. Opt. Phys.* **2015**, 48, 234104. Copyright 2018 IOP Publishing.

A multi target approach to control chemical reactions in their inhomogeneous solvent environment

Daniel Keefer, Sebastian Thallmair, Julius P P Zauleck and Regina de Vivie-Riedle

Department Chemie Ludwig-Maximilians-Universität München, D-81377 München, Germany

E-mail: regina.de-vivie@cup.uni-muenchen.de

Received 21 April 2015, revised 6 August 2015

Accepted for publication 9 September 2015

Published 6 October 2015



CrossMark

Abstract

Shaped laser pulses offer a powerful tool to manipulate molecular quantum systems. Their application to chemical reactions in solution is a promising concept to redesign chemical synthesis. Along this road, theoretical developments to include the solvent surrounding are necessary. An appropriate theoretical treatment is helpful to understand the underlying mechanisms. In our approach we simulate the solvent by randomly selected snapshots from molecular dynamics trajectories. We use multi target optimal control theory to optimize pulses for the various arrangements of explicit solvent molecules simultaneously. This constitutes a major challenge for the control algorithm, as the solvent configurations introduce a large inhomogeneity to the potential surfaces. We investigate how the algorithm handles the new challenges and how well the controllability of the system is preserved with increasing complexity. Additionally, we introduce a way to statistically estimate the efficiency of the optimized laser pulses in the complete thermodynamical ensemble.

Keywords: coherent control, solvent environment, quantum dynamics, methylation reaction

(Some figures may appear in colour only in the online journal)

1. Introduction

Molecular systems and chemical reactions can be influenced by interacting with their quantum nature [1]. One well established method to achieve this is using shaped laser pulses [2, 3]. A perspective of their wide application range in molecular science is given in [4]. Successful applications reach from selective bond breaking in gas phase [5] over photoselective excitation in liquid phase [6] up to optical control in large biological systems [7]. In coherent quantum control, the pulses often act as photochemical reaction triggers in redistributing the population among electronic or vibrational states in a way which favors or enables the intended reaction pathway. The underlying mechanism is an interference of optical pathways and matter waves. For theoreticians, a well established method to apply coherent control and to tailor laser pulses is quantum optimal control theory (OCT) [8–17]. With an extension to the standard OCT

algorithm, i.e. multi target optimal control theory (MTOCT), it is also possible to require one laser pulse to attain multiple control targets simultaneously [18]. In this work, we use MTOCT to control the vibrational state population in a molecular system in an inhomogeneous environment. For a chemist, such an environment is an everyday case as chemical synthesis usually takes place in solution. Here, the inhomogeneous environment is created by the diversity of possible arrangements of solvent molecules around the reactant.

Chemical processes are susceptible to the various effects introduced by specific solvents [19]. One well known solvent effect is based on the electrostatic interaction between molecular dipoles. Certain structures along the reaction pathway may be stabilized or destabilized based on this influence [19–21]. Besides this, dynamic solvent effects arise during ultrafast processes taking place on a timescale reaching from femtoseconds to few picoseconds [22–26]. If molecular motions with major amplitudes happen within a short

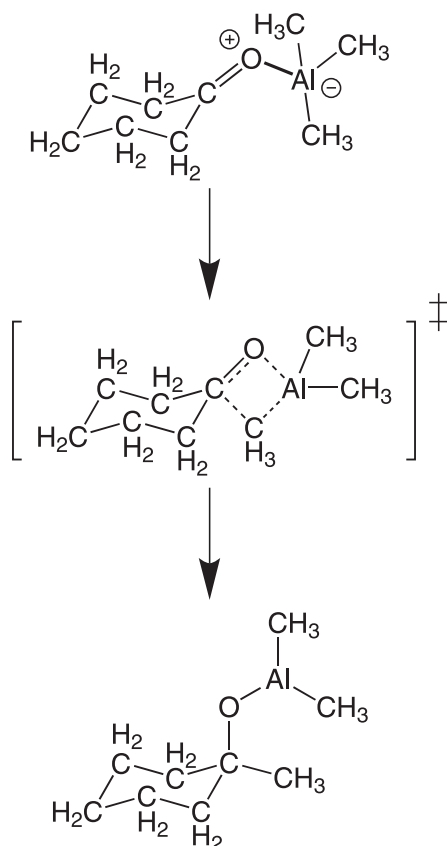


Figure 1. Methylation reaction with cyclohexanone (ChnO) and trimethylaluminum (AlMe_3). One methyl group of the AlMe_3 gets relocated to the ChnO ring.

timescale, local hindrance or preference of certain reaction pathways may be the consequence due to the steric effect of the solvent cage.

The system on which the present investigations are made is a methylation reaction of cyclohexanone (ChnO) and trimethylaluminum (AlMe_3) with tetrahydrofuran (THF) as solvent, where one of the methyl groups attached to the aluminium gets relocated to the ChnO ring. Figure 1 provides a schematic overview on the reaction. For a similar organo-metallic compound, infrared (IR) control investigations were made addressing the chemoselectivity of a Grignard reactant exposed to a composition of different cyclic ketones [27]. This class of reactions is also relevant for organic chemistry, as the addition of molecular fragments on carbonyl groups can be a convenient way to initiate chemical reaction chains [28, 29]. Additionally, the formation of carbon–carbon bonds is a big issue in chemical synthesis, and investigating new ways to accomplish this has led to several Nobel prize winning works [30–32]. Also, the addition of molecular fragments on functional groups often necessitates the elaborate usage of protecting groups [33], for example in the total synthesis of natural products [34, 35]. Laser control potentially offers an efficient alternative for the discrimination between chemically similar functional groups [27].

As the controlling laser pulses are highly specific to the problem they are optimized for, an accurate theoretical

description of the solvent effects is desirable. One approach to account for solvent effects in laser pulse optimizations is presented for example in [36, 37] and uses semi-classical on-the-fly dynamics combined with local control theory for the shaping of the electric field. Another commonly used approach uses density matrix theory [38, 39] to introduce a dissipative coupling to an external bath. Examples for molecular quantum control in dissipative systems can be found in [40–44]. From a spectroscopical point of view, this method describes homogeneous broadening. An inhomogeneous broadening, which arises from different microscopic surroundings for each molecule, is not described. In this work we present a new approach that takes into account the explicit solvent molecules and thereby inhomogeneous broadening. It relies on a method that combines a classical treatment of solvent molecules with a quantum dynamical treatment of the reactant (QD/MD approach) and has been introduced recently on the example of a photochemical bond cleavage via electronically excited states [26]. In the present work, we use this approach to set up the framework for vibrational quantum control investigations. Out of molecular dynamics (MD) trajectories, multiple solvent arrangements are extracted, where each of them alters the potential energy surface (PES) of the reaction individually and by that directly affects the vibrational level structure of the reactant. The complete solvent configuration space is reduced to its influence on the PES, resulting in an effective configuration space.

Several snapshots of the effective configuration space can be combined to approximate the thermodynamical distribution in solution. They are assembled in the multi target Hamiltonian to formulate a control problem representing the inhomogeneous environment of a chemical reaction in solution. Increasing inhomogeneity of the system leads to an increase in complexity of the control task, and the main questions which arise and to which this work will give insights and answers to are: How does the algorithm deal with the increasing inhomogeneity of the system, and to which degree is the controllability of the system preserved for an increasing complexity?

2. OCT for systems in inhomogeneous environments

To set up the multi target control problem, different solvent arrangements around the reactant were extracted from MD simulations. The reactant was located in the middle of the cubic simulation box (side length: 40 Å), and the box was filled with 291 THF molecules according to its liquid density of 0.89 g cm^{-3} at room temperature [45] (figure 2(a)). The reactant geometry and location was frozen during the MD simulations, as all QD simulations and laser excitation processes start from the molecular ground state minimum. The MD simulations themselves were conducted with the program package GROMACS [46], using the velocity-verlet-integrator [47] with a time step of 1 fs and the OPLS-AA force field [48]. The Berendsen thermostat [49] was included to couple the simulation box with an external temperature bath. To

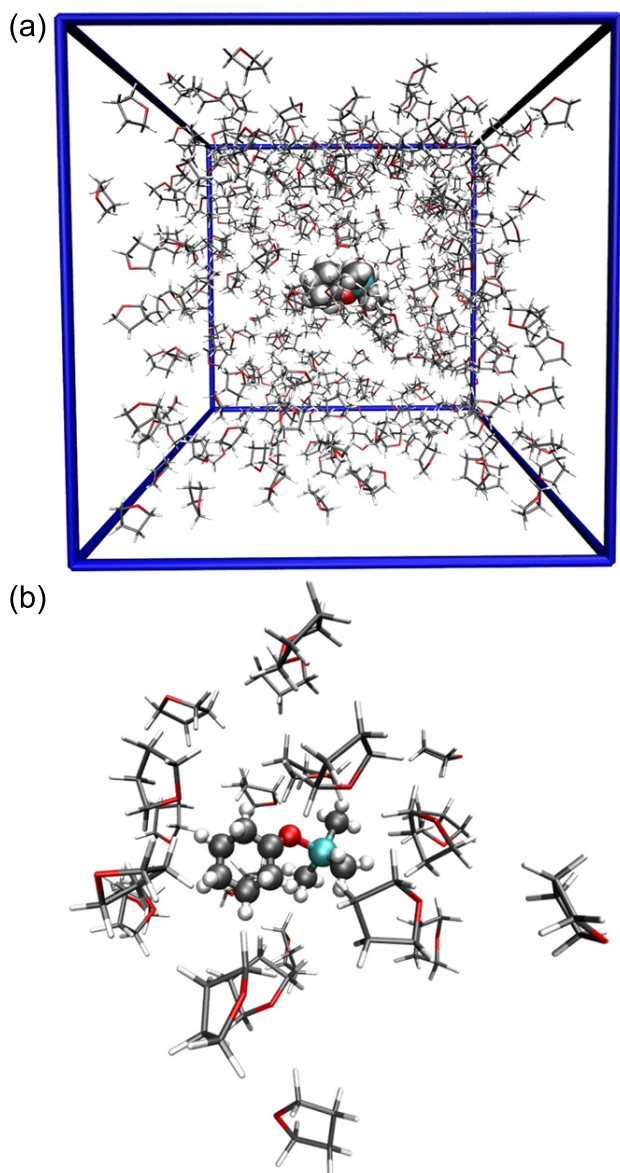


Figure 2. (a) Full size cubic MD simulation box with a side length of 40 Å. The reactant is located and frozen in the middle of the box, with the solvent molecules moving around it. (b) Exemplary snapshot taken at random time from the full simulation box, reduced to the essential solvent cage around the reactant.

avoid possible symmetrical interdependences within the simulation, several trajectories were started from different points in the phase space, each with random starting velocities. After equilibrating the system for 20 ps and monitoring the temperature, solvent arrangement snapshots were taken from the simulation box at random times, while accounting for a sufficient amount of decorrelation time. Within each snapshot, the amount of solvent molecules was reduced to the ones lying within a cutoff radius of 7.5 Å to allow only for the innermost solvation shells. The distance between fragment and solvent was determined between their closest two atoms. The solvent molecules with larger distance than the cutoff radius are discarded. Figure 2(b) provides a picture of an

exemplary solvent configuration. After the snapshots were extracted, the geometries and positions of the solvent molecules were frozen and the reaction process itself was treated. By freezing the solvent molecules in a first step, we neglect the homogeneous broadening, which makes our method complementary to the commonly used density matrix formalism. Our results show that the inhomogeneity of the surrounding has a tremendous effect on the PES and is an important issue.

The model coordinate we use to describe the carbon-carbon bond formation and in which the control optimizations are performed is the one-dimensional intrinsic reaction coordinate (IRC). In prospective experiments, it is primarily the carbonyl mode which will be addressed to overcome the energy barrier between the reactant and the transition state. First investigations on this mode revealed only a negligible influence of the solvent on the vibrational spectrum. Successful ladder climbing and selective excitation of the carbonyl mode in metal-carbonyl complexes has been observed experimentally, where both chirped IR-pulses [50–52] as well as IR pulse shaping techniques [53] were used. However, in order to steer the investigated molecular system into the direction of the transition state, backbone vibrations with major amplitude will have to be stimulated at some point. In contrast to the carbonyl mode, the effects of surrounding solvent molecules is expected to be large for those vibrations due to major amplitudes of the molecular movement. For the purpose of this work, which is to study how the OCT algorithm can deal with an inhomogeneous solvent environment, the IRC is an eligible coordinate. As the backbone vibrations which need to be activated in prospective experiments are included in the IRC coordinate, the corresponding control optimizations may give a first idea about the actualities to be encountered in experiments. In order to obtain the PES along this coordinate within a given snapshot, both the solute and all solvent molecules within the cutoff radius are treated quantum chemically. The minimum structure of the reactant in the respective solvent cage is replaced by different structures along the IRC path while complying with the Eckart conditions [54]. For the quantum chemical (QC) calculations we used the methods of density functional theory—as implemented in the program package Gaussian 09 [55]—with the M06-2X functional [56] and the 6-31G(d) basis set [57].

Out of the IRC, only the region between the reactant minimum and the transition state is considered. The reaction is assumed to proceed to the product state once the transition state is reached. Starting from the transition state region, the pure IRC is only defined until reaching the minimum structure. To keep the wave packet within the relevant region, a repulsive barrier behind the minimum is needed. Therefore, an extrapolation of the molecular geometry was conducted. The molecule was displaced along the opposite direction of the displacement vector pointing from the minimum geometry to the closest IRC point. A few examples of resulting PESs along the IRC in different solvent cages as well as the one in the gas phase are shown in figure 3. Each PES was set to zero energy at its own minimum. Two aspects attract attention in this figure: first, in general the interaction of the solvent

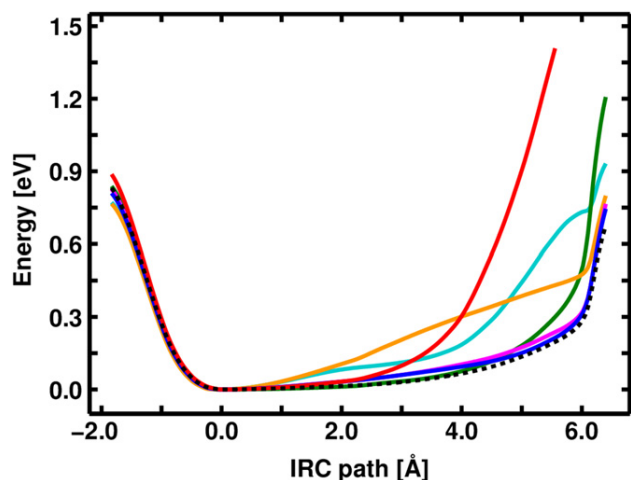


Figure 3. PESs along the IRC path in different solvent cages. The x-axis shows the total displacement relative to the minimum structure, with the transition state being located at around 6.2 Å. The black dashed line represents the PES of the reaction in the gas phase as a reference; cyan: snapshot 1; red: snapshot 2; blue: snapshot 3; magenta: snapshot 4; orange: snapshot 5; green: snapshot 6.

molecules on the solute hinders the reaction, which is indicated by the higher lying curves of the snapshots. In fact, out of all 15 snapshots which were investigated, there are only very rare cases of a PES lying partly and marginally lower than the one for the gas phase. The second aspect is that the shapes of the different snapshot PESs differ greatly from each other. This is due to solvent molecules hindering the reaction pathway at different states of the reaction, which is determined by the positions of the solvent molecules in a particular snapshot. Within the corresponding PESs, the vibrational eigenfunctions were calculated. They represent the different shapes of the PESs along the IRC in different solvent configurations.

The QD simulations and OCT optimizations for the different solvent configurations are performed in the eigenfunction picture. As a first approach for our investigations, we assume that there is no considerable motion of the solvent molecules during the optimization process. The Hamiltonian \hat{H}_{single} for a single solvent configuration contains the energy levels E_j of the j th eigenfunction, the transition dipole moments μ_{ij} between the eigenstates and the electric field strength $\varepsilon(t)$ of the applied laser field. With J being the number of eigenstates included and written in matrix form, the Hamiltonian reads

$$\hat{H}_{\text{single}}(t) = \begin{pmatrix} E_1 & 0 & \dots & 0 \\ 0 & E_2 & & \\ \vdots & & \ddots & \\ 0 & & & E_J \end{pmatrix} - \varepsilon(t) \begin{pmatrix} \mu_{11} & \mu_{12} & \dots & \mu_{1J} \\ \mu_{21} & \mu_{22} & & \\ \vdots & & \ddots & \\ \mu_{J1} & & & \mu_{JJ} \end{pmatrix} \quad (1)$$

$$= \underline{\underline{Q}}_n - \varepsilon(t) \underline{\underline{M}}_n, \quad (2)$$

To set up a multi target control problem, several of these snapshots are combined and the multi target Hamiltonian

$\hat{H}_{mt}(t)$ for MTOCT optimizations [17, 18] reads

$$\hat{H}_{mt}(t) = \begin{pmatrix} \underline{\underline{Q}}_1 & 0 & \dots & 0 \\ 0 & \underline{\underline{Q}}_2 & & \\ \vdots & & \ddots & \\ 0 & & & \underline{\underline{Q}}_N \end{pmatrix} - \varepsilon(t) \begin{pmatrix} \underline{\underline{M}}_1 & 0 & \dots & 0 \\ 0 & \underline{\underline{M}}_2 & & \\ \vdots & & \ddots & \\ 0 & & & \underline{\underline{M}}_N \end{pmatrix}, \quad (3)$$

where N is the number of snapshots included. This multi target Hamiltonian can be regarded as a Hamilton operator which acts on non-interacting systems.

Within the MTOCT formalism, many control aims can be addressed simultaneously [18]. The accordant term for the control aim $F[\psi_{i1}(t), \psi_{i2}(t), \dots, \psi_{iN}(t)]$ uses the initial wave functions $\psi_{ik}(t)$ and the predefined final target states $\phi_{fk}(T)$, whose overlap is to be maximized by the algorithm:

$$F[\psi_{i1}(t), \psi_{i2}(t), \dots, \psi_{iN}(t)] = \sum_{k=1}^N |\langle \psi_{ik}(t) | \phi_{fk}(T) \rangle|^2. \quad (4)$$

It contains a sum over all control objectives k , which in our case means a maximum amount of population yield Y in the target state $\nu = 4$ in all k snapshots.

Concerning the actual optimization algorithm, the Krotov method [58–60] has been used. The Krotov change parameter α was varied between 1 and 20 for the various pulse optimizations. It is part of a cost function within the OCT algorithm which amongst other things penalizes high pulse intensities. The central frequency of the initial Gaussian shaped guess pulses was set according to the energy of the $0 \rightarrow 1$ transition within a single snapshot, and in the case of multi target systems several guess pulses have been created according to these transitions. The full width at half maximum (FWHM) of the guess pulses was in a range between 0.8 and 2 ps. To keep the pulse complexity as low as possible, a frequency filter [27, 61] was used to suppress unnecessary overtone transitions. Additionally, to keep results on pulse optimizations comparable, the laser pulses were restricted to the same time duration of about 11 ps in all systems. The rotational relaxation time of common organic solvents is about 1 ps [62], which is shorter than this pulse duration. However, it was found experimentally in the example of $\text{W}(\text{CO})_6$ solved in n -hexane that the optimal pulse duration for laser pulses exciting a carbonyl mode is about 4 ps [53]. Additionally, the vibrational relaxation times being observed in this example were about 50 ps for $\nu = 3$, which is well above the pulse durations used here.

By optimizing a laser pulse for a specific number of L solvent arrangements simultaneously, a certain finite subset A_L of the effective configuration space is covered. The effective configuration space reduces the complete solvent configuration space to its influence on the PES. A method for obtaining a statistical estimate on the efficiency of the optimal pulse for the subset A_L in the effective configuration space is

introduced in the following. The estimate is based on the population yield $Y_{i \rightarrow j}$, which a laser pulse being optimized for snapshot i achieves in the target state of snapshot j . This yield $Y_{i \rightarrow j}$ will generally not be the same as $Y_{j \rightarrow i}$. Hence, there are two data sets which can be generated here, corresponding to the direction in which the yield is determined (i.e. for which snapshot of the pair i, j the pulse was optimized). With N being the amount of a random sample of snapshots, $N_C = (N(N-1))/2$ constitutes the number of pairs contained in the random sample. Note that these point pairs are not independent from each other, as changes in snapshot i will affect all $Y_{i \rightarrow j}$.

Within one data set, the population yields $Y_{i \rightarrow j}$ are evaluated to compute the empirical distribution function $F(y)$:

$$F(y) = \frac{1}{N_C} \sum_{i=1}^{N_C} \sum_{j>i}^1 \mathbf{1}\{Y_{i \rightarrow j} \leq y\}, \quad (5)$$

with y reaching from 0 (no population yield) to 1 (maximum population yield). For a given y , this empirical distribution function indicates the fraction of a random sample of $Y_{i \rightarrow j}$ having a lower or equal population yield than y .

To statistically estimate the population yield which a pulse being optimized for a subset A_L achieves in the effective configuration space, three requirements need to be met:

- (I) All snapshots in A_L are chosen randomly.
- (II) Out of all snapshots i contained in A_L , the population yield in an additional snapshot m is determined by the largest $Y_{i \rightarrow m}$.
- (III) Using the largest $Y_{i \rightarrow m}$, $Y_{A_L \rightarrow m}$ is calculated according to $Y_{A_L \rightarrow m} = Y_{i \rightarrow m} \cdot Y_{A_L \rightarrow i}$.

Due to (II), the probability for a snapshot m in the effective configuration space outside of A_L to have a lower yield than a given y is given by $F_L(y) = (F(y))^L$. For $N_C \rightarrow \infty$, its derivative gives the probability distribution $P_L(y)$ according to

$$P_L(y) = \frac{d}{dy} (F(y))^L. \quad (6)$$

The integral $\int_{y_0}^{y_0 + \Delta y} P_L(y) dy$ gives the probability of the optimal pulse for A_L to yield a population in the interval $[y_0; y_0 + \Delta y]$ for a random snapshot in the effective configuration space. The expectation value of $P_L(y)$

$$\langle y \rangle = \int_0^1 P_L(y) y dy \quad (7)$$

gives a mean value for the population yield which is achieved by this pulse in the complete space. If the optimal pulse for A_L yields a population of $Y_{A_L} = 100\%$ in its own system, it is estimated to yield a mean population $\langle y \rangle$ in an additional snapshot m within the effective configuration space. To estimate the population yield Y_{eff} , which this pulse is expected to achieve in the effective configuration space, the mean value $\langle y \rangle$ has to be multiplied by Y_{A_L} .

It should be noted that for a finite subset A_L the empirical distribution function is not continuous and therefore its derivative is ill defined leading to noise in a numerical derivative.

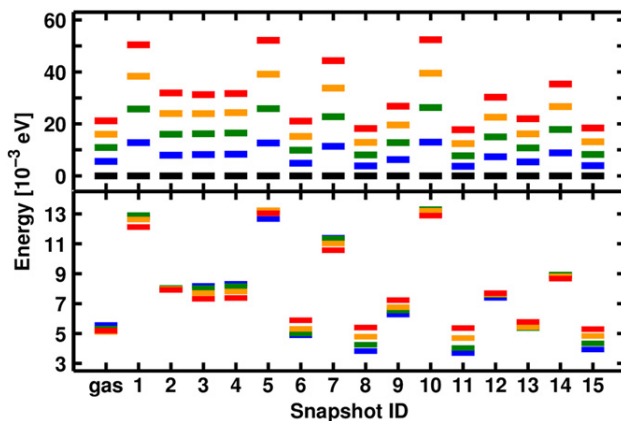


Figure 4. Top: energy levels of the five lowest vibrational eigenstates in different solvent configurations. Energies are relative to the lowest vibrational state within each snapshot. Black: $\nu = 0$; blue: $\nu = 1$; green: $\nu = 2$; orange: $\nu = 3$; red: $\nu = 4$. Bottom: transition energies for the lowest $\Delta\nu = 1$ transitions in each solvent configuration. The color code corresponds to the picture above, with the upper state of the transition being marked. Blue: $0 \rightarrow 1$; green: $1 \rightarrow 2$; orange: $2 \rightarrow 3$; red: $3 \rightarrow 4$.

As a result the obtained probability distribution $P_L(y)$ might not be normalized, which can be seen as a reflection of the imperfection of finite data sets. Thus, for the calculation of the expectation value $\langle y \rangle$ we suggest a renormalization of $P_L(y)$ beforehand.

3. Vibrational control in single solvent configurations

The individuality of the previously discussed PESs in the different solvent cages reflects itself in the vibrational state structure. In figure 4 (top), the energy levels for the five lowest eigenstates are presented for 15 snapshots which were investigated thoroughly in the scope of this work. A comparison among the given snapshots reveals a vast diversity in the energy spacing. In the most extreme cases, e.g. comparing snapshots 15 and 10, the spacing between the energy levels gets even more than doubled. Another aspect of the individuality of the solvent configurations can be seen in the bottom part of figure 4, where the $\Delta\nu = 1$ transition energies between the vibrational states are shown. While for example in snapshot 11 the transition energies are well spread, they are much closer to each other in snapshot 2, depending on the anharmonicity of the corresponding PES. This means that some solvent configurations offer the possibility to individually address the separate transitions, while in others the control task gets more complex due to an almost equidistant vibrational energy spacing. Based on these varieties depicted in figure 4, control tasks can be composed with different degrees of difficulty.

The mechanism by which the algorithm chooses to achieve the control aim (maximum population in $\nu = 4$) is presented in figure 5, which contains the results of a control optimization on snapshot 1 (PES with the cyan curve in

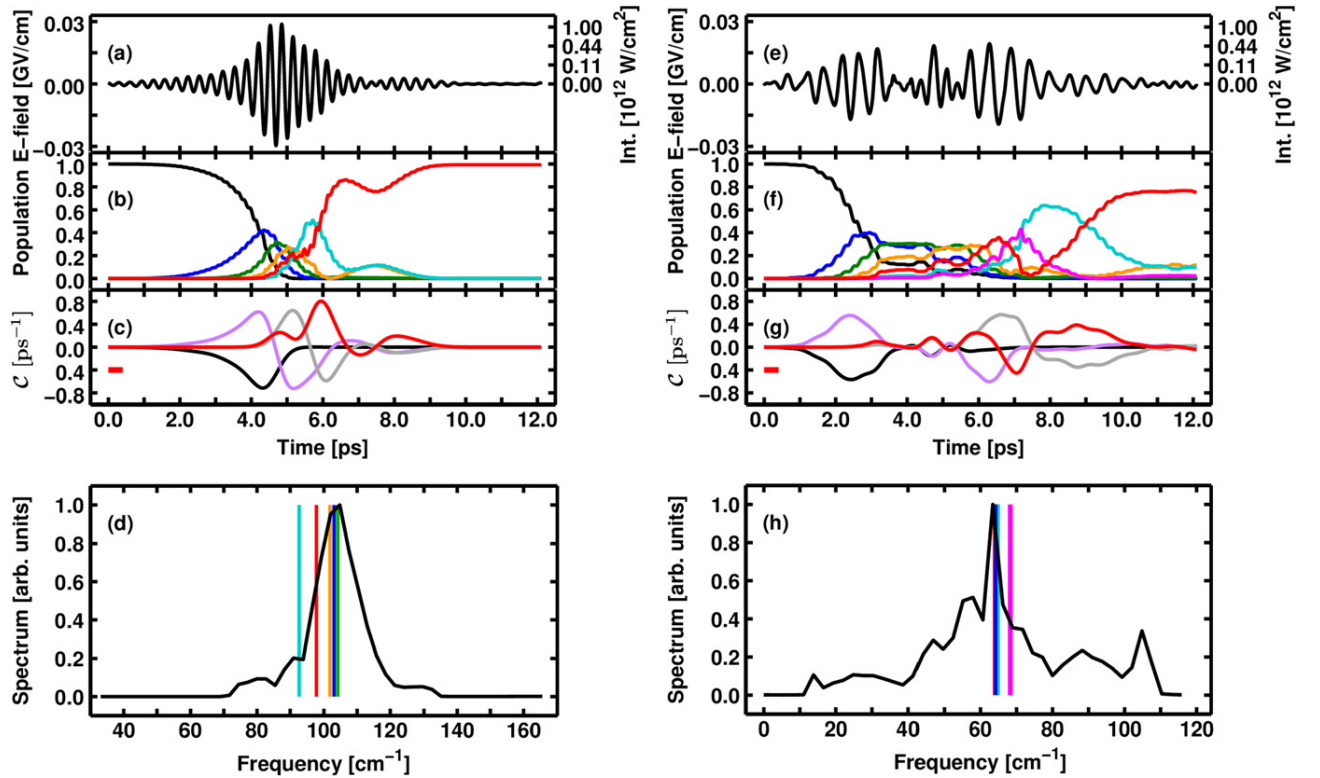


Figure 5. Laser control in snapshots 1 (left) and 2 (right). (a) and (e): Laser pulses transferring 99% (snapshot 1) and 76% (snapshot 2) population from the vibrational ground state $\nu = 0$ to the vibrational state $\nu = 4$. The intensity is implied in a quadratic scale. (b) and (f): Population evolution during the excitation process. Black: $\nu = 0$; blue: $\nu = 1$; green: $\nu = 2$; orange: $\nu = 3$; red: $\nu = 4$; cyan: $\nu = 5$; magenta: $\nu = 6$. Population of higher states is not depicted as they are not populated significantly. (c) and (g): Control indicator $\mathcal{C}(t)$ according to equation (8). The red bar indicates the FWHM of $g(t' - t)$; black: $\nu = 0$; violet: states from $\nu = 1$ to $\nu = 3$; red: $\nu = 4$; gray: states above $\nu = 4$. (d) and (h): Spectra (black) of the laser pulses shown in (a). The colored vertical bars correspond to the $\Delta\nu = 1$ transitions, with the higher of the two respective states adapting the color code according to (b); blue: $0 \rightarrow 1$, green: $1 \rightarrow 2$; orange: $2 \rightarrow 3$; red: $3 \rightarrow 4$; cyan: $4 \rightarrow 5$; magenta: $5 \rightarrow 6$. In (h), the $\Delta\nu = 1$ transition energies from $\nu = 0$ up to $\nu = 5$ overlap. The spectra of the pulses were restricted to an upper frequency of 135 cm^{-1} in snapshot 1 and 110 cm^{-1} in snapshot 2 to suppress overtones of these transitions.

figure 3). The controlling laser pulse is given in figure 5(a), its spectrum in figure 5(d) and the population evolution during the excitation process in figure 5(b). The pulse exhibits a rather smooth shape also reflected in the excitation process, which shows a typical ladder climbing mechanism [63]. At 5.5 ps, the laser pulse starts to discriminate between the neighboring states and shifts 99% population to the target state. The reason why this is easily achievable gets clear when inspecting the spectrum of the pulse (figure 5(d)). The $\Delta\nu = 1$ transition energies between $\nu = 0$ and $\nu = 3$ are very close to each other, which is why the pulse is able to address all these transitions with one frequency. Due to the $3 \rightarrow 4$ and $4 \rightarrow 5$ transitions (red and cyan bars) being more separate from each other, they are accessible without addressing the neighboring transitions as well, and thus without a competing population transfer back to the lower or further into higher states.

As a further evaluation tool for the control approach of the laser pulse, the time derivative of the population evolution is considered. At times where the absolute value of the derivative is large, the population in the respective state increases or decreases considerably, which means that the snapshot is affected by the controlling pulse at this time. The

laser field oscillations are also evident in the population evolution (see figures 5(b) and (f)) and would lead to many small peaks in the derivative, which makes an evaluation difficult. To overcome this, a convolution with a normalized Gaussian function $g(t' - t)$ is conducted to obtain the control indicator $\mathcal{C}(t)$. With the population yield $Y(t)$ and the time t , $\mathcal{C}(t)$ is calculated according to

$$\mathcal{C}(t) = \int_{-\infty}^{\infty} g(t' - t) \left(\frac{dY(t')}{dt'} \right) dt'. \quad (8)$$

with the Gaussian function

$$g(t' - t) = \frac{2\sqrt{\ln 2}}{\text{FWHM}\sqrt{\pi}} \exp \left(4 \ln 2 \left(\frac{t' - t}{\text{FWHM}} \right)^2 \right). \quad (9)$$

The FWHM of $g(t' - t)$ was chosen to be 0.4 ps. The result of this procedure is presented in figures 5(c) and (g), along with red bars indicating the FWHM of $g(t' - t)$. Showing $\mathcal{C}(t)$ does not provide additional information in the single snapshot cases, but it is a valuable tool when looking at multi target systems to properly resolve the times at which the laser pulse affects the system.

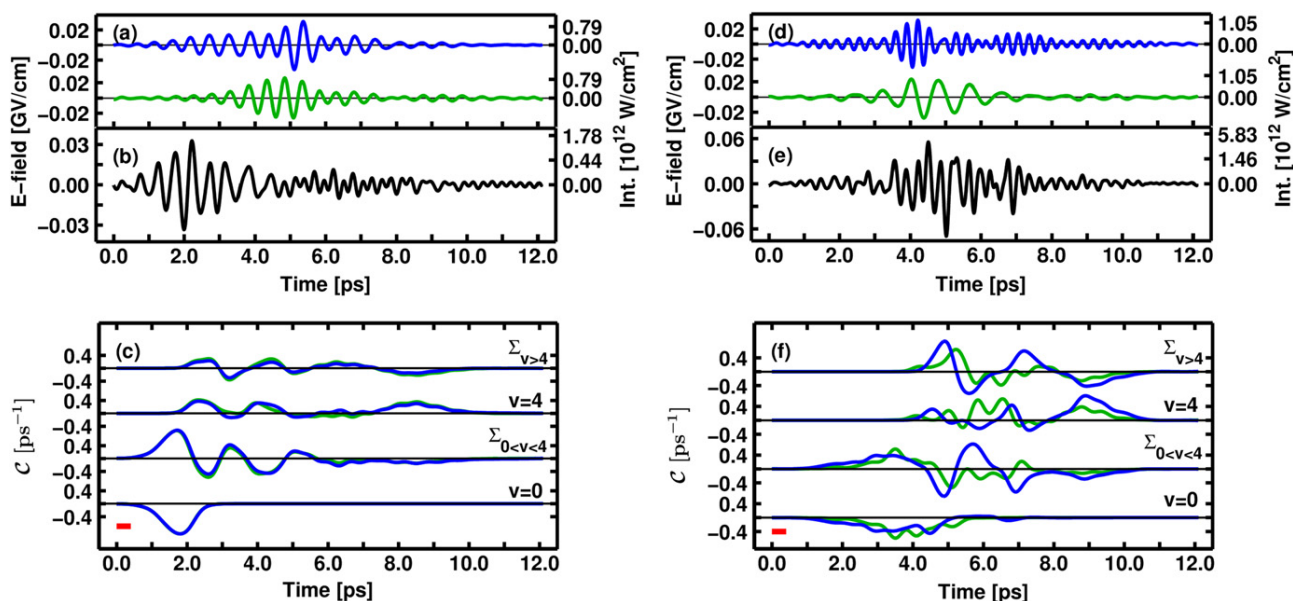


Figure 6. Laser control in multi target systems composed of snapshots 3 and 4 ($c2s$ system, left) and snapshots 5 and 6 ($c2d$ system, right). (a) and (d): Laser pulses which were optimized for a maximum population transfer in the respective snapshots; blue: laser pulses for snapshots 3 and 5; green: laser pulses for snapshots 4 and 6. (b) and (e): Laser pulses optimized for the $c2s$ and $c2d$ system, transferring close to 100% ($c2s$) and 98% ($c2d$) population from the ground state to the vibrational state $\nu = 4$. The intensity is implied in a quadratic scale. (c) and (f): Control indicator $\mathcal{C}(t)$ according to equation (8) during the excitation process for indicated states as labeled in the picture. Color code according to (a) and (d). The states from $\nu = 1$ up to $\nu = 3$ as well as the states above $\nu = 4$ have been summed. The red bars indicate the FWHM of $g(t' - t)$ according to equation (9).

Switching to another solvent cage with different properties, significant changes of the laser pulse properties and the control mechanism are observed. To emphasize the differences, the results of a control simulation on snapshot 2 (PES with the red curve in figure 3) are depicted in figure 5, with the controlling laser pulse in figure 5(e), its spectrum in figure 5(h) and the population evolution during the excitation process in figure 5(f). The laser pulse, while having about the same intensity as the one for snapshot 1 (figure 5(a)), exhibits a more complex shape with a kind of double pulse structure. This is reflected in the population evolution showing two time windows (around 2–3 ps and 7–9 ps) in which most of the population transfer happens. Another difference is that the final population yield in the target state (red) equals $Y_2 = 76\%$ here in contrast to the $Y_1 = 99\%$ in snapshot 1. Additionally, in snapshot 2 there is a significant intermediate population transfer to the $\nu = 6$ state (magenta). The reason for both differences lies in the $\Delta\nu = 1$ transition energies, which are shown in figure 5(h) along with the spectrum of the pulse. The $5 \rightarrow 6$ transition (magenta) is the only one being noticeably separate from the lower ones and thus the only one that can be addressed individually. This is why in the population transfer a detour via this state is chosen by the algorithm. Both transitions from the $\nu = 4$ target state to the neighboring states overlay with other transitions, and thus a complete population transfer to the target state through discrimination of neighboring states can not be achieved within the given pulse duration in the cost function.

The individuality of the previously discussed solvent configurations becomes even more noticeable when applying

the optimized laser pulses to the respective other snapshot. In both cases, the population yield $Y_{i \rightarrow j}$ in the target state is very close to zero, and in snapshot 2 the whole amount of population does not even leave the ground state because the $0 \rightarrow 1$ transition energy is outside the frequency range of the pulse. This demonstrates the necessity of using the multi target Hamiltonian and optimizing laser pulses which work on multiple snapshots simultaneously.

4. Simultaneous control in multiple solvent configurations

The laser pulse controlling two very similar—in terms of energy spacing—snapshots like 3 and 4 (combining 2 similar snapshots $\hat{=} c2s$ system, see figures 3 and 4) is presented in figure 6(b) with the black curve, along with the two laser pulses which were optimized for the separate solvent configurations (figure 6(a)). Although these two pulses are very much alike, the $c2s$ system pulse is a bit different as the region of maximum intensity is shifted to earlier times. The behavior of the pulse in this region is not changed considerably however, and the maximum intensity stays at about the same value. In terms of population yield in the target state, the laser pulse for the $c2s$ system achieves a value of $Y_{c2s} = 99\%$. To evaluate if there is a penalty in the population yield introduced by controlling both solvent configurations simultaneously compared to controlling them individually,

the preserve ratio p is introduced. It is given according to

$$p = \frac{Y_{A_L}}{\frac{1}{L} \sum_{i=1}^L Y_i}, \quad (10)$$

i.e. as the ratio of the achieved population yield Y_{A_L} in the target state of the multi target system to the sum over the yields Y_i achieved by individual optimal control of each snapshot included. In case of the $c2s$ system p is very close to one, which means that there is no penalty and the controllability is well preserved. However, when applying the optimal pulse for snapshot 3 to snapshot 4 and vice versa, the population yield is $Y_{3 \rightarrow 4} = 80\%$ and $Y_{4 \rightarrow 3} = 70\%$ respectively. This shows that the MTOCT algorithm has improved the laser pulse for the multi target system. From the control indicator $\mathcal{C}(t)$ in figure 6(b) it can be deduced that at all times the controlling pulse affects both snapshots (color code according to the laser pulses in (a)) almost identically.

The situation changes however when combining two solvent arrangements with different properties, as it is the case with snapshots 5 and 6 (combining 2 different snapshots $\hat{=}$ $c2d$ system, see figures 3 and 4). The optimal laser pulse for the $c2d$ system (figure 6(e)) is significantly different in comparison to the optimized pulses for the respective individual snapshots (figure 6(d)). The intensity is nearly doubled and the pulse structure is much more complex, not only in comparison with the single snapshot pulses but also with the laser pulse controlling the $c2s$ system. This reflects the increased complexity of the control task when treating snapshots with different energy spacing and anharmonicity. The major difference to the $c2s$ system however lies in how the laser pulse affects the system. To illustrate this, the control indicator $\mathcal{C}(t)$ for all important vibrational states is drawn in figure 6(f). Within the specific states the control indicators for the respective snapshots differ from each other. As the transition energies of the two snapshots are well separated, the laser pulse can act independently on the two subsystems. Additionally, the graphs imply that there is a higher fluctuation of population transfer compared to the $c2s$ system (figure 6(c)), indicating that the global control mechanism is not as straight forward. Nevertheless, the final population yield of $Y_{c2d} = 98\%$ is obtained in the target state $v = 4$, resulting in a preserve ratio of $p = 0.98$ and thus almost no penalty in population yield. An estimate on the population yield of the $c2$ pulses in the effective configuration space reveals similar Y_{eff} values of 9.4% ($c2s$ pulse) and 9.2% ($c2d$ pulse). Note that two data sets can be regarded at the calculation of $\langle y \rangle$ and Y_{eff} , as the second summation in equation (5) can be made over all $j > i$ or all $j < i$. The $\langle y \rangle$ values obtained by both data sets are similar to each other—i.e. 0.094 and 0.096 for the $c2$ systems—which is why average values between the two data sets are used.

To further increase the control task, three solvent configurations with differing properties were combined to one system, i.e. snapshots 4–6 ($\hat{=}$ $c3d$ system). The preserve ratio p also reaches a value of 0.98 here. The optimized laser pulse (figure 7(a)) exhibits a pulse structure with similar complexity to the laser pulse for the $c2d$ system, but has a higher intensity

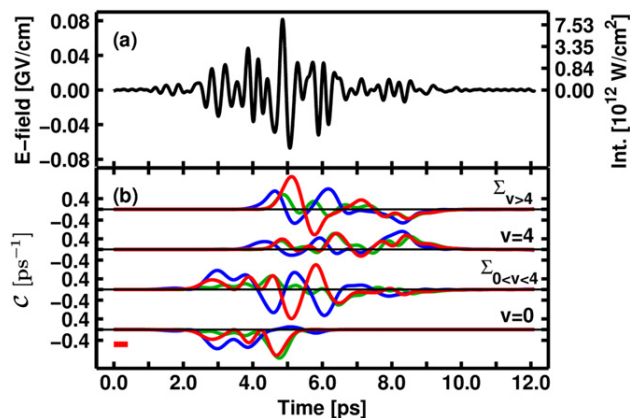


Figure 7. Laser control in a system composed of snapshots 4–6 ($c3d$ system). (a): Laser pulse optimized for the $c3d$ system, transferring 94% population from the ground state to the vibrational state $v = 4$. The intensity is implied in a quadratic scale. (b) Control indicator $\mathcal{C}(t)$ according to equation (8) during the excitation process for indicated states as labeled in the picture. Red: snapshot 4; blue: snapshot 5; green: snapshot 6. The states from $v = 1$ up to $v = 3$ as well as the states above $v = 4$ have been summed. The red bar indicates the FWHM of $g(t' - t)$ according to equation (9).

than the ones for the $c2$ systems. Inspecting the control indicator $\mathcal{C}(t)$ in figure 7(b), the curves for snapshots 5 (blue) and 6 (green) deviate from each other in all states and almost at all times, as it was the case in the $c2d$ system. The curve for snapshot 4 (red) however overlaps with the one for snapshot 6 at some times, e.g. in $v = 0$ around 5 ps, in the states higher than $v = 4$ ($\Sigma_{v>4}$) beyond 6.5 ps and in the target state $v = 4$ for most of the time. Generally it seems advantageous for the optimized pulse to realize the final population transfer into the target state simultaneously in all snapshots.

This behavior persists when incrementally adding more snapshots, as done to create the $c4d$, $c5d$ and $c6d$ system (for a detailed composition of these systems and the parameters of the controlling laser pulses, see table 1). For these systems, $\mathcal{C}(t)$ for the target state $v = 4$ is illustrated in figure 8 (all other states qualitatively show the same behavior). The curves for $\mathcal{C}(t)$ mostly evolve individually. There are times where multiple snapshots are controlled simultaneously, but there are no two snapshots where this is the case for the complete propagation time, as it is the case in the $c2s$ system. Another interesting fact can be spotted when focusing on snapshot 4 (red curve) and snapshot 6 (green curve). They do not exhibit the same extent of simultaneous behavior in the $c4d$ system (figure 8 bottom) as they do in the $c3d$ system (7(b), $v = 4$). This trend continues in the $c5d$ system, where they evolve quite different from each other. Thus a roughly similar treatment of two snapshots in one multi target system does not entail them being treated similarly when adding other snapshots with different properties to the system.

Another interesting aspect can be seen when comparing pulse intensities, which enter the OCT functional via the cost function. To ensure comparability, the cost function was kept similar for all pulse optimizations. The intensity values for the optimized pulses of all discussed systems are listed in table 1.

Table 1. Details on OCT optimizations for different control systems. The maximum pulse intensities of the optimized pulses are shown, as well as the yield in the target state $\nu = 4$. The preserve ratio p is given according to equation (10). The mean value $\langle y \rangle$ is given according to equation (7) and indicates an estimate of the fraction of the efficient configuration space which is covered by the pulse. The rightmost column specifies the population yield Y_{eff} which the pulse is estimated to achieve in the effective configuration space.

System ID	Included snapshot IDs	Max. pulse int. (10^{12} W cm $^{-2}$)	Y (%)	p	$\langle y \rangle$	Y_{eff} (%)
1	1	1.17	99.4	1.00	0.040	3.95
2	2	1.53	76.3	1.00	0.040	3.03
3	3	1.47	99.1	1.00	0.040	3.93
4	4	0.92	99.0	1.00	0.040	3.93
5	5	1.98	99.0	1.00	0.040	3.93
6	6	1.01	99.9	1.00	0.040	3.97
<i>c2s</i>	3; 4	1.48	99.0	> 0.99	0.095	9.4
<i>c2d</i>	5; 6	6.33	97.7	0.98	0.095	9.2
<i>c3d</i>	4; 5; 6	11.12	97.4	0.98	0.122	11.9
<i>c4d</i>	4; 5; 6; 7	12.90	97.1	0.97	0.150	14.6
<i>c5d</i>	4; 5; 6; 7; 8	12.75	96.6	0.97	0.178	17.2
<i>c6d</i>	4; 5; 6; 7; 8; 9	10.94	94.0	0.94	0.205	19.2
<i>c16</i>	Complete set specified in figure 4	7.86	63.8	0.66	0.368	23.5

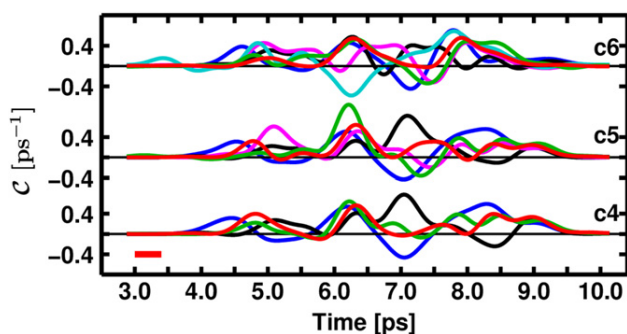


Figure 8. Control indicator $\mathcal{C}(t)$ (see equation (8)) for the target state $\nu = 4$ in systems consisting of 4 (*c4d*, bottom), 5 (*c5d*, middle) and 6 (*c6d*, top) snapshots. A laser pulse was optimized for each multi target system, and the graphs in this figure correspond to the control indicator of the optimized pulses. For a detailed list of included snapshots and characteristics of the controlling laser pulse, see table 1. Red: snapshot 4; blue: snapshot 5; green: snapshot 6; black: snapshot 7; magenta: snapshot 8; cyan: snapshot 9. The red bar indicates the FWHM of $g(t' - t)$ according to equation (9).

The maximum pulse intensities for the single snapshots and the *c2s* system with the homogeneous environment are comparable. For the increasing complexity in the *c2d* and larger systems higher intensities are used. However, in the row of increasing difficulty from the *c3d* to the *c16* system, the pulse intensity does not increase continuously. For example, the intensity of the *c5d* pulse is higher than the one of the *c6d* pulse, although all snapshots of the *c5d* system are included in the *c6d* system. Despite similar pulse intensities the increasing control demand can be overcome. Nevertheless, the preserve ratio p is slowly decreasing with an increasing complexity and reaches a value of 63.8% for the *c16* system. Considering the great diversity in the properties of the snapshots, the controllability is still preserved to a remarkable extent.

So far the snapshots from the *c2d* up to the *c6d* system were not chosen randomly but with an as different as possible energy spacing of the vibrational levels. A random choice of snapshots allows for similar snapshots being included in one multi target system. Thus the estimated population yields Y_{eff} are expected to be higher than the respective ones listed in table 1 if the snapshots are chosen randomly. For a given number of snapshots, there are two factors that determine the efficiency of the optimized laser pulse for the effective configuration space. On one hand, a larger fraction of the effective configuration space is covered when more and more snapshots are included. On the other hand, an increasing number of snapshots entails a more difficult control task, resulting in lower population yields Y_{A_L} . As a result, Y_{eff} increases by about 10% from the *c2d* to the *c6d* system, and by only 4% to the *c16* system. Encouragingly, for the *c6d* system already an estimated population yield of $Y_{\text{eff}} = 19.2\%$ is sufficient for prospective experiments. With a consecutive application of the same pulse, 15 repetitions will achieve an overall yield of 95% in the experimental sample volume covered by the focus of the laser beam.

5. Summary

The present work deals with the effects of an inhomogeneous environment—e.g. as introduced by solvent surroundings—on a chemical reaction and the resulting challenges for vibrational control. We present an approach to handle these challenges for laser control. The recently developed QD/MD ansatz [26] is used to explicitly include THF solvent molecules in the theoretical treatment of the carbon-carbon bond formation between cyclohexanone and trimethylaluminium. Therefor fifteen solvent arrangements were extracted from MD snapshots. Geometries along the gas phase IRC, which we used as our model coordinate,

were inserted into the extracted solvent cages while accounting for the first solvation shell to test the environmental influence. Within each snapshot, the PES along the IRC including the explicit solvent environment was calculated quantum chemically. This reduces the complete solvent configuration space to its influence on the corresponding PESs, leading to an effective configuration space. The different shapes of the PESs directly affect the vibrational level structure. Large differences both in the magnitude of the energy spacing as well as in the anharmonicity and the absolute energetic position were found. Based on these findings, a qualitative statement on the challenges for the control task can be made.

The MTOCT formalism was used to address different solvent configurations at the same time. Laser pulses were optimized for vibrational ladder climbing in the molecular system in different solvent arrangements simultaneously. The optimization aim was to transfer the population to the vibrational state $\nu = 4$ in every snapshot. Control tasks with different degrees of complexity were formulated by combining several snapshots with different energy spacing of the vibrational levels in a multi target system. One prominent feature was that the pulse was switching its focus in between the snapshots during the optimization. The increasing inhomogeneity of the environment entailed more complex pulse structures, while there was only a slight decrease of population yield in the target state. Even in a system containing sixteen random snapshots, the controllability of the system remained surprisingly high with a population yield of 63.8%.

A statistical estimate on how efficient the optimized laser pulses work for the effective configuration space was performed. Even for a multi target system consisting of only six different snapshots, a population yield of $Y_{\text{eff}} = 19.2\%$ was estimated. Assuming that only 1% of the excited molecules actually follow the reaction pathway to the desired product, 2000 consecutive pulses would achieve an overall product yield of 95%. With a common kilohertz repetition rate, only two seconds of laser application would be required. This shows that theoretically optimized laser pulses could be a promising future tool in chemical synthesis.

A few aspects for further improvement are planned in the future. Based on the statistical evaluation introduced in this work, an optimal number of snapshots for a given multi target system can be identified. With an increasing size of this system, the two competing factors of increasing degree of control difficulty and better sampling of the effective configuration space determine an optimal number of snapshots for a given cost function which defines the pulse duration and maximum intensity. Another aspect is the accuracy of the theoretical description of the reaction process, which can be increased by extending the dimensionality for the QD simulations. To also account for the homogeneous broadening arising from solvent dynamics, a simultaneous simulation of reactant and solvent can be aimed for.

Acknowledgments

Financial support by the Deutsche Forschungsgemeinschaft through the excellence cluster Munich-Centre for Advanced Photonics (MAP) and the SFB749 is acknowledged. We thank Paul Knochel for fruitful discussions.

References

- [1] Shapiro M and Brumer P 2012 *Quantum Control of Molecular Processes (2nd Revised and Enlarged Edition)* (Weinheim: Wiley-VCH Verlag GmbH & Co KGaA)
- [2] Brixner T and Gerber G 2003 *ChemPhysChem* **4** 418
- [3] Nuernberger P, Vogt G, Brixner T and Gerber G 2007 *Phys. Chem. Chem. Phys.* **9** 2470
- [4] Rabitz H, de Vivie-Riedle R, Motzkus M and Kompa K L 2000 *Science* **288** 824–8
- [5] Assion A, Baumert T, Bergt M, Brixner T, Kiefer B, Seyfried V, Strehle M and Gerber G 1998 *Science* **282** 919–22
- [6] Brixner T, Damrauer N H, Niklaus P and Gerber G 2001 *Nature* **414** 57
- [7] Herek J L, Wohlleben W, Cogdell R J, Zeidler D and Motzkus M 2002 *Nature* **417** 533
- [8] Tannor D and Rice S A 1985 *J. Chem. Phys.* **83** 5013
- [9] Peirce A P, Dahleh M A and Rabitz H 1988 *Phys. Rev. A* **37** 4950
- [10] Kosloff R, Rice S A, Gaspard P, Tersigni S and Tannor D J 1989 *Chem. Phys.* **139** 201
- [11] Brumer P and Shapiro M 1986 *Chem. Phys. Lett.* **126** 541
- [12] Shapiro M, Hepburn J W and Brumer P 1988 *Chem. Phys. Lett.* **149** 451
- [13] Zhu W, Botina J and Rabitz H 1998 *J. Chem. Phys.* **108** 1953
- [14] Zhu W and Rabitz H 1998 *J. Chem. Phys.* **109** 385
- [15] Sundermann K and de Vivie-Riedle R 1999 *J. Chem. Phys.* **110** 1896
- [16] Werschnik J and Gross E K U 2007 *J. Phys. B: At. Mol. Opt. Phys.* **40** R175
- [17] von den Hoff P, Thallmair S, Kowalewski M, Siemering R and de Vivie-Riedle R 2012 *Phys. Chem. Chem. Phys.* **14** 14460–85
- [18] Tesch C M and de Vivie-Riedle R 2002 *Phys. Rev. Lett.* **89** 157901
- [19] Reichardt C and Welton T 2011 *Solvents and Solvent Effects in Organic Chemistry* (Weinheim: Wiley-VCH Verlag GmbH & Co KGaA)
- [20] Sailer C F, Thallmair S, Fingerhut B P, Nolte C, Ammer J, Mayr H, de Vivie-Riedle R, Pugliesi I and Riedle E 2013 *ChemPhysChem* **14** 1423–37
- [21] Struebing H, Ganase Z, Karamertzanis P G, Sioukrou E, Haycock P, Piccione P M, Armstrong A, Galindo A and Adjiman C S 2013 *Nat. Chem.* **5** 952–7
- [22] Benjamin I and Wilson K R 1989 *J. Chem. Phys.* **90** 4176–97
- [23] Moskun A C, Jailaubekov A E, Bradforth S E, Tao G and Stratt R M 2006 *Science* **311** 1907–11
- [24] Zhang Y, Oliver T A A, Ashfold M N R and Bradforth S E 2012 *Faraday Discuss.* **157** 141–63
- [25] Thallmair S, Kowalewski M, Zauleck J P P, Roos M K and de Vivie-Riedle R 2014 *J. Phys. Chem. Lett.* **5** 3480–5
- [26] Thallmair S, Zauleck J P P and de Vivie-Riedle R 2015 *J. Chem. Theory Comput.* **11** 1987–95
- [27] Gollub C, Kowalewski M, Thallmair S and de Vivie-Riedle R 2010 *Phys. Chem. Chem. Phys.* **12** 15780
- [28] Metzger A, Bernhardt S, Manolikakes G and Knochel P 2010 *Angew. Chem. Int. Ed.* **49** 4665–8

- [29] Krasovskiy A, Kopp F and Knochel P 2006 *Angew. Chem. Int. Ed.* **45** 497–500
- [30] Grignard V 1900 *C. R. Hebd. Seances Acad. Sci. C* **130** 1322–4
- [31] Diels O and Alder K 1928 *Liebigs Ann. Chem.* **460** 98–122
- [32] Heck R F 1968 *J. Am. Chem. Soc.* **90** 5518–5526, 5531, 5538, 5542
- [33] Clayden J, Greeves N and Warren S 2012 *Organic Chemistry* (New York: Oxford University Press)
- [34] Ellerbrock P, Armanino N and Trauner D 2014 *Angew. Chem. Int. Ed.* **53** 13414–8
- [35] Hog D T, Huber F M E, Mayer P and Trauner D 2014 *Angew. Chem. Int. Ed.* **53** 8513–7
- [36] Curchod B F E, Penfold T J, Rothlisberger U and Tavernelli I 2011 *Phys. Rev. A* **84** 042507
- [37] Curchod B F E, Penfold T J, Rothlisberger U and Tavernelli I 2013 *CHIMIA* **67** 218–21
- [38] Fano U 1957 *Rev. Mod. Phys.* **29** 74
- [39] Blum K 1981 *Density Matrix Theory and Applications* (New York: Plenum)
- [40] Gao S, Strömquist J and Lundqvist B I 2001 *Phys. Rev. Lett.* **86** 1805
- [41] Ohtsuki Y, Nakagami K, Zhu W and Rabitz H 2003 *Chem. Phys.* **287** 197–216
- [42] Beyvers S, Ohtsuki Y and Saalfrank P 2006 *J. Chem. Phys.* **124** 234706
- [43] Tremblay J C and Saalfrank P 2008 *Phys. Rev. A* **78** 063408
- [44] Chenel A, Meier C, Dive G and Desouter-Lecomte M 2015 *J. Chem. Phys.* **142** 024307
- [45] O'Neil Merck Maryadele J and Co I E 2006 *The Merck Index: An Encyclopedia of Chemicals, Drugs, and Biologicals* (NJ, USA: Elsevier, Whitehouse Station)
- [46] van der Spoel D, Lindahl E, Hess B, Groenhof G, Mark A E and Berendsen H J C 2005 *J. Comput. Chem.* **26** 1701–18
- [47] Swope W C, Andersen H C, Berens P H and Wilson K R 1982 *J. Chem. Phys.* **76** 637–49
- [48] Jorgensen W L, Maxwell D S and Tirado-Rives J 1996 *J. Am. Chem. Soc.* **118** 11225–36
- [49] Berendsen H J C, Postma J P M, van Gunsteren W F, DiNola A and Haak J R 1984 *J. Chem. Phys.* **81** 3684
- [50] Witte T, Hornung T, Windhorn D, Proch D, de Vivie-Riedle R and Motzkus M 2003 *J. Chem. Phys.* **118** 2021
- [51] Witte T, Yeston J S, Motzkus M, Heilweil E J and Kompa K L 2004 *Chem. Phys. Lett.* **392** 156
- [52] Ventalon C, Fraser J M, Vos M H, Alexandrou A, Martin J L and Joffre M 2004 *Proc. Natl Acad. Sci. USA* **101** 13216–20
- [53] Strasfeld D B, Shim S H and Zanni M T 2007 *Phys. Rev. Lett.* **99** 038102
- [54] Eckart C 1935 *Phys. Rev.* **47** 552
- [55] Frisch M J *et al* 2009 Gaussian 09 Revision D.01 Gaussian Inc. Wallingford, CT
- [56] Zhao J and Truhlar D G 2008 *Theor. Chem. Acc.* **120** 215–41
- [57] Hehre W J, Ditchfield R and Pople J A 1972 *J. Chem. Phys.* **56** 2257
- [58] Tannor D, Kazakov V and Orlov V 1992 *Time Dependent Molecular Quantum Dynamics* (Sausalito, CA: University Science Books) pp 347–60
- [59] Somloi J, Kazakov V A and Tannor D 1993 *Chem. Phys.* **172** 85–98
- [60] Palao J P and Kosloff R 2003 *Phys. Rev. A* **68** 062308
- [61] Gollub C, Kowalewski M and de Vivie-Riedle R 2008 *Phys. Rev. Lett.* **101** 073002
- [62] Hornig M L, Gardecki J A, Papazyan A and Maroncelli M 1995 *J. Phys. Chem.* **99** 17311–37
- [63] Gollub C, Korff B M R, Kompa K L and de Vivie-Riedle R 2007 *Phys. Chem. Chem. Phys.* **9** 369–76

2.2. Including Fluctuations and Dynamics of the Solvent Environment

Building on the findings from the previous section, advances toward a mobile solvent environment are made in the article “Theoretical Quantum Control of Fluctuating Molecular Energy Levels in Complex Chemical Environments”, which has been submitted to the journal *Advanced Quantum Technologies*. In the previous article, the solvent cage — and thus also the energy level structure — was frozen during the QD propagation. In a more realistic case however, especially for timescales where molecular translation becomes relevant, the movement of solvent atoms should be included in the simulation protocol. In the article presented in this section, the snapshots from MD trajectories are not taken at random times, but after every 5 femtoseconds over a duration of 2.5 picoseconds. The PES and vibrational level structure is again evaluated for every snapshot, yielding the time-resolved influence of a single and mobile environmental configuration on the reaction process.

- Five different trajectories of 2.5 ps are inspected with respect to the fluctuation of the vibrational IRC levels. The timescale on which the level spacing changes from one extreme case to another due to the environment is revealed to be around 300 fs. As the controlling laser pulse achieving selective vibrational excitation is active for about 2 ps, this complicates the control task, as the addressed levels may fluctuate in and out of the pulse spectrum several times. Fluctuation patterns are observed to repeat in between trajectories.
- Different optimization strategies in the OCT framework are used to find laser pulses maximizing the population in $\nu=4$. Static solvent cages like in chapter 2.1 are used in single- and multi-target Hamiltonians, and different fluctuation patterns from the investigated trajectories are incorporated in the simulation. All optimized pulses — even the ones optimized only for static solvent cages — achieve a certain amount of population when applied to the fluctuating case.
- Different control strategies are suggested for possible experiments based on these findings. While some laser pulses are more efficient than others, all of them are efficient in a certain number of situations which they were not optimized for, hinting at a reasonable amount of controllability of a thermodynamic ensemble. There often is a trade-off between generality and complexity of laser pulses, i.e. more complex and intense laser pulses are efficient in a higher number of situations. While the concrete capabilities of experimental setups changes from lab to lab, this trade-off is very individual, where the present study suggests that decreased generality can be overcome by higher repetition rate or longer application times, as the environmental influence will switch to the optimized scenario at some time.
- Fluctuations were modified artificially from very fast to very slow oscillations compared to the pulse duration to check if there are timescales which the laser pulse can not handle. Control was found to be easier when the fluctuations are very fast or very slow compared to the pulse duration, while fluctuations on similar timescales emerged as the most complicated ones. Although more complex pulses are necessary to control these cases, vibrational excitation to the target level was achieved in all cases.

Hereafter, the article “Theoretical Quantum Control of Fluctuating Molecular Energy Levels in Complex Chemical Environments” submitted to the journal *Advanced Quantum Technologies* is reprinted.

WILEY-VCH

DOI: 10.1002/ ((please add manuscript number))

Article type: Full Paper

Theoretical Quantum Control of Fluctuating Molecular Energy Levels in Complex Chemical Environments*Daniel Keefer and Regina de Vivie-Riedle**

Department Chemie, Ludwig-Maximilians-Universität München, D-81377 München, Germany

E-mail: regina.de_vivie@cup.uni-muenchen.de

Keywords: coherent control, quantum dynamics, shaped laser pulses, solvent effects

Abstract text: In the present study, quantum control simulations are performed to explore the theoretical and practical limits of controlling applied synthetic chemistry in solution. The time-resolved influence of a molecular environment is revealed to fluctuate on a time-scale of few hundred femtoseconds. Laser pulse optimizations are performed for different control scenarios, giving general experimental guidelines on how to find a reasonable tradeoff between pulse complexity and population yield. Few-cycle flexible terahertz pulses are found to be capable of handling the complexities which are introduced by a fluctuating environment to the quantum properties of the molecular system. Besides the practical limitations in pulse generation and shaping, there seem to be no theoretical limits to controlling the investigated process with its environmental fluctuations. As the chosen model system involves a methyl group transfer and carbon-carbon formation, it stands representative for other commonly performed synthetic schemes in modern organic and pharmaceutical chemistry.

1. Introduction

In molecular quantum control, specifically shaped laser pulses are used to steer nuclear motion.^[1-4] Numerous successful experiments have been reported, ranging from selective photodissociation in the gas phase,^[5] controlled isomerization processes in the liquid phase^[6,7] or energy flow optimization in biological protein complex participating in photosynthesis.^[8]

WILEY-VCH

Going beyond selective bond cleavage or isomerization, the most ambitious goal in coherent control of molecules has always been to steer applied chemical synthesis. With modern synthetic chemistry becoming more and more sophisticated, for example in the preparation of pharmaceutically applicable molecules or natural products,^[9–11] each additional synthetic step increases the cost and lowers the product yield. Using tailored light fields to steer molecular motion by interacting with their quantum matter wave properties can potentially offer shortcuts to complex synthetic routes. Many efforts towards controlling chemical synthesis have thus been made, with the latest experimental study reporting vibrational acceleration of a bimolecular alcoholic ground state reaction leading to urethane formation,^[12] but concrete synthetic application has not been achieved to date.

While experimental development constantly increases the performance of modern light sources and improves pulse shaping techniques to generate more capable laser pulses, theoretical studies aim at revealing the mechanistic properties and difficulties of quantum control in solution and investigate whether they can be handled both in principle and practical. There exist different approaches to include environmental effects in quantum control simulations. Within the density matrix formalism, where Lindblad- and Redfield-type master equations simulate the temporal evolution of mixed and pure quantum state densities, system-bath interaction terms affect the population distribution and decoherence behavior of density matrix states. Effects which are described by this formalism are for example the dephasing influence of the environment on the molecular system, how this affects quantum control and whether this can be overcome by pulse shaping.^[13–18] Another approach uses the time-dependent Schrödinger equation (TDSE) to simulate the time evolution of the molecular quantum system, represented by the Hamiltonian, and explicitly includes solvent molecules in the computation of molecular properties.^[19,20] With respect to quantum control, this approach has been used to describe selective vibrational excitation of the carboxy-hemoglobin carbonyl mode within its protein environment,^[21] and for vibrational initiation of a methyl transfer reaction in a tetrahydrofuran

WILEY-VCH

(THF) solution.^[22] Different solvent configurations were found to influence the potential energy surface (PES), and thus the relevant properties for quantum control, in a similar fashion to the inhomogeneous line broadening in spectroscopy.^[23] In the latter study, the control strategy was to include multiple different solvent configurations in the laser pulse optimization to eventually converge to the thermodynamic distribution being present in a chemical flask and show that this complexity can be handled in general. The solvent molecules in this initial study were assumed to remain static during the picosecond control process.

The present study builds on the previous findings and further improves the theoretical description by including the time evolution of the explicit solvent molecules during the quantum control of the chemical reaction. The timescale on which the environmental influence changes between extreme cases is revealed. This has major implications for potential quantum control, which is discussed with respect to controllability. Besides examining this from a conceptual point of view, concrete and practical guidelines for potential quantum control experiments in solution are given.

2. Methodology

The theoretical approach in the present study uses a combined quantum dynamical treatment of the chemical reactant with a classical time-evolution of solvent molecules (QD/MD procedure).^[20] Our model coordinate uses the intrinsic reaction coordinate (IRC) of the methyl transfer in the gas phase depicted in **Figure 1**. We use the section between reactant and transition state, as after reaching the transition state with optical excitation, the reaction is assumed to evolve toward the product state. The molecular geometry is extrapolated from the reactant geometry using the negative IRC displacement vector. In this way, the potential curve depicted in Figure 1d is generated. Subsequently, the reactant molecule is placed in a MD simulation cube with 30 Å box length, which is then filled with THF molecules according to the liquid pressure of 0.89 gcm⁻³ at room temperature.^[24] The reactant is kept frozen, which can

WILEY-VCH

slightly affect the solvent movement in the MD trajectory but ensures comparability as all pulse optimizations start from the same ground state geometry. After an equilibration time of 20 ps the solvent molecules are propagated using the Velocity-Verlet integrator^[25] and the OPLS-AA force field^[26] as implemented in the program package GROMACS^[27]. Using five different initial starting geometries and random initial velocities, a current snapshot of the geometry is taken every 5 fs over a duration of 2500 fs. Each of the 500 solvent configurations is reduced to the nearest solvation shell, using a cutoff-radius of 8 Å between the closest two atoms of reactant and solvent. Subsequently, the potential energy curve of the IRC is reevaluated using density functional theory with the M06-2X^[28] functional and the 6-31G(d)^[29] basis set as implemented in the program package GAUSSIAN16,^[30] while satisfying the Eckart conditions to exclude the external translatory and rotatory degrees of freedom.^[31] All solvent molecules within the cutoff region are included in the QM system to account for quantum effects in the environmental influence. For each solvent configuration along the 2500 fs MD trajectory, the vibrational eigenfunctions were evaluated. Their absolute and relative energetic position serve both as a measure for the degree of the environmental influence and as a target for quantum control optimizations, since vibrational excitation is a common scheme in triggering ground state molecular processes.^[12,32,33] Although the one-dimensional nonlinear IRC does not resemble a molecular normal mode which is usually targeted by laser pulses, it is composed of a linear combination of these normal modes and contains all information about the molecular movement leading to the methyl transfer reaction. After depositing energy to the molecule, for example via the easily addressable carbonyl mode, these motions leading to the chemical reaction must be triggered at some point. The one-dimensional IRC can be regarded as a model coordinate derived from a real chemical process, which incorporates the relevant atomic motion in a compressed manner and is thus well-suited to investigate the environmental influence on such a process. Using the eigenfunctions as possible control targets serves as a convenient basis to investigate whether the arising complexities can be controlled.

WILEY-VCH

After evaluating the vibrational energy levels every 5 fs along the 2500 fs MD trajectories, they are concatenated and interpolated to obtain each vibrational level $E_n(t)$ as a function of time with the time step used in the QD simulation. The TDSE is solved using the Chebyshev propagation scheme,^[34] where the Hamiltonian in matrix representation reads

$$\hat{H}(t) = \hat{Q}(t) - \varepsilon(t) \cdot \hat{\mu} = \begin{pmatrix} E_1(t) & \cdots & 0 \\ \vdots & \ddots & \vdots \\ 0 & \cdots & E_n(t) \end{pmatrix} - \varepsilon(t) \cdot \begin{pmatrix} \mu_{11} & \cdots & \mu_{1n} \\ \vdots & \ddots & \vdots \\ \mu_{n1} & \cdots & \mu_{nn} \end{pmatrix}. \quad (1)$$

The matrix $\hat{Q}(t)$ contains the vibrational level energies of the IRC on its diagonal, where each level $E_n(t)$ exhibits its individual time-dependence due to fluctuations of the solvent molecules, and $\varepsilon(t)$ represents the electric field. The elements of the dipole matrix $\hat{\mu}$ show negligible fluctuation along the MD trajectory, which is why the time-dependence was discarded here.

In contrast another explicit scheme, where random snapshots along a MD trajectory are used to parametrize the environmental influence within a fluctuating Hamiltonian, here the molecular reactant is considered within its individual and mobile microscopic environment. The remaining approximation, in contrast to recent theoretical advances which simultaneously propagate QD and MD domains,^[35] is that the influence of the quantum system dynamics on the solvent environment is not included, as the reactant is kept frozen during the MD simulation.

The according Newtonian equation of motion reads

$$M_I \ddot{X}_I = -\nabla_I (\sum_J \hat{V}_{IJ}^E + \langle \psi^S(t_0) | \hat{V}_I^{ES} | \psi^S(t_0) \rangle), \quad (2)$$

where the interaction of quantum system S and environment E with particles I and J is always evaluated at the geometry used in the starting point t_0 of the QD propagation (i.e. the reactant geometry). The TDSE solved for the QD propagation reads

$$i\hbar \frac{\partial}{\partial t} \psi^S = \hat{H}(t) \psi^S = [\hat{H}_0 + V^{ES}(t)] \psi^S, \quad (3)$$

where the system wave function ψ^S evolves according to the Hamiltonian $\hat{H}(t)$ containing a time-dependent quantum mechanical interaction energy $V^{ES}(t)$ in the reduced solvent cage, changing the vibrational level structure.

WILEY-VCH

If the laser field $\varepsilon(t)$ in Equation 1 is changed, the time evolution of the molecular quantum system changes. Optimal control theory (OCT)^[36–41] is an optimization algorithm which tailors $\varepsilon(t)$ to enforce a desired state at final time T using the global optimization functional

$$J(\psi_i(t), \psi_f(t), \varepsilon(t)) = F(\psi_i) - \int_0^T s(t) |\varepsilon(t)|^2 - \int_0^T \psi_f(t) G[\psi_i(t), \varepsilon(t)] dt, \quad (4)$$

with the initial wave function ψ_i and the final wave function ψ_f . The third term in Equation 4 is an auxiliary constraint requiring the TDSE to be fulfilled. The second term contains the electric field $\varepsilon(t)$ and a time-dependent function $s(t)$ containing a Gaussian shape function to ensure smooth switching on and off behavior of the field, and the Krotov change parameter, which determines the degree to which the electric field can change within each iteration of the optimization.^[41] In the present study the optimization aim $F(\tau)$ was chosen as an overlap target

$$F[\psi_i] = |\langle \psi_i(T) | \phi_f \rangle|^2 \quad (5)$$

between the initial molecular wave function $\psi_i(T)$ at final time T with a defined target state ϕ_f . The latter one was designed to contain maximum population in the fifth vibrational level (v_4) at final time T , corresponding to a state-to-state optimization from v_0 to v_4 . In all optimizations, the initial guess field was designed to be resonant with the mean $v_0 \rightarrow v_1$ transition along the given trajectory, with a full-width at half maximum (FWHM) of 500 fs and an intensity of 0.05 GVcm⁻². A frequency filter^[42] was used to keep the pulse spectrum below 0.03 eV. Multi-target OCT^[41,43] optimizations were conducted as well, extending the optimization aim in Equation 5 to a sum over several optimization aims and using the multi-target Hamiltonian

$$\hat{H}_{MT}(t) = \begin{pmatrix} \hat{Q}_1(t) & \cdots & 0 \\ \vdots & \ddots & \vdots \\ 0 & \cdots & \hat{Q}_n(t) \end{pmatrix} - \varepsilon(t) \cdot \begin{pmatrix} \hat{\mu}_1 & \cdots & 0 \\ \vdots & \ddots & \vdots \\ 0 & \cdots & \hat{\mu}_n \end{pmatrix}, \quad (6)$$

where each single matrix Q_n and μ_n contains the energy levels and transition dipoles for a single solvent cage (compare Equation 1). Using this multi-target Hamiltonian, the controlling laser pulse is required to be effective in multiple solvent cages at the same time. If not stated

WILEY-VCH

otherwise, all optimized laser pulses in this study were designed to yield a population of 50 % in the target vibrational state. A total simulation time of 2500 fs was chosen for pulse optimizations, as these are typical coherence times of molecular vibrations as for example the experimentally measured carbonyl mode within $W(CO)_6$.^[44]

3. Results and Discussion

3.1 Time resolved environmental influence

The vibrational level structure along a 2500 fs MD trajectory is drawn in **Figure 2**. Within this time frame, the energetic position of a particular level can change by a factor of two. Extreme cases of environmental influence are caused by solvent molecules moving in and out of the reaction pathway of the methyl transfer (see Figure 1). If the methyl transfer, and the associated minor atomic movement in other parts of the reactant molecule, is unobstructed by the solvent cage, the potential energy curve resembles the unperturbed case, leading to a smaller energy spacing between the vibrational levels, as it is the case for example at 700 fs in the trajectory shown in Figure 2. When a solvent molecule is located close to the methyl transfer pathway (red arrow in Figure 1c), steric obstruction between reactant and solvent molecular moieties occurs, introducing an additional barrier along the reaction pathway (see blue curve in Figure 1d) and increasing the energy spacing between vibrational levels. This is the case for example at 350 fs in Figure 2. While the extreme cases of environmental influence have been revealed before,^[22] the first major result presented here is the timescale on which it fluctuates. The fluctuations revealed in Figure 2a are composed of two contributions. Smaller fluctuations happen on the low femtosecond timescale, which can be attributed to minor atomic displacements due to vibrations in the solvent molecules. This causes no challenge for a controlling laser pulse however, as the energy range of this fluctuation is very small and covered by the pulse carrier frequency. Larger fluctuations between the extreme cases can happen within 300 fs. This means that if the control mechanism happens on the low fs timescale, as it is for example the case in the control of excited state processes involving conical intersections,^[45]

assuming a static environment can be a valid approximation. In the present case, where vibrational initiation of a ground state reaction is performed with picosecond laser pulses, a femtosecond environmental fluctuation will affect the control mechanism and the complexity of the control task.

Figure 2b shows the $v_0 \rightarrow v_1$ transition and validates the discussed findings in other MD trajectories with different initial conditions. Both the degree of extreme cases and the time scale of environmental fluctuation is found to be the same in five investigated trajectories. As Figure 2a reveals a similar evolution of all vibrational levels, Figure 2b only shows the $v_0 \rightarrow v_1$ as the elementary vibrational transition. An interesting feature here is the repetition of patterns among the five trajectories, for example between 300 fs and 1200 fs in run 4 and between 700 fs and 1500 fs in run 1. This suggests that while the $v_0 \rightarrow v_1$ transition considerably fluctuates along the MD trajectories, the diversity of fluctuation patterns in a thermodynamic ensemble is rather small and a certain degree of convergence is observed in the rather small sample size of five trajectories.

3.2 Quantum Control Strategies

The aimed for control mechanism is vibrational ladder climbing up to v_4 , using all subsequent $\Delta v=1$ transitions by choosing the carrier frequency of the initial controlling laser pulse to be resonant with this energy spacing.^[32,33,44]

We examine different quantum control strategies and their ability to control the environmental fluctuations with a perspective on future experimental realization. The first strategy entirely disregards environmental fluctuations during the laser pulse optimization, and afterwards applies this pulse to the fluctuating case to check for its potential success. Two exemplary laser pulses for such static optimizations are depicted in **Figure 3** a and b, exhibiting very different pulse shapes. While the laser pulse in Figure 3a resembles a few-cycle pulse with comparably low field strength, the laser pulse in Figure 3b is much more complex and intense. The laser pulses are then applied to the fluctuating case, and the population yield is evaluated to measure

WILEY-VCH

the efficiency. To increase the sample size, the five different MD runs were concatenated in time, obtaining a fluctuating level structure over a total of 12500 fs (see **Figure 4b**, depicting the concatenated $v_0 \rightarrow v_I$ transition). In steps of 10 fs, the optimized laser pulse was shifted and applied along the concatenated MD runs. A quantum dynamical propagation was performed for each temporal position of the pulse to evaluate the population yield. While yielding 50 % population in the target state for its own optimized static case, the fluctuating environment imposes a very different scenario. Nevertheless, there are times where up to 20 % population reaches the target state in the fluctuating case, for example between 5000 fs and 5500 fs or at 10000 fs in **Figure 4c**. Each point in time here corresponds to a propagation with the maximum of the electric field being located at that point, i.e. the yield at 5000 fs corresponds to a quantum dynamical situation where the maximum of the laser pulse is located at 5000 fs. The same procedure was conducted with other pulses which were optimized for static environment, showing similar population yields in the fluctuating scenario. This demonstrates one advantage of the first control strategy, as the simplest laser pulse with the highest experimental feasibility can be chosen among a high diversity and manifold of cases.

The second control strategy directly uses the time-dependent potential in response to the fluctuating environment in the pulse optimization. Five different laser pulses were optimized corresponding to the five MD trajectories in **Figure 2b**. The most feasible of these five pulses is depicted in **Figure 3c**. It belongs to the MD trajectory 5 and exhibits a more structured pulse shape and higher intensity than the simplest laser pulse optimized for a non-fluctuating system (**Figure 3a**). This can be entirely attributed to the much more complex control task of handling a fluctuating situation. The same procedure as in the previous case is applied and the laser pulse is shifted along the concatenated MD trajectories (**Figure 4b**). Again, QD propagations were started at each temporal position in an interval of 10 fs and the population in the target state was evaluated. The result is sketched in **Figure 4d** and reveals a very high population yield of up to 40 % even at times for which the laser pulse is not initially optimized for. In fact, the

WILEY-VCH

population yield stays considerably high along the concatenated MD runs. This supports the previously observed repetition of fluctuating patterns and suggests that the complete thermodynamic ensemble may be manageable.

While the higher yield is no surprise due to the control task being much closer to the realistic case of a fluctuating environment, it comes at the prize of a more demanding laser pulse in terms of experimental realization. This is also the case using a third control strategy, which involves multi-target optimization of multiple static cases simultaneously. Six different situations along the five MD trajectories were combined in a multi-target OCT simulation, optimizing a laser pulse to achieve population transfer in all cases at the same time. The corresponding optimized laser pulse in Figure 3d is even more complex than the other ones and requires a much higher intensity. When applied to the fluctuating case (Figure 4b), it is understandably more efficient than the pulse which was optimized for a single static case, however it is not more efficient than the laser pulse which was optimized for the fluctuating case.

Based on the requirements and performance of the three different optimization strategies, we turn to the question of experimental realization, which always necessitates a manageable trade-off between pulse complexity and population yield. Even with a rather straight-forward laser pulse optimized for a frozen configuration (Figure 3a), a considerable amount of population yield can be achieved at certain times of the fluctuating system. This validates the findings of earlier experimental studies using trains of Gaussian shaped pulses.^[3,46,47] The temporal distance between two single pulses within the train was 300 fs, and a considerable increase in the efficiency of excitation processes in chemical solution was observed in contrast to using single pulses.^[3,46,47] It is however rewarding to use a more complex laser pulse which is optimized for the actual fluctuating case, should a specific experimental laboratory be capable of realizing the more complex wave form and higher intensity that is required. While the first control strategy can run into the problem of the repetition rate not matching the times where the

WILEY-VCH

molecular situation is favorable (for example at 2000 fs, 6000 fs or 11000 fs in Figure 4c), this is not an issue for the second control strategy, as the corresponding laser pulse is almost always effective along the investigated time span of MD trajectories. The decision which control strategy to use depends on the equipment of the specific experimental laboratory in wave form synthesis and pulse modulation. The assistance of theoretical simulations can be highly beneficial in exploring the boundaries within which the trade-off between pulse complexity and population yield can and should be made.

3.3 Theoretical Limits of Fluctuation Control

Besides the practical control of different scenarios, it is useful to explore the theoretical limits for quantum control of fluctuating energy levels caused by the molecular environment. For this purpose, the vibrational level structure is modulated artificially to fluctuate between the extreme cases on different time scales. While in the previous sections a simulation time of 2500 fs was chosen in pulse optimizations to match vibrational coherence times, the simulation time for this purpose was extended to 12000 fs to cover a high range and versatility of fluctuation time scales with respect to the pulse wave length. Exemplary created cases are drawn in **Figure 5a**, where the red lines correspond to the extreme cases found in Figure 2 and the black line represents the $v_0 \rightarrow v_1$ transition, sinusoidally fluctuating with a period between 100 fs and 12000 fs. The initial guess pulses for the OCT optimizations were set to have the mean frequency of the sinusoidal fluctuation (0.012 eV) and a FWHM of 1000 fs. If the fluctuation is very fast compared to this pulse duration (Figure 5a), the optimized laser pulse nearly maintains its Gaussian envelope. As the fluctuation is much faster than the pulse duration, the $\Delta v=1$ transition very often matches the pulse frequency and the current situation is almost always favorable, rendering a precise timing of the pulse unnecessary. If the energy fluctuation is very slow compared to the pulse duration, the shape of the optimized laser pulse is again nearly Gaussian, as the fluctuation is very slow compared to the pulse duration and does not shift away from the carrier frequency. In cases where the energy levels strongly fluctuate around the carrier

WILEY-VCH

frequency several times, the control task becomes more difficult (Figure 5b). This could be handled with a broader spectrum of the controlling laser pulse, leading to shorter pulses, which however comes at the cost of selectivity as many transitions are unspecifically addressed. The most important conclusion to be drawn from this series of simulations however is that for all tested cases – very fast, very slow and all in-between periods of fluctuation – a laser pulse could be optimized to achieve a population yield of 50 % in the target state. This is even possible if several different fluctuation periods are combined in a multi-target optimization, as demonstrated in Figure 5d. While there may be experimental limits in realizing the complex light fields, the environmental fluctuation of a molecular environment affecting a chemical reaction imposes no theoretical limits on the controllability of this reaction.

4. Conclusion

Using a combination of quantum dynamical simulations, laser pulse optimizations, electronic structure theory and classical solvent propagation, the time-dependent influence of a molecular solvent environment on the controllability of a chemical methyl transfer reaction was revealed. The individual movement of solvent molecules was found to be responsible for a drastic fluctuation of vibrational energy levels being relevant for quantum control. Major fluctuations between extreme cases were found to happen on a timescale of few hundred femtoseconds, which is slower than the few-fs pulse durations of modern photochemistry and -physics, but comparable to coherence times and the pulse durations used to trigger molecular vibrations. Laser pulses were successfully optimized to handle this complex control task. With respect to experimental realization, guidelines were given to find a reasonable trade-off between pulse complexity and efficiency, where a decision for both ends of this range has merits, and the concrete compromise depends on the circumstances in the specific experimental laboratory. Few-cycle and flexible terahertz pulses were found to be capable of achieving control, ranging from very simple to rather complex pulse shapes and wave forms. As sub-cycle modulation of

WILEY-VCH

terahertz laser pulses is possible with modern setups,^[48,49] the presented theoretical results can have practical implications.

To explore possible theoretical limitations, the vibrational level fluctuations were modulated artificially to oscillate between extreme cases with periods of 100 fs up to 12000 fs. Several different cases were combined in multi-target optimizations. For every artificially created scenario, it was possible to optimize a laser pulse achieving at least 50 % population yield in the target state, suggesting that besides possible experimental limitations of pulse generation and shaping, there exist no theoretical limits in the controllability of a fluctuating molecular environment on a chemical reaction like methyl transfer.

Acknowledgements

Financial support by the Deutsche Forschungsgemeinschaft through the SFB749 and the excellence cluster Munich-Centre for Advanced Photonics is acknowledged.

Received: ((will be filled in by the editorial staff))

Revised: ((will be filled in by the editorial staff))

Published online: ((will be filled in by the editorial staff))

References

- [1] H. Rabitz, R. de Vivie-Riedle, M. Motzkus, K. L. Kompa, *Science* **2000**, 288, 824.
- [2] M. Dantus, V. V. Lozovoy, *Chem. Rev.* **2004**, 104, 1813.
- [3] P. Nuernberger, G. Vogt, T. Brixner, G. Gerber, *Phys. Chem. Chem. Phys.* **2007**, 9 (20), 2470.
- [4] D. Keefer, R. de Vivie-Riedle, *Acc. Chem. Res.* **2018**, 51, 2279.
- [5] A. Assion, T. Baumert, M. Bergt, T. Brixner, B. Kiefer, V. Seyfried, M. Strehle, G. Gerber, *Science* **1998**, 282, 919.
- [6] G. Vogt, G. Krampert, P. Niklaus, P. Nuernberger, G. Gerber, *Phys. Rev. Lett.* **2005**, 94, 068305.
- [7] V. I. Prokhorenko, A. M. Nagy, S. A. Waschuk, L. S. Brown, R. R. Birge, R. J. D.

WILEY-VCH

- Miller, *Science* **2006**, *313* (5791), 1257–1261.
- [8] J. L. Herek, W. Wohlleben, R. J. Cogdell, D. Zeidler, M. Motzkus, *Nature* **2002**, *417*, 533.
- [9] H.-D. Hao, D. Trauner, *J. Am. Chem. Soc.* **2017**, *139*, 4117.
- [10] I. S. Makarov, C. E. Brocklehurst, K. Karaghiosoff, G. Koch, P. Knochel, *Angew. Chemie Int. Ed.* **2017**, *56*, 12774.
- [11] D. Trauner, *Angew. Chemie Int. Ed.* **2018**, *57*, 4177.
- [12] T. Stensitzki, Y. Yang, V. Kozich, A. A. Ahmed, F. Kössl, O. Kühn, K. Heyne, *Nat. Chem.* **2018**, *10*, 126.
- [13] S. Gao, J. Strömquist, B. I. Lundqvist, *Phys. Rev. Lett.* **2001**, *86*, 1805.
- [14] Y. Ohtsuki, K. Nakagami, W. Zhu, H. Rabitz, *Chem. Phys.* **2003**, *287*, 197.
- [15] J. C. Tremblay, P. Saalfrank, *Phys. Rev. A* **2008**, *78*, 063408.
- [16] A. Chenel, C. Meier, G. Dive, M. Desouter-Lecomte, *J. Chem. Phys.* **2015**, *142*, 024307.
- [17] S. J. Glaser, U. Boscain, T. Calarco, C. P. Koch, W. Köckenberger, R. Kosloff, I. Kuprov, B. Luy, S. Schirmer, T. Schulte-Herbrüggen, D. Sugny, F. K. Wilhelm, *Eur. Phys. J. D* **2015**, *69*, 279.
- [18] C. P. Koch, *J. Phys. Condens. Matter* **2016**, *28*, 213001.
- [19] C. Falvo, C. Meier, *J. Chem. Phys.* **2011**, *134*, 214106.
- [20] S. Thallmair, J. P. P. Zauleck, R. de Vivie-Riedle, *J. Chem. Theory Comput.* **2015**, *11*, 1987.
- [21] A. Debnath, C. Falvo, C. Meier, *J. Phys. Chem. A* **2013**, *117*, 12884.
- [22] D. Keefer, S. Thallmair, J. P. P. Zauleck, R. de Vivie-Riedle, *J. Phys. B At. Mol. Opt. Phys.* **2015**, *48*, 234003.
- [23] P. H. Berens, K. R. Wilson, *J. Chem. Phys.* **1981**, *74*, 4872.
- [24] G. R. Greenstein, *Ref. Rev.* **2007**, *21*, 40.

WILEY-VCH

- [25] W. C. Swope, H. C. Andersen, P. H. Berens, K. R. Wilson, *J. Chem. Phys.* **1982**, *76*, 637–649.
- [26] W. L. Jorgensen, D. S. Maxwell, J. Tirado-Rives, *J. Am. Chem. Soc.* **1996**, *118*, 11225.
- [27] M. J. Abraham, T. Murtola, R. Schulz, S. Páll, J. C. Smith, B. Hess, E. Lindahl, *SoftwareX* **2015**, *1–2*, 19.
- [28] Y. Zhao, D. G. Truhlar, *Theor. Chem. Acc.* **2008**, *120*, 215.
- [29] W. J. Hehre, K. Ditchfield, J. A. Pople, *J. Chem. Phys.* **1972**, *56*, 2257.
- [30] M. J. Frisch, G. W. Trucks, H. B. Schlegel, G. E. Scuseria, M. A. Robb, J. R. Cheeseman, G. Scalmani, V. Barone, G. A. Petersson, H. Nakatsuji, X. Li, M. Caricato, A. V. Marenich, J. Bloino, B. G. Janesko, R. Gomperts, B. Mennucci, H. P. Hratchian, J. V. Ortiz, A. F. Izmaylov, J. L. Sonnenberg, D. Williams-Young, F. Ding, F. Lipparini, F. Egidi, J. Goings, B. Peng, A. Petrone, T. Henderson, D. Ranasinghe, V. G. Zakrzewski, J. Gao, N. Rega, G. Zheng, W. Liang, M. Hada, M. Ehara, K. Toyota, R. Fukuda, J. Hasegawa, M. Ishida, T. Nakajima, Y. Honda, O. Kitao, H. Nakai, T. Vreven, K. Throssell, J. A. Montgomery Jr., J. E. Peralta, F. Ogliaro, M. J. Bearpark, J. J. Heyd, E. N. Brothers, K. N. Kudin, V. N. Staroverov, T. A. Keith, R. Kobayashi, J. Normand, K. Raghavachari, A. P. Rendell, J. C. Burant, S. S. Iyengar, J. Tomasi, M. Cossi, J. M. Millam, M. Klene, C. Adamo, R. Cammi, J. W. Ochterski, R. L. Martin, K. Morokuma, O. Farkas, J. B. Foresman, D. J. Fox, Gaussian16 Revision B.01. **2016**.
- [31] C. Eckart, *Phys. Rev.* **1935**, *47*, 552.
- [32] C. Ventalon, J. M. Fraser, M. H. Vos, A. Alexandrou, J.-L. Martin, M. Joffre, *Proc. Natl. Acad. Sci.* **2004**, *101*, 13216.
- [33] T. Witte, J. . Yeston, M. Motzkus, E. . Heilweil, K.-L. Kompa, *Chem. Phys. Lett.* **2004**, *392*, 156.
- [34] H. Tal-Ezer, R. Kosloff, *J. Chem. Phys.* **1984**, *81*, 3967.
- [35] J. P. P. Zauleck, M. T. Peschel, F. Rott, S. Thallmair, R. De Vivie-Riedle, *J. Phys.*

WILEY-VCH

Chem. A **2018**, *122*, 2849.

- [36] D. J. Tannor, S. A. Rice, *J. Chem. Phys.* **1985**, *83*, 5013.
- [37] A. P. Peirce, M. A. Dahleh, H. Rabitz, *Phys. Rev. A* **1988**, *37*, 4950.
- [38] W. Zhu, J. Botina, H. Rabitz, *J. Chem. Phys.* **1998**, *108*, 1953.
- [39] W. Zhu, H. Rabitz, *J. Chem. Phys.* **1998**, *109*, 385.
- [40] J. P. Palao, R. Kosloff, *Phys. Rev. A - At. Mol. Opt. Phys.* **2003**, *68*, 13.
- [41] P. von den Hoff, S. Thallmair, M. Kowalewski, R. Siemering, R. de Vivie-Riedle, *Phys. Chem. Chem. Phys.* **2012**, *14*, 14460.
- [42] C. Gollub, M. Kowalewski, R. de Vivie-Riedle, *Phys. Rev. Lett.* **2008**, *101*, 073002.
- [43] C. M. Tesch, R. de Vivie-Riedle, *Phys. Rev. Lett.* **2002**, *89*, 157901.
- [44] D. B. Strasfeld, S. H. Shim, M. T. Zanni, *Phys. Rev. Lett.* **2007**, *99*, 1.
- [45] D. Keefer, S. Thallmair, S. Matsika, R. de Vivie-Riedle, *J. Am. Chem. Soc.* **2017**, *139*, 5061.
- [46] T. Okada, I. Otake, R. Mizoguchi, K. Onda, S. S. Kano, A. Wada, *J. Chem. Phys.* **2004**, *121*, 6386.
- [47] I. Otake, S. S. Kano, A. Wada, *J. Chem. Phys.* **2006**, *124*, 014501.
- [48] C. Riek, P. Sulzer, M. Seeger, A. S. Moskalenko, G. Burkard, D. V. Seletskiy, A. Leitenstorfer, *Nature* **2017**, *541*, 376.
- [49] J. Bühler, J. Allerbeck, G. Fitzky, D. Brida, A. Leitenstorfer, *Optica* **2018**, *5*, 821.

WILEY-VCH

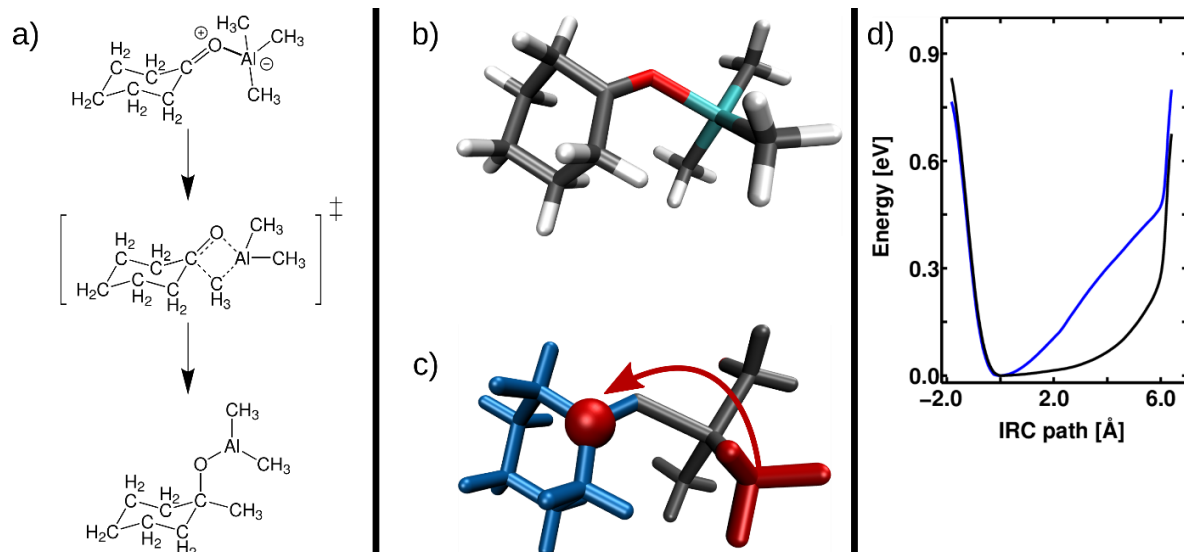


Figure 1. Methyl transfer reaction between cyclohexanone and trimethylaluminum including carbon-carbon bond formation. **a)** Reactant, transition state and product of the reaction. **b-c)** Reaction pathway of the methyl group (red) relocating to the carbon atom of the carbonyl group in the cyclohexanone ring. **d)** Potential energy curve of the IRC between reactant state at 0 Å and the transition state at 6.2 Å, with the barrier at the left created by extrapolation of the molecular geometry according to the IRC displacement vector. The black curve represents the gas phase potential, and the blue curve shows the potential curve within an exemplary solvent cage.

WILEY-VCH

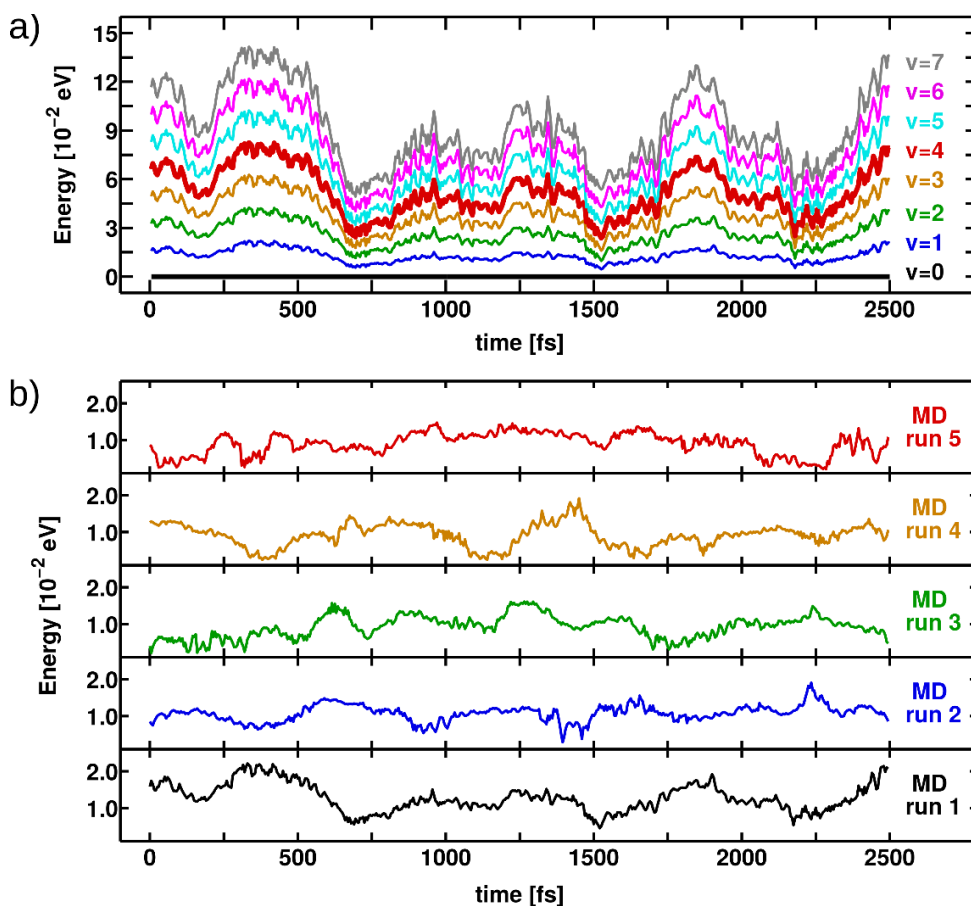


Figure 2. Fluctuating vibrational level structure of the methyl transfer reaction due to environmental influence. **a)** Vibrational levels of the IRC along MD run 1; $v=4$ is highlighted as the target state for laser pulse optimizations. Fluctuations between extreme cases happens on a time-scale of 300 fs and similarly in all levels. **b)** $v_0 \rightarrow v_1$ transition in five different MD runs, all showing similar ranges and time-scales of fluctuation.

WILEY-VCH

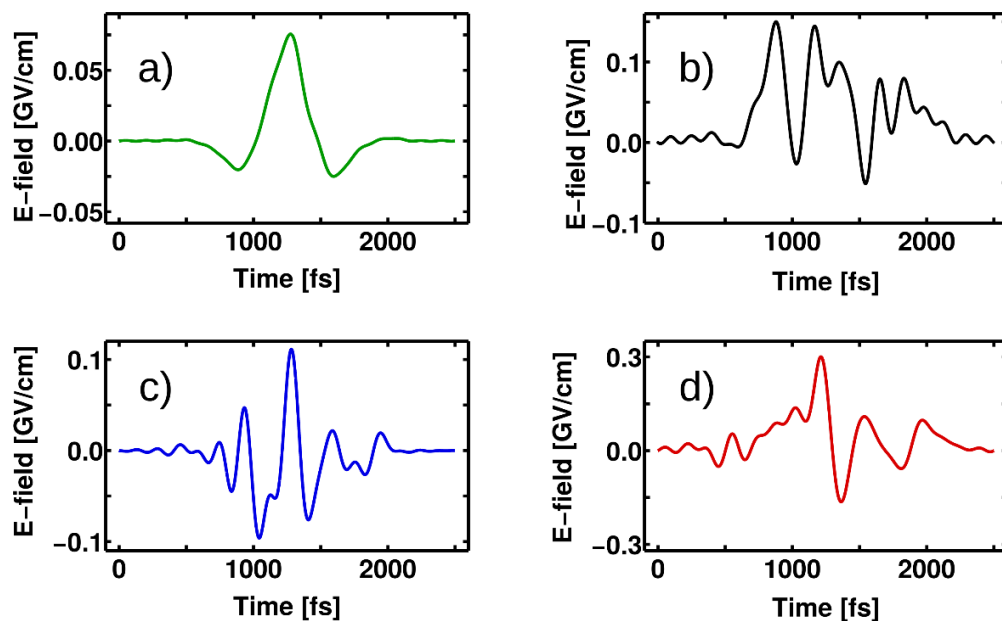


Figure 3. Optimized laser pulses according to different scenarios. **a-b)** Both laser pulses were optimized for a specific situation within the MD trajectory and disregarding environmental fluctuation (static vibrational levels). **c)** Optimized laser pulse for the fluctuating level structure of MD run 5. **d)** Multi-target optimization using six different static cases simultaneously.

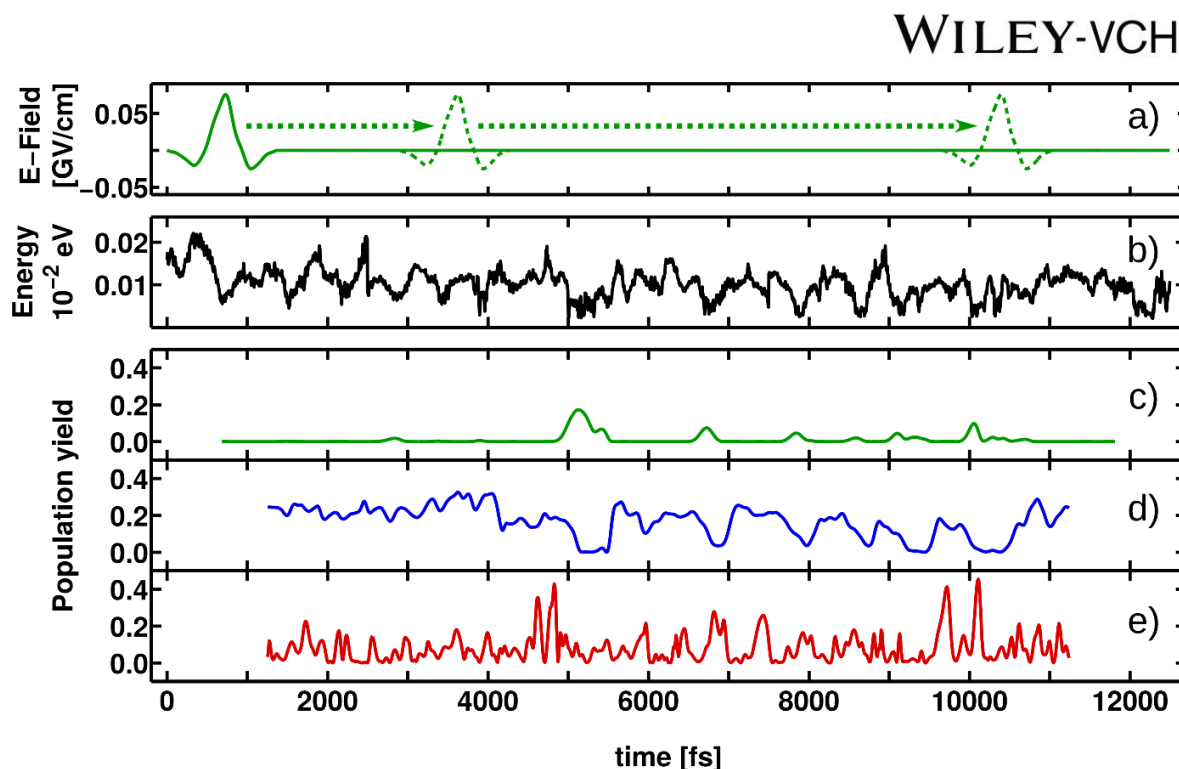


Figure 4. Application of different laser pulses to the concatenated fluctuation of MD runs 1 to 5, with the color code corresponding to Figure 3. **a)** Sketch of the procedure: A laser pulses is applied with the time of maximum pulse intensity being shifted over the whole 12500 fs, and a quantum dynamical propagation is performed for each point to evaluate the population yield. **b)** Concatenated $v_0 \rightarrow v_1$ transition of MD runs 1 to 5. **c)** Population yield of quantum dynamical propagations using the laser pulse in Figure 3a. Each point in time corresponds to a propagation with the maximum of the electric field being located at that point, i.e. the yield at 5000 fs corresponds to a quantum dynamical situation where the maximum of the laser pulse is located at 5000 fs. **d)** Time-dependent population yields using the laser pulse in Figure 3c. **e)** Time-dependent population yields using the laser pulse in Figure 3d.

WILEY-VCH

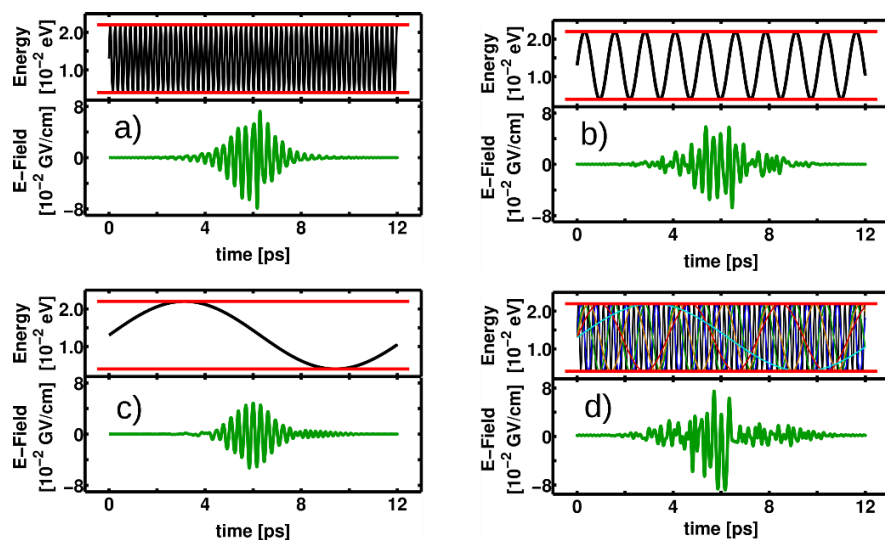


Figure 5. Optimized laser pulses for artificially created fluctuation periods. Red lines mark the extreme cases found in Figure 2. The black lines indicate the $v_0 \rightarrow v_1$ transition oscillating between the red lines with different sinusoidal periods. The top part of d) shows the multi-target scenario combining multiple different periods.

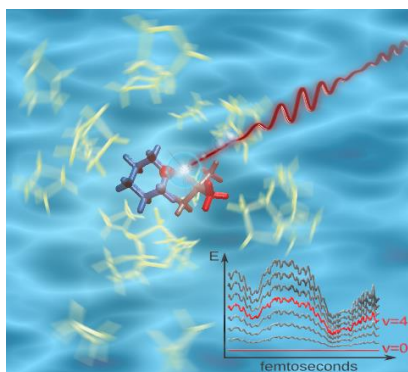
WILEY-VCH

Toc-entry: **Shaped few-cycle terahertz pulses** control a chemical system in its fluctuating solvent environment by selective vibrational excitation.

Keywords: **coherent control, quantum dynamics, shaped laser pulses, solvent effects**

Daniel Keefer and Regina de Vivie-Riedle*

Theoretical Quantum Control of Fluctuating Molecular Properties in Complex Chemical Environments



Chapter 3.

Photorelaxation of Uracil: Monitoring and Preparing an Elusive State Leading to Photolesions

The two studies presented in this chapter deal with specific aspects of the formation of photolesions in the genetic code. The single and double strands of nucleic acids are built up by the canonical nucleobases adenine, cytosine, guanine, thymine and uracil, which are chemically connected by sugar/phosphate backbones. The genetic information of living organisms is encoded in the specific base sequence within the strands. Chemical modifications of the nucleobases, like oxidation or hydrolysis, are known to cause severe diseases should they not get repaired properly [145]. One possible source for the chemical modification of nucleobases is the absorption of UV light [11], as it is irradiated for example by the sun. After UV absorption the molecule enters an electronically excited state, which can induce photochemical reactions and potentially lead to skin cancer [146–148]. All canonical nucleobases are known to be susceptible to this process, where the CPD and Dewar lesions are the most prominent examples [149, 150]. However, in most cases, all nucleobases are known to exhibit ultrafast relaxation channels back to the electronic ground state through various CoIns [151–157], which is why they are extensively investigated both theoretically and experimentally in the ultrafast community. This efficient relaxation mechanism does not involve chemical modification, but leads back to the initial geometry, where after arriving in the ground state again, the additional energy is just dissipated through vibrational heat. These ultrafast relaxation pathways are regarded as a main reason for the high photostability of the canonical nucleobases, and their obstruction can directly be linked to the formation of photodamage [82–84]. Additionally, UV radiation was more intense on the earth surface in the early days of life, and being more stable towards photodamage than other competitors, and thus being able to survive this selection pressure, is regarded as the main reason why DNA and RNA are built up by exactly these nucleobases.

In the case of uracil, which is also the nucleobase of interest in this chapter, there is both theoretical and experimental literature elucidating different aspects of the photorelaxation mechanism (see introduction and references in publication **2**, reprinted in chapter 3.1). In summary, experimental lifetimes in isolated uracil have been observed from 50 fs to around 2 ps, while theoretical studies revolved around investigating the excited state landscape and character. The first excited state of uracil is a $n \rightarrow \pi^*$, while the second excited state is a $\pi \rightarrow \pi^*$ state and also the first optically addressable one. From here, the molecule passes a S_2/S_1 CoIn, after which it relaxes further to the electronic ground state. Additionally, a local minimum has been found as an additional important structure in the relaxation process [85]. Building on this knowledge and using the identified structures along the relaxation path, the studies presented here monitor the WP on its way to the first CoIn after UV excita-

tion. The first study in chapter 3.1 investigates isolated uracil, as it is commonly investigated in ultrafast pump-probe experiments. By shaping the excitation pulse adapted to experimental parameters, the limiting cases of very fast versus very slow relaxation are explored to make statements about the photostability. Using the results and optimized laser pulses, experiments are suggested to artificially prepare a long-living WP in the S_2 state for better spectroscopic characterization and possibly to explore other photochemical pathways. The second study in chapter 3.2 uses the QD/MD approach to investigate the ultrafast relaxation mechanism after an unbiased UV excitation of uracil in its native environment, an RNA strand. This environment is found to drastically affect the relaxation pathway in some cases, and by using different combinations of neighboring bases statements are made about whether there are configurations favoring either photostability or photodamage.

3.1. Isolated uracil: Quantum Control to Accelerate and Prevent Relaxation

The following article “Controlling Photorelaxation in Uracil with Shaped Laser Pulses: A Theoretical Assessment” published in the *Journal of the American Chemical Society* presents the first WP simulations of the relaxation process in isolated neutral uracil. The laser pulse which is used to excite uracil are adapted from experimental parameters used in Ref. [85]. After showing how the WP evolves after UV excitation, OCT is used to explore the two limiting cases of very fast versus very slow relaxation times.

The key points of the article are:

- The presented PES exhibits a double-well structure, with a small barrier between the S_2 minimum and the S_2/S_1 CoIn seam. After UV excitation, the WP evolves from the Franck-Condon (FC) to the S_2 minimum and subsequently crosses the barrier to the CoIn. The relaxation time is defined as the time after which half of the population has left the S_2 state. It is observed to be around 170 fs and corresponds well to the experiments from which the pulse parameters were taken.
- Acceleration of this process with an OCT optimization of the excitation pulse was achieved, but only by about 22%, corresponding 142 fs. This suggests that the natural conditions in uracil are already very efficient.
- A laser pulse is presented which traps the WP in the local S_2 minimum for more than 50 ps, while only having a full width at half maximum (FWHM) of 4 fs. As the trapping timescale is significantly longer than the pulse duration, in a possible experimental realization this gives time to for example use a second laser pulse trying to possibly find other photochemical pathways by steering the WP in other directions. Besides the short duration and high intensity, the presented laser pulse is surprisingly simple and almost Gaussian shaped, rendering it experimentally feasible.

Hereafter, the article “Controlling Photorelaxation in Uracil with Shaped Laser Pulses: A Theoretical Assessment” published in the *Journal of the American Chemical Society* is reprinted with permission from *J. Am. Chem. Soc.* **2017**, 139, 5061. Copyright 2017 American Chemical Society.

Controlling Photorelaxation in Uracil with Shaped Laser Pulses: A Theoretical Assessment

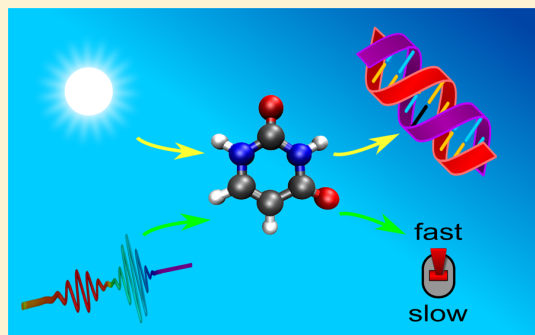
Daniel Keefer,[†] Sebastian Thallmair,^{†,||} Spiridoula Matsika,^{‡,||} and Regina de Vivie-Riedle^{*,†,||}

[†]Department Chemie, Ludwig-Maximilians-Universität München, D-81377 München, Germany

[‡]Department of Chemistry, Temple University, Philadelphia, Pennsylvania 19122, United States

S Supporting Information

ABSTRACT: The RNA nucleobase uracil can suffer from photo-damage when exposed to UV light, which may lead to severe biological defects. To prevent this from happening in most cases, uracil exhibits an ultrafast relaxation mechanism from the electronically excited state back to the ground state. In our theoretical work, we demonstrate how this process can be significantly influenced using shaped laser pulses. This not only sheds new light on how efficient nature is in preventing biologically momentous photo-damage. We also show a way to entirely prevent photorelaxation by preparing a long-living wave packet in the excited state. This can enable new experiments dedicated to finding the photochemical pathways leading to uracil photodamage. The optimized laser pulses we present fulfill all requirements to be experimentally accessible.



INTRODUCTION

Nucleobases are key players in processing and storing genetic information. The crucial factor for their photostability is the excited state dynamics, which has been studied extensively both theoretically and experimentally. In this work we focus on uracil, which exhibits ultrafast relaxation back to the ground state after photoexcitation. This is the mechanism by which potential photodamage is prevented in every living organism exposed to sunlight. By trying to influence this process with shaped laser pulses, we can not only learn a lot about the characteristics and limits of this process but also propose novel experiments which finally might detect the photochemical pathways leading to this photodamage.

Up to date, several gas-phase pump–probe experiments on uracil have shown that the excited state population decays ultrafast, displaying a biexponential decay.^{1–7} Various relaxation times ranging from 50 fs to 2.4 ps have been observed in these studies. To unravel the underlying process, various theoretical studies were performed exploring the excited state energy landscape. Many of them reside in a static picture, using variations of CASSCF/CASPT2 and multi-reference configuration interaction (MRCI) methods,^{8–15} time-dependent density functional theory,^{16–18} or coupled cluster theory.¹⁹ Overviews on how the different methods behave in describing uracil are given in refs 20 and 21. Dynamical studies have been performed as well, mainly based on semiclassical surface-hopping approaches^{22–27} or classical molecular dynamics in solution.²⁸ In terms of quantum dynamics, there are only two studies on the closely related thymine,^{29,30} and one study on cationic uracil using the multi-configuration time-dependent Hartree method.³¹ To the best

of our knowledge, the present work contains the first quantum dynamical study on neutral uracil.

All of the previously listed theoretical studies agree that the ultrafast relaxation process in uracil is driven by conical intersections (CoIns), although there is some disagreement about the exact pathways. The first excited state S_1 is a dark $n\pi^*$ state, while the S_2 is a bright $\pi\pi^*$ state. After photoexcitation to this state, the first relaxation step occurs via a S_2/S_1 CoIn. Depending on the level of electronic structure theory, a shallow minimum on the S_2 surface exists, which is separated by a small barrier from the S_2/S_1 CoIn. The height and even the existence of this barrier are still under debate. Part of our results are suited to suggest experiments which can bring this debate to a conclusion.

In the present work we perform quantum dynamical simulations on reduced-dimensional potential energy surfaces (PESs), where the S_2 minimum and the barrier toward the S_2/S_1 CoIn play a major role. We show how the relaxation process out of the S_2 state can be influenced with the help of shaped laser pulses, which we design with optimal control theory (OCT). It has been tried to achieve this control task with the help of closed-loop learning experiments,³² but without much success. Support from theory might be beneficial to this, and with the insights gained from the present work, successful control experiments on uracil may be possible in the future.

Received: November 22, 2016

Published: February 10, 2017

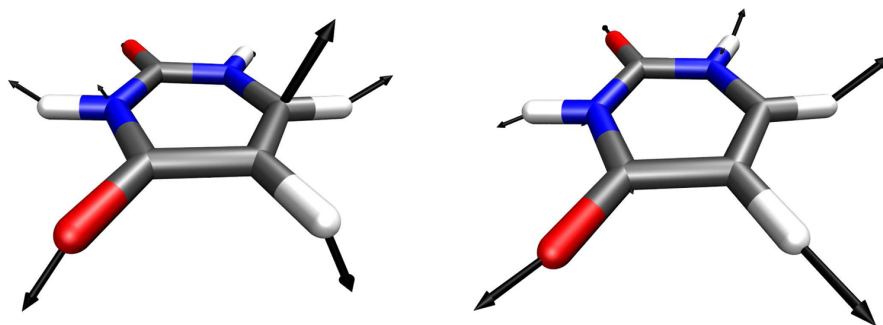


Figure 1. Ground state minimum structure of uracil. The coordinate vector $q_{\text{FC} \rightarrow \text{CoIn}}$ on the left describes an out of plane deformation, and $q_{\text{FC} \rightarrow \text{S}_2 \text{ min}}$ on the right is mainly some bond elongations within the plane of the ring.

RELAXATION MECHANISM AFTER AN UNBIASED PHOTOEXCITATION

The coordinates we use to represent uracil are derived from three optimized structures which play a major role in the photoinduced process: the Franck–Condon (FC) point, the S_2 minimum and the S_2/S_1 CoIn. The FC structure of uracil along with the two coordinate vectors are illustrated in Figure 1. The first coordinate $q_{\text{FC} \rightarrow \text{CoIn}}$ is defined by the normalized vector pointing from the FC point to the optimized S_2/S_1 CoIn. The other coordinate $q_{\text{FC} \rightarrow \text{S}_2 \text{ min}}$ is obtained by orthonormalization of the vector pointing from the FC point to the S_2 minimum with respect to $q_{\text{FC} \rightarrow \text{CoIn}}$. Together these vectors span a two-dimensional (2D) coordinate space. While not being able to describe other photochemical pathways, this reduced-dimensional coordinate space is the best one to properly sample the relaxation mechanism as all important structures along this pathway are included. The accordant S_2 PES is drawn in Figure 2 and exhibits a double-

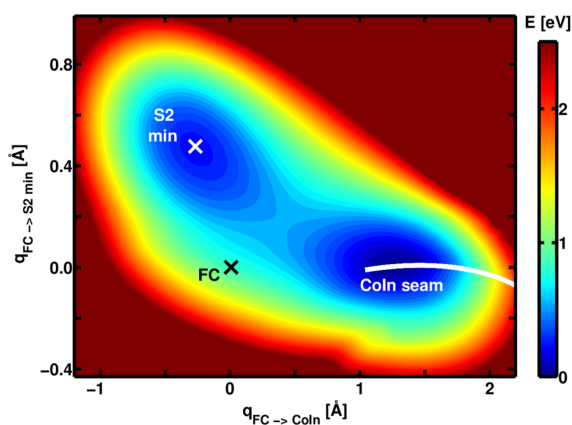


Figure 2. S_2 PES of uracil spanned by the Franck–Condon point (FC), the local S_2 minimum, and the optimized CoIn. The white curved line indicates the area where the non-adiabatic coupling takes significant values.

well structure, with a barrier in between the wells which is energetically lower than the FC region. Another prominent feature is that the CoIn is not only present as one point but in fact as a seam within the PES.

To transfer the wave packet (WP) from the electronic ground state to the S_2 state, we optimized a pump pulse with OCT with the only optimization aim being maximum

population in the S_2 state. The initial guess pulse was adapted to experimental parameters³³ with a full width at half maximum (fwhm) of 32 fs and a peak intensity of $3 \times 10^{11} \text{ W}\cdot\text{cm}^{-2}$. It already achieves 98% population in the S_2 state. After optimization, the population yield is close to 100%. The resulting laser pulse is shown in Figure 3a along with its spectrogram, and will be referred to as the *unbiased pump pulse* in the following. There were no major tweaks during the optimization, and the pulse still looks almost perfectly Gaussian shaped. It excites a rather delocalized WP on the S_2 surface, which evolves from the FC point toward the S_2 minimum (see Figure 4a) and oscillates back to the FC region. Subsequent to the second oscillation cycle, a part of the WP splits and travels over the barrier toward the CoIn seam, where it decays to the S_1 state. During the following oscillations this is continued until the S_2 state is completely depopulated. Due to the delocalized shape of the WP, there is a rather continuous flow of population toward the CoIn seam. This is also reflected in the population curve, which is drawn in Figure 4d with the red line. It has a smooth shape, indicating a continuous decay of the WP via the CoIn. To characterize the relaxation process, we use the time where half of the population has left the S_2 state, which is 186 fs in case of the unbiased pump pulse. This relaxation time is the key factor in terms of photostability, as spending less time in the excited state, competing pathways potentially leading to photodamage are less likely to be taken.

HOW TO INFLUENCE THE MECHANISM: ACCELERATION AND WAVE PACKET TRAP

Based on the observed WP dynamics, we defined two opposite control aims through the projection operator in the OCT algorithm (see SI, Figure S3 for details). One control aim is geared toward an acceleration of the relaxation process by maximizing the probability density of the WP in the region of the CoIn seam as early as possible. This can be interpreted as challenging nature when it comes to preventing photodamage by trying to find more efficient relaxation pathways. The second control aim has the intention to keep the WP in the region of the S_2 minimum as long as possible to efficiently trap it there. Despite the long time frame of this control aim, the pulse duration is tried to be kept as short as possible.

We optimized laser pulses for both control aims, which will be further referred to as the *accelerating* and the *trapping* laser pulse. Their success is reflected in the population curves for the S_2 state in Figure 4d. In case of the accelerating laser pulse (black population curve), the time where half of the WP

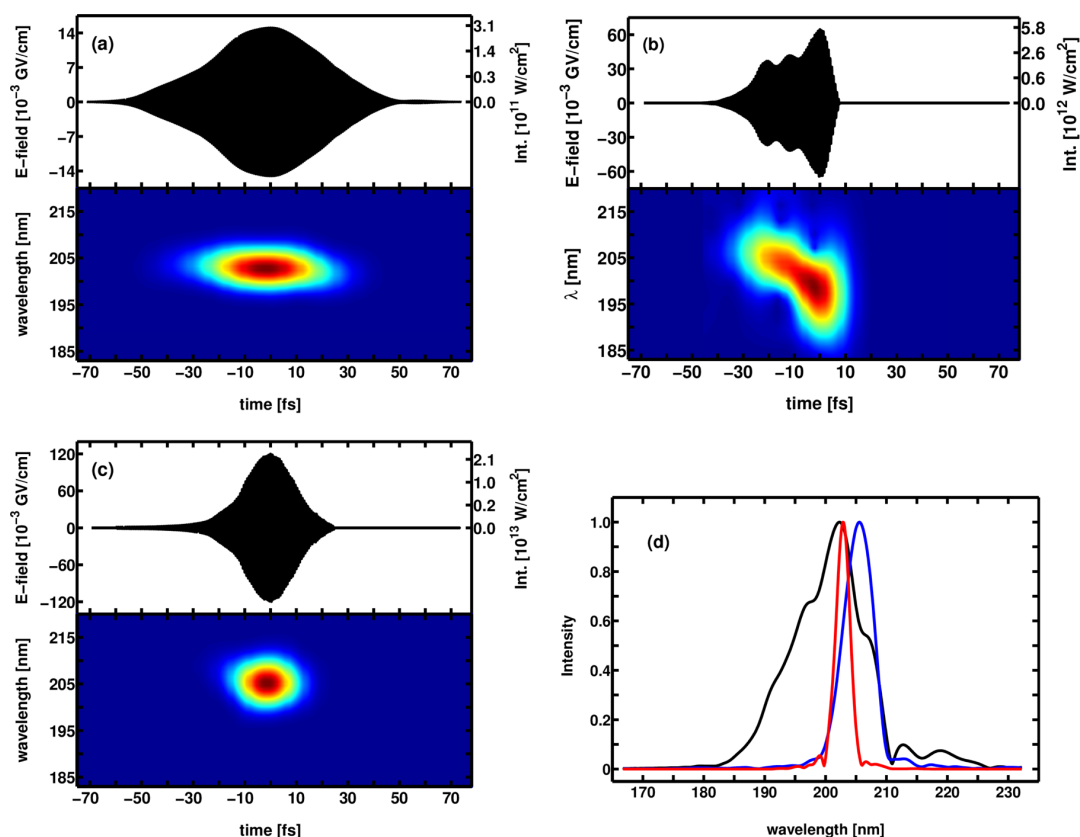


Figure 3. (a–c) Laser pulses and spectrograms after optimization with respect to the formulated control aims, i.e., optimization for (a) an unbiased optimal pump into the S_2 , (b) steering the WP to the CoIn seam, and (c) trapping the WP in the S_2 minimum. (d) Spectra of the laser pulses shown in (a)–(c) with the red line belonging to (a), the black line to (b), and the blue line to (c).

has left the S_2 state is lowered to 146 fs in contrast to the 186 fs in case of the unbiased pump pulse (red population curve). This corresponds to a speedup of 22%, which on one hand is a noticeable amount. On the other hand this shows that an unbiased photoexcitation already follows a very efficient relaxation mechanism to prevent photodamage in uracil. The according WP dynamics in Figure 4b reveal the mechanism behind the acceleration. The laser pulse keeps the WP more local in space in contrast to the unbiased pump pulse. The evolution of the WP is similar; namely, two oscillations through the S_2 minimum before the WP splits for the first time, and some parts start to flow toward the CoIn. The difference is that the parts which split up and travel to the CoIn are larger when the accelerating laser pulse is applied, which leads to an overall faster relaxation. The crucial moment of the first WP splitting, which identifies the characteristics in both cases, is shown in Figure 4a,b with the white lines. The more local shape of the WP is also reflected in the population curve (Figure 4d). In contrast to the smooth shape of the red curve, which corresponds to a delocalized WP, there are steps present in the black curve belonging to the accelerating laser pulse. These steps are in accordance with the time the WP needs to oscillate through the S_2 minimum, which is between 45 and 50 fs. Note that the direct path from the FC point to the CoIn is not accessible due to unfavorable gradients on the PES.

Additional to the acceleration of the relaxation process, it is also possible to trap the majority of the WP on the S_2 surface.

As indicated by the blue curve in Figure 4d, almost 1 ps after photoexcitation with the trapping laser pulse, 80% of the population is still located in the S_2 state. In fact, half of the population is still remaining in the S_2 state after 5.5 ps although the pulse duration is in the low fs range. The WP evolution of this trap is sketched in Figure 4c. After entering the S_2 PES at the FC point, the WP evolves in the direction of the S_2 minimum like in the other two cases. Only a small part of the WP overcomes the barrier toward the CoIn, whereas now the remaining part (about 80%; WP with the white lines in Figure 4c) forms a rather defined structure with four nodes. It has significant overlap with low-energy eigenfunctions which are located exclusively or predominantly in the local S_2 minimum. The mechanism behind this trap can be deduced from Figure 4d, where the inlay shows the magnified population curves during the pumping process into the S_2 state. Due to the higher pulse intensity, the population curve exhibits fast oscillations following the pulse frequency. Additionally, there are three dips in the excitation process of the trap pulse. These two issues indicate that small parts of the WP are constantly transferred back and forth between the S_0 and the S_2 state. On the bottom line this process slows down the WP, as the gradient of the PES between the FC point and the S_2 minimum in the S_0 state points in the opposite direction than the one in the S_2 state. Having less kinetic energy, the WP is not able to overcome the barrier toward the CoIn seam and stays in the S_2 minimum. Besides various other possible follow up studies to be proposed later,

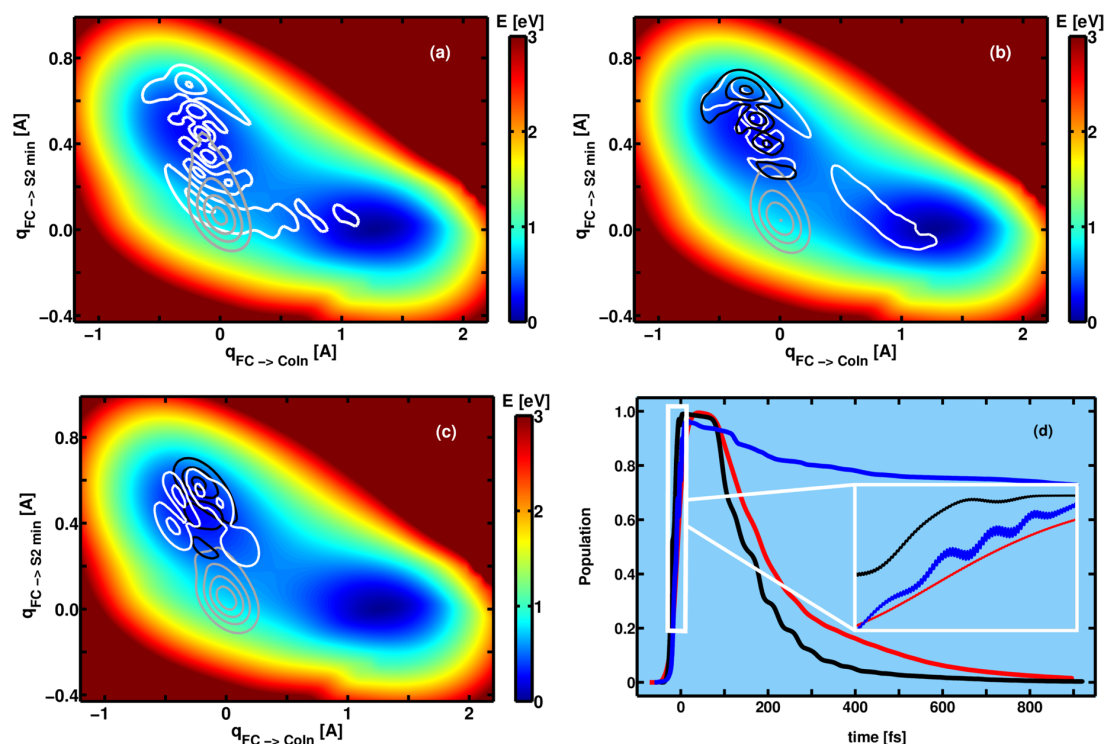


Figure 4. Wave packet dynamics on the S_2 surface and population course according to the laser pulses shown in Figure 3. (a) Excitation with the unbiased pump pulse: gray, WP at -34.9 fs; white, WP at 104.2 fs. (b) Steer to the CoIn: gray, WP at -22.9 fs; black, WP at 46.0 fs; white, WP at 93.2 fs. (c) Trap in the S_2 minimum: gray, WP at -16.2 fs; black, WP at 15.3 fs; white, WP at 868.0 fs. (d) Population course according to the dynamics shown in (a)–(c) with the red line belonging to (a), the black line to (b), and the blue line to (c). The white-framed inlay on the right is an enlargement of the short time frame around 0 fs.

if the mechanism we suggest here can be realized experimentally, a very strong argument can be made in favor of the existence of the barrier between the S_2 minimum and the S_2/S_1 CoIn.

For a closer comparison of the laser pulses achieving the control aims, they are drawn together in Figure 3b,c, along with the unbiased pump pulse (Figure 3a). In contrast to the latter one, the accelerating laser pulse is shorter in time and more intense. It also has an upchirp toward higher frequencies, whereas the unbiased pump pulse has no chirp. The spectrogram in Figure 3b exhibits some degree of fine structure, which is necessary to achieve the control aim. A simple Gaussian shaped pulse with the corresponding amount of chirp did not achieve an acceleration of the photorelaxation. Another feature of the accelerating pulse is a shift of the central frequency toward higher frequencies, which gives the excited WP a higher momentum benefiting a faster passage over the potential barrier and thereby faster relaxation. The key feature of the trapping laser pulse (Figure 3c) is a higher intensity, which is necessary to realize the fast oscillations in the population curve in order to slow down the WP. To reduce the momentum of the WP even further, the central frequency is slightly shifted toward lower frequencies in contrast to the other two pulses. Overall, the spectrograms of all three laser pulses are rather smooth. This was one main goal of the optimizations and was realized via a cost functional in the OCT algorithm which penalizes high intensities, tries to keep the pulses Gaussian shaped and cuts off unnecessary frequency components^{34,35} (the cost functional containing

these features is represented by $s(t)$ in eq 1). Due to their low complexity, all three laser pulses should be experimentally accessible. The central frequencies should be taken with a pinch of salt, as multi-configurational methods are known to struggle in yielding the correct excitation energies in uracil, which should not influence the observed mechanisms, however (typically an experimental excitation is achieved with laser pulses having their central wavelength around 260 nm³³). For experimental generation, the accelerating laser field requires a 7 fs and the trapping laser field a 15 fs input pulse. Also note that it is sufficient to modify the unbiased pump pulse in order to achieve both control aims, and no second color is needed. Due to these facts, this theoretical study should have a suggestive character for prospective control experiments.

■ CONTROL MECHANISMS IN THE PRESENCE OF A THIRD DIMENSION

By reducing the photorelaxation of uracil to two reactive coordinates (Figure 1) which are built up by several normal modes, an approximation is made. To verify the results we obtained in this coordinate space, we extended it to three dimensions. Therefore, five different 3D spaces were constructed by adding five different normal modes in their harmonic description to the 2D PES. To test for a variety of cases, normal modes of uracil from different spectral regions and with different kinetic coupling strengths to the existing 2D space were taken: a nitrogen–hydrogen stretching mode, a carbon–hydrogen stretching mode, a carbon–hydrogen

Table 1. Efficiency of Presented Laser Pulses in Different Coordinate Spaces^a

coordinate	frequency [cm ⁻¹]	kin. coupling [10 ⁻⁵ a.u.]		t _{1/2} [fs]		
		q _{FC→CoIn}	q _{FC→S₂min}	pump	steer	p _{S₂} [%], trap
q _{FC→CoIn}	900		7.05	186	146	76.0
q _{FC→S₂min}	480	7.05				
q _{NHs}	3473	0.04	0.05	186	146	75.8
q _{CHs}	3051	1.41	2.96	186	146	75.7
q _{COs}	1762	0.54	1.09	188	147	75.1
q _{CHb}	1170	0.11	2.74	185	153	76.3
q _{oop}	723	0.03	0.03	186	146	75.8

^aThe upper section depicts the 2D coordinate space for which the laser pulses were optimized. The bottom section shows different 3D spaces, which were constructed by augmenting the 2D space by different normal modes: N–H stretching (q_{NHs}), C–H stretching (q_{CHs}), C–H bending (q_{CHb}), C–O stretch (q_{COs}), and an out-of-plane deformation of the ring (q_{oop}). The third and fourth columns show the kinetic coupling strength to the coordinates of the 2D space according to the G-matrix formalism.^{36–39} The fifth and sixth columns give the times at which half of the population has left the S₂ state for pump pulse and steer pulse, respectively. The right-most column lists the amount of the population still located in the S₂ state after 600 fs when the trap pulse is applied.

bending mode, a carbonyl mode, and a deformation mode of the planar ring (see Table 1 for details). The previously presented laser pulses were applied to the respective 3D spaces, and as it can be learned from Table 1, they stay effective and fulfill the control aims for which they were optimized. This behavior was expected to a certain degree due to the good agreement between experimental and simulated relaxation times.

In summary, the present study demonstrates that the ultrafast relaxation dynamics of the RNA-base uracil is well controllable. On our reduced-dimensional PESs we performed WP dynamics to simulate the possibilities of influencing the relaxation process after photoexcitation. With the help of OCT we designed laser pulses to achieve two opposed control aims. We were able to accelerate the relaxation to the S₁ state by about 22%. The fact that this speedup could not be enlarged further suggests that an unbiased photoexcitation—as from a conceptual point of view it is the case in nature—already leads to a very efficient mechanism to prevent photodamage on uracil. Furthermore, we showed how the relaxation process can be delayed significantly by trapping the WP in the local S₂ minimum. As this trap occurs on a time scale which is much longer than the pulse duration, other light fields and spectroscopic techniques could be used to steer the WP from the FC region and explore the S₂ landscape on a whole new level, inspiring the quantum control spectroscopy approach. The pathway(s) leading to the biologically momentous photodamage might be identified and mechanistically understood. The laser pulses we designed are oriented on experimental data and thus should be able to serve as direct guidelines for prospective experiments of this kind.

COMPUTATIONAL METHODS

The PESs we used—along with the transition dipole moments and non-adiabatic couplings—were calculated using MRCI with an active space of 12 electrons in 9 orbitals (12,9), and only single excitations allowed out of the active space into the virtual space, which constitutes a reasonable trade-off between accuracy and the necessary computation time to construct a 2D surface. Although MRCI methods struggle in predicting the correct vertical excitation energies and CASPT2 is usually the method of choice for obtaining highly accurate results, MRCIS was found to map the topology and barrier heights much more similar to CASPT2 than to for example CASSCF (see Table 3 in ref 33 for a summary of various computational

methods used on uracil). While the vertical excitation energy only impacts the central frequency of the laser pulse, the topology and barrier heights are the crucial properties for the WP dynamics and control mechanisms, and thus MRCIS is a reasonable method to use here. The orbitals used in the MRCI calculations were obtained from an average of three states CASSCF (SA3-CASSCF) with the same active space (12,9). All calculations were conducted with the COLUMBUS software package^{40–42} with the cc-pVDZ basis set. The geometries of the CoIn and the S₂ minimum were obtained in previous works^{8,11} using the same methodology.

For the quantum dynamical simulations we solved the time-dependent Schrödinger equation (TDSE) on a spatial grid using the Chebychev propagation scheme.⁴³ To set up the kinetic energy operator in the reduced-dimensional coordinate space, the G-matrix formalism was employed.^{36–39} The non-adiabatic couplings were implemented as the norm of the total vector. The complete OCT functional⁴⁴ we used to optimize the laser fields reads

$$J[\psi_f(t), \psi_i(t), \epsilon(t)] = F[\psi_f(t)] - \int_0^T s(t)|\epsilon(t)|^2 dt - \int_0^T \psi_f(t)G[\psi_f(t), \epsilon(t)] dt \quad (1)$$

with the initial wave function $\psi_i(t)$, the laser field $\epsilon(t)$, and the final wave function $\psi_f(t)$, and with $G[\psi_f(t), \epsilon(t)]$ representing the TDSE. The first term in eq 1 denotes the optimization aim, which we defined using a projection operator \hat{P} :

$$F[\psi_f(t)] = \langle \psi_f(T) | \hat{P} | \psi_f(T) \rangle \quad \text{with} \quad \hat{P} = |\psi_f\rangle\langle\psi_f| \quad (2)$$

The function $s(t)$ in the second term of eq 1 contains the Krotov change parameter α ,⁴⁵ a shape function to ensure smooth switching on and off behavior of the laser field and a frequency filter^{34,35} to suppress unwanted frequencies. Details on the laser field optimizations—such as the shape of the projection operator, frequency windows, and the choice of α —can be found in the SI.

ASSOCIATED CONTENT

Supporting Information

The Supporting Information is available free of charge on the ACS Publications website at DOI: 10.1021/jacs.6b12033.

Details about the quantum dynamical simulations and OCT optimizations, including the S₀ and S₁ PESs along with the coordinate vectors, transition dipole moments, non-adiabatic couplings, G-matrix elements, and optimized structures, including total energies; parameters about laser pulse optimizations such as the Krotov

change parameter α , frequency windows, and target operators (PDF)

AUTHOR INFORMATION

Corresponding Author

*regina.de_vivie@cup.uni-muenchen.de

ORCID

Spiridoula Matsika: 0000-0003-2773-3979

Regina de Vivie-Riedle: 0000-0002-7877-5979

Present Address

^{||}S.T.: Groningen Biomolecular Sciences and Biotechnology Institute and The Zernike Institute for Advanced Material, University of Groningen, Nijenborgh 7, 9747 AG Groningen, The Netherlands

Author Contributions

[§]D.K. and S.T. contributed equally to this work.

Notes

The authors declare no competing financial interest.

ACKNOWLEDGMENTS

Financial support by the Deutsche Forschungsgemeinschaft through the excellence cluster Munich-Centre for Advanced Photonics (MAP) and the SFB749 is acknowledged. S.M. acknowledges support from the U.S. Department of Energy under Award No. DE-FG02-08ER15983, and from the Alexander von Humboldt Foundation.

REFERENCES

- (1) Kang, H.; Lee, K. T.; Jung, B.; Ko, Y. J.; Kim, S. K. *J. Am. Chem. Soc.* **2002**, *124*, 12958.
- (2) He, Y.; Wu, C.; Kong, W. *J. Phys. Chem. A* **2003**, *107*, 5145.
- (3) Crespo-Hernandez, C. E.; Cohen, B.; Hare, P. M.; Kohler, B. *Chem. Rev.* **2004**, *104*, 1977.
- (4) Ullrich, S.; Schultz, T.; Zgierski, M. Z.; Stolow, A. *Phys. Chem. Chem. Phys.* **2004**, *6*, 2796.
- (5) Canuel, C.; Mons, M.; Piuze, F.; Tardivel, B.; Dimicoli, I.; Elhanine, M. *J. Chem. Phys.* **2005**, *122*, 074316.
- (6) Middleton, C. T.; de La Harpe, K.; Su, C.; Law, Y. K.; Crespo-Hernandez, C. E.; Kohler, B. *Annu. Rev. Phys. Chem.* **2009**, *60*, 217–239.
- (7) Kotur, M.; Weinacht, T.; Zhou, C.; Matsika, S. *IEEE J. Sel. Top. Quantum Electron.* **2012**, *18*, 187–194.
- (8) Matsika, S. *J. Phys. Chem. A* **2004**, *108*, 7584.
- (9) Merchán, M.; Gonzalez-Luque, R.; Climent, T.; Serrano-Andrés, L.; Rodriguez, E.; Reguero, M.; Peláez, D. *J. Phys. Chem. B* **2006**, *110*, 26471–26476.
- (10) Mercier, Y.; Santoro, F.; Reguero, M.; Improta, R. *J. Phys. Chem. B* **2008**, *112*, 10769–10772.
- (11) Yoshikawa, A.; Matsika, S. *Chem. Phys.* **2008**, *347*, 393–404.
- (12) Merchán, M.; Serrano-Andrés, L. *J. Photochem. Photobiol., C* **2009**, *10*, 21–32.
- (13) Delchev, V. B.; Sobolewski, A. L.; Domcke, W. *Phys. Chem. Chem. Phys.* **2010**, *12*, 5007–5015.
- (14) Mercier, Y.; Reguero, M. *Int. J. Quantum Chem.* **2011**, *111*, 3405–3415.
- (15) Yamazaki, S.; Taketsugu, T. *J. Phys. Chem. A* **2012**, *116*, 491–503.
- (16) Gustavsson, T.; Banyasz, A.; Lazzarotto, E.; Markovitsi, D.; Scalmani, G.; Frisch, M. J.; Barone, V.; Improta, R. *J. Am. Chem. Soc.* **2006**, *128*, 607–619.
- (17) Santoro, F.; Barone, V.; Gustavsson, T.; Improta, R. *J. Am. Chem. Soc.* **2006**, *128*, 16312–16322.
- (18) Zhang, X.; Herbert, J. M. *J. Phys. Chem. B* **2014**, *118*, 7806–7817.
- (19) Zgierski, M. Z.; Patchkovskii, S.; Fujiwara, T.; Lim, E. C. *J. Phys. Chem. A* **2005**, *109*, 9384–9387.
- (20) Mai, S.; Richter, M.; Marquetand, P.; González, L. *Top. Curr. Chem.* **2014**, *355*, 99–153.
- (21) Improta, R.; Santoro, F.; Blancafort, F. *Chem. Rev.* **2016**, *116*, 3540–3593.
- (22) Hudock, H. R.; Levine, B. G.; Thompson, A. L.; Satzger, H.; Townsend, D.; Gador, N.; Ullrich, S.; Stolow, A.; Martinez, T. J. *J. Phys. Chem. A* **2007**, *111*, 8500–8501.
- (23) Lan, Z. G.; Fabiano, E.; Thiel, W. *J. Phys. Chem. B* **2009**, *113*, 3548–3555.
- (24) Barbatti, M.; Aquino, A. J. A.; Szymczak, J. J.; Nachtigallova, D.; Hobza, P.; Lischka, H. *Proc. Natl. Acad. Sci. U. S. A.* **2010**, *107*, 21453–21458.
- (25) Nachtigallova, D.; Aquino, A. J. A.; Szymczak, J. J.; Barbatti, M.; Hobza, P.; Lischka, H. *J. Phys. Chem. A* **2011**, *115*, S247–S255.
- (26) Fingerhut, B. P.; Dorfman, K. E.; Mukamel, S. *J. Phys. Chem. Lett.* **2013**, *4*, 1933–1942.
- (27) Richter, M.; Marquetand, P.; González, L. *Phys. Chem. Chem. Phys.* **2014**, *16*, 24423.
- (28) Nieber, H.; Doltsinis, N. L. *Chem. Phys.* **2008**, *347*, 405–412.
- (29) Picconi, D.; Lami, A.; Santoro, F. *J. Chem. Phys.* **2012**, *136*, 244104.
- (30) Picconi, D.; Barone, V.; Lami, A.; Santoro, F.; Improta, R. *ChemPhysChem* **2011**, *12*, 1957–1968.
- (31) Assmann, M.; Köppel, H.; Matsika, S. *J. Phys. Chem. A* **2015**, *119*, 866–875.
- (32) Matsika, S.; Zhou, C.; Kotur, M.; Weinacht, T. C. *Faraday Discuss.* **2011**, *153*, 247–260.
- (33) Matsika, S.; Spanner, M.; Kotur, M.; Weinacht, T. C. *J. Phys. Chem. A* **2013**, *117*, 12796–12801.
- (34) Gollub, C.; Kowalewski, M.; de Vivie-Riedle, R. *Phys. Rev. Lett.* **2008**, *101*, 073002.
- (35) Gollub, C.; Kowalewski, M.; Thallmair, S.; de Vivie-Riedle, R. *Phys. Chem. Chem. Phys.* **2010**, *12*, 15780.
- (36) Wilson, E. B., Jr.; Decius, J. C.; Cross, P. C. *Molecular Vibrations*; McGraw-Hill: New York, 1955.
- (37) Schaad, L.; Hu, J. *J. Mol. Struct.: THEOCHEM* **1989**, *185*, 203–215.
- (38) Kowalewski, M.; Mikosch, J.; Wester, R.; de Vivie-Riedle, R. *J. Phys. Chem. A* **2014**, *118*, 4661–4669.
- (39) Thallmair, S.; Roos, M. K.; de Vivie-Riedle, R. *J. Chem. Phys.* **2016**, *144*, 234104.
- (40) Lischka, H.; Müller, T.; Szalay, P. G.; Shavitt, I.; Pitzer, R. M.; Shepard, R. In *Wiley Interdisciplinary Reviews: Computational Molecular Science (WIREs:CMS)* Allen, W., Ed.; Wiley: Weinheim, 2011; Vol. 1, pp 191–199.
- (41) Lischka, H.; Shepard, R.; Pitzer, R. M.; Shavitt, I.; Dallos, M.; Müller, T.; Szalay, P. G.; Seth, M.; Kedziora, G. S.; Yabushita, S.; Zhang, Z. *Phys. Chem. Chem. Phys.* **2001**, *3*, 664.
- (42) Lischka, H.; Shepard, R.; Shavitt, I.; Pitzer, R. M.; Dallos, M.; Müller, T.; Szalay, P. G.; Brown, F. B.; Ahlrichs, R.; Böhm, H. J.; Chang, A.; Comeau, D. C.; Gdanitz, R.; Dachsels, H.; Ehrhardt, C.; Ernzerhof, M.; Höchtl, P.; Irl, S.; Kedziora, G.; Kovar, T.; Parasuk, V.; Pepper, M. J. M.; Scharf, P.; Schiffer, H.; Schindler, M.; Schüler, M.; Seth, M.; Stahlberg, E. A.; Zhao, J.-G.; Yabushita, S.; Zhang, Z.; Barbatti, M.; Matsika, S.; Schuurmann, M.; Yarkony, D. R.; Brozell, S. R.; Beck, E. V.; Blaudeau, J. P.; Ruckebauer, M.; Sellner, B.; Plasser, F.; Szymczak, J. J. *COLUMBUS*, an ab initio electronic structure program, release 7.0, 2015.
- (43) Tal-Ezer, H.; Kosloff, R. *J. Chem. Phys.* **1984**, *81*, 3967.
- (44) von den Hoff, P.; Thallmair, S.; Kowalewski, M.; Siemering, R.; de Vivie-Riedle, R. *Phys. Chem. Chem. Phys.* **2012**, *14*, 14460–14485.
- (45) Palao, J. P.; Kosloff, R. *Phys. Rev. A: At, Mol, Opt. Phys.* **2003**, *68*, 062308.

3.2. The Influence of an RNA Strand and Different Base Sequences

Moving from laboratory-based experiments to more natural scenarios, the article “RNA Environment is Responsible for Decreased Photostability of Uracil” published in the *Journal of the American Chemical Society* investigates the relaxation mechanism not on isolated uracil but explicitly including the RNA environment. Additionally, instead of using a femtosecond laser pulse for excitation, the WP is simply put on the S_2 surface to simulate an unbiased excitation. In contrast to chapter 2, where the PES is recalculated completely in every snapshot, a separate solvent potential is computed for every snapshot with the means of QM/MM, where the neighboring nucleobases and the sugar/phosphate backbone connecting these bases are treated on the QM level, while the rest of the strand and the surrounding water molecules are treated on the MM level.

Using this setup for WP simulations, the key points of the following article are:

- The RNA environment is revealed to significantly affect the PES and thereby the WP behavior. While from a sample size of 275 snapshots most looked similar to the isolated case, scenarios are found where the relative energy of critical regions on the PES is changed, the barrier between S_2 minimum and CoIn is raised or removed, and completely new minima form. The behavior of the WP changes significantly in these cases.
- A statistical evaluation on the investigated sample size reveals a faster relaxation time in 5%, a similar relaxation time to the unperturbed case in 82%, and a faster relaxation time in 13% of snapshots. Assuming that from these 13% of slower relaxation only a few actually lead to photolesions, this on one hand confirms the high photostability of uracil by being unaffected from the environment in most cases, while it also can be concluded that the environmental effect in critical cases directly can be identified as the responsible factor for the formation of photolesions.
- Within the investigated sample size, ten different neighboring base sequences were used to check whether there are more or less critical configurations leading to extended excited state lifetimes. Assigning the excited state lifetimes to the four possible neighbors adenine, guanine, cytosine and uracil, it is observed that slower relaxation occurs with all of them and that therefore this mechanism of delayed excited state relaxation can be regarded as base-independent.

It should be noted that this relaxation on a single nucleobase is only one aspect of a bigger picture, as often an optical excitation within the strand leads to electronic delocalization due to base stacking, which was also identified to be responsible for increased excited state lifetimes [9]. The extend to which this delocalization occurs is still under debate [158], while the present article demonstrates that excited state longevity can occur locally, without the need for delocalization events. Effects like these are very hard to resolve experimentally, as on one hand competing pathways like delocalization or the simultaneous excitation of many nucleobases due to all of them absorbing in the same spectral region give a complex picture where the targeted effect might be hard to extract. On the other hand, the relaxation time is also measured on a certain sample size, where the delayed relaxation occurring in few snapshots might be invisible. Theoretical studies are therefore an important contribution and valuable tool to contribute to the complete picture.

Hereafter, the article “RNA Environment is Responsible for Decreased Photostability of Uracil” published in the *Journal of the American Chemical Society* is reprinted with

permission from *J. Am. Chem. Soc.* **2018**, *140*, 8714. Copyright 2018 American Chemical Society.

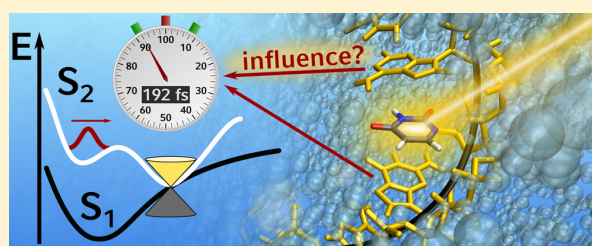
RNA Environment Is Responsible for Decreased Photostability of Uracil

Sebastian Reiter, Daniel Keefer, and Regina de Vivie-Riedle*[✉]

Department Chemie, Ludwig-Maximilians-Universität München, D-81377 München, Germany

S Supporting Information

ABSTRACT: UV light can induce chemical reactions in nucleic acids and thereby damage the genetic code. Like all of the five primary nucleobases, the isolated RNA base uracil exhibits ultrafast, nonradiative relaxation after photoexcitation, which helps to avoid photodamage most of the time. Nevertheless, within RNA and DNA strands, commonly occurring photolesions have been reported and are often ascribed to long-lived and delocalized excited states. Our quantum dynamical study now shows that excited-state longevity can also occur on a single nucleobase, without the need for delocalization. We include the effects of an atomistic RNA surrounding in wave packet simulations and explore the photorelaxation of uracil in its native biological environment. This reveals that steric hindrance through embedding in an RNA strand can inhibit the ultrafast relaxation mechanism of uracil, promoting excited-state longevity and potential photodamage. This process is nearly independent from the specific combination of neighboring bases.



INTRODUCTION

UV radiation can cause severe damage to the genetic information by chemically altering the nucleobases of DNA and RNA. All five canonical nucleobases found today are extraordinarily stable toward photodamage, which is also seen as the reason why they survived the evolutionary selection pressure in the early days of life, when solar radiation on the surface of the earth was more intense than today.^{1,2} This high photostability is usually attributed to ultrafast relaxation channels from electronically excited states back to the initial ground state, which have been reported both theoretically and experimentally for all five isolated bases.^{3–9} Obstruction of these relaxation channels can be directly linked to the formation of photodamage.^{10–12}

One of the most common photolesions, the cyclobutane pyrimidine dimer (CPD) has been extensively investigated for thymine,^{13–19} which is structurally closely related to the subject of this paper, uracil. It has been shown that CPD formation originates mainly from excitation to a singlet $^1\pi\pi^*$ state¹⁵ and can happen within just 1 ps after excitation for favorable initial molecular geometries.¹³ Triplet channels leading to CPD damage are also known but generally produce much lower yields.^{14,16–18} Experimentally, the singlet $^1\pi\pi^*$ state is usually excited with UVC radiation (200–290 nm) because of the strong absorption in this range.^{3,4,6–9} Although the UVC wavelengths are filtered by the atmosphere, lower energy UVB radiation (290–320 nm) that does reach the surface of the earth can also induce harmful yields of photolesions in RNA under physiological conditions.²⁰

Transferring these results to uracil, we will focus on the first relaxation step out of the bright $^1\pi\pi^*$ S_2 state in our

investigation. In isolated uracil, this relaxation takes place within the ultrafast femtosecond regime, which is regarded as one of the main reasons for photostability. A recent quantum dynamical study on isolated uracil uncovered the possibility of inhibiting this ultrafast relaxation and preparing a long-living nuclear wave packet (WP) in the S_2 state with a tailored laser pulse, which might pave the way for experiments related to the formation of photodamage.²¹

However, the factor that induces excited-state longevity and therefore enables photochemical reactions in nature is not a laser field but the molecular environment of the nucleobases.^{22,23} In our present theoretical study, we show that embedding of uracil in its natural nucleic acid environment may directly inhibit the ultrafast relaxation process responsible for photostability. Long-lived excited states in oligo- and polynucleotides are often ascribed to delocalization events in base stacks, such as excimer or exciton formation, where the extent of excited-state delocalization has long been subject to debate.^{24–33} While this undoubtedly constitutes an important photochemical pathway in nucleic acids, we report that prevention of ultrafast photorelaxation can also occur on single nucleobases, without the need for delocalization events. For adenine, this was suggested previously by correlating quantum mechanics/molecular mechanics (QM/MM) energy profiles with experimental lifetimes.³⁴ In the present study, we can directly extract excited-state lifetimes from quantum dynamical simulations of uracil under atomistic consideration of the natural RNA environment. Moreover, we shed light on

Received: March 22, 2018

Published: June 26, 2018

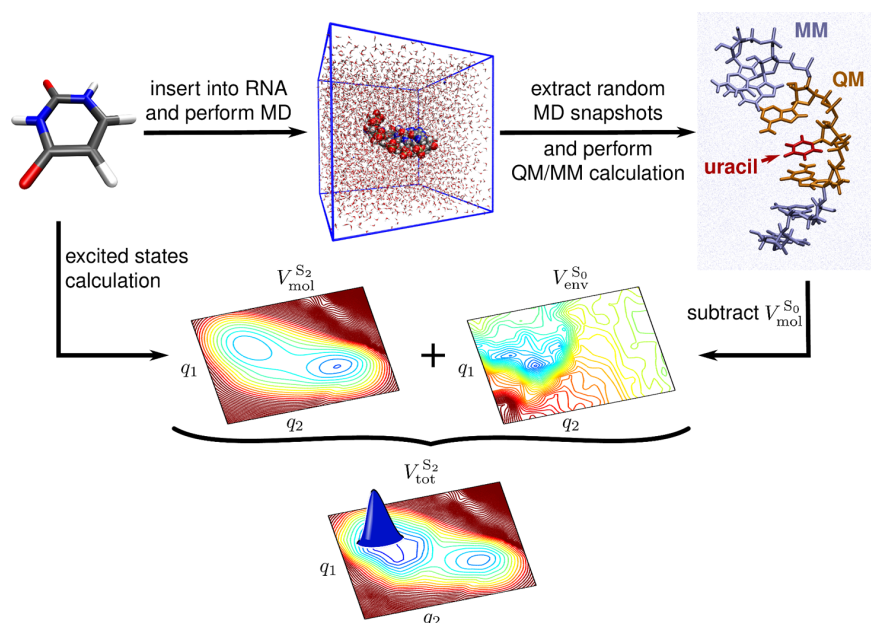


Figure 1. Flowchart for the combined QD/MD approach. Environmental conformations are sampled with classical MD trajectories and are used to compute an environmental potential \hat{V}_{env} on a QM/MM level of theory. \hat{V}_{env} is subsequently added to a precomputed high-level excited-state PES of the isolated base in order to perform wave packet dynamics under explicit consideration of the atomistic surrounding.

whether specific combinations of neighboring bases are more or less beneficial for this process and, thus, for the potential formation of photodamage.

COMPUTATION OF ENVIRONMENTAL INFLUENCES

We performed quantum dynamical WP propagations on multiscale QM/MM potential energy surfaces (PESs)³⁵ as described in detail hereafter. As a reference for our calculations, we used a previously published, two-dimensional (2D) PES of isolated uracil in its bright S_2 state ($1\pi\pi^*$) on the MRCI(12,9)/cc-pVDZ level of theory.²¹ Containing the optimized molecular geometries of uracil at the Franck–Condon (FC) point, the S_2 -minimum, and a conical intersection (CoIn) seam between S_2 and S_1 ($n\pi^*$), it has proven to reproduce experimental relaxation times well in quantum dynamical simulations.²¹

To include the effects of a biological environment, we employed a modified version of the quantum dynamics/molecular dynamics (QD/MD) approach,³⁶ which is schematically drawn in Figure 1.

Here, the temporal evolution of the WP is described by the time-dependent Schrödinger equation (TDSE)

$$i\hbar \frac{\partial}{\partial t} \Psi = (\hat{T}_{\text{nuc}} + \hat{V}_{\text{mol}} + \hat{V}_{\text{env}}) \Psi \quad (1)$$

with the nuclear kinetic energy \hat{T}_{nuc} , the potential energy of the solute \hat{V}_{mol} , and the environment potential \hat{V}_{env} . In our case, \hat{V}_{mol} represents the high-level S_2 -PES of isolated uracil, while \hat{V}_{env} contains the environmental influence and was computed as follows: In a first step, the conformations of 10 different uracil-containing RNA sequences in water were sampled by running MD trajectories and extracting 25 geometry snapshots per sequence at random times (total: 250 snapshots). We tested doubling the number of snapshots for the base sequence

5'-GAGUAGG-3' from 25 to 50 but observed no changes in the distribution of slower and faster relaxation times out of S_2 . Since this study focuses on the rare occurrence of delayed relaxation rather than on the computation of average values, we concluded that 25 random snapshots per base sequence were an adequate number of samples for the purposes of this investigation.

Next, we used QM/MM calculations (DFT-D3/M06-2X/6-31G**/Amber14Sb) with a QM region comprised of uracil, two neighboring bases, and the connecting sugar phosphate backbone (see also top right of Figure 1) to raster the 2D-PES of uracil and to obtain an atomistic evaluation of environmental influence for each snapshot. With around 100 atoms in the QM region and 250 PESs to be calculated, this is highly demanding in terms of computational effort, which is why we performed these calculations at the Leibniz Supercomputing Center in Munich. We also tested the effects of including water molecules in a 5 Å radius around the central uracil moiety in the QM region for several snapshots (~200 QM atoms) but found that the statistical results presented in the next section were not influenced by this. Moreover, Roßbach and Ochsenfeld showed that QM/MM energies of DNA strands converge beyond the first layer of adjacent nucleobases.³⁷ Testing one snapshot, we observed similar convergence for the PES topography and excited-state lifetime. To avoid double-counting of \hat{V}_{mol} , the PES of isolated uracil on the DFT-D3/M06-2X/6-31G** level of theory was subtracted from the QM/MM potential, yielding \hat{V}_{env} .

This interaction potential was finally added to the excited-state PES of isolated uracil, $\hat{V}_{\text{mol}}^{S_2}$, and WP simulations were performed on the obtained PES for every snapshot by launching a nuclear WP from the FC point, where it enters the S_2 state after excitation. Adding the environmental influence on the ground state to the excited-state potential is a justifiable approximation in our case since the charge distribution of uracil after excitation to the $\pi\pi^*$ S_2 state is in

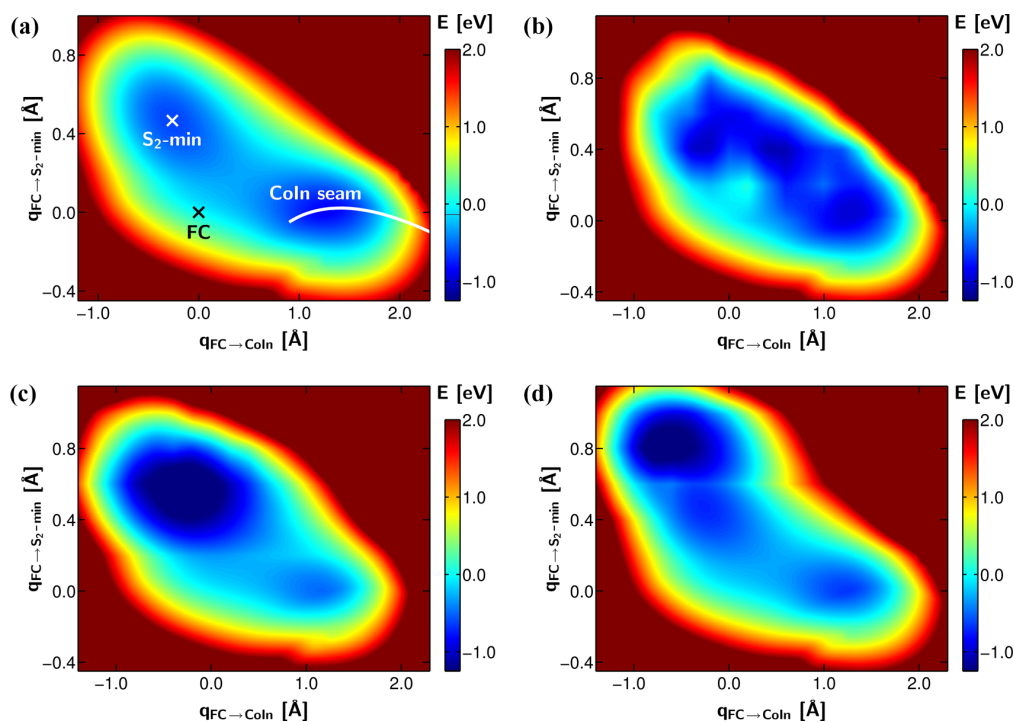


Figure 2. Examples for strong environmental influence on the S_2 -PES of uracil. The PESs were constructed by adding \hat{V}_{env} (see Figure 1) to the S_2 -PES (MRCI(12,9)/cc-pVDZ) of the isolated base. Note that these are extreme cases and for most conformational snapshots the PES closely resembles the one of the isolated base.

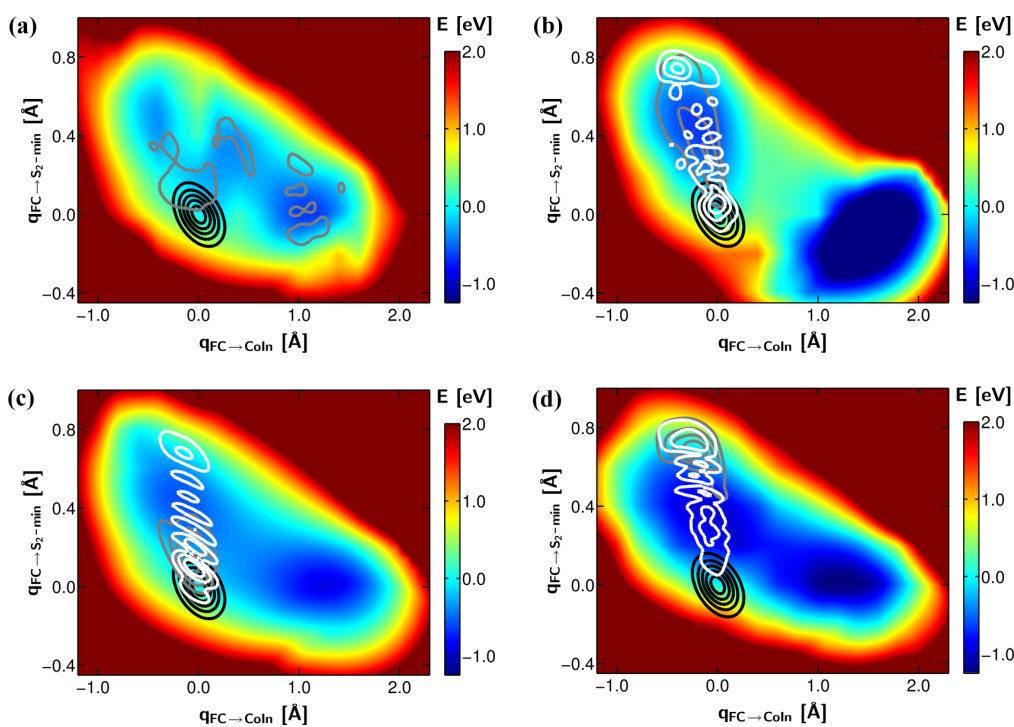


Figure 3. Exemplary nuclear WPs on the S_2 -PES of uracil at 0 fs (black), 50 fs (gray), and 500 fs (white). Snapshots from the RNA sequence (a, b) 5'-GACUCGG-3', (c) 5'-GAGUUGG-3', and (d) 5'-GAAUAGG-3'. The WPs start at the FC point, evolve toward the S_2 -minimum, and decay through the CoIn seam with vastly different relaxation times. In (a), the WP has already completely decayed before 500 fs. Animations of these quantum dynamical propagations are available in the online version of this article.

close agreement with that in the ground state (see [Supporting Information](#) for details). The electrostatic interaction of this excited state with the environment will therefore be very similar to the ground-state interaction.

For the isolated base, it has been shown that the inclusion of a third dimension in the coordinate space does not change the lifetimes extracted from these WP simulations.²¹ Moreover, we tested the inclusion of five normal modes, covering a wide range of molecular degrees of freedom, in the 2D coordinate space for five different MD snapshots but did not find any relevant new pathways in the third dimension (see [Supporting Information](#) for details).

RESULTS AND DISCUSSION

The influence of a biological environment can drastically alter the PES of isolated uracil. Examples for this are drawn in [Figure 2b–d](#) with the PES of the isolated nucleobase as a reference in [Figure 2a](#). We observed several stabilizing and destabilizing effects, such as lowering of the barrier between S_2 -minimum and CoIn seam ([Figure 2b](#)), the relative stabilization of one of the two minima ([Figure 2c](#)), and even the formation of a new minimum on the PES ([Figure 2d](#)).

Nevertheless, the examples depicted in [Figure 2](#) are extreme cases, and the majority of the 250 calculated PESs closely resemble the one of the isolated nucleobase. Linking the molecular structure to the PES topography, we noted stabilizing effects by hydrogen bonds from uracil to the sugar phosphate backbone. A similar interaction occurs when positively polarized hydrogen atoms of the uracil moiety are located favorably in the Coulomb field of the more electronegative nitrogen atoms in neighboring bases. Rises in energy could mostly be attributed to steric hindrances in the environment that impede the out-of-plane movement of uracil along the coordinate vectors of the PES.

As could be expected, such environmentally induced changes in the excited-state PES topography can have a strong effect on the path of a nuclear WP and, therefore, the relaxation time back to the ground state. In the isolated base, the WP undergoes two oscillations between the FC point and S_2 -minimum, before decaying through the CoIn to S_1 with a lifetime of $t_{1/2} = 192$ fs. We define the excited-state lifetime $t_{1/2}$ as the time where half of the population has decayed from S_2 .

The environmental influence on the WP behavior is illustrated in [Figure 3](#). In [Figure 3a](#) and [b](#), two different snapshots of the base sequence 5'-GACUCGG-3' are drawn, where the WPs are launched from the FC point and exhibit significantly different time evolution. The WP in [Figure 3a](#) reaches the CoIn after a very short time ($t_{1/2} = 76$ fs) and only one oscillation through the S_2 -minimum, whereas the WP in [Figure 3b](#) remains trapped in the S_2 state for several picoseconds ($t_{1/2} = 3.5$ ps). Despite this trap, we observe that after a long amount of time, even the lower energetic parts of the WP eventually decay to S_1 , which can be explained by tunneling through the barrier to the CoIn. Another notable quantum effect is that even in cases where the PES closely resembles the one of isolated uracil ([Figure 3c](#)), minor topographical changes in critical areas of the PES, especially in the regions around the FC point and S_2 -minimum, can strongly decelerate the relaxation. This can also be observed in snapshots where the barrier between S_2 -minimum and CoIn is lowered ([Figure 3d](#)). Usually, a reduced barrier height leads to the assumption of faster relaxation times, which is not true in some of our cases. We attribute this counterintuitive

behavior to a lack of initial momentum in the direction of the CoIn because of changed potential energy gradients in the FC region and at the turning point beyond the S_2 -minimum. In such cases, the coherence of the WP hinders its evolution toward the CoIn and, thus, over the barrier. The extracted relaxation time is, therefore, insensitive to the height of the barrier. This observation emphasizes the need for true quantum dynamical simulations to obtain an accurate picture of photophysical relaxation processes, additional to comparing single-point energies.

The discussed effects can occur in all of the base sequences we tested. In this context, [Figure 4](#) compiles the population

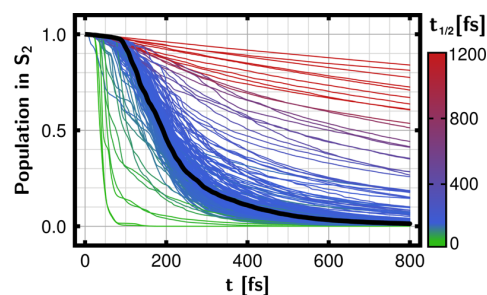


Figure 4. Temporal evolution of the population in the electronic S_2 state of uracil in 250 different environmental snapshots compared to the reference population for the isolated base (black). The color of the curves indicates how much the half-life differs from the reference of 192 fs. While most snapshots exhibit lifetimes similar to that of the isolated base, about 13% decay slower and might promote photodamage.

decay curves of all 250 quantum dynamical simulations with the color encoding the respective half-life in S_2 . The majority of snapshots (82%) decay with a half-life in the range of ± 50 fs around the reference of 192 fs, while 5% exhibit significantly accelerated relaxation. This is in line with the high photostability of uracil, even inside an RNA strand. Nonetheless, 13% of the 250 sampled environmental conformations cause delayed relaxation and sometimes even increase the lifetime in S_2 more than 10-fold. For the closely related thymine, it has been demonstrated that this might already be enough for harmful photochemical reactions to take place.¹³ Since our PESs only include the monomer-like decay channel of uracil, these results indicate that steric influences of the environment alone can account for long excited state lifetimes and, therefore, can potentially enable the formation of photolesions.

To find out whether there are neighboring bases that favor this behavior, we considered 10 RNA sequences in our simulations, each with a different combination of uracil-adjacent nucleobases. For each possible neighboring base A, C, G, and U, we extracted the percentage of faster ($t_{1/2} < 142$ fs), similar ($t_{1/2} = (192 \pm 50)$ fs), and slower ($t_{1/2} > 242$ fs) relaxation times as compared to the reference in all snapshots containing the respective base next to uracil. The obtained results are visualized in [Figure 5](#) for each neighboring base. In all cases, the majority of samples exhibit lifetimes in S_2 that are very similar to the one in isolated uracil. Snapshots that induce faster or slower population decay occur for all four possible neighboring bases, with a clear trend toward the latter. There are no pronounced differences between the individual bases, and thus, we conclude that no single neighboring base is

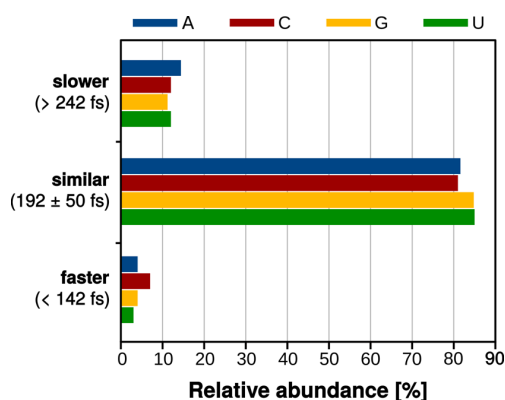


Figure 5. Relative abundance (in percent) of slower, and faster relaxation times $t_{1/2}$ for each neighboring base in a total of 10 different RNA sequences of the type 5'-GAXUYGG-3', as compared to isolated uracil (192 fs). As the percentages are very similar for all four possible neighbors, we conclude that no particular base promotes delayed relaxation in uracil by sterical hindrance.

distinctly responsible for the promotion of excited-state longevity and thereby photodamage in uracil.

CONCLUSIONS

To summarize, our present study illustrates that the ultrafast photorelaxation of the RNA-base uracil can be strongly impeded by the steric influence of its biological surrounding. By modeling an atomistic environment with multiscale QM/MM calculations and investigating the relaxation process of photoexcited uracil with quantum dynamical simulations, we demonstrated that long relaxation times of several picoseconds can occur in the monomer-like decay channel without the need for excited-state delocalization. With ultrafast relaxation being regarded as the main reason for photostability, it is conceivable that this long excited state lifetime is one of the mechanisms which enable the formation of photolesions in nucleic acid strands. Sampling a total of 250 environmental conformations in 10 different uracil-containing base sequences, we found longer relaxation times in about 13% of cases, while only 5% decayed significantly faster than in the isolated base. We noted that even small changes in the PES topography can dramatically influence the excited-state lifetime as compared to the isolated nucleobase. A majority of 82% showed very similar relaxation times to the one in isolated uracil, which is in line with the fact that photodamage is a rare event in nature, especially if we assume that only a small share of these 13% might actually lead to harmful photochemical reactions. There is no particular neighboring base that promotes trapping in the excited state and, therefore, photodamage, so we conclude that this is rather a general effect of sterical hindrance in the RNA environment.

COMPUTATIONAL DETAILS

The optimized molecular structures of uracil^{38,39} (MRCI-(12,9)/cc-pVDZ), used to construct the 2D coordinate space, as well as the excited-state PES of isolated uracil²¹ and the coordinate vectors²¹ for PES construction have been adopted from previous works as cited earlier. For convenience, they are also included in the Supporting Information of this article.

The structures of 10 RNA single strand A-type helices with the seven-base sequences outlined in Figure 6 were generated

with the web-application Make-NA.⁴⁰ In every strand, the fourth base (uracil) was replaced with the optimized ground state geometry of uracil.

		base on 5' end			
		G	A	C	U
base on 3' end	G	GUG	AUG	CUG	UUG
	A	GUA	AUA	CUA	UUA
	C	GUC	AUC	CUC	UUC
	U	GUU	AUU	CUU	UUU

Figure 6. Overview of the possible combinations of nucleobases in direct vicinity of uracil. The ones chosen for this study are highlighted in a darker shade and were complemented by a leading 5'-GA segment and a GG-3'-tail (e.g., 5'-GA-GUA-GG-3').

The prepared RNA strands were placed in a cubic box with 5.2 nm edge length and were solvated in TIP3P⁴¹ water before neutralizing the system with sodium ions. Using the Gromacs 5.1.2^{42,43} software in combination with the Amber14SB^{44–47} force field, integration of Newton's equations was carried out with the Velocity Verlet integrator⁴⁸ over a period of 100 ps with a time step of 1 fs and using five different starting conditions per RNA sequence. Temperature control was achieved with the Berendsen thermostat⁴⁹ at 298.15 K. The system was equilibrated by propagating for 10 ps before extracting snapshots. To separate quantum from classical movement, the internal motion of uracil was frozen with the Rattle⁵⁰ algorithm during the simulations. This approximation might slightly influence the MD but enables a better comparison of the quantum dynamical simulations as all WPs start at the same FC point.

Multiscale QM/MM calculations were performed with the ChemShell 3.6.0^{51–53} environment on the CoolMUC-2 infrastructure of the Leibniz Supercomputing Center. Here, the QM part of the calculations was carried out at the DFT-D3/M06-2X/6-31G* level of theory⁵⁴ with the Gaussian09⁵⁵ package, while the energy of the MM subsystem was evaluated with the DL POLY 2 module⁵⁶ using the TIP3P⁴¹ and Amber14SB^{44–47} force fields for water and RNA, respectively. An electrostatic embedding scheme⁵⁷ was used to couple the two subsystems via the link-atom^{52,58} approach. Overpolarization of the QM region in the vicinity of the link atom was avoided by shifting classical charges away from the boundary region.⁵² The QM subsystem was chosen to contain uracil with two neighboring bases and the interconnecting sugar-phosphate backbone (see also top right of Figure 1). Specifically, the cuts between QM and MM regions went through the P–5'O and 3'O–P bonds. PESs were constructed in the 2D coordinate space described by Keefer et al.²¹ and using the approach explained in the methodology section.

Using these PESs, the TDSE (eq 1) was solved on a spatial grid with 128 × 128 points using the Chebyshev⁵⁹ propagation scheme for WP simulations. To represent the kinetic energy

operator in reduced coordinates, we employed the Wilson G-matrix formalism.^{36,60,61} Nonadiabatic couplings between S_2 and S_1 were adopted from previous works and can be found there along with the G-matrix elements.²¹ The WP was absorbed by a masking function after crossing the CoIn to the S_1 state.

■ ASSOCIATED CONTENT

📄 Supporting Information

The Supporting Information is available free of charge on the ACS Publications website at DOI: 10.1021/jacs.8b02962.

Optimized molecular geometries and coordinate vectors spanning the potential energy surfaces; electric dipole moments and electrostatic potentials for the first few excited states of uracil QM/MM potential energy scans in three dimensions

(PDF)

Animation of the quantum dynamical propagations for the isolated base

(AVI)

Animation of the quantum dynamical propagations shown in Figure 3a

(AVI)

Animation of the quantum dynamical propagations shown in Figure 3b

(AVI)

Animation of the quantum dynamical propagations shown in Figure 3c

(AVI)

Animation of the quantum dynamical propagations shown in Figure 3d

(AVI)

■ AUTHOR INFORMATION

Corresponding Author

*regina.de_vivie@cup.uni-muenchen.de

ORCID

Regina de Vivie-Riedle: 0000-0002-7877-5979

Notes

The authors declare no competing financial interest.

■ ACKNOWLEDGMENTS

We thank Spiridoula Matsika for the fruitful collaboration in our previous study on uracil, which served as the basis for this manuscript. Financial support by the Deutsche Forschungsgemeinschaft through the excellence cluster Munich-Centre for Advanced Photonics (MAP) and the SFB749 is acknowledged. The authors gratefully acknowledge the compute and data resources provided by the Leibniz Supercomputing Center. D. K. acknowledges financial support by the Dr. Klaus Römer foundation.

■ REFERENCES

- (1) Sagan, C. J. *Theor. Biol.* **1973**, *39*, 195.
- (2) Beckstead, A. A.; Zhang, Y.; de Vries, M. S.; Kohler, B. *Phys. Chem. Chem. Phys.* **2016**, *18*, 24228.
- (3) Kang, H.; Lee, K. T.; Jung, B.; Ko, Y. J.; Kim, S. K. *J. Am. Chem. Soc.* **2002**, *124*, 12958.
- (4) He, Y.; Wu, C.; Kong, W. J. *Phys. Chem. A* **2003**, *107*, 5145.
- (5) Crespo-Hernández, C. E.; Cohen, B.; Hare, P. M.; Kohler, B. *Chem. Rev.* **2004**, *104*, 1977.
- (6) Ullrich, S.; Schultz, T.; Zgierski, M. Z.; Stolow, A. *Phys. Chem. Chem. Phys.* **2004**, *6*, 2796.
- (7) Canuel, C.; Mons, M.; Piuze, F.; Tardivel, B.; Dimicoli, I.; Elhanine, M. J. *Chem. Phys.* **2005**, *122*, 074316.
- (8) Middleton, C. T.; de La Harpe, K.; Su, C.; Law, Y. K.; Crespo-Hernández, C. E.; Kohler, B. *Annu. Rev. Phys. Chem.* **2009**, *60*, 217.
- (9) Kotur, M.; Weinacht, T. C.; Zhou, C.; Matsika, S. *IEEE J. Sel. Top. Quantum Electron.* **2012**, *18*, 187.
- (10) Tommasi, S.; Denissenko, M. F.; Pfeifer, G. P. *Cancer Res.* **1997**, *57*, 4727.
- (11) Esposito, L.; Banyasz, A.; Douki, T.; Perron, M.; Markovitsi, D.; Improta, R. *J. Am. Chem. Soc.* **2014**, *136*, 10838.
- (12) Martínez-Fernández, L.; Pepino, A. J.; Segarra-Martí, J.; Jovaišaitė, J.; Vaya, I.; Nenov, A.; Markovitsi, D.; Gustavsson, T.; Banyasz, A.; Garavelli, M.; Improta, R. *J. Am. Chem. Soc.* **2017**, *139*, 7780.
- (13) Schreier, W. J.; Schrader, T. E.; Koller, F. O.; Gilch, P.; Crespo-Hernández, C. E.; Swaminathan, V. N.; Carell, T.; Zinth, W.; Kohler, B. *Science* **2007**, *315*, 625.
- (14) Kwok, W.-M.; Ma, C.; Phillips, D. L. *J. Am. Chem. Soc.* **2008**, *130*, 5131.
- (15) Schreier, W. J.; Kubon, J.; Regner, N.; Haiser, K.; Schrader, T. E.; Zinth, W.; Clivio, P.; Gilch, P. *J. Am. Chem. Soc.* **2009**, *131*, 5038.
- (16) Ákos Bányász; Douki, T.; Improta, R.; Gustavsson, T.; Onidas, D.; Vayá, I.; Perron, M.; Markovitsi, D. *J. Am. Chem. Soc.* **2012**, *134*, 14834.
- (17) Pilles, B. M.; Bucher, D. B.; Liu, L.; Clivio, P.; Gilch, P.; Zinth, W.; Schreier, W. J. *J. Phys. Chem. Lett.* **2014**, *5*, 1616.
- (18) Liu, L.; Pilles, B. M.; Gontcharov, J.; Bucher, D. B.; Zinth, W. *J. Phys. Chem. B* **2016**, *120*, 292.
- (19) Conti, I.; Martínez-Fernández, L.; Esposito, L.; Hofinger, S.; Nenov, A.; Garavelli, M.; Improta, R. *Chem. - Eur. J.* **2017**, *23*, 15177.
- (20) Wurtmann, E. J.; Wolin, S. L. *Crit. Rev. Biochem. Mol. Biol.* **2009**, *44*, 34.
- (21) Keefer, D.; Thallmair, S.; Matsika, S.; de Vivie-Riedle, R. *J. Am. Chem. Soc.* **2017**, *139*, 5061.
- (22) *Photoinduced Phenomena in Nucleic Acids I*; Barbatti, M., Borin, A. C., Ullrich, S., Eds.; Springer International Publishing: Basel, Switzerland, 2015.
- (23) Improta, R.; Santoro, F.; Blancafort, L. *Chem. Rev.* **2016**, *116*, 3540.
- (24) Tinoco, I. *J. Am. Chem. Soc.* **1960**, *82*, 4785.
- (25) Eisinger, J.; Shulman, R. G. *Science* **1968**, *161*, 1311.
- (26) Crespo-Hernández, C. E.; Cohen, B.; Kohler, B. *Nature* **2005**, *436*, 1141.
- (27) Buchvarov, I.; Wang, Q.; Raytchev, M.; Trifonov, A.; Fiebig, T. *Proc. Natl. Acad. Sci. U. S. A.* **2007**, *104*, 4794.
- (28) Kadhane, U.; Holm, A. I. S.; Hoffmann, S. V.; Nielsen, S. B. *Phys. Rev. E* **2008**, *77*, 021901.
- (29) Takaya, T.; Su, C.; de La Harpe, K.; Crespo-Hernández, C. E.; Kohler, B. *Proc. Natl. Acad. Sci. U. S. A.* **2008**, *105*, 10285.
- (30) Lange, A. W.; Herbert, J. M. *J. Am. Chem. Soc.* **2009**, *131*, 3913.
- (31) Markovitsi, D.; Gustavsson, T.; Banyasz, A. *Mutat. Res., Rev. Mutat. Res.* **2010**, *704*, 21.
- (32) Chen, J.; Zhang, Y.; Kohler, B. In *Photoinduced Phenomena in Nucleic Acids II*; Barbatti, M., Borin, A. C., Ullrich, S., Eds.; Springer International Publishing: Basel, Switzerland, 2014; p 39.
- (33) Nogueira, J. J.; Plasser, F.; González, L. *Chem. Sci.* **2017**, *8*, 5682.
- (34) Conti, I.; Altoè, P.; Stenta, M.; Garavelli, M.; Orlandi, G. *Phys. Chem. Chem. Phys.* **2010**, *12*, 5016.
- (35) Warshel, A.; Levitt, M. *J. Mol. Biol.* **1976**, *103*, 227.
- (36) Thallmair, S.; Zauleck, J. P. P.; de Vivie-Riedle, R. *J. Chem. Theory Comput.* **2015**, *11*, 1987.
- (37) Roßbach, S.; Ochsenfeld, C. *J. Chem. Theory Comput.* **2017**, *13*, 1102.
- (38) Matsika, S. *J. Phys. Chem. A* **2004**, *108*, 7584.
- (39) Yoshikawa, A.; Matsika, S. *Chem. Phys.* **2008**, *347*, 393.

- (40) Stroud, J. *Make-NA*, v. 0.10; <http://structure.usc.edu/make-na/server.html> (accessed Oct 23, 2017).
- (41) Jorgensen, W. L.; Chandrasekhar, J.; Madura, J. D.; Impey, R. W.; Klein, M. L. *J. Chem. Phys.* **1983**, *79*, 926.
- (42) Pronk, S.; Páll, S.; Schulz, R.; Larsson, P.; Bjelkmar, P.; Apostolov, R.; Shirts, M. R.; Smith, J. C.; Kasson, P. M.; van der Spoel, D.; Hess, B.; Lindahl, E. *Bioinformatics* **2013**, *29*, 845.
- (43) Abraham, M. J.; Murtola, T.; Schulz, R.; Páll, S.; Smith, J. C.; Hess, B.; Lindahl, E. *SoftwareX* **2015**, *1*, 19.
- (44) Graf, J.; Nguyen, P. H.; Stock, G.; Schwabe, H. *J. Am. Chem. Soc.* **2007**, *129*, 1179.
- (45) Wickstrom, L.; Okur, A.; Simmerling, C. *Biophys. J.* **2009**, *97*, 853.
- (46) Lindorff-Larsen, K.; Piana, S.; Palmo, K.; Maragakis, P.; Klepeis, J. L.; Dror, R. O.; Shaw, D. E. *Proteins: Struct., Funct., Genet.* **2010**, *78*, 1950.
- (47) Nguyen, H.; Roe, D. R.; Simmerling, C. *J. Chem. Theory Comput.* **2013**, *9*, 2020.
- (48) Swope, W. C.; Andersen, H. C.; Berens, P. H.; Wilson, K. R. *J. Chem. Phys.* **1982**, *76*, 637.
- (49) Berendsen, H. J. C.; Postma, J. P. M.; van Gunsteren, W. F.; DiNola, A.; Haak, J. R. *J. Chem. Phys.* **1984**, *81*, 3684.
- (50) Andersen, H. C. *J. Comput. Phys.* **1983**, *52*, 24.
- (51) *ChemShell*, v. 3.6; a Computational Chemistry Shell; <http://www.chemshell.org>, accessed July 2, 2017.
- (52) Sherwood, P.; de Vries, A. H.; Guest, M. F.; Schreckenbach, G.; Catlow, C. R. A.; French, S. A.; Sokol, A. A.; Bromley, S. T.; Thiel, W.; Turner, A. J.; Billeter, S.; Terstegen, F.; Thiel, S.; Kendrick, J.; Rogers, S. C.; Casci, J.; Watson, M.; King, F.; Karlsen, E.; Sjøvoll, M.; Fahmi, A.; Schäfer, A.; Lennartz, C. *J. Mol. Struct.: THEOCHEM* **2003**, *632*, 1.
- (53) Metz, S.; Kästner, J.; Sokol, A. A.; Keal, T. W.; Sherwood, P. *WIREs Comput. Mol. Sci.* **2014**, *4*, 101.
- (54) Grimme, S.; Antony, J.; Ehrlich, S.; Krieg, H. *J. Chem. Phys.* **2010**, *132*, 154104.
- (55) Frisch, M. J.; Trucks, G. W.; Schlegel, H. B.; Scuseria, G. E.; Robb, M. A.; Cheeseman, J. R.; Scalmani, G.; Barone, V.; Mennucci, B.; Petersson, G. A.; Nakatsuji, H.; Caricato, M.; Li, X.; Hratchian, H. P.; Izmaylov, A. F.; Bloino, J.; Zheng, G.; Sonnenberg, J. L.; Hada, M.; Ehara, M.; Toyota, K.; Fukuda, R.; Hasegawa, J.; Ishida, M.; Nakajima, T.; Honda, Y.; Kitao, O.; Nakai, H.; Vreven, T.; Montgomery, J. A., Jr.; Peralta, J. E.; Ogliaro, F.; Bearpark, M.; Heyd, J. J.; Brothers, E.; Kudin, K. N.; Staroverov, V. N.; Kobayashi, R.; Normand, J.; Raghavachari, K.; Rendell, A.; Burant, J. C.; Iyengar, S. S.; Tomasi, J.; Cossi, M.; Rega, N.; Millam, J. M.; Klene, M.; Knox, J. E.; Cross, J. B.; Bakken, V.; Adamo, C.; Jaramillo, J.; Gomperts, R.; Stratmann, R. E.; Yazyev, O.; Austin, A. J.; Cammi, R.; Pomelli, C.; Ochterski, J. W.; Martin, R. L.; Morokuma, K.; Zakrzewski, V. G.; Voth, G. A.; Salvador, P.; Dannenberg, J. J.; Dapprich, S.; Daniels, A. D.; Farkas, O.; Foresman, J. B.; Ortiz, J. V.; Cioslowski, J.; Fox, D. J. *Gaussian 09*, revision D.01; Gaussian, Inc.: Wallingford, CT, 2009.
- (56) Smith, W.; Forester, T. *J. Mol. Graphics* **1996**, *14*, 136.
- (57) Bakowies, D.; Thiel, W. *J. Phys. Chem.* **1996**, *100*, 10580.
- (58) Eichler, U.; Kölmel, C. M.; Sauer, J. *J. Comput. Chem.* **1997**, *18*, 463.
- (59) Tal-Ezer, H.; Kosloff, R. *J. Chem. Phys.* **1984**, *81*, 3967.
- (60) Schaad, L. J.; Hu, J. *J. Mol. Struct.: THEOCHEM* **1989**, *185*, 203.
- (61) Kowalewski, M.; Mikosch, J.; Wester, R.; de Vivie-Riedle, R. *J. Phys. Chem. A* **2014**, *118*, 4661.

Chapter 4.

Implications of the Quantum Control Results for Future Studies

Besides the detailed presentation of specific results to a specialized audience, it is useful to once in a while take a step back and evaluate the relevance of the results for a broader audience. This is especially true for interdisciplinary fields like the ultrafast molecular sciences, where among others the different research areas of laser source development, pulse application, preparative chemistry, interrogative physics like optical spectroscopy, theoretical method development and applied simulations overlap. Novel chemistry and physics can often be discovered at the borderlines and points of contact between the different areas, and for this purpose it is helpful to identify possible overlap and stimulate or inspire collaborations.

The following article uses the quantum control results presented in chapters 2 and 3.1 and evaluates their implications for future applications. After the first successful quantum control experiments on molecular systems [25], a vast activity in this field entailed the accomplishment of several remarkable control aims, like the ones mentioned in the introduction of this thesis. During the last years, the field somewhat struggled in finding the next powerful application. One of its most ambitious goals — finding broad application in chemical synthesis — has not been reached to date, and in this connection the article discovers the chemical environment as one aspect which might be responsible for this and suggests possible ways to overcome it. The second possible application revolves around optical spectroscopy. With OCT simulations being constantly developed to more closely correspond to experimental conditions [48], this resulted in a surprisingly simple laser pulse achieving a complex control task: Preparing a long-living WP in the excited state of uracil, which is possibly a precursor state for RNA photodamage (cf. chapter 3.1). Being able to optimize experimentally accessible laser pulses, the ability of theoretical simulations to specifically design tailored laser pulses for experimental applications in spectroscopy and QOC might substantially enhance the capabilities of these studies.

The article “Pathways to New Applications for Quantum Control” published in *Accounts of Chemical Research* gives a personal evaluation of the current status and future potential of QOC studies, based on the results presented in this thesis and highlighting the following key points:

- The simulation framework and optimization procedure of OCT is explained to a non-special audience with the goal to demonstrate its capabilities, features and limits. By nature, OCT is a purely mathematical procedure with no regards for experimentally accessible pulse shapes. Correspondence to the experimental domain is achieved by several additions to the algorithm, for example restricting the pulse spectrum to a given window, which significantly enhances the predictive and suggestive quality for experiments.

- These new capabilities recently enabled simulations to predict a surprisingly smooth laser pulse with experimentally accessible parameters to prepare a long-living excited state in uracil. This scheme is discussed to be useful for spectroscopic applications in general, where the predictive quality of laser pulse optimizations can be used to design, assist and enable novel spectroscopic experiments which depend upon the preparation of very specific and WPs.
- With respect to quantum control of complex synthetic processes involving the formation of new bonds, the solvent environment was identified to drastically complicate this control task. The global nature of the OCT algorithm enables feasibility studies on whether the arising complexities can be overcome. From these simulations, control strategies can be suggested to optimize experimental yields with respect to these features. This is associated with the recently emerging field of flow chemistry, where sample volumes are mixed in small and controlled volumes under continuous flow, benefiting the application of laser pulses for several reasons and potentially increasing the chances for a successful application of quantum control.

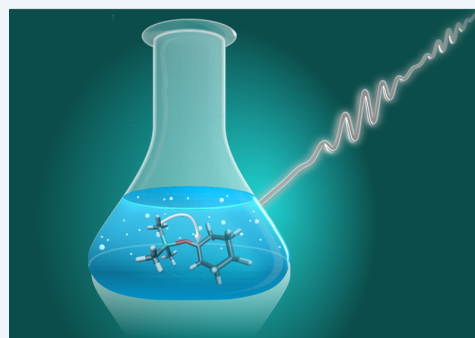
Hereafter, the article “Pathways to New Applications for Quantum Control” published in *Accounts of Chemical Research* is reprinted with permission from *Acc. Chem. Res.* **2018**, *51*, 2279. Copyright 2018 American Chemical Society.

Pathways to New Applications for Quantum Control

Daniel Keefer and Regina de Vivie-Riedle*

Department Chemie, Ludwig-Maximilians-Universität München, D-81377 München, Germany

CONSPECTUS: In 1998, the first successful quantum control experiment with application to a molecular framework was conducted with a shaped laser pulse, optimizing the branching ratio between different organometallic reaction channels. This work induced a vast activity in quantum control during the next 10 years, and different optimization aims were achieved in the gas phase, liquid phase, and even in biologically relevant molecules like light-harvesting complexes. Accompanying and preceding this development were important advances in theoretical quantum control simulations. They predicted several control scenarios and explained how and why quantum control experiments work. After many successful proofs of concept in molecular science, the big challenge is to expand its huge conceptual potential of directly being able to steer nuclear and/or electronic motion to more applied implementations. In this Account, based on several recent advances, we give a personal evaluation of where the field of molecular quantum control is at the moment and especially where we think promising applications can be in the near future.



One of these paths leads to synthetic chemistry. The synthesis of novel pharmaceutical compounds or natural products often involves many synthetic steps, each one devouring resources and lowering the product yield. Shaped laser pulses can possibly act as photonic reagents and shorten the synthetic route toward the desired product. Chemical synthesis usually takes place in solution, and by including explicit solvent molecules in our quantum control simulations, we were able to identify their highly inhomogeneous influence on chemical reactions and how this affects potential quantum control. More important, we demonstrated for a synthetically relevant example that these complications can be overcome in theory, and laser pulses can be optimized to initiate the desired carbon–carbon bond formation. Putting this into context with the recently emerging concept of flow chemistry, which brings several practical advantages to the application of laser pulses, we want to encourage experimental groups to exploit this concept.

Another path was opened by several additions to the commonly used laser pulse optimization algorithm (optimal control theory, OCT), several of which were developed in our group. The OCT algorithm as such is a purely mathematical optimization procedure, with no direct relation to experimental requirements. This means that usually the electric fields obtained out of OCT optimizations do not resemble laser pulses that can be achieved experimentally. However, the previously mentioned additions are aimed at closing the gap toward the experiment. In a recent quantum control study of our group, these algorithmic developments came to fruition. We were able to suggest a shaped laser pulse which can induce a long-living wave packet in the excited state of uracil. This might pave the way for novel experiments dedicated to investigating the formation of biological photodamage in DNA and RNA. The pulse we suggest is surprisingly simple because of the extended OCT algorithm and fulfills all criteria to be experimentally accessible.

1. INTRODUCTION

The general purpose of quantum control is the same as in all synthetic chemistry, namely to manipulate chemical processes in favor of a desired product, or to even enable the formation of novel molecular compounds. Traditionally, this is achieved by control parameters such as temperature, pressure, catalysts, or different solvents. This means the controller influences the chemical process by interacting with molecular properties such as acidity, local steric hindrance, or the stability of leaving groups. In quantum control, the controller influences molecules by directly interacting with their quantum nature. Being quantum objects, the properties and the behavior of molecules are encoded in their wave function ψ (i.e., they are matter waves) and can be affected by using light waves,

specifically in the form of shaped laser pulses, acting as photonic catalysts.

The conceptual success of quantum control has been demonstrated experimentally on many examples and in many areas. After the first conceptual quantum control experiments on photoexcitation of sodium iodide,¹ applications to chemical problems followed with selective photodissociation in the gas phase,² energy flow optimization in the light-harvesting complex LH2,³ isomerization efficiency of dye molecules in the liquid phase⁴ or isomerization of retinal,⁵ and many others. Additionally, various theories have been developed to under-

Received: May 30, 2018

Published: August 28, 2018



stand how quantum control mechanisms work and to explore the characteristics, limits, and possibilities of quantum control.^{6–12} The purpose of this Account, however, is not to give a comprehensive review of either experimental or theoretical accomplishments, which has been done in several topical reviews.^{10,12–15} We would rather like to look ahead and inspire the field in its search for new applications, based on a personal viewpoint and on recent findings. After introducing the theoretical formalism which we use to simulate molecular wave packets (WPs) and the application and design of light fields, we highlight a few recent key advances which connect to two possible pathways toward new applications for the field of quantum control: synthetic chemistry, which always has been a main goal to apply shaped laser pulses to but has not been possible to make broadly applicable to date (primarily because of the cost of photons), and spectroscopy, where we demonstrate with a biologically relevant example how quantum control simulations can help to explore novel experimental regimes.

2. SIMULATION FRAMEWORK

In this section we intend to give an illustrative description of the formalism which helps us to simulate the time evolution of molecules and their interaction with light. There are several different approaches to simulations with this goal, which have been reviewed in detail elsewhere,^{10–12} and each has their own purposes and advantages. Again, we will focus on the formalism we use in our group.

On the very short temporal and very low spatial scale (below nanoseconds and nanometers), atoms and molecules behave like matter waves and their behavior and properties are encoded in the molecular wave function ψ . The temporal evolution of molecules is thus given by the time-dependent Schrödinger equation (TDSE) for atomic nuclei

$$i\hbar \frac{\partial}{\partial t} \psi(x_i, t) = \hat{H} \psi(x_i, t) \quad (1)$$

with the imaginary number i , the reduced Planck constant \hbar , the Hamiltonian operator \hat{H} (more on its structure later), the Cartesian degrees of freedom x_i , and the time t . The molecules used in chemistry usually have more than 10 degrees of freedom ($3N - 6$, with N being the number of atoms), which means $\psi(x_i, t)$ is a high-dimensional wave function. A solution of the TDSE is, however, feasible only in very few spatial coordinates, which is why before the TDSE is solved the coordinate space must be reduced. We do this by selecting up to three specific dimensions, which can be, for example, specific vibrational modes playing the most important role during a chemical process. To improve this representation and describe chemical processes more accurately, we use the concept of reactive coordinates, where normal modes are combined in a single coordinate. To give the reader an impression of how such a coordinate space may look, in Figure 1 the coordinates we used to describe the photo-relaxation process of the RNA nucleobase uracil (section 4) are shown.¹⁶ Finding an adequate number of dimensions and the most representative ones for an optimal low-dimensional representation is a nontrivial process, and often, in addition to chemical intuition, a significant amount of preparatory study time has to be invested. Our group recently put great effort into improving the process and results of dimensionality reduction by using automated procedures and even the

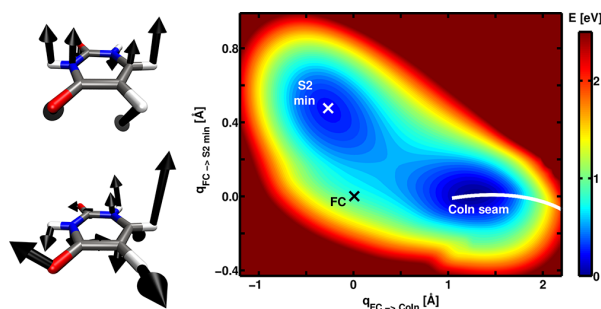


Figure 1. Left: Displacement vectors of the two coordinates q setting up the two-dimensional coordinate space.¹⁶ The reactive coordinates are combined of several normal modes, where the top displacement vector describes the motion from the Franck–Condon point to the CoIn seam and the second displacement vector from the Franck–Condon point to the S2 minimum. Right: PES of the electronically excited S2 states, obtained by quantum chemical calculations for structures along the coordinate vector displacements.

techniques of machine learning,^{17,18} which have already proven to be successful for molecular examples of relevant size.

After an adequate low-dimensional coordinate space q is found, the Hamiltonian \hat{H} needs to be set up. Including the interaction with an external electric field (e.g., a laser pulse), it can be written as

$$\begin{aligned} \hat{H} &= \hat{T}_q + \hat{V}_{\text{el}} - \hat{Z}(t) \\ &= -\frac{\hbar}{2} \sum_{r=1}^M \sum_{s=1}^M \frac{\partial}{\partial q_r} \left[G_{rs} \frac{\partial}{\partial q_s} \right] + \hat{V}_{\text{el}} - \hat{\mu} \varepsilon(t) \end{aligned} \quad (2)$$

and contains three terms. The kinetic operator \hat{T}_q is set up according to Wilson's G-matrix formalism with the reduced coordinates r and s . A detailed description of this formalism can be found in ref 19. The G-matrix $G_{rs} = \sum_{i=1}^{3N} \frac{1}{m_i} \frac{\partial q_r}{\partial x_i} \frac{\partial q_s}{\partial x_i}$ itself contains the reduced mass along each dimension in q , along with kinetic couplings between two dimensions r and s . The second term, V_{el} , contains the electronic energy E_{el} along the reactive coordinates and is obtained through electronic structure calculations (quantum chemistry). Assuming the Born–Oppenheimer approximation holds, which states that the movement of electrons and nuclei can be separated because they move on different time scales (i.e., electrons move much faster than nuclei), for each possible molecular structure along our reactive coordinates the electronic energy can be computed beforehand as a stationary solution to the electronic Schrödinger equation $\hat{H}_{\text{el}} \psi_{\text{el}} = E_{\text{el}} \psi_{\text{el}}$. Doing so, we arrive at the concept of potential energy surfaces (PESs), and as an example, the PES of uracil along the previously mentioned two dimensions is drawn in Figure 1.

Often, as usually a high level of theoretical accuracy is desired and especially if electronically excited states are involved, this is already computationally very demanding, and much effort is put into finding an adequate method and basis set to achieve a reasonable trade-off between sufficient accuracy and manageable computation time. The third term in eq 2 contains the dipole operator $\hat{\mu}$, which is also obtained by electronic structure calculations at every structure in the coordinate space, and the applied electric field $\varepsilon(t)$. Inserting the Hamiltonian \hat{H} from eq 2 into eq 1, the time evolution of a molecular system under the influence of an electric field can be

simulated. In ultrafast molecular science (below nanoseconds), usually pulsed lasers are used which have parameters like carrier frequency, intensity, phase, or temporal and spectral width. Examples of shaped laser pulses which also will be discussed later in this Account can be found in Figure 2. When

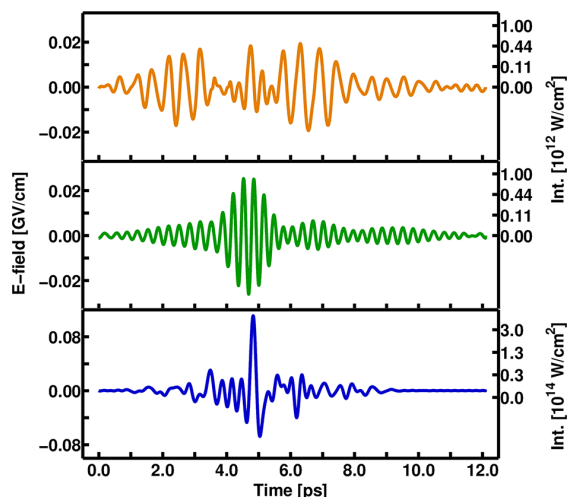


Figure 2. Optimized laser pulses for quantum control in different snapshots according to Figure 6. The color code of the top and middle pulse corresponds to Figure 6c. For the two different scenarios, different laser pulses are needed for successful quantum control. The laser pulse with the blue line was optimized to simultaneously excite six different cases.

one or more of these parameters are modified, the Hamiltonian (eq 2) is changed and thus the time evolution of the molecular quantum system according to eq 1. Such simulations can be useful for different aspects, for example to mechanistically understand time-resolved laser experiments, and the question one usually asks is: If a specific form of $\epsilon(t)$ is applied, how does the molecule behave and how does the wave function $\psi(T)$ look at final time T ?

Now, we can reverse the question and ask: If we want to prepare a specific target wave function $\psi_f(t)$, is there an optimal electric field $\epsilon(t)$ to achieve this aim and what does it look like? This brings us to the concept of quantum control simulations, where we for example try to maximize the population (and thus the experimental yield) in the desired product channel while discriminating loss channels. The theoretical formalism which allows us to design laser pulses is called quantum optimal control theory. Predominantly developed in the groups of Tannor^{7,20} and Rabitz,^{6,21} we have reviewed it extensively elsewhere^{10,12} for rather specialized audiences. We use and introduce OCT in the wave function framework, but it can also be applied to other formalisms (e.g., using a density matrix²²), and there also exist other alternatives for finding laser pulses for a given control problem (e.g., adaptive quantum pathway control^{23,24}). For this Account, it is useful to state the main equation of OCT and briefly discuss a few tweaks which are mandatory to achieve experimental accessibility of the resulting laser pulses. The general OCT functional reads

$$J[\psi_i(t), \psi_f(t), \epsilon(t)] = \mathcal{F}(t) - \int_0^T \alpha(t) |\epsilon(t)|^2 dt - \int_0^T \left\langle \psi_f(t) \left| i\hat{H} + \frac{\partial}{\partial t} \right| \psi_i(t) \right\rangle dt \quad (3)$$

and depends on the initial wave function $\psi_i(t)$ at the start of the simulation, the final wave function $\psi_f(t)$ to be prepared, and the electric field $\epsilon(t)$. For the third term in eq 3, we introduced the Dirac notation, where the two vertical lines indicate multiplication of left and right element, the operator $i\hat{H} + \frac{\partial}{\partial t}$ acts on $\psi_i(t)$, and the brackets $\langle \dots \rangle$ request integration over the wave function space. Differentiation of J with respect to $\psi_i(t)$ and $\psi_f(t)$ gives equations of motion for forward and backward propagation, and differentiation with respect to $\epsilon(t)$ gives an instruction for the construction of $\epsilon(t)$. Finding the maximum of J is an iterative procedure using these three equations, which is sketched in Figure 3. Each iteration

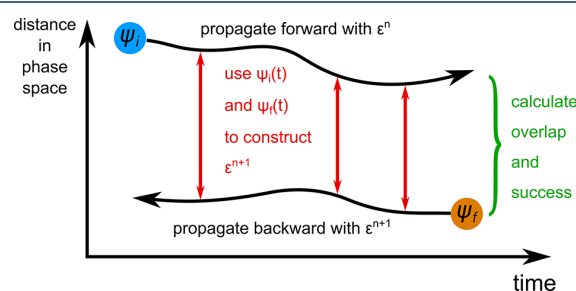


Figure 3. Schematic description of the OCT scheme, which is described in detail in ref 10. The initial wave function ψ_i represents the molecule in its initial state, and the target wave function ψ_f defines the optimization aim. The electric field $\epsilon(t)$ is constructed using ψ_i and ψ_f in each time step.

involves at least one quantum dynamical propagation, and often many iterative cycles are necessary to find an optimal field. The OCT functional contains three terms, where the first term $\mathcal{F}(t)$ defines the optimization aim. This can be either the overlap of a specific target wave function $|\langle \psi_i(T) | \phi_f \rangle|^2$ or the maximization of population in a specific area of the PES by using a projection operator $\langle \psi_i(T) | P | \psi_i(T) \rangle$ (see Figure 4). In more practical terms, through $\mathcal{F}(t)$ we can define a certain channel for our chemical reaction or photochemical process which we want to take. The third term in eq 3 includes the TDSE along with the Lagrange multiplier $\psi_f(t)$. The second term of eq 3 contains the electric field $\epsilon(t)$ along with the time-dependent cost function $\alpha(t) = \alpha_0/s(t)$. As OCT is a purely mathematical procedure, the optimized field does not necessarily look like an experimental laser pulse or even like a smooth function of time but can have any imaginable shape. To achieve connection to experimental conditions, several additions are included in our OCT formulation. This comprises the shape function $s(t)$ which ensures smooth on and off switching behavior of the electric field by impressing for example a Gaussian shape, or the parameter α_0 to penalize high pulse intensities. The addition which was especially useful in the simulations presented in this Account is the usage of a frequency filter.⁸ Its mathematical description is discussed in refs 8 and 10, while there are also other implementations of frequency constraints.²⁵ In principle, features at any point of the frequency scale of the electric field can emerge as valid

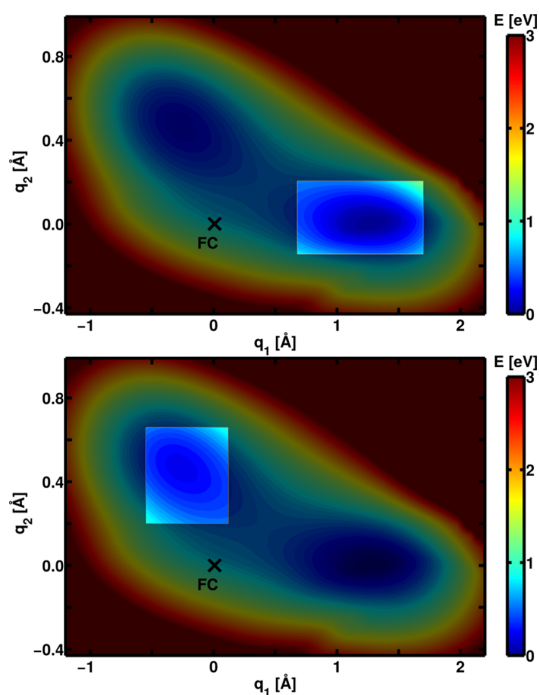


Figure 4. Projection operators setting up the control aim for quantum control in uracil, with the marked areas as the target regions. The operator on top was used together with a short final simulation time to maximize the population at the CoIn seam as early as possible and led to the pulse shown in Figure 5 on the right. The bottom operator was used together with a very long final simulation time to maximize the population in the local S2 minimum for as long as possible and led to the pulse shown in Figure 7.

solutions to the OCT functional. This does not correspond to experimental pulse generation usually yielding a smooth Gaussian distribution around a central frequency. By being able to suppress unwanted frequencies through the frequency filter, we can keep the pulse spectrum in a defined window and

more strongly correlate to physical experiments. This for example includes the suppression of zero-frequency components in the laser field (i.e., the field integral over time stays zero). A demonstration of the frequency filter is given in Figure 5, where two results of laser pulse optimizations with the same goal (discussed in section 4) are depicted, one with and the other without the frequency filter. It should be emphasized at this point that the main approximation is still the low-dimensional representation of the molecule in grid-based quantum dynamics. If all relevant reactive molecular modes are included, the control mechanism found with OCT is valid. Possible couplings to other inactive molecular modes can only affect the overall yield due to loss channels, which we have tested for in ref 16.

Having all these tools at hand, applications of OCT to molecular examples and how the results make us optimistic about the new application pathways are presented in the next sections.

3. QUANTUM CONTROL FOR SYNTHETIC CHEMISTRY

Chemical synthesis is about rearranging and connecting atoms from precursor molecules in a specific way to achieve the desired target molecule. Chemists use concepts like acidity, leaving group stability, electron affinity, and others to make these rearrangements happen. As target molecules become more and more complex (for example, in the synthesis of natural products or pharmaceutically applicable molecules), the synthetic effort increases. With each additional synthetic step, the final product yield gets lower and the cost increases. By offering additional tools and using different concepts, quantum control may provide shortcuts on complex synthetic routes at points where traditional tools and concepts have their limits. The application of shaped laser pulses to chemical reactions has its own limitations; because of these limitations, this has not become an applied concept yet. In recent years, however, evidence was gathered that several limitations can be overcome.

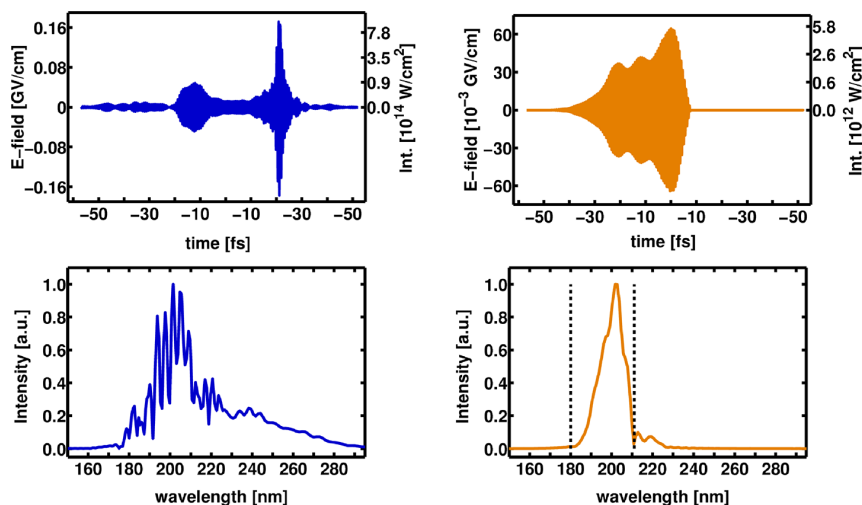


Figure 5. Optimized laser pulses in temporal and spectral representation, with the same optimization aim of accelerating uracil photorelaxation. Besides a higher penalty for pulse intensity, at the optimization of the pulse with the orange line, a frequency filter was used to keep the pulse spectrum in the region between 180 and 210 nm.

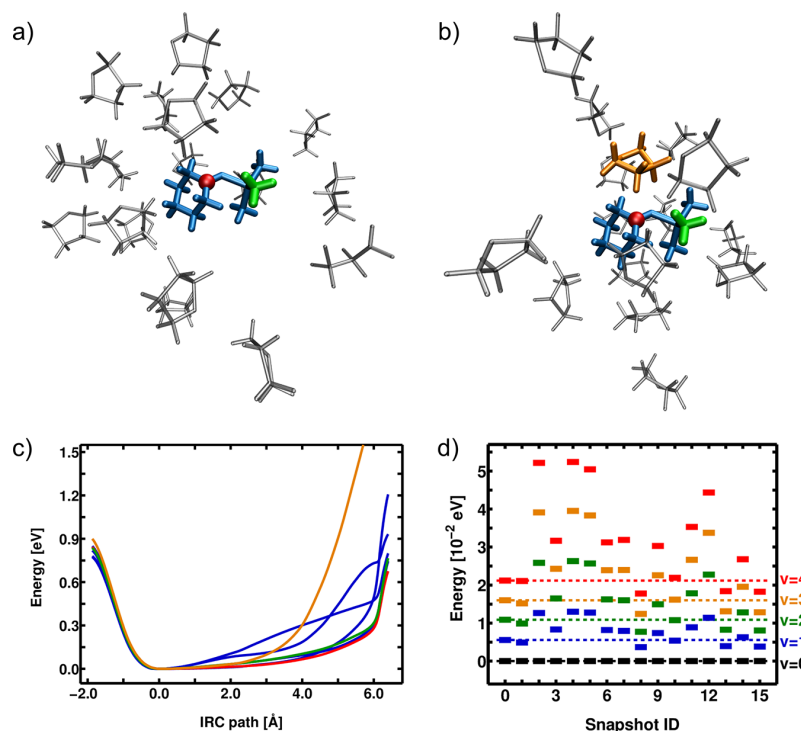


Figure 6. Vibrational quantum control of a molecular rearrangement in solution. (a) The methyl group in green can relocate to the carbon atom in red without steric obstruction by solvent molecules. (b) A solvent molecule (orange) is in the way of the reaction pathway, leading to steric obstruction. Both cases are found in the thermodynamic distribution present in a chemical flask. (c) Potential energy curves along the relaxation pathway. The gas-phase reference is drawn in red, the curve belonging to the solvent cage in panel a is like the gas phase and drawn in green, while the orange curve belongs to the rearrangement in panel b and shows a significantly higher barrier due to steric interactions with the solvent molecule. (d) Vibrational energy levels of the rearrangement in 15 different solvent cages. In cases where the potential energy curves change, the vibrational level structure is different (e.g., compare snapshot IDs 2 and 3), and thus the conditions for successful quantum control change.

One large complexity which we identified and tackled in our group originates from the presence of solvent molecules. In ref 26, we described the characteristics and extent of this influence and asked the question if the arising difficulties can be handled. The system on which we carried out our study is a methyl group transfer from trimethylaluminum to a cyclohexanone ring in the solvent tetrahydrofuran, which form a preallocated complex (Figure 6, top). This type of reaction is representative in several ways, as carbon–carbon bond formations are on one hand hard to accomplish and on the other hand constitute key synthetic steps toward pharmaceutically applicable molecules. While in the gas phase every molecule in a homogeneous sample has the same properties due to not interacting with other molecules, this changes in the liquid domain (Figure 6). Here, each reactant molecule is surrounded by a cage of solvent molecules, and the exact shape of this cage varies significantly if we consider a thermodynamic ensemble, as is the case in a flask. The path of the relocating methyl group may be unobstructed in some cases (Figure 6a), while in other cases there can be a solvent molecule located along the reaction path (Figure 6b), leading to strong steric and electrostatic interactions. Thus, the relevant properties for successful laser control can change. In the gas phase, this situation is present for rotational states even without the influence of surroundings.²⁷ In the case of a vibrational initiation of the reaction, i.e., using infrared or terahertz laser pulses to trigger the relevant backbone-modes for the methyl group transfer, this means the vibrational level structure of the

molecule can change. To investigate this in a compact and conceptual manner, we computed the vibrational levels of the one-dimensional reaction coordinate. This gives a measure of the extent of the solvent influence on the reaction and serves as a target for quantum control optimizations, aiming at efficient vibrational excitation. The heterogeneity of the vibrational level structure is shown in Figure 6d for 15 different solvent cages. While in the gas phase only the leftmost scenario is found, and the controlling laser pulse can be kept simple, it will not be efficient in solution where all 15 and more different scenarios are present at the same time. To achieve reasonable controllability, a laser pulse needs to address several scenarios at the same time. In ref 26, we demonstrate that this is achievable by using multitarget OCT.²⁸ Multitarget OCT works by extending the optimization aim $\mathcal{F}(t)$ in eq 3 with a summation over multiple optimization aims and thus requiring one laser pulse to achieve all of them at the same time. We chose the vibrational level $\nu = 4$ (see Figure 6d) as the optimization aim and combined snapshots with very different properties in one optimization. The optimized laser pulse achieved significant population yield in the target state. By means of statistical evaluations, we also showed that the optimized pulses are reasonably efficient in the whole thermodynamic ensemble. This study can be regarded as a general proof of concept for chemical control problems, as heterogeneous molecular properties will always be present when major molecular movement is aimed to be steered in solution. By showing that it can be handled in principle, we

want to encourage experimental quantum control groups to continue their efforts and exploit the pathway to chemical synthesis.

A related theoretical study, while using slightly different methods, found similar complexities.²⁹ For the example of CO-stretch excitation in carboxyhemoglobin, they were also able to find laser pulses which overcome the arising complexities and selectively populate vibrational target levels. Very recently, the concept of selective vibrational excitation in solution even found experimental realization, as it was possible together with theoretical support to accelerate a bimolecular reaction with infrared laser pulses.³⁰ The OH-stretching mode of an alcoholic reactant leading to urethane and polyurethane formation was selectively excited, increasing the reaction rate by up to 24%. Achieving vibrational acceleration of ground-state reactions has long been tried and was mostly impeded by competing processes, such as intramolecular redistribution of the vibrational energy. With the success of the discussed study, strong hints are gathered that this might nevertheless be possible, and the challenge now is to transfer this concept to other chemical reactions to potentially make it broadly applicable.

Another development which further opens the pathway to chemical synthesis is the approach of flow chemistry. This technique was developed a couple of years ago for organic synthesis and is being adapted by more and more groups around the world. For recent successful applications of this concept, we refer the reader to exemplary references,^{31–35} but this is by no means a comprehensive list. In contrast to traditional synthesis which happens mainly in flasks or similar vessels, the reaction takes place in a much smaller volume. In continuous flow reactors, compounds are mixed at low rates (e.g., 6 mL/min in ref 35) and in low-diameter tubes. Thus, a much bigger share of the reacting molecules is covered by the pulse focus and formed main and side products are transported out of the beam volume very fast. Because of these advantages, the cost of photons potentially can be kept at a level which is similar to the cost of several complex synthetic steps involving cumbersome protecting groups. Altogether, this is a promising setup for the potential application of shaped laser pulses and another reason to be optimistic about a successful implementation.

4. QUANTUM CONTROL TO PREPARE WAVE PACKETS FOR SPECTROSCOPY

In this section, we illustrate how quantum control can be used to propose novel spectroscopic experiments. In view of an experimental realization, pulse intensities need to be as low as possible, the spectral position and broadness must be in accessible ranges, and the spectral smoothness of the pulse should be reasonable. Within OCT, the terms enabling these necessities are described in section 2.

The molecular example we performed our simulations on is the photorelaxation of the RNA nucleobase uracil.¹⁶ Like all canonical nucleobases, uracil exhibits ultrafast relaxation back to the ground state after photoexcitation. This process takes several hundred femtoseconds and has been analyzed both theoretically and experimentally (for a comprehensive list of references covering both theory and experiment, we refer the reader to the introduction section of ref 16 and to a recent review³⁶). The efficiency of this ultrafast relaxation is believed to be a main reason for the photostability of uracil, as other photochemical pathways leading to chemical modification are

heavily discriminated in most cases. The state out of which photodamage can possibly be formed is highly elusive, complicating a substantiated spectroscopic characterization. We modified the exciting femtosecond laser pulse in a way that traps the WP in the S_2 state, extending the lifetime from around 180 fs to over 50 ps.¹⁶ Thus, in an experimental realization, there is time to interact with the trapped WP and identify or even explore other photochemical pathways which potentially lead to photodamage. The laser pulse which achieves this trap is shown in Figure 7. The spectral and

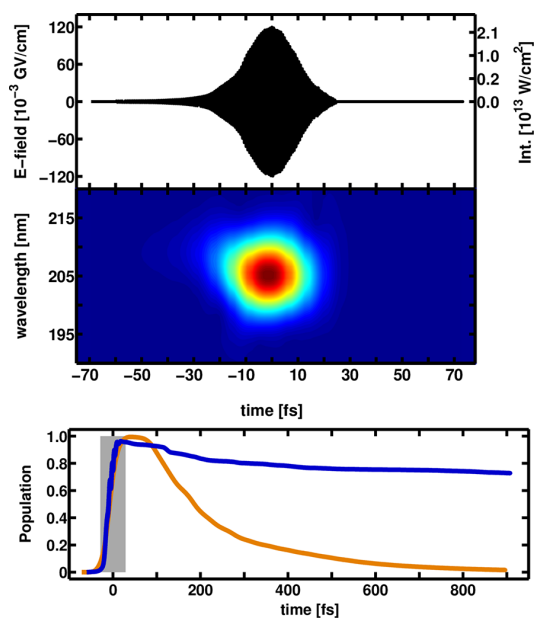


Figure 7. Successful quantum control for the photorelaxation of uracil. The laser pulse is shown together with its spectrogram and is surprisingly simple with an almost perfect Gaussian shape; because of this, it should be experimentally accessible. The central frequency matches the calculated transition from the S_0 to the S_2 state, which is known to be overestimated and thus needs to be shifted to 266 nm, which was used in the corresponding experiment. The population curve with the blue line corresponds to application of the optimized laser pulse, while the orange curve represents an unbiased excitation used in ref 37. The gray bar indicates the time where the laser pulse is active and shows that the trap is effective on a much longer time scale.

temporal shape is very smooth, and the central wavelength of the corresponding experimental study³⁷ was adapted to the calculated energy gap; the fwhm is also within experimental accessibility. The pulse intensity is considerable but can be lowered to a certain extent at the cost of efficiency of the trap mechanism. We also tried to optimize a pulse which accelerates the relaxation mechanism (Figure 5 with the orange line) and were able to reduce the S_2 lifetime by 22%. The optimization aim $\mathcal{F}(t)$ for both control aims is sketched Figure 4 and uses the projection operator discussed in section 2.

By demonstrating that it is possible to design experimentally accessible laser pulses with very defined biological applications, we want to highlight this possible pathway for the combined field of theoretical and experimental quantum control and spectroscopy.^{38–40} Going beyond proof-of-concept studies, we would like to convince experimentalists of the capabilities of theoretical simulations to design novel spectroscopic experi-

ments, and we encourage theoreticians to specifically aim in the direction of proposing experimental applications. Combined with dynamic influences of the respective environment, for example, an RNA strand on the excited state landscape of uracil, temporally competing photochemical pathways can be identified and selectively addressed with shaped light fields.

5. SUMMARY AND CONCLUDING REMARKS

In this Account, we reflected on recent advances in the field of molecular quantum control and how they can potentially open the door to new applications. One door leads to synthetic chemistry, which predominantly is conducted in the liquid phase. Theoretical studies unraveled the highly heterogeneous influence of an explicit solvent environment on the molecular properties of a thermodynamic ensemble.^{26,29} This greatly affects the control scenario and is possibly one of the reasons why the powerful concept of quantum control could not be made broadly applicable to chemical synthesis to date. Based on the demonstration that it is possible to optimize laser pulses that overcome the arising complexity, combined with a recent experimental study that actually achieved an acceleration of a bimolecular ground-state reaction with infrared laser pulses,³⁰ new hope is arising. In addition, the concept of flow chemistry was developed and adapted by several synthetic chemistry groups in the last years.^{31–35} This can potentially further benefit the application of shaped laser pulses to chemical synthesis, as reactants are mixed in a small volume and in a very controlled manner compared to the traditional usage of flasks.

Another door follows the concept of quantum control spectroscopy.^{38–40} Using the example of the photorelaxation of the RNA nucleobase uracil, it was demonstrated that quantum control can be used to design a specific form of WP for novel spectroscopic experiments.¹⁶ This was enabled by several additions to the laser pulse optimization algorithm (see section 2), which proved to be successful in keeping optimized laser pulses in experimentally accessible regions. A simple laser pulse was optimized to fulfill a crucial control task: To trap photoexcited uracil in its electronically excited state, which is one precursor state for the potential formation of photodamage. This state usually decays very fast within a few hundred femtoseconds, which is very important for RNA photostability but disadvantageous for a potential spectroscopic characterization. By being able to delay this process to a time scale much longer than the duration of the controlling laser pulse, a better investigation of the pathways leading to photodamage might be possible in the future. With this example, we would like to advertise the recent state and possibilities of theoretical quantum control simulations to experimental groups and encourage collaborations of this kind, where simulations can be used not only to understand and interpret spectroscopic experiments but also to propose experimentally accessible pulse shapes for the preparation of specific WPs. At this, the experimental accessibility very much depends on the specific experimental laser setup. Within this Account, we focused primarily on generic criteria, like restricting the pulse spectrum to few frequency components, as well as keeping the pulse intensity as low as possible. Other criteria include, for example, the occurrence of phase jumps or the amount of *chirp* (i.e., temporal variation of frequencies within a pulse spectrum), where the exact boundaries of what is possible vary significantly from one laboratory to another. Thus, the definition of *experimental accessibility* is best worked

out in close correspondence with the laser physicist carrying out the planned experiment.

AUTHOR INFORMATION

Corresponding Author

*E-mail: regina.de_vivie@cup.uni-muenchen.de.

ORCID

Regina de Vivie-Riedle: 0000-0002-7877-5979

Notes

The authors declare no competing financial interest.

Biographies

Daniel Keefer was born in Schwäbisch Gmünd, Germany. He received the Master of Science in chemistry from the Ludwig-Maximilians-University of Munich in 2014. During his Master thesis and ongoing Ph.D. work, he performed theoretical studies on coherent control of molecules with biological application and in complex environments.

Regina de Vivie-Riedle was born in Wuppertal, Germany. She graduated in chemistry from the Friedrich-Wilhelm-University of Bonn, Germany, in 1987. In 1997, she did the Habilitation in Theoretical Chemistry at the Freie University Berlin. She did two Postdocs, one at the MPI for Quantum Optics (MPQ) in Garching, Germany and one at the Joint Institute for Laboratory Astrophysics (JILA) in Boulder, CO. From 1997 to 2002 she was a C3 professor at the MPQ. Since 2003, she has been the leader of the theoretical femtoscience group at the Ludwig-Maximilians-University in Munich. Her research topics are ultrafast photoinduced molecular dynamics and coherent control theory.

ACKNOWLEDGMENTS

We thank Paul Knochel and Dirk Trauner for fruitful discussions regarding the application of quantum control to synthetic chemistry. Financial support by the Deutsche Forschungsgemeinschaft through the SFB749 and the Munich-Centre for Advanced Photonics cluster of excellence is acknowledged.

REFERENCES

- (1) Zhu, L.; Kleiman, V.; Li, X.; Lu, S. P.; Trentelman, K.; Gordon, R. J. Coherent Laser Control of the Product Distribution Obtained in the Photoexcitation of HI. *Science* **1995**, *270*, 77–80.
- (2) Assion, A.; Baumert, T.; Bergt, M.; Brixner, T.; Kiefer, B.; Seyfried, V.; Strehle, M.; Gerber, G. Control of Chemical Reactions by Feedback-Optimized Phase-Shaped Femtosecond Laser Pulses. *Science* **1998**, *282*, 919–922.
- (3) Herek, J. L.; Wohlleben, W.; Cogdell, R. J.; Zeidler, D.; Motzkus, M. Quantum Control of Energy Flow in Light Harvesting. *Nature* **2002**, *417*, 533–535.
- (4) Vogt, G.; Krampert, G.; Niklaus, P.; Nuernberger, P.; Gerber, G. Optimal Control of Photoisomerization. *Phys. Rev. Lett.* **2005**, *94*, 068305.
- (5) Prokhorenko, V. I.; Nagy, A. M.; Waschuk, S. A.; Brown, L. S.; Birge, R. R.; Miller, R. J. D. Coherent Control of Retinal Isomerization in Bacteriorhodopsin. *Science* **2006**, *313*, 1257–1261.
- (6) Peirce, A. P.; Dahleh, M. A.; Rabitz, H. Optimal Control of Quantum-Mechanical Systems: Existence, Numerical Approximation, and Applications. *Phys. Rev. A: At., Mol., Opt. Phys.* **1988**, *37*, 4950–4964.
- (7) Kosloff, R.; Rice, S. A.; Gaspard, P.; Tersigni, S.; Tannor, D. J. Wavepacket Dancing: Achieving Chemical Selectivity by Shaping Light Pulses. *Chem. Phys.* **1989**, *139*, 201–220.

- (8) Gollub, C.; Kowalewski, M.; de Vivie-Riedle, R. Monotonic Convergent Optimal Control Theory with Strict Limitations on the Spectrum of Optimized Laser Fields. *Phys. Rev. Lett.* **2008**, *101*, 073002.
- (9) Rabitz, H. Focus on Quantum Control. *New J. Phys.* **2009**, *11*, 105030.
- (10) von den Hoff, P.; Thallmair, S.; Kowalewski, M.; Siemering, R.; de Vivie-Riedle, R. Optimal Control Theory – Closing the Gap between Theory and Experiment. *Phys. Chem. Chem. Phys.* **2012**, *14*, 14460.
- (11) Glaser, S. J.; Boscain, U.; Calarco, T.; Koch, C. P.; Köckenberger, W.; Kosloff, R.; Kuprov, I.; Luy, B.; Schirmer, S.; Schulte-Herbrüggen, T.; Sugny, D.; Wilhelm, F. K. Training Schrödinger's Cat: Quantum Optimal Control. *Eur. Phys. J. D* **2015**, *69*, 279.
- (12) Thallmair, S.; Keefer, D.; Rott, F.; de Vivie-Riedle, R. Simulating the Control of Molecular Reactions via Modulated Light Fields: From Gas Phase to Solution. *J. Phys. B: At, Mol. Opt. Phys.* **2017**, *50*, 082001.
- (13) Brixner, T.; Gerber, G. Quantum Control of Gas-Phase and Liquid-Phase Femtochemistry. *ChemPhysChem* **2003**, *4*, 418–438.
- (14) Dantus, M.; Lozovoy, V. V. Experimental Coherent Laser Control of Physicochemical Processes. *Chem. Rev.* **2004**, *104*, 1813–1860.
- (15) Nuernberger, P.; Vogt, G.; Brixner, T.; Gerber, G. Femtosecond Quantum Control of Molecular Dynamics in the Condensed Phase. *Phys. Chem. Chem. Phys.* **2007**, *9*, 2470.
- (16) Keefer, D.; Thallmair, S.; Matsika, S.; de Vivie-Riedle, R. Controlling Photorelaxation in Uracil with Shaped Laser Pulses: A Theoretical Assessment. *J. Am. Chem. Soc.* **2017**, *139*, 5061–5066.
- (17) Zauleck, J. P. P.; Thallmair, S.; Loipersberger, M.; de Vivie-Riedle, R. Two New Methods To Generate Internal Coordinates for Molecular Wave Packet Dynamics in Reduced Dimensions. *J. Chem. Theory Comput.* **2016**, *12*, 5698–5708.
- (18) Zauleck, J. P. P.; de Vivie-Riedle, R. Constructing Grids for Molecular Quantum Dynamics Using an Autoencoder. *J. Chem. Theory Comput.* **2018**, *14*, 55–62.
- (19) Thallmair, S.; Roos, M. K.; de Vivie-Riedle, R. Design of Specially Adapted Reactive Coordinates to Economically Compute Potential and Kinetic Energy Operators Including Geometry Relaxation. *J. Chem. Phys.* **2016**, *144*, 234104.
- (20) Tannor, D. J.; Rice, S. A. Control of Selectivity of Chemical Reaction via Control of Wave Packet Evolution. *J. Chem. Phys.* **1985**, *83*, 5013–5018.
- (21) Zhu, W.; Rabitz, H. A Rapid Monotonically Convergent Iteration Algorithm for Quantum Optimal Control over the Expectation Value of a Positive Definite Operator. *J. Chem. Phys.* **1998**, *109*, 385–391.
- (22) Koch, C. P. Controlling Open Quantum Systems: Tools, Achievements, and Limitations. *J. Phys.: Condens. Matter* **2016**, *28*, 213001.
- (23) Mitra, A.; Rabitz, H. Identifying Mechanisms in the Control of Quantum Dynamics through Hamiltonian Encoding. *Phys. Rev. A: At, Mol., Opt. Phys.* **2003**, *67*, 033407.
- (24) Rey-de-Castro, R.; Leghtas, Z.; Rabitz, H. Manipulating Quantum Pathways on the Fly. *Phys. Rev. Lett.* **2013**, *110*, 223601.
- (25) Reich, D. M.; Palao, J. P.; Koch, C. P. Optimal Control under Spectral Constraints: Enforcing Multi-Photon Absorption Pathways. *J. Mod. Opt.* **2014**, *61*, 822–827.
- (26) Keefer, D.; Thallmair, S.; Zauleck, J. P. P.; de Vivie-Riedle, R. A Multi Target Approach to Control Chemical Reactions in Their Inhomogeneous Solvent Environment. *J. Phys. B: At, Mol. Opt. Phys.* **2015**, *48*, 234003.
- (27) Berens, P. H.; Wilson, K. R. Molecular Dynamics and Spectra. I. Diatomic Rotation and Vibration. *J. Chem. Phys.* **1981**, *74*, 4872–4882.
- (28) Tesch, C. M.; de Vivie-Riedle, R. Quantum Computation with Vibrationally Excited Molecules. *Phys. Rev. Lett.* **2002**, *89*, 157901.
- (29) Debnath, A.; Falvo, C.; Meier, C. State-Selective Excitation of the CO Stretch in Carboxyhemoglobin by Mid-IR Laser Pulse Shaping: A Theoretical Investigation. *J. Phys. Chem. A* **2013**, *117*, 12884–12888.
- (30) Stensitzki, T.; Yang, Y.; Kozich, V.; Ahmed, A. A.; Kössl, F.; Kühn, O.; Heyne, K. Acceleration of a Ground-State Reaction by Selective Femtosecond-Infrared-Laser-Pulse Excitation. *Nat. Chem.* **2018**, *10*, 126–131.
- (31) Brodmann, T.; Koos, P.; Metzger, A.; Knochel, P.; Ley, S. V. Continuous Preparation of Arylmagnesium Reagents in Flow with Inline IR Monitoring. *Org. Process Res. Dev.* **2012**, *16*, 1102–1113.
- (32) Nagaki, A.; Imai, K.; Ishiuchi, S.; Yoshida, J. Reactions of Difunctional Electrophiles with Functionalized Aryllithium Compounds: Remarkable Chemoselectivity by Flash Chemistry. *Angew. Chem., Int. Ed.* **2015**, *54*, 1914–1918.
- (33) Ghislieri, D.; Gilmore, K.; Seeberger, P. H. Chemical Assembly Systems: Layered Control for Divergent, Continuous, Multistep Syntheses of Active Pharmaceutical Ingredients. *Angew. Chem., Int. Ed.* **2014**, *54*. DOI: 10.1002/anie.201409765
- (34) Battilocchio, C.; Feist, F.; Hafner, A.; Simon, M.; Tran, D. N.; Allwood, D. M.; Blakemore, D. C.; Ley, S. V. Iterative Reactions of Transient Boronic Acids Enable Sequential C–C Bond Formation. *Nat. Chem.* **2016**, *8*, 360–367.
- (35) Ketels, M.; Ganiek, M. A.; Weidmann, N.; Knochel, P. Synthesis of Polyfunctional Diorganomagnesium and Diorganozinc Reagents through In Situ Trapping Halogen-Lithium Exchange of Highly Functionalized (Hetero)Aryl Halides in Continuous Flow. *Angew. Chem., Int. Ed.* **2017**, *56*, 12770–12773.
- (36) Improta, R.; Santoro, F.; Blancafort, L. Quantum Mechanical Studies on the Photophysics and the Photochemistry of Nucleic Acids and Nucleobases. *Chem. Rev.* **2016**, *116*, 3540–3593.
- (37) Matsika, S.; Spanner, M.; Kotur, M.; Weinacht, T. C. Ultrafast Relaxation Dynamics of Uracil Probed via Strong Field Dissociative Ionization. *J. Phys. Chem. A* **2013**, *117*, 12796–12801.
- (38) Wohlleben, W.; Backup, T.; Herek, J. L.; Motzkus, M. Coherent Control for Spectroscopy and Manipulation of Biological Dynamics. *ChemPhysChem* **2005**, *6*, 850–857.
- (39) Möhring, J.; Backup, T.; Motzkus, M. A Quantum Control Spectroscopy Approach by Direct UV Femtosecond Pulse Shaping. *IEEE J. Sel. Top. Quantum Electron.* **2012**, *18*, 449–459.
- (40) Consani, C.; Ruetzel, S.; Nuernberger, P.; Brixner, T. Quantum Control Spectroscopy of Competing Reaction Pathways in a Molecular Switch. *J. Phys. Chem. A* **2014**, *118*, 11364–11372.

Chapter 5.

UV-Induced Self-Repair of a Photolesion in a DNA Strand

Up until now, the WP simulations and OCT optimizations presented in chapters 3 and 4 had the goal to deepen the understanding of UV induced photolesions in RNA. In the present chapter, we not only move from RNA to DNA, but from the formation of harmful structures to their repair. Despite the high photostability of nucleobases, the 6-4 and CPD lesions frequently occur and were identified as the main photoproducts caused by UV radiation [159]. The repair of such lesions is known to be conducted by enzymes called photolyases [160]. Needing visible light around 400 nm for their own activation, they bind to the damaged region and catalytically restore the undamaged structure [160]. Another repair mechanism is called nucleotide excision repair, where oligonucleotide sequences containing the damaged region are removed and the intact sequence is refilled by DNA polymerase [161, 162].

Recently, an experimental study even found the direct repair of a CPD lesion by UV absorption of a neighboring guanine (G) adenine (A) sequence [86], which does not need additional proteins to participate. The authors artificially synthesized oligonucleotides containing the CPD lesion and different neighboring base sequences. Within a double strand sequence containing the GAT=TAG sequence (see Figure 5.1), illumination with UVB light of 290 nm was found to initiate repair through cleavage of the two bonds covalently connecting the two thymines.

In the control experiment on the isolated T=T sequence without adjacent A and G, the repair rate was significantly lower [86]. The suggested mechanism is based on charge transfer and exciplex states within the DNA nucleobases. After UV absorption, the authors observe a zwitterionic G^+A^- state with a lifetime of 300 ps. From here, the electron can further migrate to the CPD region and initiate bond cleavage. Some specifics about the suggested mechanism remain unclear however, as these quantities are not easy to extract experimentally. It is for example not known if the optical excitation occurs locally on G and then spreads to A, or if the $G \rightarrow A$ charge transfer is excited directly. Also, the abundance and accessibility of exciplex states usually depends on the relative spatial orientation of the two participating molecules, where this configurational space will probably not be very small within the ensemble of the measured sample. The present chapter tries to give some insight to these questions with the machinery of QC. Excited states of the GA sequence within the oligonucleotide are calculated with different methods and goals to subsequently answer the following questions:

- (1) How big is the exciplexic strength depending on the relative GA orientation? How abundant and accessible are they?
- (2) Does the first charge transfer with the electron moving from G to A get directly excited, or does the initial excitation happen locally on G?

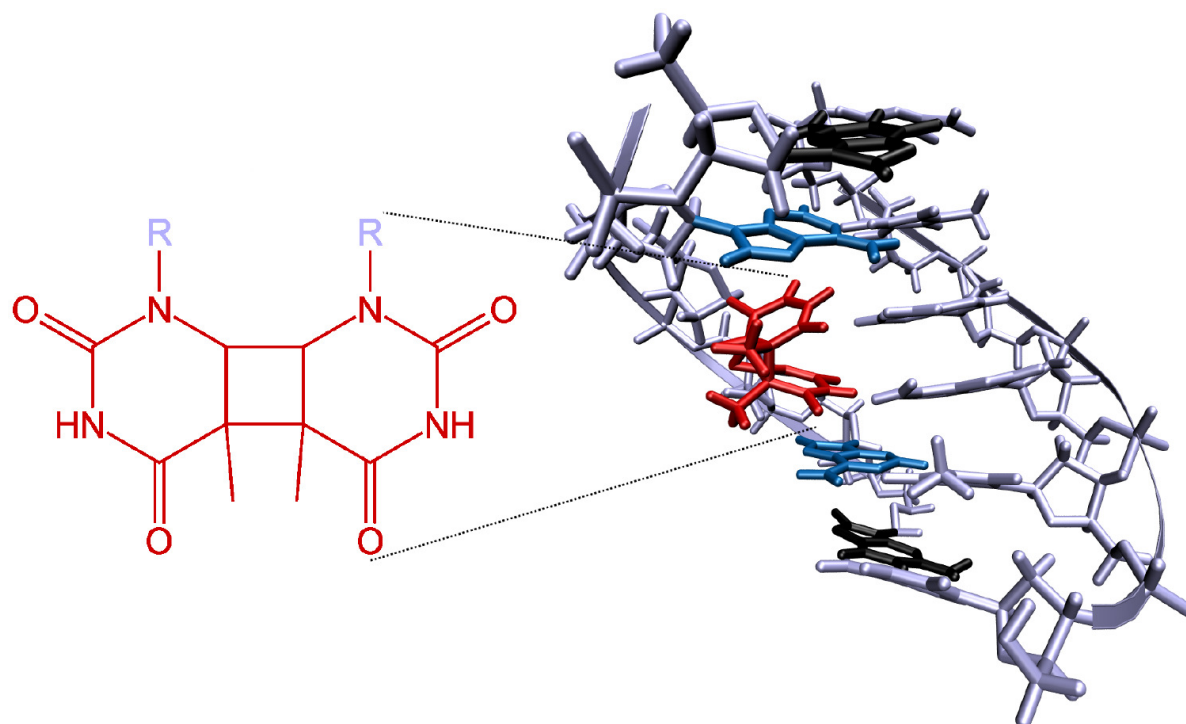


Figure 5.1.: Oligonucleotide sequence containing the CPD lesion in red, flanked by adenine (blue) and guanine (black) on both sides and with the complementary strand. Figure taken from Ref. [163]

The goal is to give an assessment whether the proposed mechanism is feasible, and possibly resolve the mechanistic details which are responsible. The first results of this study were presented on the *Conference on Ultrafast Phenomena 2018* in Hamburg. Therefore, the conference proceedings mentioned as number **11** in the list of publications in this thesis will explain the essential statements of this project once they get published. The present chapter is based on the Bachelor thesis of Vitus Besel [163], performed under the authors supervision and guidance, and lays out the procedure and results in more detail, while the overall study is still in progress.

5.1. Exciplex States Between Guanine and Adenine

To tackle the first question formulated on page 79, the configurational space of relative GA orientation must be sampled efficiently. For this reason, the GA system is initially treated in isolated form, without the connecting sugar phosphate backbone or other environmental features. The orientation space is sampled by manual displacement of the initial GA geometry depicted in Figure 5.2. The goal is to create a library of the orientational space which contains the corresponding exciplexic strengths. At a later point, a conformational analysis could be performed on a swarm of MD trajectories sampling the thermodynamic ensemble, and orientations with high and low occurrence could be identified to make statements about the overall accessibility of exciplexes. For this reason, A was displaced along the indicated x, y and z axis in Figure 5.2 with respect to G, and also rotated around the indicated angle α . Tilting of the molecular planes was not considered, as from a single trajectory which was

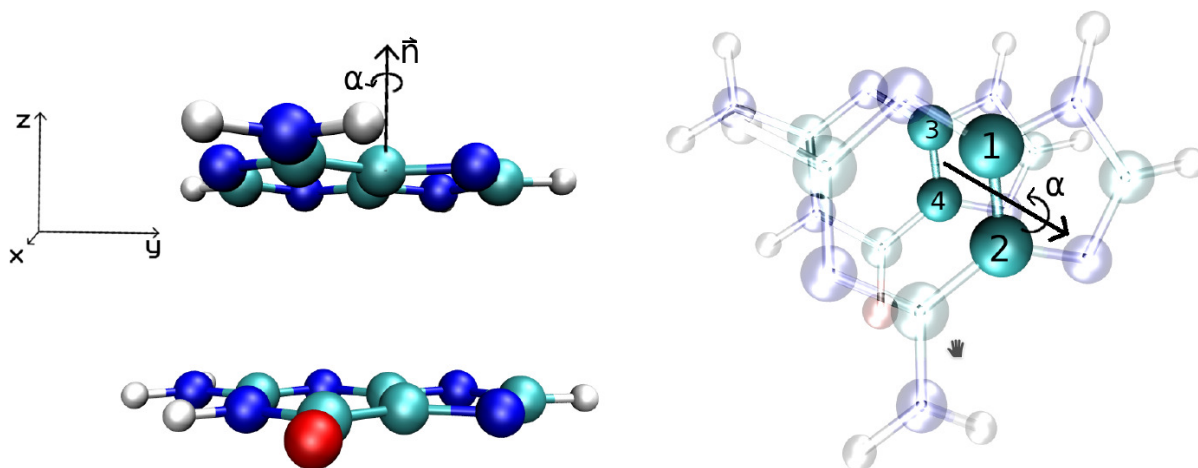


Figure 5.2.: Initial orientation of the GA geometry. The two nucleobases are placed on top of each other, with a distance of 3.56 Å between the C1-C2 and the C3-C4 bond centers. The spatial coordinate axes x, y and z are indicated, according to which A on top will be displaced. The angle α describes a rotation around the C1-C2 bond center. Figure taken from Ref. [163]

performed for the oligonucleotide in water this motion played only a negligible role on the first glance.

The basis for a quantification of the exciplexic strength is the calculation of excited states and molecular orbitals. As a large amount of calculations must be performed, the cost-efficient TDDFT was used. The functional wB97X-D [164] was chosen for the calculations, being a hybrid functional containing a Hartree-Fock exchange correction based on the interelectronic distance. This is necessary to capture long-ranged effects and counteracting the intrinsic weakness of TDDFT not being able to describe charge transfer properties accurately. The cc-pVDZ basis set [165] was used, and all calculations were performed with the program package GAUSSIAN16 [166] for the lowest 15 electronic states. The orbitals were visualized with the program package GaussView6 with an isovalue of 0.02. The formation or existence of an exciplex means that the electron density is located in orbitals which are shared between the two molecules. If by optical excitation electron density is transferred into unoccupied orbitals of this character, an exciplex is excited. To quantify this for the different orientations, the orbitals were classified into five different groups a – e, as drawn in Figure 5.3.

This classification is no absolute criterion as it depends on the isovalue, but using the same isovalue for all structures ensures comparability and is suitable for a relative classification. Orbitals a and b were considered to contribute to the exciplexic strength, whereas orbitals c, d and e do not. In every calculation, the lowest five excited states were investigated for excitation into these orbitals. These contributions were quantified according to

$$X_n = \frac{\sum_{ab} C_{a,b}}{\sum_{abcde} C_{a,b,c,d,e}}, \quad (5.1)$$

where C are the excitation coefficients for the corresponding orbitals a to e, and X_n gives the share of total contributions into them in the excited state n . The average over the lowest 5 states n was taken according to

$$\gamma = \frac{1}{N} \sum_{n=1}^N X_n, \quad (5.2)$$

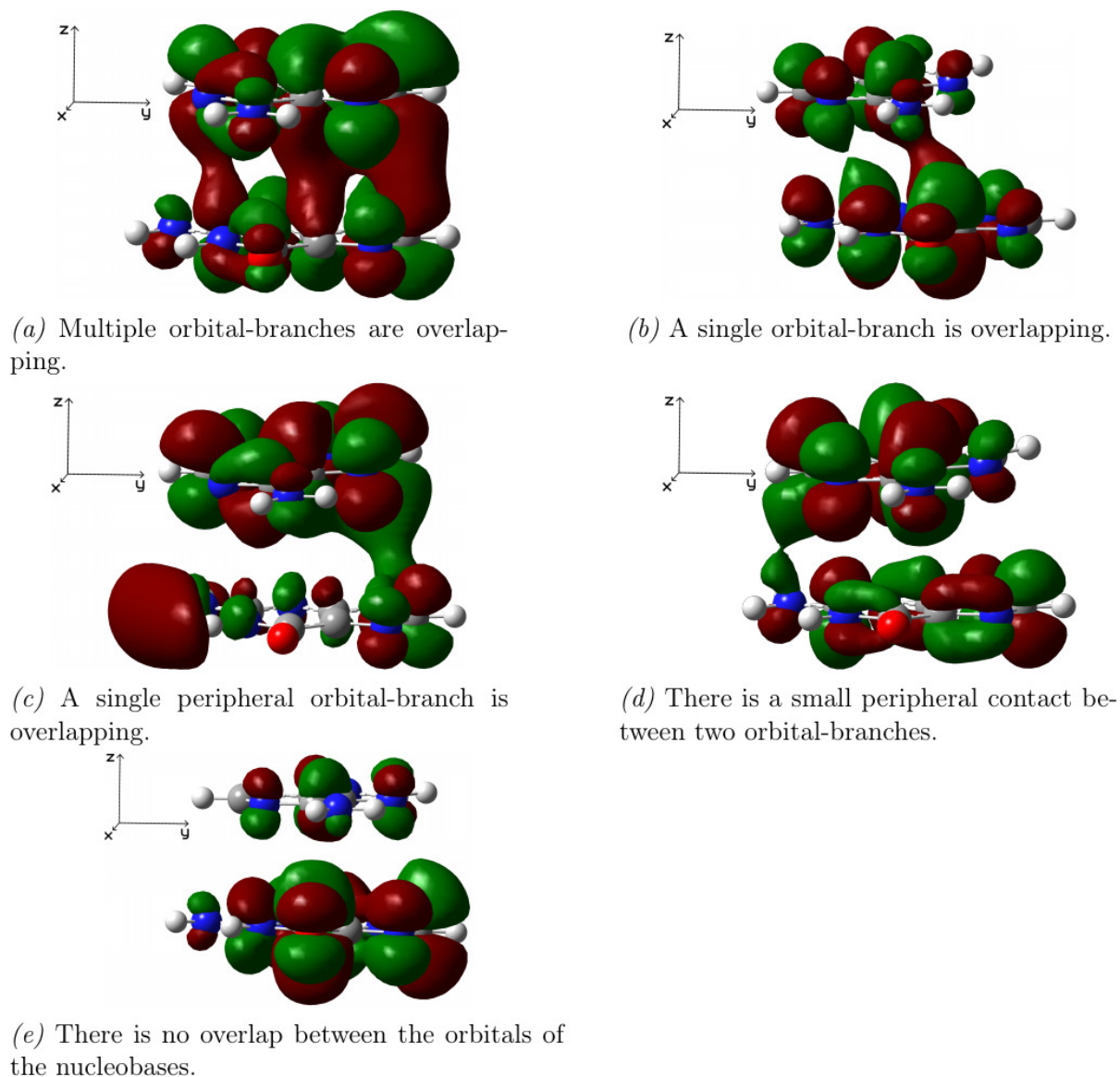
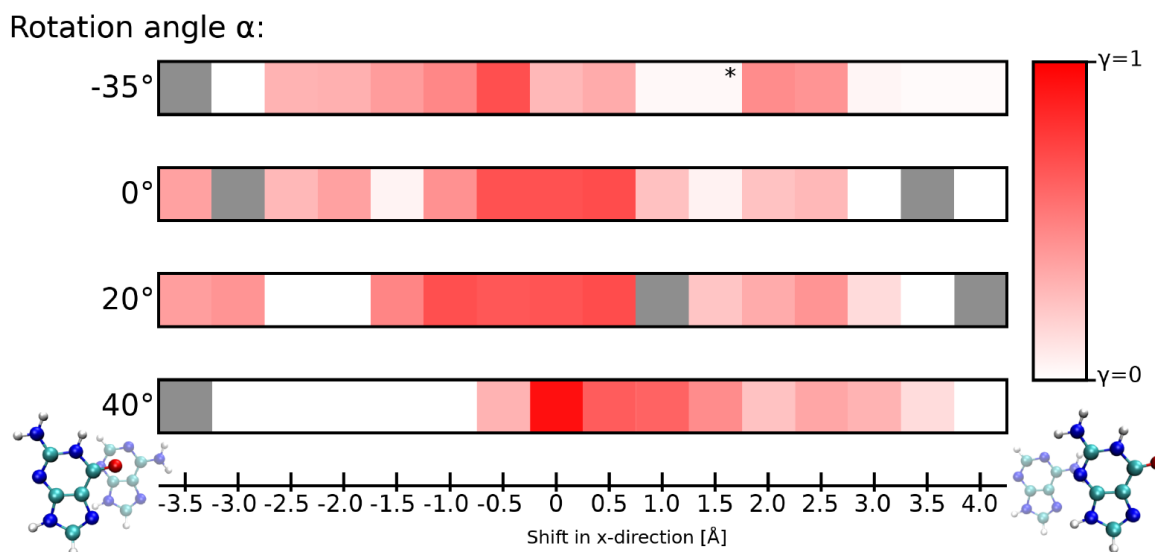
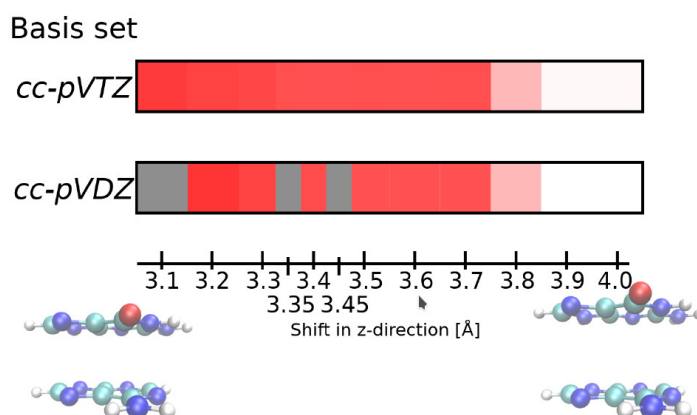


Figure 5.3.: Molecular orbitals of the GA system, with a classification according to their amount of overlap from strong (a) to none (e). Figure taken from Ref. [163]

and γ is defined as the exciplexic strength of the geometry. It can take values between 0 and 1, where 0 means that within the lowest excited states there is no contribution of an exciplex excitation, and 1 means all participating excitation coefficients include the orbitals a and b. This allows for a rough estimation which relative orientations of G and A might be beneficial for the proposed self repair mechanism. Exemplary scans of the GA orientation are shown in Figure 5.4. For all scans, the reference geometry at 0 Å was defined as the one with the highest atomic overlap between G and A, which does not necessarily mean there is also the highest orbital overlap. However, y is always highest at displacement values close to 0 Å. It exhibits an oscillation behavior, for example in the scan for $\alpha = 0$. The region around 0 Å exhibits the highest γ , where moving in both directions it decreases first and then increases again (e.g. at ± 2.0 Å). Another interesting feature is that while γ is highest around 0 Å, it also can take significant values at larger displacements, for example at -3.5 Å in



(a) Horizontal shift with different rotation angles α according to Figure 5.2



(b) Vertical shift along the z-axis

Figure 5.4.: Excimeric strength γ in different orientations of G and A according to the color scale on the right. In (a), there is an oscillation feature when shifting along the x-axis, as the exciplexic strength is strongest around 0 Å and then decreases and increases again in both directions. The comparison of basis sets in (b) shows identical results and a rather sharp transition from high to low exciplexic strength at 3.8 Å. Figure taken from Ref. [163]

the scans for $\alpha = 0^\circ$ and $\alpha = 20^\circ$. These features also occur in other scans along the y-axis and with different rotation angles, suggesting that within the thermodynamic configuration space there will at least frequently occur orientations where exciplex excitation is feasible. The vertical scan along the z-axis — i.e. increasing the distance between the molecular planes of G and A — was performed not only for the cc-pVDZ but also for the more expensive cc-pVTZ basis set, which exhibits similar behavior. There is a rather sharp transition from high to no exciplexic strength in the region of 3.8 Å. A first investigation of a single MD trajectory of the oligonucleotide exhibited GA distances usually around 3.6 Å to 3.7 Å, where higher and lower values were found to be less common. Despite the definition and classification of γ according to the molecular orbitals is somewhat flexible, this also supports the suggestion that

exciplex formation can frequently occur within the strand. Overall, the hints gathered thus far support the first step of the formulated mechanism by the authors in Ref. [86].

5.2. Excited State Characterization Using CASSCF and QM(CASPT2)/MM

The TDDFT calculations in the previous sections were useful to sample a large configuration space and get an idea about exciplex formation. However, more accurate methods are needed to properly characterize the participating excited states and evaluate whether the excitation energies are within the experimentally accessible region. The WF based CASSCF and CASPT2 methods offer a convenient framework to successively tune the trade-off between accuracy and computational cost by increasing the sizes of the active space. All CASSCF and CASPT2 calculations were performed with the program package MOLCAS [167]. To initially get a feeling on how the orbitals in the active space behave, CASSCF calculations were performed on two isolated GA geometries with different input orbitals, active space sizes and basis sets. The excited state characteristics of an exemplary series of CASSCF calculations is shown in table 5.1. The general findings are listed in the following:

- For different tested cases, the cc-pVDZ basis gave similar results as the larger cc-pVTZ basis. For this reason, the cc-pVDZ basis was used from here on.
- All orbitals in the active spaces were π or π^* , where the orbital density is usually located at one of the two nucleobases. Attempts were made to include the oxygen lone-pair in the active space, as it sometimes had relevant contributions in the TDDFT simulations in the previous chapter. It always rotated out of the active space after optimization however, which is why symmetrical active spaces (i.e., including the same number of electrons and orbitals, and a π^* orbital for every π orbital) were used from here on.
- Incrementally increasing the active space from (4,4) to (16,16) often lowered the excitation energies from around 6.9 eV to around 5.6 eV. This is still well above the experimental excitation energy of 4.3 eV however. The computation time, measured in total CPU hours, increased from 2 h for the (4,4) over 10 h for the (12,12) and 97 h for (14,14) to 88 days for the (16,16) active space.
- There is no clear convergence of the excited state character toward higher active space sizes in most states. For the S_1 state however, the character does not change anymore when making it larger than (8,8). Most of the excitations occur local either on G or on A, while the direct charge transfer excitations always occur from G to A.

This last point is interesting in view of the suggested initial step of the repair mechanism, where the GAT=TAG sequence was found to exhibit efficient repair yields, while this was not found for AGT=TGA. In all CASSCF calculations, the excitation energies were well above the experimental one. Since CASSCF is known to struggle with giving correct excitation energies, the methodology was extended to CASPT2. Here, second-order perturbation theory is performed on top of the CASSCF wave function. This means while the orbitals themselves are not changed, excitation energies, the contribution coefficients of the orbitals and the ordering of states can change. CASPT2 calculations were performed for the same geometries as indicated in Table 5.1. Additionally, the calculations were performed in a QM/MM fashion to also include the

Table 5.1.: Excitation energies in eV and excited state character in different state-averaged CASSCF calculations with 5 states. Active space sizes indicate number of electrons and number of orbitals, separated by a comma. The two geometries were extracted from an MD trajectory and reduced to containing only G and A.

State	4,4	6,6	8,8	10,10	12,12	14,14	16,16
geometry 1							
S ₁	6.85	6.58	5.75	5.62	5.80	5.66	5.65
	$\pi_G \rightarrow \pi_A^*$	$\pi_G \rightarrow \pi_G^*$	$\pi_A \rightarrow \pi_A^*$	$\pi_A \rightarrow \pi_A^*$	$\pi_A \rightarrow \pi_A^*$	$\pi_A \rightarrow \pi_A^*$	$\pi_A \rightarrow \pi_A^*$
S ₂	7.29	6.60	6.59	6.60	7.11	6.68	6.18
	$\pi_A \rightarrow \pi_A^*$	$\pi_G \rightarrow \pi_G^*$	$\pi_G \rightarrow \pi_G^*$	$\pi_G \rightarrow \pi_G^*$	$\pi_G \rightarrow \pi_A^*$	$\pi_G \rightarrow \pi_G^*$	$\pi_G \rightarrow \pi_G^*$
S ₃	7.39	7.19	7.16	7.16	7.26	7.30	7.01
	$\pi_A \rightarrow \pi_A^*$	$\pi_G \rightarrow \pi_A^*$	$\pi_A \rightarrow \pi_A^*$	$\pi_G \rightarrow \pi_A^*$	$\pi_A \rightarrow \pi_A^*$	$\pi_A \rightarrow \pi_A^*$	$\pi_G \rightarrow \pi_A^*$
S ₄	7.70	7.48	7.56	7.51	7.39	7.42	7.29
	$\pi_A \rightarrow \pi_A^*$	$\pi_A \rightarrow \pi_A^*$	$\pi_G \rightarrow \pi_A^*$	$\pi_G \rightarrow \pi_A^*$	$\pi_G \rightarrow \pi_G^*$	$\pi_A \rightarrow \pi_A^*$	$\pi_A \rightarrow \pi_A^*$
geometry 2							
S ₁	6.91	6.57	5.74	6.46	6.32	5.66	5.64
	$\pi_G \rightarrow \pi_A^*$	$\pi_G \rightarrow \pi_G^*$	$\pi_A \rightarrow \pi_A^*$	$\pi_A \rightarrow \pi_A^*$	$\pi_A \rightarrow \pi_A^*$	$\pi_A \rightarrow \pi_A^*$	$\pi_A \rightarrow \pi_A^*$
S ₂	7.27	6.62	6.60	7.09	7.08	7.11	6.19
	$\pi_A \rightarrow \pi_A^*$	$\pi_G \rightarrow \pi_G^*$	$\pi_G \rightarrow \pi_G^*$	$\pi_A \rightarrow \pi_A^*$	$\pi_A \rightarrow \pi_A^*$	$\pi_G \rightarrow \pi_G^*$	$\pi_G \rightarrow \pi_G^*$
S ₃	7.42	7.26	7.18	7.21	7.18	7.21	7.00
	$\pi_G \rightarrow \pi_A^*$	$\pi_G \rightarrow \pi_A^*$	$\pi_A \rightarrow \pi_A^*$	$\pi_A \rightarrow \pi_A^*$	$\pi_G \rightarrow \pi_{G/A}^*$	$\pi_A \rightarrow \pi_A^*$	$\pi_G \rightarrow \pi_G^*$
S ₄	7.63	7.41	7.63	7.38	7.37	7.37	7.30
	$\pi_A \rightarrow \pi_A^*$	$\pi_G \rightarrow \pi_A^*$	$\pi_G \rightarrow \pi_A^*$	$\pi_G \rightarrow \pi_G^*$	$\pi_G \rightarrow \pi_G^*$	$\pi_G \rightarrow \pi_G^*$	$\pi_A \rightarrow \pi_A^*$
CPU time	2 h	2 h	2.5 h	2.5 h	10 h	97 h	88 d

Table 5.2.: Excitation energies in eV and excited state character in different CASPT2 calculations. Active space sizes indicate number of electrons and number of orbitals, separated by a comma. The two geometries correspond to the ones in Table 5.1, while now the rest of the oligonucleotide and the surrounding water are included in the MM region of the QM/MM calculations.

State	geometry 1			geometry 2		
	8,8	10,10	12,12	8,8	10,10	12,12
S ₁	5.26	3.92	2.28	3.31	2.86	4.51
	$\pi_G \rightarrow \pi_G^*$	$\pi_G \rightarrow \pi_G^*$	$\pi_{G/A} \rightarrow \pi_A^*$	$\pi_G \rightarrow \pi_A^*$	$\pi_{G/A} \rightarrow \pi_A^*$	$\pi_G \rightarrow \pi_{G/A}^*$
S ₂	5.47	5.59	4.34	6.13	4.92	5.64
	$\pi_A \rightarrow \pi_A^*$	$\pi_A \rightarrow \pi_A^*$	$\pi_G \rightarrow \pi_G^*$	$\pi_{G/A} \rightarrow \pi_A^*$	$\pi_{G/A} \rightarrow \pi_A^*$	$\pi_A \rightarrow \pi_A^*$
S ₃	5.77	5.98	5.38	6.39	6.01	6.16
	$\pi_A \rightarrow \pi_A^*$	$\pi_A \rightarrow \pi_A^*$	$\pi_G \rightarrow \pi_A^*$	$\pi_A \rightarrow \pi_{G/A}^*$	$\pi_G \rightarrow \pi_G^*$	$\pi_A \rightarrow \pi_A^*$
					$\pi_A \rightarrow \pi_A^*$	

effects of the environment. G and A were included in the QM region treated with CASPT2, while the rest of the oligonucleotide double strand as drawn in Figure 5.1 and surrounding water molecules were treated on the MM level using the AMBER99 force field [168]. The corresponding excitation energies and characters are listed in Table 5.2.

Several things can be concluded from there:

- The combination of CASPT2 and the QM/MM environment yields excitation energies in the experimentally accessible region around 4.3 eV, sometimes even below, for both geometries.
- All states below 5 eV exhibit either local G excitation or charge transfer excitation from G to A. Almost all states with contributions from occupied A orbitals are above the experimental energy.
- In the ascending row from the (8,8) to the (12,12) active space, the excited state character sometimes changes when including more orbitals. It seems relatively stable for the lowest state at least however.
- While the lowest states in geometry 1 exhibits mostly local excitations, geometry 2 has strong charge transfer or exciplex character as there are many mixed and cross-excitations.

The geometry dependence is especially interesting here. While some significant conclusions can be drawn from these two structures already, it is desirable to perform these calculations for many different snapshots of the oligonucleotide along different MD trajectories. With this, a statistical picture of local versus charge transfer excitation could be obtained. Like in the CASSCF calculations, the lowest excited states predominantly exhibit either local G or a G to A charge transfer excitation. Whether the local G excitation evolves towards an electron migration to A remains to be investigated — e.g. with semiclassical surface hopping techniques — but the general conclusion drawn from the calculations presented here is that the first step of the experimentally suggested mechanism seems to be plausible.

Chapter 6.

Summary and outlook

In this thesis, theoretical studies were presented simulating the evolution and control of molecular WPs in complex atomistic environments. The environmental types ranged from the chemical solution of an organic synthesis to the biologic domain of an RNA strand including nucleobases, sugar phosphate backbone and surrounding water. In each case, the environment was found to considerably influence the quantum dynamical behavior and the relevant molecular properties for successful quantum control.

After laying out the general simulation framework in chapter 1, the two studies in chapter 2 dealt with the potential quantum control of a methyl transfer reaction in a chemical solution (in this case: THF). Exploiting its capabilities to the synthetically relevant domain has been a big goal of quantum control since its beginning. However, despite several control aims being reached in the liquid phase, e.g. isomerization control, a broad application in chemical synthesis remains to be accomplished. The studies in chapter 2 used an exemplary synthetic step involving carbon-carbon bond formation to on one hand identify the complexities which arise from an explicit solvent environment and on the other hand assess whether it is feasible to overcome them. This study also takes a step toward bimolecular reactions, which are much harder to control than unimolecular ones due to diffusion processes. In this study, the two molecules performing the reaction – trimethylaluminium and cyclohexanone – form a preallocated complex by the aluminium coordinating to oxygen. Therefore, a rather fixed geometry can be assumed for the simulation, and in practical realizations the quantum yield is much higher compared to a bimolecular reaction of non-coordinating molecules. First, MD trajectories were started to sample the thermodynamic movement of THF solvent atoms around the frozen reactant. In different randomly chosen snapshots of the current solvent configuration, the potential curve of the IRC describing the methyl group transfer was calculated, while now the solvent cage remained frozen. The vibrational eigenfunctions of the perturbed potentials were evaluated, which serve as a measure for the environmental influence. The latter was found to be considerable in various snapshots, where the level spacing was observed to be up to double the amount compared to the unperturbed case. Additionally, the harmonicity of the potentials was affected, changing the separation of the different vibrational transitions from completely overlapping (harmonic case) to well-separated. Envisioning a vibrational initiation of the reaction — i.e. selective addressing of different vibrational transitions — this can severely complicate the control task, and corresponds to the inhomogeneous line broadening found in spectroscopy. The vibrational level $\nu = 4$ was chosen as the control target, and quantum control optimizations were performed in the multi-target framework to optimize laser pulses which can achieve selective vibrational excitation in multiple snapshots simultaneously. Although this control scheme alone can not induce the reaction, as the energy climb does not reach the transition barrier, it can be regarded as a model study for vibrational excitation of the crucial reactive modes leading to the reaction pathway after for example deposit-

ing additional energy via the easily accessible carbonyl mode (see proposed scheme in Figure 2.1). The multi-target optimizations revealed that the population yield in the target level can be considerable even for Hamiltonians where several vastly different snapshots are incorporated. A statistical estimate was employed, which revealed that a laser pulse being optimized for only 6 different solvent cages can already achieve significant yields in the complete solvent configuration space.

Going beyond the approximation of a static solvent cage, the time-resolved fluctuation of the molecular energy levels due to environmental propagation was revealed. Extreme cases of environmental influence were found to oscillate in the mid-femtosecond range. Since pulse durations in this example were around 1-2 picoseconds, this additionally complicates the control task. Optimizations were performed for different fluctuation scenarios, and also pulses which were optimized for static solvent cages before were now applied to the fluctuating case. Surprisingly, all laser pulses were found to be efficient in scenarios which they were not optimized for to some extent, which is very encouraging when thinking about many more solvent snapshots being present in a thermodynamic ensemble. Optimization and control strategies were presented, tuning the trade-off between pulse complexity and globality (i.e. for how many cases it is optimized for). More specifically, thinking about potential experiments, it was discussed to be feasible to use a simple laser pulse being optimized for a rather special case, and wait long enough for favorable scenarios to occur, while employing an appropriate repetition rate. Besides the practical implications, the timescale of the energy level fluctuation was modified artificially to investigate whether there are more or less problematic cases. When the oscillations occurred either very fast or very slow compared to the pulse duration, control was easily achieved, as the controlling laser pulse either finds a continuously favorable situation due to slow fluctuation, or a mean field of it due to very fast fluctuation. Even the most problematic scenarios, where fluctuations occurred only several times during pulse duration, could be controlled. Altogether, the studies presented in chapter 2 could encourage experimentalists trying to make quantum control feasible in the synthetically relevant domain, as it was shown that the arising complexities can be handled. Naturally, there exist additional effects which are not included in the presented model, such as energy dissipation to the environment, and there also exist practical limitations on which pulse shapes, intensities and frequencies can be realized, but from the theoretical perspective the inhomogeneous influence of an explicit solvent environment is controllable.

Chapter 3 dealt with the photorelaxation of the RNA nucleobase uracil in the isolated case and embedded in the RNA environment. The first study in chapter 3.1 presented the two-dimensional coordinate space which was used to simulate the relaxation of the WP out of the S_2 state. It is constructed from geometries which were previously identified to play a major role during the relaxation. WP simulations yielded an excited state lifetime of around 170 fs, along with the detailed pathway of the WP moving from the FC point through the S_2 minimum and over a barrier toward the CoIn seam. This relaxation time was accelerated and delayed by tailoring the exciting laser pulse using OCT. The most prominent result is a 4 fs pulse which traps the WP in the excited state for over 50 ps and which exhibits experimentally accessible parameters and shape. As the inhibition of efficient relaxation pathways can directly be linked to the increased formation of photolesions, this critical state could now be artificially prepared in a laboratory environment in isolated uracil, should the proposed experiment be realized. Besides allowing for a better spectroscopic characterization, other photochemical pathways potentially leading to photolesions might

be explored after the trap, if not automatically then potentially with the help of an additional laser pulse to steer the WP.

The study in chapter 3.2 investigated this relaxation mechanism in the natural RNA/water environment. QM/MM calculations in different environmental snapshots were performed, obtaining an environmental potential for each configuration and adding it to the S_2 PES of isolated uracil. The relaxation pathway was affected drastically in some cases, leading to delayed relaxation times in around 10% of cases. With this, the direct influence of the explicit RNA environment was found to be responsible for the occurrence of long-lived excited states and thus potential photolesions. The mechanism which is usually regarded to be responsible for prolonged excited state lifetimes is the delocalization of the electronic excitation, where the degree of the delocalization is still subject of recent and ongoing studies [158]. With the simulations in chapter 3.2, only the local excitation and relaxation pathway in uracil are investigated, and it is concluded that long-lived excited states can also occur locally, without the need of delocalization events. By testing 10 different neighboring base sequences, this mechanism was found to be independent of the specific neighbor.

Finally, in chapter 5 the UV-induced self-repair of the commonly occurring CPD lesion in DNA was investigated. It was found experimentally in a GAT=TAG oligonucleotide that this specific sequence exhibits self-repair of the covalently bound thymines after UV excitation [86]. The proposed mechanism — excitation of G, followed by electron transfer to A, and subsequent electron transfer to the T=T lesion initiating bond cleavage — was verified by performing excited state calculations. In the first part, TDDFT was used to sample various G to A orientations with respect to possible formation of exciplexes. Within the sampled configuration space, it was found that exciplex formation is often possible, favoring a potential electron transfer. In the second part, QM/MM CASPT2 simulations were performed for the complete oligonucleotide, with G and A in the QM region. Excitation energies of the first excited state were within experimental range, while the excited state character was either local excitation on G or direct charge transfer excitation from G to A. Although only two geometries from a MD trajectory have been investigated so far, this already suggests that the proposed mechanism is reasonable. Additional geometries need to be investigated to obtain a significant sample size which allows statistic conclusions about the experimental sample. Additionally, it remains to be investigated whether local G excitation also leads to an electron transfer to A, which could be performed for example with semi-classical means.

The presented studies have two major implications for future applications and follow-up studies. The quantum control studies on the chemical system in chapter 2 could encourage experimentalists to use the presented knowledge and potentially assist them in making advances toward the synthetic domain. From the theoretical point of view, it is desirable to go beyond the feasibility assessment and suggest how the complete control mechanism drawn in Figure 2.1 might be realized. The main challenge here will be to demonstrate how to steer the WP into the reactive IRC mode after carbonyl excitation. The vibrational level structure in the energetic region of the transition state needs to be evaluated, and a laser pulse must be optimized which accomplishes efficient coupling between the two modes and selectively addresses the reactive one. Other methods like a coupled QD/MD propagation as suggested in Ref. [81] or density matrix simulations could investigate the controllability of other sources of environmental influence, like energy dissipation to the solvent. The quantum control study on uracil can be regarded as an instruction for potential experiments. Also, as all canonical nucleobases exhibit very fast relaxation times, the suggested mech-

anism could potentially be transferred or at least be seen as a good starting point for related studies on other nucleobases. The latter also applies for the simulations in RNA, where it would be interesting to investigate whether the same mechanism is found in other nucleobases. In either case, only the initial relaxation step from S_2 to S_1 was considered. Photodamage is known to also occur from delayed S_1 to ground state relaxation. Potential investigation of this mechanism would require other additional reactive coordinates however, as the two-dimensional space which was used here is specifically designed to describe relaxation out of the S_2 state.

Appendix A.

Supporting information for chapter 3.1

In the following, the supporting information of the article “Controlling Photorelaxation in Uracil with Shaped Laser Pulses: A Theoretical Assessment” published in the *Journal of the American Chemical Society* is reprinted with permission from *J. Am. Chem. Soc.* **2017**, *139*, 5061. Copyright 2017 American Chemical Society. It contains the optimized structures of FC, S₂ minimum and the CoIn, as well as the displacement vectors of the 2D coordinate space constructed from these three structures. G-Matrix elements, transition dipole moments, non-adiabatic coupling matrix element (NACME), and details for pulse optimizations like the projection operator for the control aim are given.

Supporting information for:
Controlling Photorelaxation in Uracil with
Shaped Laser Pulses: A Theoretical
Assessment

Supporting information

Daniel Keefer,[†] Sebastian Thallmair,^{†,¶} Spiridoula Matsika,[‡] and Regina de
Vivie-Riedle^{*,†}

*Department Chemie, Ludwig-Maximilians-Universität München, D-81377 München,
Germany, and Department of Chemistry, Temple University, Philadelphia, Pennsylvania
19122, United States*

E-mail: regina.de_vivie@cup.uni-muenchen.de

*To whom correspondence should be addressed

[†]Department Chemie, Ludwig-Maximilians-Universität München, D-81377 München, Germany

[‡]Department of Chemistry, Temple University, Philadelphia, Pennsylvania 19122, United States

[¶]Current address: Groningen Biomolecular Sciences and Biotechnology Institute and The Zernike Institute for Advanced Material, University of Groningen, Nijenborgh 7, 9747 AG Groningen, The Netherlands

Optimized structures and coordinate vectors

This section contains the optimized structures of the Franck-Condon (FC) point, the S_2 minimum and the S_2/S_1 conical intersection (CoIn), as already found in previous works.^{S1,S2} They have been optimized with the COLUMBUS program package^{S3-S5} using multi-reference configuration interaction (MRCI) with a (12,9) active space and the cc-pVDZ basis. These three structures span a two-dimensional coordinate space, with the first coordinate $q_{FC \rightarrow CoIn}$ being the normalized vector pointing from the FC to the S_2/S_1 CoIn, and the second coordinate being the vector pointing from the FC to the S_2 minimum, orthonormalized with respect to $q_{FC \rightarrow CoIn}$.

Ground state minimum structure			
Absolute energy: -412.624433 Hartree			
N	-0.949104	-0.054982	0.000000
N	0.983694	1.198645	0.000000
C	-0.389225	1.200077	0.000000
C	1.734922	0.051763	0.000000
C	1.165253	-1.172332	0.000000
C	-0.292517	-1.286427	0.000000
O	-0.909614	-2.314371	0.000000
O	-1.038471	2.209750	0.000000
H	-1.950663	-0.078792	0.000000
H	1.416417	2.097983	0.000000
H	2.804600	0.196935	0.000000
H	1.752062	-2.075605	0.000000

S ₂ minimum structure			
Absolute energy: -412.417827 Hartree			
N	-0.926348	-0.085981	0.035097
N	0.972975	1.190911	0.041305
C	-0.389514	1.190311	0.000145
C	1.817058	0.113236	-0.029692
C	1.155229	-1.212691	-0.065028
C	-0.200258	-1.252228	0.007623
O	-1.011447	-2.288678	0.013046
O	-1.066201	2.186465	-0.044068
H	-1.924115	-0.166824	0.089539
H	1.364363	2.112580	0.096968
H	2.787327	0.270215	0.428083
H	1.730164	-2.117779	-0.148483

S ₂ /S ₁ CoIn structure			
Absolute energy: -412.427053 Hartree			
N	-0.875590	-0.061424	-0.438801
N	0.992269	1.175157	0.169818
C	-0.398243	1.138717	0.002335
C	1.749110	0.128037	-0.224914
C	1.145232	-1.192330	0.081665
C	-0.232660	-1.279499	-0.051994
O	-0.995549	-2.232124	0.209019
O	-1.050462	2.133167	0.172808
H	-1.875903	-0.102508	-0.487059
H	1.358342	2.108083	0.253583
H	2.762919	0.307878	-0.544136
H	1.654763	-1.868903	0.752027

<i>q</i> _{FC→CoIn} coordinate vector			
N	0.057502	-0.005039	0.343227
N	0.006707	-0.018372	-0.132830
C	-0.007054	-0.047996	-0.001826
C	0.011098	0.059661	0.175926
C	-0.015660	-0.015642	-0.063878
C	0.046820	0.005419	0.040670
O	-0.067218	0.064333	-0.163493
O	-0.009380	-0.059903	-0.135169
H	0.058477	-0.018551	0.380974
H	-0.045426	0.007900	-0.198351
H	-0.032603	0.086779	0.425620
H	-0.076106	0.161681	-0.588230

	$q_{FC \rightarrow S_2min}$ coordinate vector		
N	0.009693	-0.068540	-0.177225
N	-0.030079	-0.004179	0.196680
C	0.004651	0.013444	0.001717
C	0.183304	0.098417	-0.202115
C	-0.011570	-0.082378	-0.103531
C	0.179959	0.075719	-0.012915
O	-0.186903	0.011389	0.153882
O	-0.057633	-0.009116	-0.000792
H	0.017807	-0.191438	-0.078670
H	-0.087184	0.028100	0.376049
H	-0.015696	0.105498	0.677693
H	0.006355	-0.220491	0.097587

G-matrix elements

In our quantum dynamical simulations, the kinetic energy operator \hat{T}_q for internal coordinates q_r is set up with the G-matrix formalism:^{S6-S9}

$$\hat{T}_q \simeq -\frac{1}{2} \sum_{r=1}^M \sum_{s=1}^M \frac{\partial}{\partial q_r} \left[G_{rs} \frac{\partial}{\partial q_s} \right]. \quad (1)$$

The G-matrix G_{rs} notes

$$G_{rs} = \sum_{i=1}^{3N} \frac{1}{m_i} \frac{\partial q_r}{\partial x_i} \frac{\partial q_s}{\partial x_i} \quad (2)$$

and contains the derivative of the internal coordinates q_r with respect to the cartesian coordinates x_i . It is most conveniently accessible via its inverse elements

$$(G^{-1})_{rs} = \sum_{i=1}^{3N} m_i \frac{\partial x_i}{\partial q_r} \frac{\partial x_i}{\partial q_s}. \quad (3)$$

As the coordinates we use are linear, the G-matrix values are position independent and can be interpreted as the reciprocal reduced mass along this coordinate.

Table S1: G-matrix elements setting up the kinetic energy operator for the quantum dynamical simulations

element	coordinate	value [au]
G_{rr}	$q_{FC \rightarrow CoIn}$	$1.671 \cdot 10^{-4}$
G_{ss}	$q_{FC \rightarrow S_2 min}$	$1.388 \cdot 10^{-4}$
G_{rs}	kinetic coupling	$-0.704 \cdot 10^{-4}$

Potential energy surface, transition dipole moments and non-adiabatic coupling

This chapter contains pictures of the data acquired with electronic structure theory, which serve as a setup for the quantum dynamical simulations. The methodology is the same as described in the previous section.

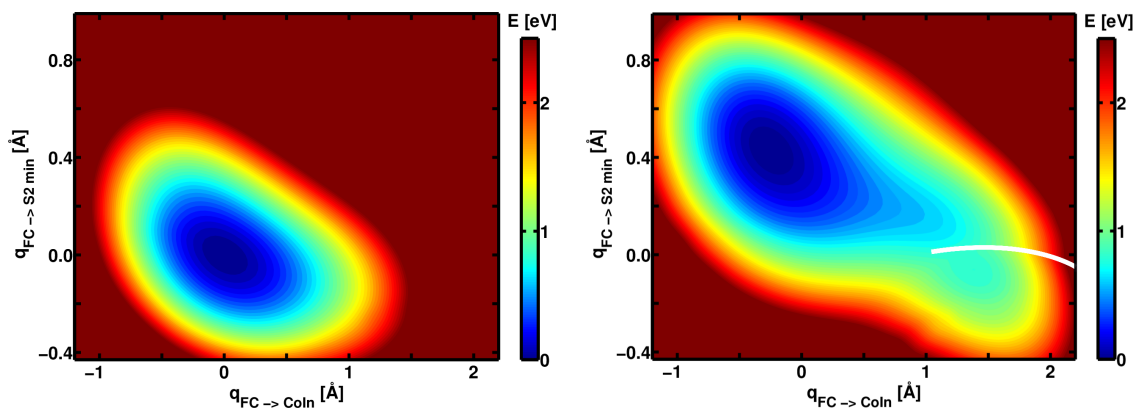


Figure S1: **Reduced-dimensional Potential energy surfaces** of Uracil, with the ground state (left) and the dark n/π^* S_1 state (right), with the S_2/S_1 CoIn sketched in white.

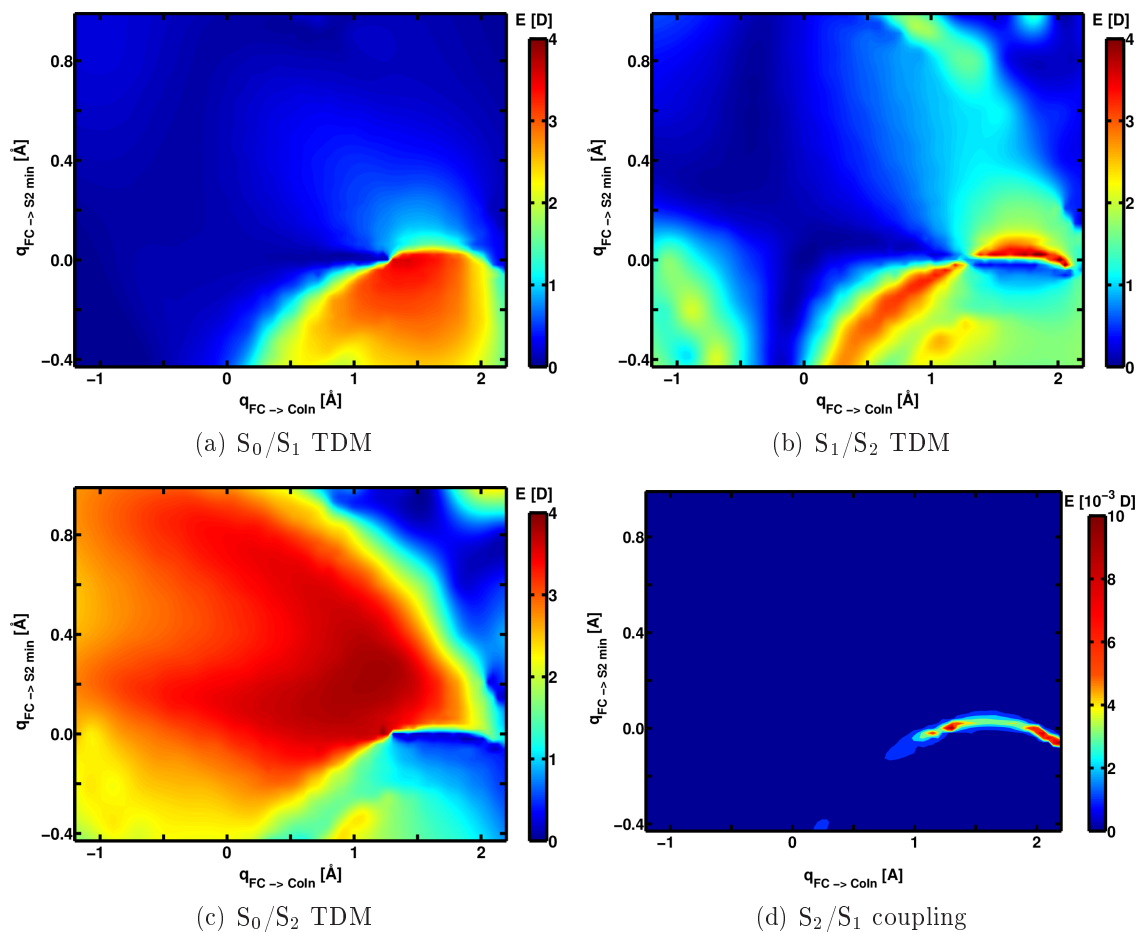


Figure S2: (a) – (c): **Transition dipole moments** of the bottom three electronic states. In the Franck-Condon region (0 \AA for both coordinates) only the TDM between the S_0 and the S_2 has significant values. (d): **Non-adiabatic coupling** between the S_2 and S_1 state.

Details on pulse optimizations

The complete optimal control theory (OCT) functional we used to optimize the laser pulses is explained in the main document and rewritten here for convenience:

$$J[\psi_i(t), \psi_f(t), \varepsilon(t)] = F[\psi_i(t)] - \int_0^T s(t)|\varepsilon(t)|^2 dt - \int_0^T \psi_f(t)G[\psi_i(t), \varepsilon(t)]dt. \quad (4)$$

The optimization aim is expressed via a projection operator and takes the form

$$F[\psi_i(t)] = \langle \psi_i(T) | \hat{P} | \psi_i(T) \rangle \quad \text{with} \quad \hat{P} = |\psi_i\rangle\langle\psi_i|. \quad (5)$$

With the help of this projection operator, we defined two control aims by selecting regions on the potential energy surface (PES) where the population of the wave packet is to be maximized at the end of the propagation time. For an acceleration of the relaxation process, the projection operator covered the area of the S₂/S₁ CoIn and the barrier towards the S₂ minimum (fig. S3 (a)). To find a laser pulse which traps the wave packet in the S₂ minimum region, the projection area only covered this very area (fig. S3 (b)). For final propagation times and some more details, please refer to tab. S2

Table S2: OCT details for laser pulse optimizations. All calculations were made with a time step of 0.05 fs. The Krotov change parameter α as well as the frequency filter are contained in the function $s(t)$ within the OCT functional (eq. 4)

optimization aim	final time [fs]	Krotov change parameter α	minimum frequency [au]	maximum frequency [au]
optimal pump complete S ₂ PES	145	10 – 20	0.2	0.26
acceleration fig. S3 (a)	99	2 – 10	0.2	0.26
trap fig. S3 (b)	260	2 – 10	0.2	0.24

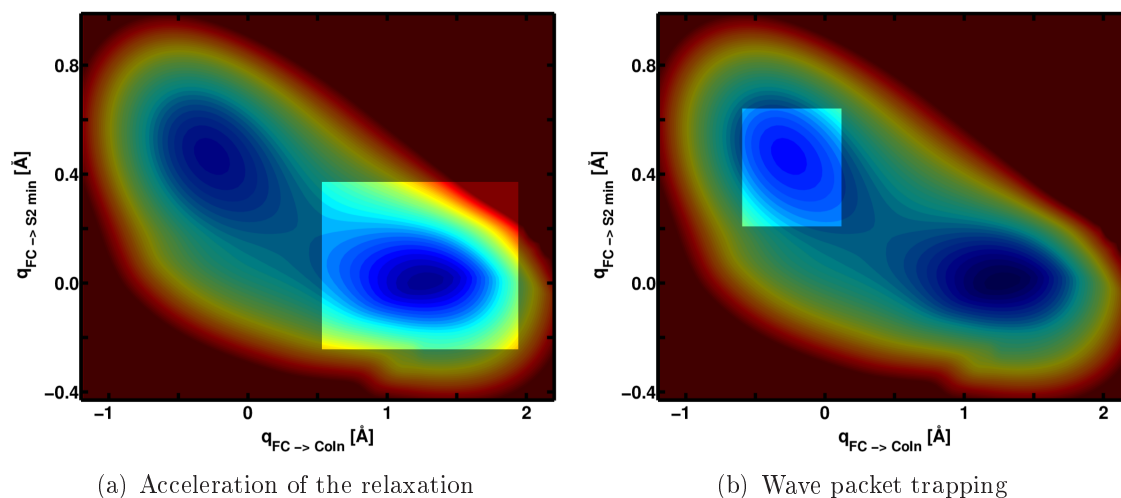


Figure S3: **Projection operator area** for OCT optimizations, which is zero at the greyed out areas.

References

- (S1) Matsika, S. *J. Phys. Chem. A* **2004**, *108*, 7584.
- (S2) Yoshikawa, A.; Matsika, S. *Chem. Phys.* **2008**, *347*, 393 – 404.
- (S3) Lischka, H.; Müller, T.; Szalay, P. G.; Shavitt, I.; Pitzer, R. M.; Shepard, R.; Ed.: Allen, W. *Wiley Interdisciplinary Reviews: Computational Molecular Science (WIREs:CMS)* **2011**, *1*, 191 – 199.
- (S4) Lischka, H.; Shepard, R.; Pitzer, R. M.; Shavitt, I.; Dallos, M.; Müller, T.; Szalay, P. G.; Seth, M.; Kedziora, G. S.; Yabushita, S.; Zhang, Z. *Phys. Chem. Chem. Phys.* **2001**, *3*, 664.
- (S5) Lischka, H.; Shepard, R.; Shavitt, I.; Pitzer, R. M.; Dallos, M.; Müller, T.; Szalay, P. G.; Brown, F. B.; Ahlrichs, R.; Böhm, H. J.; Chang, A.; Comeau, D. C.; Gdanitz, R.; Dachsel, H.; Ehrhardt, C.; Ernzerhof, M.; Höchtel, P.; Irle, S.; Kedziora, G.; Kovar, T.; Parasuk, V.; Pepper, M. J. M.; Scharf, P.; Schiffer, H.; Schindler, M.; Schüler, M.; Seth, M.; Stahlberg, E. A.; Zhao, J.-G.; Yabushita, S.; Zhang, Z.; Barbatti, M.; Mat-

sika, S.; Schuurmann, M.; Yarkony, D. R.; Brozell, S. R.; Beck, E. V.; Blaudeau, J. P.; Ruckebauer, M.; Sellner, B.; Plasser, F.; Szymczak, J. J. COLUMBUS, an ab initio electronic structure program, release 7.0 (2015).

(S6) Wilson Jr., E. B.; Decius, J. C.; Cross, P. C. *Molecular Vibrations*; McGraw-Hill: New York, 1955.

(S7) Schaad, L.; Hu, J. *J. Mol. Struct.: THEOCHEM* **1989**, *185*, 203–215.

(S8) Kowalewski, M.; Mikosch, J.; Wester, R.; de Vivie-Riedle, R. *J. Phys. Chem. A* **2014**, *118*, 4661–4669.

(S9) Thallmair, S.; Roos, M. K.; de Vivie-Riedle, R. *J. Chem. Phys* **2016**, *144*, 234104.

Appendix B.

Supporting information for chapter 3.2

In the following, the supporting information of the article “RNA Environment is Responsible for Decreased Photostability of Uracil” published in the *Journal of the American Chemical Society* is reprinted with permission from *J. Am. Chem. Soc.* **2018**, *140*, 8714. Copyright 2018 American Chemical Society. It again gives structures and coordinate vectors like in Appendix A. The approximation of adding a ground state environmental PES to an excited state PES is validated by showing the electric dipole momenta and electrostatic potentials of the participating states. Normal mode scans extending the 2D coordinate space to three dimensions are contained, which verify the used 2D space.

Supporting information for: RNA Environment is Responsible for Decreased Photostability of Uracil

Sebastian Reiter, Daniel Keefer, and Regina de Vivie-Riedle*

*Department Chemie, Ludwig-Maximilians-Universität München, D-81377 München,
Germany*

E-mail: regina.de.vivie@cup.uni-muenchen.de

Optimized Structures and Coordinate Vectors

This section lists the optimized molecular geometries of the Franck-Condon (FC) point, the S_2 minimum and the S_2/S_1 conical intersection (CoIn) of uracil adopted from previous works.^{S1,S2} The software package *COLUMBUS*^{S3-S5} had been used to optimize the structures on the MRCI(12,9)/cc-pVDZ level of theory. A two-dimensional coordinate space used in the quantum dynamical simulations of this work can be constructed from the normalized vector $q_{\text{FC} \rightarrow \text{CoIn}}$, pointing from the FC point to the CoIn and the orthonormalized vector $q_{\text{FC} \rightarrow S_2\text{-min}}$ pointing from the FC point to the S_2 -minimum.^{S6}

*To whom correspondence should be addressed

Ground state minimum structure			
N	-0.949 104	-0.054 982	0.000 000
N	0.983 694	1.198 645	0.000 000
C	-0.389 225	1.200 077	0.000 000
C	1.734 922	0.051 763	0.000 000
C	1.165 253	-1.172 332	0.000 000
C	-0.292 517	-1.286 427	0.000 000
O	-0.909 614	-2.314 371	0.000 000
O	-1.038 471	2.209 750	0.000 000
H	-1.950 663	-0.078 792	0.000 000
H	1.416 417	2.097 983	0.000 000
H	2.804 600	0.196 935	0.000 000
H	1.752 062	-2.075 605	0.000 000
S_2 minimum structure			
N	-0.926 348	-0.085 981	0.035 097
N	0.972 975	1.190 911	0.041 305
C	-0.389 514	1.190 311	0.000 145
C	1.817 058	0.113 236	-0.029 692
C	1.155 229	-1.212 691	-0.065 028
C	-0.200 258	-1.252 228	0.007 623
O	-1.011 447	-2.288 678	0.013 046
O	-1.066 201	2.186 465	-0.044 068
H	-1.924 115	-0.166 824	0.089 539
H	1.364 363	2.112 580	0.096 968
H	2.787 327	0.270 215	0.428 083
H	1.730 164	-2.117 779	-0.148 483
S_2/S_1 CoIn structure			
N	-0.875 590	-0.061 424	-0.438 801
N	0.992 269	1.175 157	0.169 818
C	-0.398 243	1.138 717	0.002 335
C	1.749 110	0.128 037	-0.224 914
C	1.145 232	-1.192 330	0.081 665
C	-0.232 660	-1.279 499	-0.051 994
O	-0.995 549	-2.232 124	0.209 019
O	-1.050 462	2.133 167	0.172 808
H	-1.875 903	-0.102 508	-0.487 059
H	1.358 342	2.108 083	0.253 583
H	2.762 919	0.307 878	-0.544 136
H	1.654 763	-1.868 903	0.752 027

 $q_{\text{FC} \rightarrow \text{CoIn}}$ coordinate vector

N	0.057 502	-0.005 039	0.343 227
N	0.006 707	-0.018 372	-0.132 830
C	-0.007 054	-0.047 996	-0.001 826
C	0.011 098	0.059 661	0.175 926
C	-0.015 660	-0.015 642	-0.063 878
C	0.046 820	0.005 419	0.040 670
O	-0.067 218	0.064 333	-0.163 493
O	-0.009 380	-0.059 903	-0.135 169
H	0.058 477	-0.018 551	0.380 974
H	-0.045 426	0.007 900	-0.198 351
H	-0.032 603	0.086 779	0.425 620
H	-0.076 106	0.161 681	-0.588 230

 $q_{\text{FC} \rightarrow \text{S}_2\text{-min}}$ coordinate vector

N	0.009 693	-0.068 540	-0.177 225
N	-0.030 079	-0.004 179	0.196 680
C	0.004 651	0.013 444	0.001 717
C	0.183 304	0.098 417	-0.202 115
C	-0.011 570	-0.082 378	-0.103 531
C	0.179 959	0.075 719	-0.012 915
O	-0.186 903	0.011 389	0.153 882
O	-0.057 633	-0.009 116	-0.000 792
H	0.017 807	-0.191 438	-0.078 670
H	-0.087 184	0.028 100	0.376 049
H	-0.015 696	0.105 498	0.677 693
H	0.006 355	-0.220 491	0.097 587

Electric Dipole Moments and Electrostatic Potentials of Uracil in Different Excited States

This section contains visualizations of the electric dipole moments and the electrostatic potentials of uracil in the first few excited states, each computed at both the (TD)DFT/CAM-B3LYP/6-31G(d) and the (TD)DFT/M06-2X/6-311++G(d,p) levels of theory with the *Gaussian16*^{S7} program package. The ground state structure was optimized with the respective quantum chemical method and verified with a frequency analysis prior to the excited state calculations.

The two methods yield a different ordering of the higher excited states $S_{n>3}$ (Tables S1 and S2) but the bright $\pi\pi^*$ state, which is the focus of this paper, is the S_2 state in both cases. It is clearly visible from Figures S1 and S2 that the dipole moment of this state is very close to the one of the electronic ground state in both direction and magnitude, while the other excited states can differ significantly from the ground state. The same is true for the electrostatic potential depicted in Figures S3 and S4. It is therefore reasonable to assume that the electrostatic interaction of the environment with uracil in the bright S_2 state will be very similar to that in the ground state. Thus, while not generally applicable, the approach to compute the environmental potential \hat{V}_{env} in the ground state and subsequently add a high-level excited state potential \hat{V}_{mol} is a valid approximation in our case.

Table S1. Character, vertical excitation energies and oscillator strength of the first five singlet excited states of uracil (TDDFT/CAM-B3LYP/6-31G(d)). The bright second excited state is the main focus of this study and highlighted in red.

state	character	$E_{\text{vert}}[\text{eV}]$	$E_{\text{vert}}[\text{nm}]$	f
S1	$n \rightarrow \pi^*$	5.09	243.4	0.00
S2	$\pi \rightarrow \pi^*$	5.65	219.5	0.17
S3	$n \rightarrow \pi^*$	6.40	193.6	0.00
S4	$\pi \rightarrow \pi^*$	6.73	184.3	0.04
S5	$\pi \rightarrow \pi^*$	7.18	172.7	0.14

Table S2. Character, vertical excitation energies and oscillator strength of the first five singlet excited states of uracil (TDDFT/M06-2X/6-311++G(d,p)). The bright second excited state is the main focus of this study and highlighted in red.

state	character	$E_{\text{vert}}[\text{eV}]$	$E_{\text{vert}}[\text{nm}]$	f
S1	$n \rightarrow \pi^*$	5.01	247.5	0.00
S2	$\pi \rightarrow \pi^*$	5.55	223.5	0.20
S3	$\pi \rightarrow \text{Ry}^*$	5.97	207.5	0.02
S4	$n \rightarrow \pi^*$	6.28	197.5	0.00
S5	$\pi \rightarrow \pi^*$	6.73	184.3	0.04

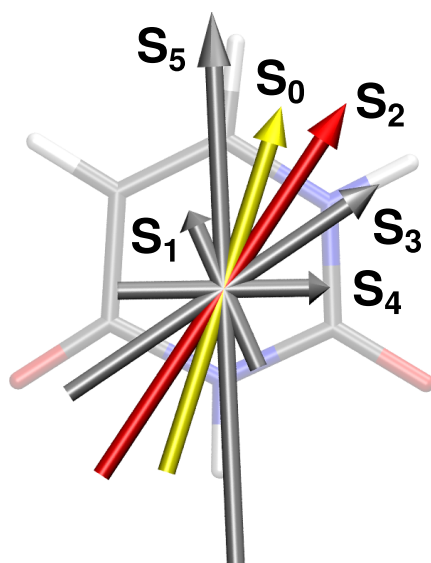


Figure S1. Electric dipole moments of the ground state and the first five excited states of uracil on the (TD)DFT/CAM-B3LYP/6-31G(d) level of theory. Note that the dipole moments of the ground state and the second excited state, that this study focuses on, are very similar in direction and magnitude.

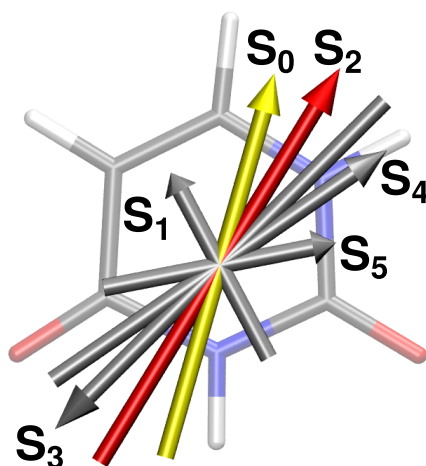


Figure S2. Electric dipole moments of the ground state and the first five excited states of uracil on the (TD)DFT/M06-2X/6-311++G(d,p) level of theory. Note that the dipole moments of the ground state and the second excited state, that this study focuses on, are very similar in direction and magnitude.

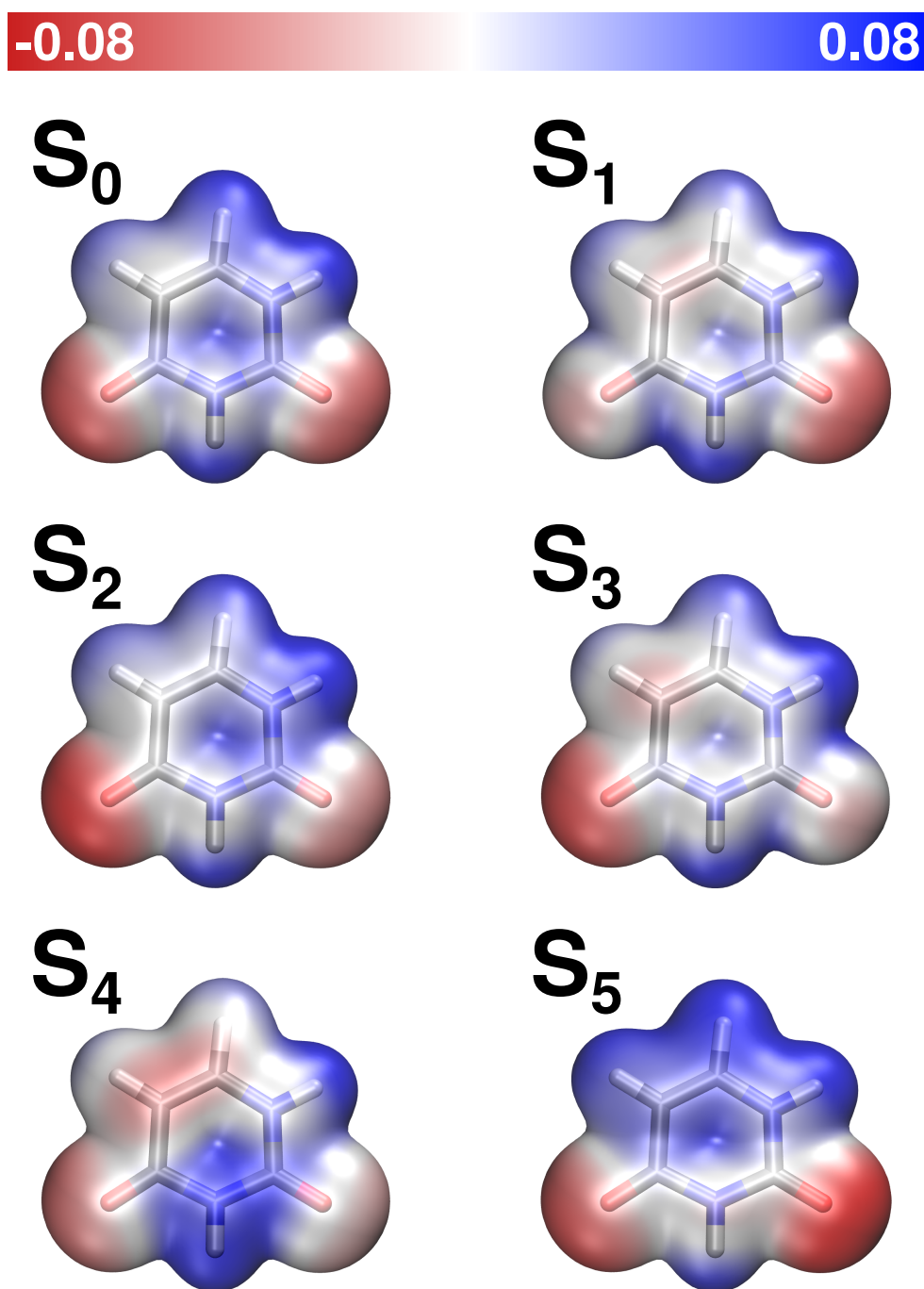


Figure S3. Electrostatic potential mapped onto the electron density (Isovalue 0.05) of uracil in the ground state and the first five excited states, computed at the (TD)DFT/CAM-B3LYP/6-31G(d) level of theory. Note that the ground state and the second excited state exhibit the same charge distribution across the nucleobase.

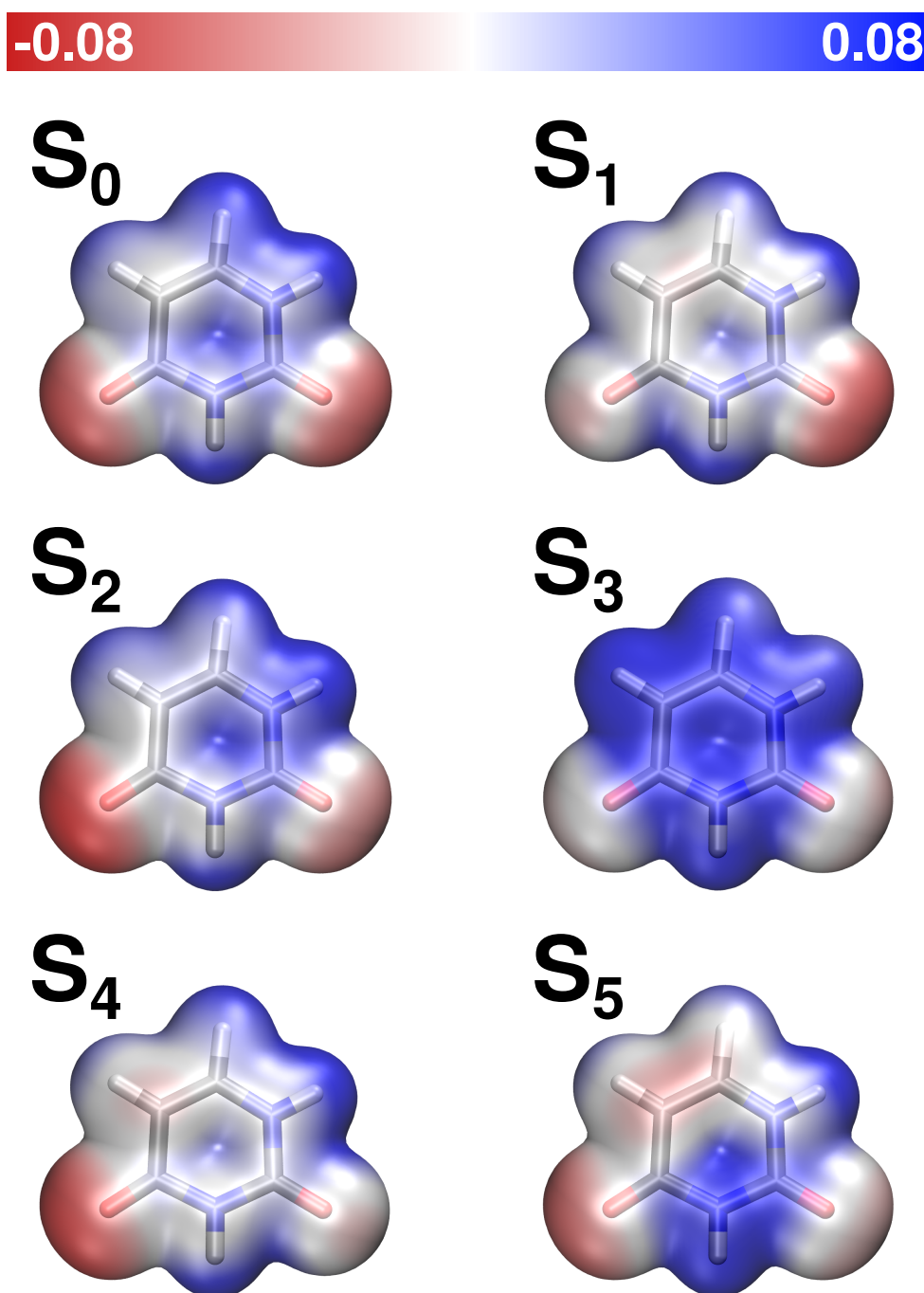


Figure S4. Electrostatic potential mapped onto the electron density (Isovalue 0.05) of uracil in the ground state and the first five excited states, computed at the (TD)DFT/M06-2X/6-311++G(d,p) level of theory. Note that the ground state and the second excited state exhibit the same charge distribution across the nucleobase.

Potential Energy Scans in Three Dimensions

Modeling the photorelaxation of uracil in two reactive coordinates is necessarily an approximation. For the isolated base, the validity of the described two-dimensional (2D) coordinate space to describe the photorelaxation of uracil has been established in a previous investigation.^{S6} However, it could be conceived that the presence of an atomistic environment opens new relaxation pathways in a different coordinate. In such a case, the potential energy would be stabilized in the third dimension in direct vicinity of the 2D space.

To check for the necessity of additional coordinates in our simulations, we extended the existing 2D space to three dimensions by adding five normal modes from different spectral regions that cover most of the molecular movement of uracil. Specifically, we chose an N–H (q_{NH_s}), a C–H (q_{CH_s}) and a C–O (q_{CO_s}) stretching mode as well as a C–H bending mode (q_{CH_b}) and an out-of-plane deformation (q_{oop}) as shown in [Table S3](#). The Cartesian coordinates of these modes are compiled on the following pages.

Table S3. Chosen normal modes to represent molecular movement of uracil in a third dimension. Vibrational frequencies were calculated with M06-2X/6-311++G(d,p) and scaled by a factor of 0.947. The normal modes cover a broad spectral range and include most molecular degrees of freedom not already covered by the 2D coordinate space.

Mode	$\tilde{\nu}[\text{cm}^{-1}]$
q_{NH_s}	3423
q_{CH_s}	3051
q_{CO_s}	1762
q_{CH_b}	1170
q_{oop}	723

$q_{\text{oop}} : \tilde{\nu} = 723 \text{ cm}^{-1}$			
N	0.00	0.00	-0.24
N	0.00	0.00	-0.22
C	0.00	0.00	0.82
C	0.00	0.00	0.04
C	0.00	0.00	-0.10
C	0.00	0.00	0.09
O	0.00	0.00	-0.03
O	0.00	0.00	-0.25
H	0.00	0.00	0.26
H	0.00	0.00	0.06
H	0.00	0.00	0.00
H	0.00	0.00	0.27
$q_{\text{CH}_b} : \tilde{\nu} = 1170 \text{ cm}^{-1}$			
N	0.09	-0.02	0.00
N	-0.04	0.08	0.00
C	-0.06	-0.10	0.00
C	0.11	-0.03	0.00
C	0.01	-0.03	0.00
C	-0.12	0.15	0.00
O	0.00	-0.02	0.00
O	-0.01	0.00	0.00
H	0.34	-0.02	0.00
H	-0.15	0.29	0.00
H	0.34	-0.04	0.00
H	-0.36	-0.67	0.00
$q_{\text{CO}_s} : \tilde{\nu} = 1762 \text{ cm}^{-1}$			
N	-0.09	0.03	0.00
N	-0.08	0.08	0.00
C	0.59	-0.31	0.00
C	0.00	-0.01	0.00
C	0.03	0.04	0.00
C	-0.19	-0.16	0.00
O	0.13	0.09	0.00
O	-0.33	0.18	0.00
H	0.26	0.03	0.00
H	0.20	-0.42	0.00
H	0.02	-0.01	0.00
H	-0.04	-0.08	0.00

$q_{\text{CH}_s} : \tilde{\nu} = 3051 \text{ cm}^{-1}$

N	0.00	0.00	0.00
N	0.00	0.00	0.00
C	0.00	0.00	0.00
C	0.01	0.09	0.00
C	0.01	-0.01	0.00
C	0.00	0.00	0.00
O	0.00	0.00	0.00
O	0.00	0.00	0.00
H	0.00	0.00	0.00
H	0.00	0.01	0.00
H	-0.07	-0.97	0.00
H	-0.17	0.10	0.00

$q_{\text{NH}_s} : \tilde{\nu} = 3423 \text{ cm}^{-1}$

N	0.00	-0.07	0.00
N	0.00	0.00	0.00
C	0.00	0.00	0.00
C	0.00	0.00	0.00
C	0.00	0.00	0.00
C	0.00	0.00	0.00
O	0.00	0.00	0.00
O	0.00	0.00	0.00
H	-0.02	1.00	0.00
H	0.01	0.00	0.00
H	0.00	0.00	0.00
H	0.00	0.00	0.00

We rastered the parts of the 2D space that are accessible to the wave packet (WP) with a grid of 14 points (Figure S5). After orthonormalizing the respective normal mode to the 2D space, we performed a potential energy scan at each of these grid points in both directions of the new coordinate, using the same quantum mechanics/molecular mechanics (QM/MM) methodology as described in the main article.

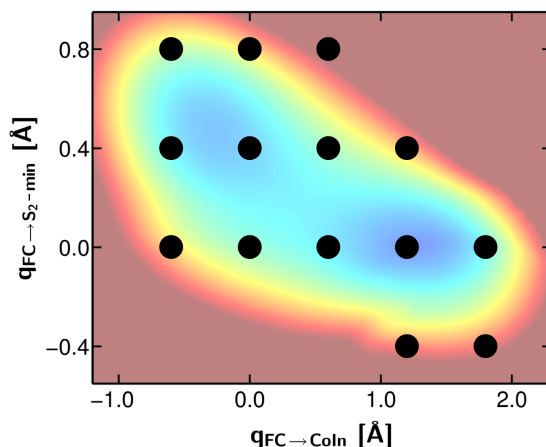


Figure S5. Grid points overlaid on the 2D-PES of uracil. At each of these points, a potential energy scan was performed along a normal mode coordinate to check for possible new relaxation pathways in a third dimension.

To account for different environmental conformations, we computed these scans for five molecular dynamics (MD) snapshots, thus giving a total of 25 three-dimensional potentials.

For a new relaxation pathway to form in a third dimension, the interaction energy \hat{V}_{env} would need to compensate the harmonic potential of the respective coordinate and cause stabilization close to the 2D space we considered in our simulations. Therefore, the sum of \hat{V}_{env} and the normal mode potentials in their harmonic representation is plotted in Figures S6 to S10. Each subplot shows a set of one-dimensional energy scans along the respective normal mode coordinate, corresponding to the grid points in Figure S5. All the scans remain harmonic in the third dimension under environmental influence. We therefore conclude that this space is well-suited to describe the photorelaxation of uracil and no new relaxation pathways can be expected in a third dimension.

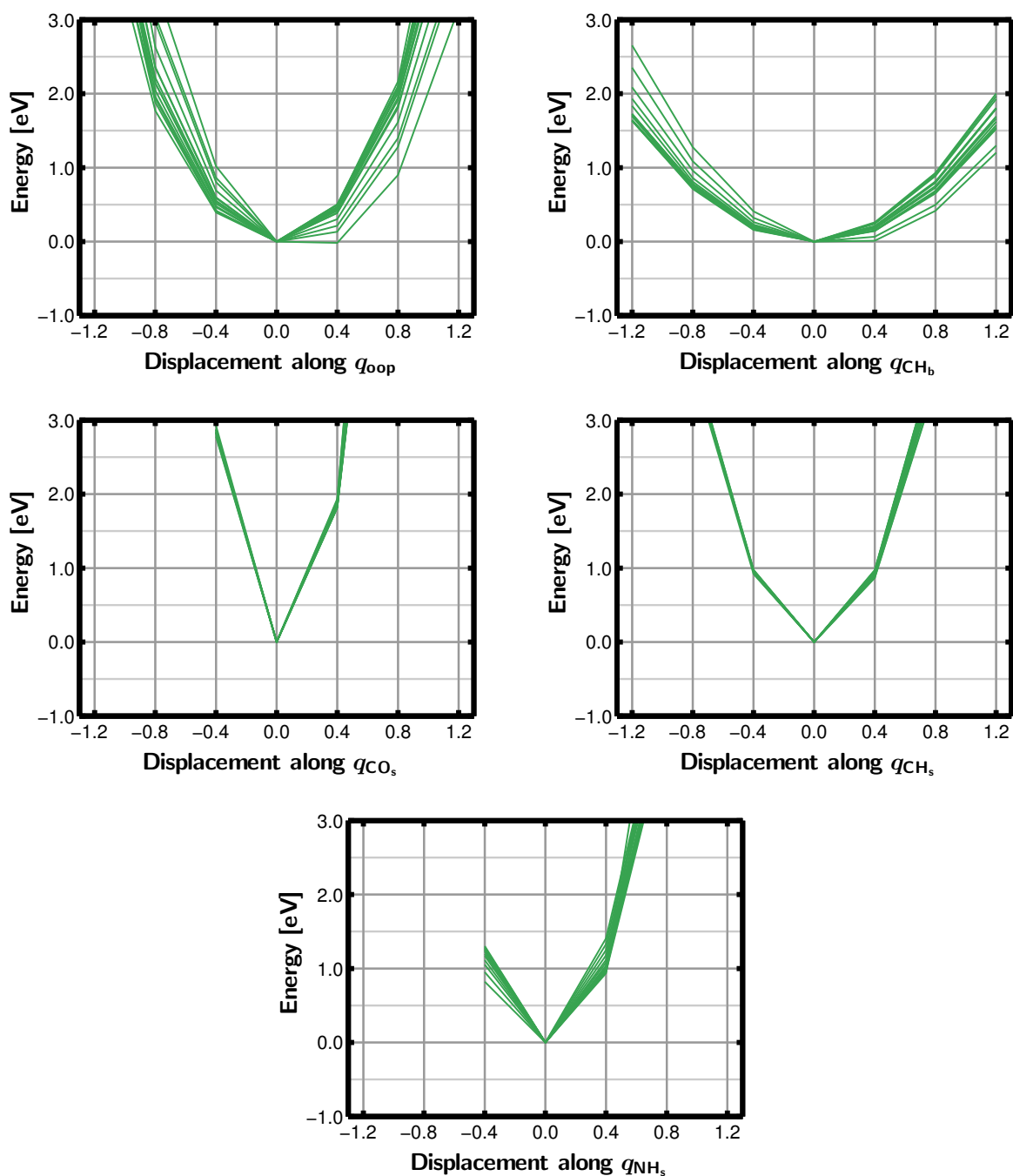


Figure S6. Sum of the harmonic potential of the respective normal mode and the environmental interaction energy \hat{V}_{env} in one MD snapshot for the base sequence 5'-GAGUAGG-3'. Each green line represents a one-dimensional potential energy scan along the normal mode coordinate, starting from one of the grid points in [Figure S5](#).

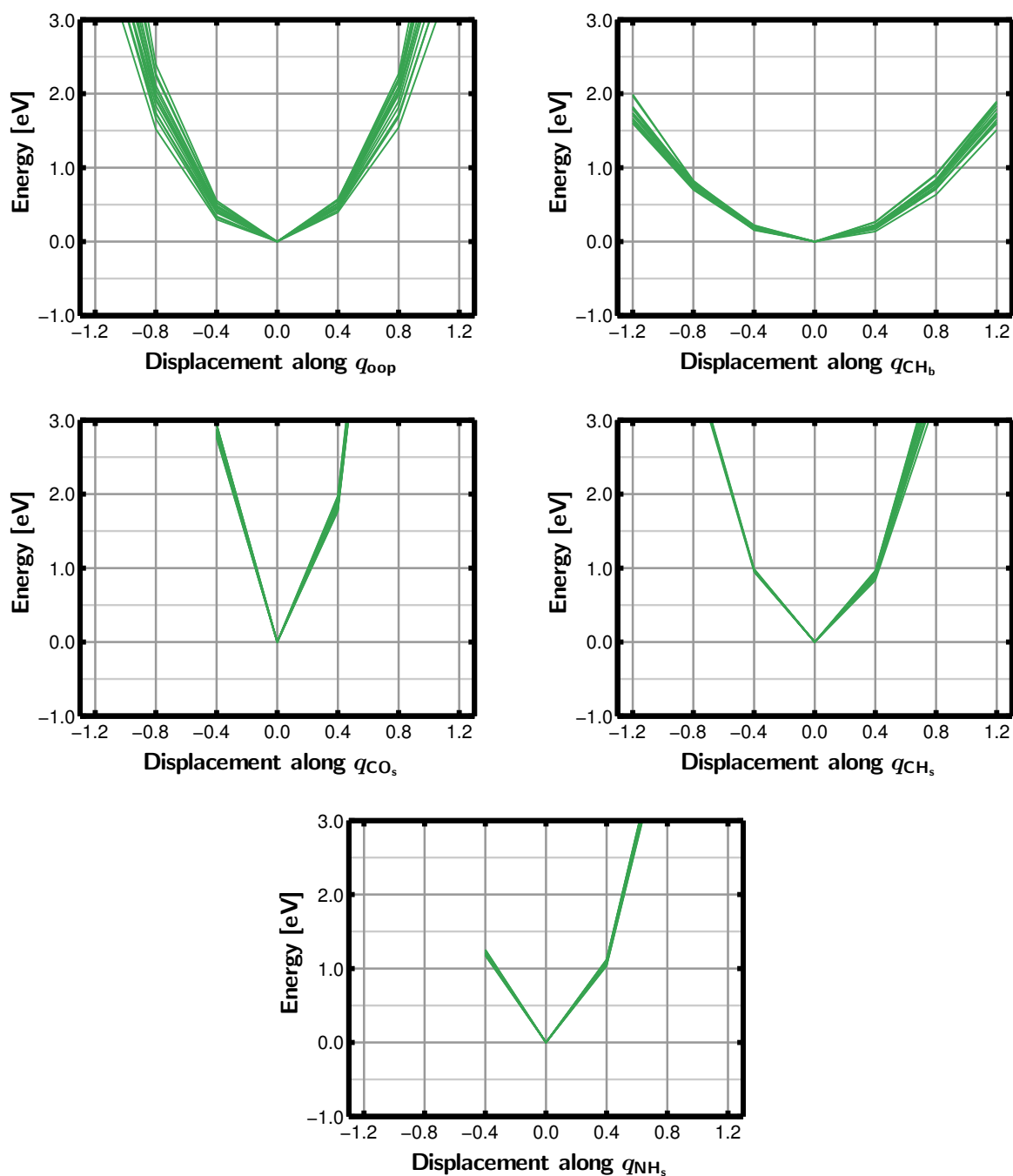


Figure S7. Sum of the harmonic potential of the respective normal mode and the environmental interaction energy \hat{V}_{env} in one MD snapshot for the base sequence 5'-GAGUAGG-3'. Each green line represents a one-dimensional potential energy scan along the normal mode coordinate, starting from one of the grid points in [Figure S5](#).

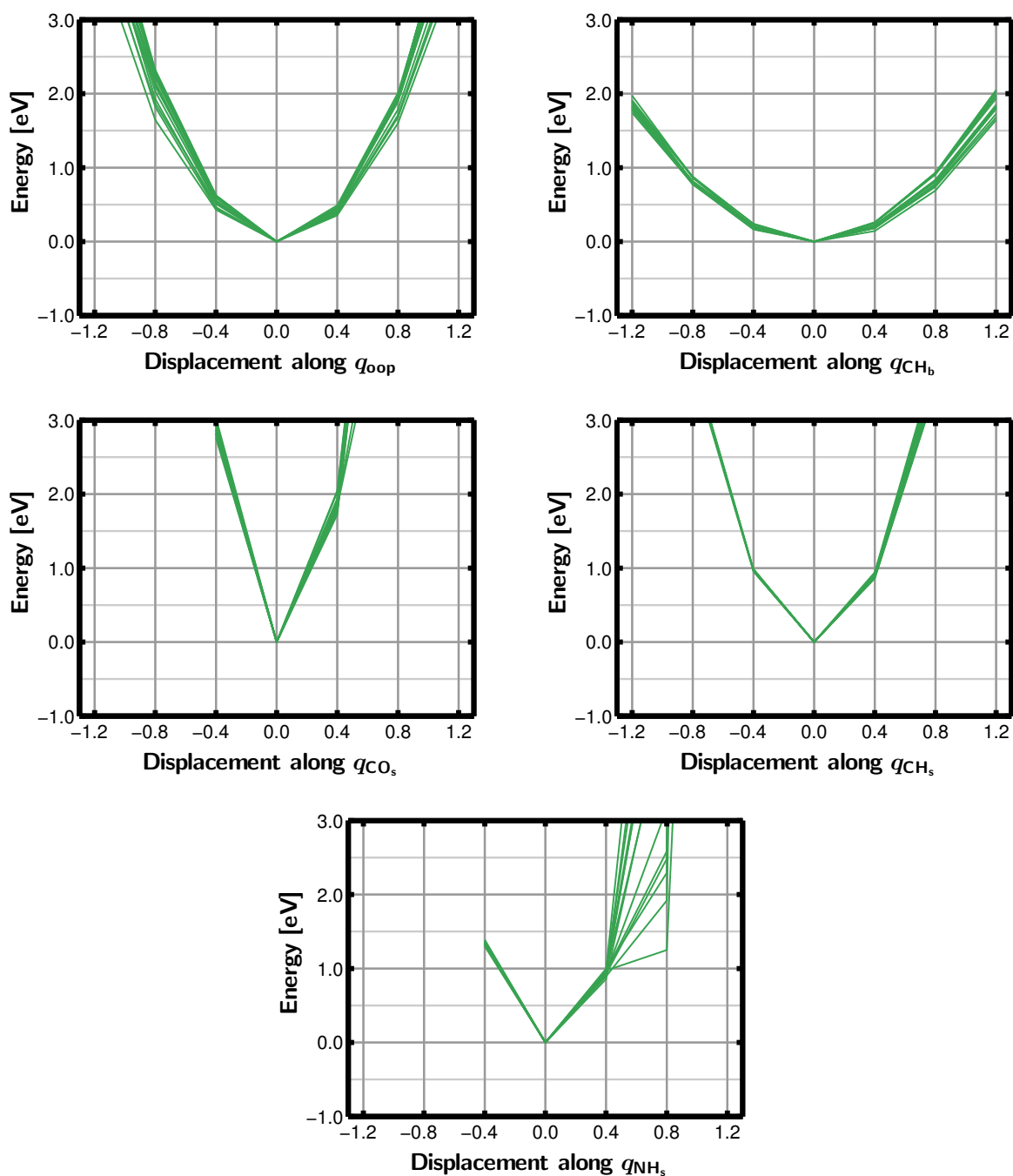


Figure S8. Sum of the harmonic potential of the respective normal mode and the environmental interaction energy \hat{V}_{env} in one MD snapshot for the base sequence 5'-GAGUAGG-3'. Each green line represents a one-dimensional potential energy scan along the normal mode coordinate, starting from one of the grid points in [Figure S5](#).

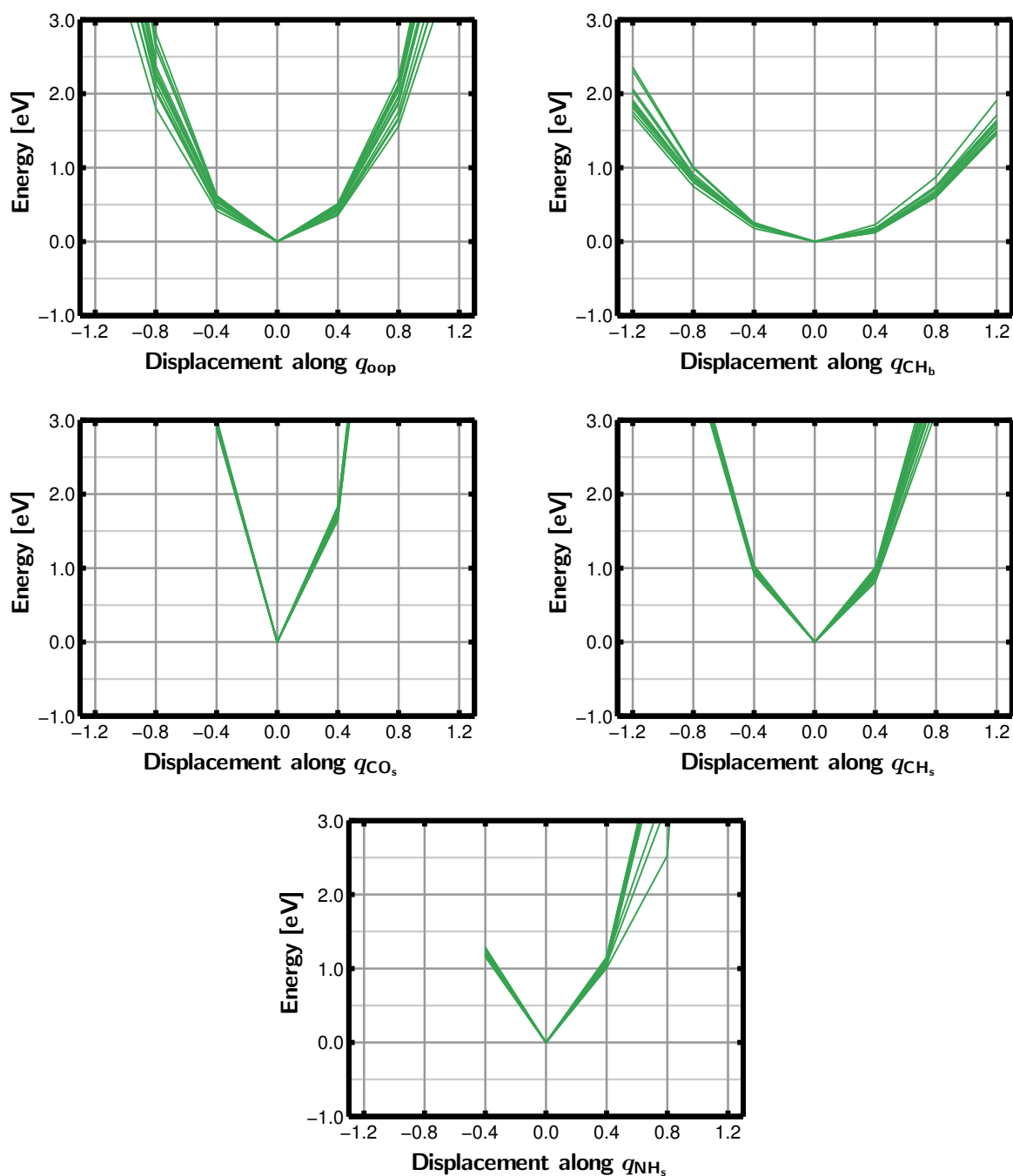


Figure S9. Sum of the harmonic potential of the respective normal mode and the environmental interaction energy \hat{V}_{env} in one MD snapshot for the base sequence 5'-GAGUAGG-3'. Each green line represents a one-dimensional potential energy scan along the normal mode coordinate, starting from one of the grid points in [Figure S5](#).

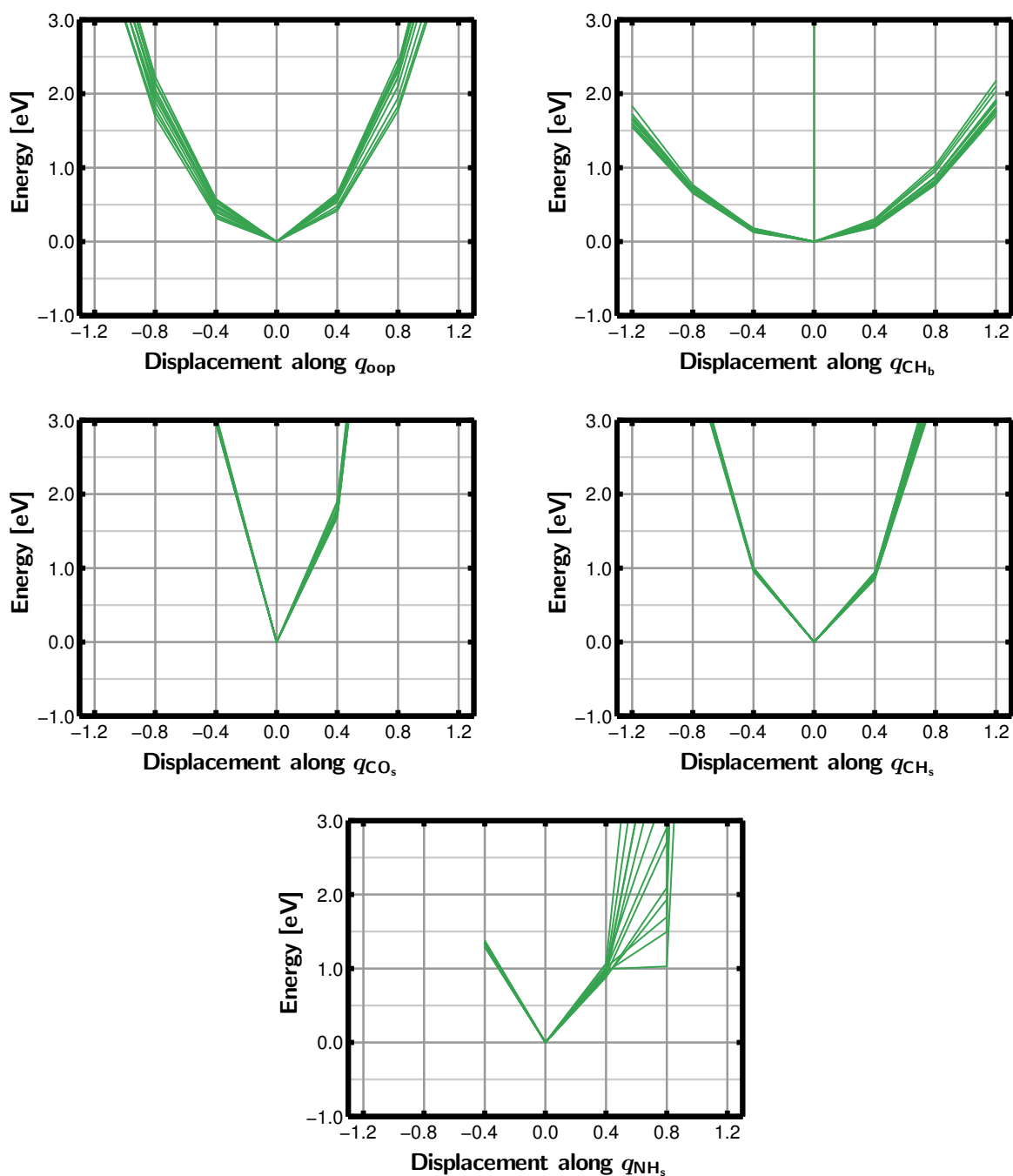


Figure S10. Sum of the harmonic potential of the respective normal mode and the environmental interaction energy \hat{V}_{env} in one MD snapshot for the base sequence 5'-GAGUAGG-3'. Each green line represents a one-dimensional potential energy scan along the normal mode coordinate, starting from one of the grid points in [Figure S5](#).

References

- (S1) Matsika, S. *J. Phys. Chem. A* **2004**, *108*, 7584.
- (S2) Yoshikawa, A.; Matsika, S. *Chem. Phys.* **2008**, *347*, 393.
- (S3) Lischka, H.; Müller, T.; Szalay, P. G.; Shavitt, I.; Pitzer, R. M.; Shepard, R. *WIREs Comput. Mol. Sci.* **2011**, *1*, 191.
- (S4) Lischka, H.; Shepard, R.; Pitzer, R. M.; Shavitt, I.; Dallos, M.; Müller, T.; Szalay, P. G.; Seth, M.; Kedziora, G. S.; Yabushita, S.; Zhang, Z. *Phys. Chem. Chem. Phys.* **2001**, *3*, 664.
- (S5) Lischka, H.; Shepard, R.; Shavitt, I.; Pitzer, R. M.; Dallos, M.; Müller, T.; Szalay, P. G.; Brown, F. B.; Ahlrichs, R.; Böhm, H. J.; Chang, A.; Comeau, D. C.; Gdanitz, R.; Dachsel, H.; Ehrhardt, C.; Ernzerhof, M.; Höchtel, P.; Irle, S.; Kedziora, G.; Kovar, T.; Parasuk, V.; Pepper, M. J. M.; Scharf, P.; Schiffer, H.; Schindler, M.; Schüler, M.; Seth, M.; Stahlberg, E. A.; Zhao, J.-G.; Yabushita, S.; Zhang, Z.; Barbatti, M.; Matsika, S.; Schuurmann, M.; Yarkony, D. R.; Brozell, S. R.; Beck, E. V.; Blaudeau, J. P.; Ruckebauer, M.; Sellner, B.; Plasser, F.; Szymczak, J. J. COLUMBUS, an ab initio electronic structure program, release 7.0 (2015).
- (S6) Keefer, D.; Thallmair, S.; Matsika, S.; de Vivie-Riedle, R. *J. Am. Chem. Soc.* **2017**, *139*, 5061.
- (S7) Frisch, M. J.; Trucks, G. W.; Schlegel, H. B.; Scuseria, G. E.; Robb, M. A.; Cheeseman, J. R.; Scalmani, G.; Barone, V.; Petersson, G. A.; Nakatsuji, H.; Li, X.; Caricato, M.; Marenich, A. V.; Bloino, J.; Janesko, B. G.; Gomperts, R.; Menucci, B.; Hratchian, H. P.; Ortiz, J. V.; Izmaylov, A. F.; Sonnenberg, J. L.; Williams-Young, D.; Ding, F.; Lipparini, F.; Egidi, F.; Goings, J.; Peng, B.; Petrone, A.; Henderson, T.; Ranasinghe, D.; Zakrzewski, V. G.; Gao, J.; Rega, N.; Zheng, G.; Liang, W.; Hada, M.; Ehara, M.; Toyota, K.; Fukuda, R.; Hasegawa, J.; Ishida, M.; Nakajima, T.;

Honda, Y.; Kitao, O.; Nakai, H.; Vreven, T.; Throssell, K.; Montgomery, J. A., Jr.; Peralta, J. E.; Ogliaro, F.; Bearpark, M. J.; Heyd, J. J.; Brothers, E. N.; Kudin, K. N.; Staroverov, V. N.; Keith, T. A.; Kobayashi, R.; Normand, J.; Raghavachari, K.; Rendell, A. P.; Burant, J. C.; Iyengar, S. S.; Tomasi, J.; Cossi, M.; Millam, J. M.; Klene, M.; Adamo, C.; Cammi, R.; Ochterski, J. W.; Martin, R. L.; Morokuma, K.; Farkas, O.; Foresman, J. B.; Fox, D. J. Gaussian16 Revision A.03, <http://www.gaussian.com>. Gaussian Inc. Wallingford CT 2016.

List of abbreviations

ADC2	second-order algebraic diagrammatic construction
CASSCF	complete active space self consistent field
CASPT2	complete active space second-order perturbation theory
COSMO	conductor-like screening model
CI	configuration interaction
CC	coupled-cluster
CoIn	conical intersection
CPD	cyclobutane pyrimidine dimer
DFT	density functional theory
DNA	deoxyribonucleic acid
DFM	dynamic fourier method
FC	Franck-Condon
FWHM	full width at half maximum
IR	infrared
IRC	intrinsic reaction coordinate
MCTDH	multi-configuration time-dependent Hartree
MTOCT	multi-target optimal control theory
MD	molecular dynamics
MM	molecular mechanics
NACME	non-adiabatic coupling matrix element
OCT	optimal control theory
PES	potential energy surface
PCM	polarizable continuum model
QC	quantum chemistry
QD	quantum dynamics
QD/MD	quantum dynamics/molecular dynamics
QM/MM	quantum mechanics/molecular mechanics

QOC	quantum optimal control
RNA	ribonucleic acid
THF	tetrahydrofurane
TDDFT	time-dependent density functional theory
TDSE	time-dependent Schrödinger equation
TS	transition state
UV	ultraviolet
WF	wavefunction
WP	wavepacket

Bibliography

- [1] H. van Amerongen, R. van Grondelle, L. Valkunas, *Photosynthetic Excitons*, WORLD SCIENTIFIC, **2000**.
- [2] *Molecular Mechanisms of Photosynthesis*, (Ed.: R. E. Blankenship), Blackwell Science Ltd, Oxford, UK, **2002**.
- [3] Y.-C. Cheng, G. R. Fleming, *Annu. Rev. Phys. Chem.* **2009**, *60*, 241–262.
- [4] E. Collini, C. Y. Wong, K. E. Wilk, P. M. Curmi, P. Brumer, G. D. Scholes, *Nature* **2010**, *463*, 644–647.
- [5] M. Garavelli, P. Celani, F. Bernardi, M. A. Robb, M. Olivucci, *J. Am. Chem. Soc.* **1997**, *119*, 6891–6901.
- [6] S. Hayashi, E. Tajkhorshid, K. Schulten, *Biophys. J.* **2009**, *96*, 403–416.
- [7] D. Polli, P. Altoè, O. Weingart, K. M. Spillane, C. Manzoni, D. Brida, G. Tomasello, G. Orlandi, P. Kukura, R. A. Mathies, M. Garavelli, G. Cerullo, *Nature* **2010**, *467*, 440–443.
- [8] N. A. Anderson, J. J. Shiang, R. J. Sension, *J. Phys. Chem. A* **1999**, *103*, 10730–10736.
- [9] C. E. Crespo-Hernández, B. Cohen, B. Kohler, *Nature* **2005**, *436*, 1141–1144.
- [10] J. Cadet, S. Mouret, J. L. Ravanat, T. Douki, *Photochem. Photobiol.* **2012**, *88*, 1048–1065.
- [11] *Photoinduced Phenomena in Nucleic Acids I*, (Eds.: M. Barbatti, A. C. Borin, S. Ullrich), Springer International Publishing, Cham, **2015**.
- [12] W. J. Schreier, P. Gilch, W. Zinth, *Annu. Rev. Phys. Chem.* **2015**, *66*, 497–519.
- [13] R. Improta, F. Santoro, L. Blancafort, *Chem. Rev.* **2016**, *116*, 3540–3593.
- [14] M. J. Rosker, M. Dantus, A. H. Zewail, *J. Chem. Phys.* **1988**, *89*, 6113–6127.
- [15] M. Dantus, M. J. Rosker, A. H. Zewail, *J. Chem. Phys.* **1988**, *89*, 6128–6140.
- [16] A. H. Zewail, *Science (80-.)*. **1988**, *242*, 1645–1653.
- [17] F. Calegari, D. Ayuso, A. Trabattoni, L. Belshaw, S. De Camillis, S. Anumula, F. Frassetto, L. Poletto, A. Palacios, P. Decleva, J. B. Greenwood, F. Martin, M. Nisoli, *Science (80-.)*. **2014**, *346*, 336–339.
- [18] P. M. Kraus, B. Mignolet, D. Baykusheva, A. Rupenyan, L. Horný, E. F. Penka, G. Grassi, O. I. Tolstikhin, J. Schneider, F. Jensen, L. B. Madsen, A. D. Bandrauk, F. Remacle, H. J. Wörner, *Science (80-.)*. **2015**, *350*, 790–795.
- [19] M. Nisoli, P. Decleva, F. Calegari, A. Palacios, F. Martín, *Chem. Rev.* **2017**, *117*, 10760–10825.
- [20] A. Weiner, D. Leaird, J. Patel, J. Wullert, *IEEE J. Quantum Electron.* **1992**, *28*, 908–920.
- [21] H. Rabitz, R. de Vivie-Riedle, M. Motzkus, K.-L. Kompa, *Science (80-.)*. **2000**, *288*, 824–828.

- [22] T. Brixner, G. Gerber, *ChemPhysChem* **2003**, *4*, 418–438.
- [23] M. Dantus, V. V. Lozovoy, *Chem. Rev.* **2004**, *104*, 1813–1860.
- [24] P. Nuernberger, G. Vogt, T. Brixner, G. Gerber, *Phys. Chem. Chem. Phys.* **2007**, *9*, 2470.
- [25] A. Assion, T. Baumert, M. Bergt, T. Brixner, B. Kiefer, V. Seyfried, M. Strehle, G. Gerber, *Science* **1998**, *282*, 919–22.
- [26] J. L. Herek, W. Wohlleben, R. J. Cogdell, D. Zeidler, M. Motzkus, *Nature* **2002**, *417*, 533–535.
- [27] G. Vogt, G. Krampert, P. Niklaus, P. Nuernberger, G. Gerber, *Phys. Rev. Lett.* **2005**, *94*, 068305.
- [28] V. I. Prokhorenko, A. M. Nagy, S. A. Waschuk, L. S. Brown, R. R. Birge, R. J. D. Miller, *Science (80-.)*. **2006**, *313*, 1257–61.
- [29] H.-D. Hao, D. Trauner, *J. Am. Chem. Soc.* **2017**, *139*, 4117–4122.
- [30] I. S. Makarov, C. E. Brocklehurst, K. Karaghiosoff, G. Koch, P. Knochel, *Angew. Chemie Int. Ed.* **2017**, *56*, 12774–12777.
- [31] D. Trauner, *Angew. Chemie Int. Ed.* **2018**, *57*, 4177–4191.
- [32] D. Stichnoth, P. Kölle, T. J. Kimbrough, E. Riedle, R. de Vivie-Riedle, D. Trauner, *Nat. Commun.* **2014**, *5*, 5597.
- [33] D. M. Schultz, T. P. Yoon, *Science (80-.)*. **2014**, *343*, 1239176–1239176.
- [34] W. A. Velema, W. Szymanski, B. L. Feringa, *J. Am. Chem. Soc.* **2014**, *136*, 2178–2191.
- [35] J. Broichhagen, J. A. Frank, D. Trauner, *Acc. Chem. Res.* **2015**, *48*, 1947–1960.
- [36] T. Stensitzki, Y. Yang, V. Kozich, A. A. Ahmed, F. Kössl, O. Kühn, K. Heyne, *Nat. Chem.* **2018**, *10*, 126–131.
- [37] R. F. Loring, S. Mukamel, *J. Chem. Phys.* **1985**, *83*, 2116–2128.
- [38] S. Mukamel, *Annu. Rev. Phys. Chem.* **2000**, *51*, 691–729.
- [39] D. J. Tannor, S. A. Rice, *J. Chem. Phys.* **1985**, *83*, 5013–5018.
- [40] D. J. Tannor, R. Kosloff, S. A. Rice, *J. Chem. Phys.* **1986**, *85*, 5805–5820.
- [41] R. S. Judson, H. Rabitz, *Phys. Rev. Lett.* **1992**, *68*, 1500–1503.
- [42] W. S. Warren, H. Rabitz, M. Dahleh, *Science (80-.)*. **1993**, *259*, 1581–1589.
- [43] D. Kosloff, R. Kosloff, *J. Comput. Phys.* **1983**, *52*, 35–53.
- [44] H. Tal-Ezer, R. Kosloff, *J. Chem. Phys.* **1984**, *81*, 3967–3971.
- [45] R. Kosloff, *J. Phys. Chem.* **1988**, *92*, 2087–2100.
- [46] A. P. Peirce, M. A. Dahleh, H. Rabitz, *Phys. Rev. A* **1988**, *37*, 4950–4964.
- [47] R. Kosloff, S. Rice, P. Gaspard, S. Tersigni, D. Tannor, *Chem. Phys.* **1989**, *139*, 201–220.
- [48] P. von den Hoff, S. Thallmair, M. Kowalewski, R. Siemering, R. de Vivie-Riedle, *Phys. Chem. Chem. Phys.* **2012**, *14*, 14460.
- [49] F. Bernardi, M. Olivucci, M. A. Robb, *Chem. Soc. Rev.* **1996**, *25*, 321.
- [50] D. R. Yarkony, *Rev. Mod. Phys.* **1996**, *68*, 985–1013.

-
- [51] *Conical Intersections: Theory, Computation and Experiment*, (Eds.: W. Domcke, D. R. Yarkony, H. Köppel), WORLD SCIENTIFIC, Singapore, **2011**.
- [52] A. Hofmann, R. de Vivie-Riedle, *J. Chem. Phys.* **2000**, *112*, 5054–5059.
- [53] J. P. P. Zauleck, S. Thallmair, M. Loipersberger, R. de Vivie-Riedle, *J. Chem. Theory Comput.* **2016**, *12*, 5698–5708.
- [54] J. P. P. Zauleck, R. de Vivie-Riedle, *J. Chem. Theory Comput.* **2018**, *14*, 55–62.
- [55] P. Hohenberg, W. Kohn, *Phys. Rev.* **1964**, *136*, B864–B871.
- [56] W. Kohn, L. J. Sham, *Phys. Rev.* **1965**, *140*, A1133–A1138.
- [57] J. A. Pople, *Angew. Chemie Int. Ed.* **1999**, *38*, 1894–1902.
- [58] E. Runge, E. K. U. Gross, *Phys. Rev. Lett.* **1984**, *52*, 997–1000.
- [59] K. Burke, J. Werschnik, E. K. U. Gross, *J. Chem. Phys.* **2005**, *123*, 062206.
- [60] A. Dreuw, M. Head-Gordon, *Chem. Rev.* **2005**, *105*, 4009–4037.
- [61] P. J. Bruna, S. D. Peyerimhoff in *Adv. Chem. Phys.* (Ed.: K. P. Lawley), John Wiley & Sons, Ltd., New York, **2007**, pp. 1–97.
- [62] K. Andersson, P. Malmqvist, B. O. Roos, *J. Chem. Phys.* **1992**, *96*, 1218–1226.
- [63] J. Finley, P.-Å. Malmqvist, B. O. Roos, L. Serrano-Andrés, *Chem. Phys. Lett.* **1998**, *288*, 299–306.
- [64] D. Roca-Sanjuán, F. Aquilante, R. Lindh, *Wiley Interdiscip. Rev. Comput. Mol. Sci.* **2012**, *2*, 585–603.
- [65] J. Schirmer, *Phys. Rev. A* **1982**, *26*, 2395–2416.
- [66] A. Dreuw, M. Wormit, *Wiley Interdiscip. Rev. Comput. Mol. Sci.* **2015**, *5*, 82–95.
- [67] C. D. Sherrill, H. F. Schaefer in *Adv. Quantum Chem.* (Ed.: P.-O. Löwdin), Academic Press, San Diego, **1999**, pp. 143–269.
- [68] O. Christiansen, H. Koch, P. Jørgensen, *Chem. Phys. Lett.* **1995**, *243*, 409–418.
- [69] A. I. Krylov, *Annu. Rev. Phys. Chem.* **2008**, *59*, 433–462.
- [70] K. Sneskov, O. Christiansen, *Wiley Interdiscip. Rev. Comput. Mol. Sci.* **2012**, *2*, 566–584.
- [71] S. Thallmair, M. Kowalewski, J. P. P. Zauleck, M. K. Roos, R. de Vivie-Riedle, *J. Phys. Chem. Lett.* **2014**, *5*, 3480–3485.
- [72] A. Warshel, M. Levitt, *J. Mol. Biol.* **1976**, *103*, 227–249.
- [73] M. J. Field, P. A. Bash, M. Karplus, *J. Comput. Chem.* **1990**, *11*, 700–733.
- [74] H. M. Senn, W. Thiel, *Angew. Chemie Int. Ed.* **2009**, *48*, 1198–1229.
- [75] B. Mennucci, *Phys. Chem. Chem. Phys.* **2013**, *15*, 6583.
- [76] S. Thallmair, J. P. P. Zauleck, R. de Vivie-Riedle, *J. Chem. Theory Comput.* **2015**, *11*, 1987–1995.
- [77] J. C. Tully, *Faraday Discuss.* **1998**, *110*, 407–419.
- [78] L. Wang, A. B. McCoy, *Phys. Chem. Chem. Phys.* **1999**, *1*, 1227–1235.
- [79] M. V. Ivanov, D. Babikov, *Chem. Phys. Lett.* **2012**, *535*, 173–176.
- [80] J. Cerezo, Y. Liu, N. Lin, X. Zhao, R. Improta, F. Santoro, *J. Chem. Theory Comput.* **2018**, *14*, 820–832.

- [81] J. P. P. Zauleck, M. T. Peschel, F. Rott, S. Thallmair, R. de Vivie-Riedle, *J. Phys. Chem. A* **2018**, *122*, 2849–2857.
- [82] S. Tommasi, M. F. Denissenko, G. P. Pfeifer, *Cancer Res.* **1997**, *57*, 4727–30.
- [83] L. Esposito, A. Banyasz, T. Douki, M. Perron, D. Markovitsi, R. Improta, *J. Am. Chem. Soc.* **2014**, *136*, 10838–10841.
- [84] L. Martínez-Fernández, A. J. Pepino, J. Segarra-Martí, J. Jovaišaitė, I. Vaya, A. Nenov, D. Markovitsi, T. Gustavsson, A. Banyasz, M. Garavelli, R. Improta, *J. Am. Chem. Soc.* **2017**, *139*, 7780–7791.
- [85] S. Matsika, M. Spanner, M. Kotur, T. C. Weinacht, *J. Phys. Chem. A* **2013**, *117*, 12796–12801.
- [86] D. B. Bucher, C. L. Kufner, A. Schlueter, T. Carell, W. Zinth, *J. Am. Chem. Soc.* **2016**, *138*, 186–190.
- [87] K. Fukui, *J. Phys. Chem.* **1970**, *74*, 4161–4163.
- [88] R. Crehuet, J. M. Bofill, *J. Chem. Phys.* **2005**, *122*, 234105.
- [89] S. Matsika, *J. Phys. Chem. A* **2004**, *108*, 7584–7590.
- [90] S. Matsika, C. Zhou, M. Kotur, T. C. Weinacht, *Faraday Discuss.* **2011**, *153*, 247.
- [91] H.-D. Meyer, U. Manthe, L. Cederbaum, *Chem. Phys. Lett.* **1990**, *165*, 73–78.
- [92] G. A. Worth, H. D. Meyer, L. S. Cederbaum, *J. Chem. Phys.* **1996**, *105*, 4412–4426.
- [93] G. A. Worth, H.-D. Meyer, L. S. Cederbaum, *J. Chem. Phys.* **1998**, *109*, 3518–3529.
- [94] H. D. Meyer, *Wiley Interdiscip. Rev. Comput. Mol. Sci.* **2012**, *2*, 351–374.
- [95] H. Nyquist, *Trans. Am. Inst. Electr. Eng.* **1928**, *47*, 617–644.
- [96] C. Shannon, *Proc. IRE* **1949**, *37*, 10–21.
- [97] F. Schüppel, M. K. Roos, R. de Vivie-Riedle, *Phys. Chem. Chem. Phys.* **2018**, *20*, 22753–22761.
- [98] B. Podolsky, *Phys. Rev.* **1928**, *32*, 812–816.
- [99] P. H. Berens, K. R. Wilson, *J. Chem. Phys.* **1981**, *74*, 4872–4882.
- [100] J. Stare, G. G. Balint-Kurti, *J. Phys. Chem. A* **2003**, *107*, 7204–7214.
- [101] S. Thallmair, M. K. Roos, R. de Vivie-Riedle, *J. Chem. Phys.* **2016**, *144*, 234104.
- [102] V. Alexandrov, D. M. A. Smith, H. Rostkowska, M. J. Nowak, L. Adamowicz, W. McCarthy, *J. Chem. Phys.* **1998**, *108*, 9685–9693.
- [103] C. Eckart, *Phys. Rev.* **1935**, *47*, 552–558.
- [104] A. Y. Dymarsky, K. N. Kudin, *J. Chem. Phys.* **2005**, *122*, 124103.
- [105] K. N. Kudin, A. Y. Dymarsky, *J. Chem. Phys.* **2005**, *122*, 224105.
- [106] W. L. Jorgensen, D. S. Maxwell, J. Tirado-Rives, *J. Am. Chem. Soc.* **1996**, *118*, 11225–11236.
- [107] J. Graf, P. H. Nguyen, G. Stock, H. Schwalbe, *J. Am. Chem. Soc.* **2007**, *129*, 1179–1189.
- [108] L. Wickstrom, A. Okur, C. Simmerling, *Biophys. J.* **2009**, *97*, 853–856.

-
- [109] K. Lindorff-Larsen, S. Piana, K. Palmo, P. Maragakis, J. L. Klepeis, R. O. Dror, D. E. Shaw, *Proteins Struct. Funct. Bioinforma.* **2010**, *78*, NA–NA.
- [110] H. Nguyen, D. R. Roe, C. Simmerling, *J. Chem. Theory Comput.* **2013**, *9*, 2020–2034.
- [111] W. L. Jorgensen, J. Chandrasekhar, J. D. Madura, R. W. Impey, M. L. Klein, *J. Chem. Phys.* **1983**, *79*, 926–935.
- [112] H. C. Andersen, *J. Comput. Phys.* **1983**, *52*, 24–34.
- [113] W. C. Swope, H. C. Andersen, P. H. Berens, K. R. Wilson, *J. Chem. Phys.* **1982**, *76*, 637–649.
- [114] J.-P. Ryckaert, G. Ciccotti, H. J. Berendsen, *J. Comput. Phys.* **1977**, *23*, 327–341.
- [115] H. J. C. Berendsen, J. P. M. Postma, W. F. van Gunsteren, A. DiNola, J. R. Haak, *J. Chem. Phys.* **1984**, *81*, 3684–3690.
- [116] D. Van Der Spoel, E. Lindahl, B. Hess, G. Groenhof, A. E. Mark, H. J. C. Berendsen, *J. Comput. Chem.* **2005**, *26*, 1701–1718.
- [117] D. R. McLaughlin, D. L. Thompson, *J. Chem. Phys.* **1973**, *59*, 4393–4405.
- [118] C. Xu, D. Xie, D. H. Zhang, S. Y. Lin, H. Guo, *J. Chem. Phys.* **2005**, *122*, 244305.
- [119] T. Ishida, G. C. Schatz, *Chem. Phys. Lett.* **1999**, *314*, 369–375.
- [120] M. Majumder, S. A. Ndengue, R. Dawes, *Mol. Phys.* **2016**, *114*, 1–18.
- [121] G. E. Fasshauer, *Meshfree Approximation Methods with Matlab*, WORLD SCIENTIFIC, **2007**.
- [122] M. Kowalewski, E. Larsson, A. Heryudono, *J. Chem. Phys.* **2016**, *145*, 084104.
- [123] C. C. Marston, G. G. Balint-Kurti, *J. Chem. Phys.* **1989**, *91*, 3571–3576.
- [124] R. Kosloff, H. Tal-Ezer, *Chem. Phys. Lett.* **1986**, *127*, 223–230.
- [125] W. Zhu, H. Rabitz, *J. Chem. Phys.* **1998**, *109*, 385–391.
- [126] W. Zhu, J. Botina, H. Rabitz, *J. Chem. Phys.* **1998**, *108*, 1953–1963.
- [127] K. Sundermann, R. de Vivie-Riedle, *J. Chem. Phys.* **1999**, *110*, 1896–1904.
- [128] S. Thallmair, D. Keefer, F. Rott, R. de Vivie-Riedle, *J. Phys. B At. Mol. Opt. Phys.* **2017**, *50*, 082001.
- [129] C. Gollub, M. Kowalewski, R. de Vivie-Riedle, *Phys. Rev. Lett.* **2008**, *101*, 073002.
- [130] U. Fano, *Rev. Mod. Phys.* **1957**, *29*, 74–93.
- [131] H.-P. Breuer, F. Petruccione, *The Theory of Open Quantum Systems*, Oxford University Press, **2007**.
- [132] Á. Rivas, S. F. Huelga, M. B. Plenio, *Reports Prog. Phys.* **2014**, *77*, 094001.
- [133] H. P. Breuer, E. M. Laine, J. Piilo, B. Vacchini, *Rev. Mod. Phys.* **2016**, *88*, 1–24.
- [134] S. Beyvers, Y. Ohtsuki, P. Saalfrank, *J. Chem. Phys.* **2006**, *124*, 234706.
- [135] Y. Ohtsuki, W. Zhu, H. Rabitz, *J. Chem. Phys.* **1999**, *110*, 9825–9832.
- [136] Y. Ohtsuki, K. Nakagami, W. Zhu, H. Rabitz, *Chem. Phys.* **2003**, *287*, 197–216.
- [137] C. P. Koch, *J. Phys. Condens. Matter* **2016**, *28*, 213001.

- [138] W. Zhu, H. Rabitz, *J. Chem. Phys.* **2003**, *118*, 6751–6757.
- [139] K. Hoki, P. Brumer, *Phys. Rev. Lett.* **2005**, *95*, 168305.
- [140] F. Shuang, H. Rabitz, *J. Chem. Phys.* **2006**, *124*, 154105.
- [141] G. Füchsel, T. Klamroth, J. C. Tremblay, P. Saalfrank, *Phys. Chem. Chem. Phys.* **2010**, *12*, 14082.
- [142] J. C. Tremblay, *J. Chem. Phys.* **2011**, *134*, 174111.
- [143] F. Caruso, S. Montangero, T. Calarco, S. F. Huelga, M. B. Plenio, *Phys. Rev. A* **2012**, *85*, 042331.
- [144] C. M. Tesch, R. de Vivie-Riedle, *Phys. Rev. Lett.* **2002**, *89*, 157901.
- [145] J. H. Hoeijmakers, *N. Engl. J. Med.* **2009**, *361*, 1475–1485.
- [146] H. Black, F. DeGruijl, P. Forbes, J. Cleaver, H. Ananthaswamy, E. DeFabo, S. Ullrich, R. Tyrrell, *J. Photochem. Photobiol. B Biol.* **1997**, *40*, 29–47.
- [147] T. Lindahl, *Science (80-.)*. **1999**, *286*, 1897–1905.
- [148] J. Cadet, E. Sage, T. Douki, *Mutat. Res. Mol. Mech. Mutagen.* **2005**, *571*, 3–17.
- [149] W. J. Schreier, T. E. Schrader, F. O. Koller, P. Gilch, C. E. Crespo-Hernandez, V. N. Swaminathan, T. Carell, W. Zinth, B. Kohler, *Science (80-.)*. **2007**, *315*, 625–629.
- [150] K. Haiser, B. P. Fingerhut, K. Heil, A. Glas, T. T. Herzog, B. M. Pilles, W. J. Schreier, W. Zinth, R. de Vivie-Riedle, T. Carell, *Angew. Chemie Int. Ed.* **2012**, *51*, 408–411.
- [151] H. Kang, K. T. Lee, B. Jung, Y. J. Ko, S. K. Kim, *J. Am. Chem. Soc.* **2002**, *124*, 12958–12959.
- [152] Y. He, C. Wu, W. Kong, *J. Phys. Chem. A* **2003**, *107*, 5145–5148.
- [153] C. E. Crespo-Hernández, B. Cohen, P. M. Hare, B. Kohler, *Chem. Rev.* **2004**, *104*, 1977–2019.
- [154] S. Ullrich, T. Schultz, M. Z. Zgierski, A. Stolow, *Phys. Chem. Chem. Phys.* **2004**, *6*, 2796.
- [155] C. Canuel, M. Mons, F. Piuizzi, B. Tardivel, I. Dimicoli, M. Elhanine, *J. Chem. Phys.* **2005**, *122*, DOI 10.1063/1.1850469.
- [156] C. T. Middleton, K. de La Harpe, C. Su, Y. K. Law, C. E. Crespo-Hernández, B. Kohler, *Annu. Rev. Phys. Chem.* **2009**, *60*, 217–39.
- [157] M. Kotur, T. C. Weinacht, Congyi Zhou, S. Matsika, *IEEE J. Sel. Top. Quantum Electron.* **2012**, *18*, 187–194.
- [158] J. J. Nogueira, F. Plasser, L. González, *Chem. Sci.* **2017**, *8*, 5682–5691.
- [159] T. Douki, A. Reynaud-Angelin, J. Cadet, E. Sage, *Biochemistry* **2003**, *42*, 9221–9226.
- [160] A. Sancar, *Chem. Rev.* **2003**, *103*, 2203–2238.
- [161] E. C. Friedberg, G. C. Walker, W. Siede, R. D. Wood, A. S. Roger, T. Ellenberger, *DNA Repair and Mutagenesis, Second Edition*, American Society of Microbiology, **2006**.
- [162] J. O. Fuss, P. K. Cooper, *PLoS Biol.* **2006**, *4*, e203.
- [163] V. Besel, Bachelor Thesis, LMU Munich, **2018**.

-
- [164] J.-D. Chai, M. Head-Gordon, *Phys. Chem. Chem. Phys.* **2008**, *10*, 6615.
- [165] T. H. Dunning, *J. Chem. Phys.* **1989**, *90*, 1007–1023.
- [166] M. J. Frisch, G. W. Trucks, H. B. Schlegel, G. E. Scuseria, M. A. Robb, J. R. Cheeseman, G. Scalmani, V. Barone, G. A. Petersson, H. Nakatsuji, X. Li, M. Caricato, A. V. Marenich, J. Bloino, B. G. Janesko, R. Gomperts, B. Mennucci, H. P. Hratchian, J. V. Ortiz, A. F. Izmaylov, J. L. Sonnenberg, D. Williams-Young, F. Ding, F. Lipparini, F. Egidi, J. Goings, B. Peng, A. Petrone, T. Henderson, D. Ranasinghe, V. G. Zakrzewski, J. Gao, N. Rega, G. Zheng, W. Liang, M. Hada, M. Ehara, K. Toyota, R. Fukuda, J. Hasegawa, M. Ishida, T. Nakajima, Y. Honda, O. Kitao, H. Nakai, T. Vreven, K. Throssell, J. A. Montgomery Jr., J. E. Peralta, F. Ogliaro, M. J. Bearpark, J. J. Heyd, E. N. Brothers, K. N. Kudin, V. N. Staroverov, T. A. Keith, R. Kobayashi, J. Normand, K. Raghavachari, A. P. Rendell, J. C. Burant, S. S. Iyengar, J. Tomasi, M. Cossi, J. M. Millam, M. Klene, C. Adamo, R. Cammi, J. W. Ochterski, R. L. Martin, K. Morokuma, O. Farkas, J. B. Foresman, D. J. Fox, Gaussian16 Revision B.01, **2016**.
- [167] F. Aquilante, J. Autschbach, R. K. Carlson, L. F. Chibotaru, M. G. Delcey, L. De Vico, I. Fdez. Galván, N. Ferré, L. M. Frutos, L. Gagliardi, M. Garavelli, A. Giussani, C. E. Hoyer, G. Li Manni, H. Lischka, D. Ma, P. Å. Malmqvist, T. Müller, A. Nenov, M. Olivucci, T. B. Pedersen, D. Peng, F. Plasser, B. Pritchard, M. Reiher, I. Rivalta, I. Schapiro, J. Segarra-Martí, M. Stenrup, D. G. Truhlar, L. Ungur, A. Valentini, S. Vancoillie, V. Veryazov, V. P. Vysotskiy, O. Weingart, F. Zapata, R. Lindh, *J. Comput. Chem.* **2016**, *37*, 506–541.
- [168] J. Wang, P. Cieplak, P. A. Kollman, *J. Comput. Chem.* **2000**, *21*, 1049–1074.

Danksagung

An dieser Stelle möchte ich einigen Personen meinen Dank aussprechen.

Als erstes danke ich meiner Doktormutter und Chefin **Prof. Dr. Regina de Vivie-Riedle** für die umfassende Unterstützung während den letzten Jahren. In der PC5-Vorlesung haben Sie mein Interesse an der Quantenkontrolle geweckt, das ich durch die Jahre bis zum Ende meiner Promotion verfolgen durfte, und das bis heute kein Bisschen abgeflacht ist. Ein besonderes Highlight waren mir außerdem die vielen Konferenzen, die ich im In- und Ausland besuchen durfte, und die eine breite wissenschaftliche Begeisterung in mir geweckt haben. Außerdem danke ich **Prof. Dr. Achim Hartschuh** für die Zweitkorrektur meiner Dissertation, und **Prof. Dr. Christian Ochsenfeld** für die hervorragenden Theorievorlesungen, die schon früh im Bachelorstudium meinen Fokus weg vom Labor und hin zur Quantenchemie gelegt haben.

Allen ehemaligen und aktuellen Arbeitskreismitgliedern und Praktikanten möchte ich für verschiedenste Dinge danken: **Thali** für die ausgezeichnete Betreuung während meiner Masterarbeit und das Etablieren des asymmetrischen Biermarkenkaufverfahrens auf Campusfesten, das wir unbedingt patentieren sollten; **Patrick** für seinen berüchtigten quantenchemischen Instinkt, der mindestens auf CCSDTQXXXX-Niveau liegt; **Robert** für die immense Erweiterung meines Brettspiel-Repertoires; **Sven** für die unabsichtliche Betreuung meiner Bachelorarbeit und die wichtige Erkenntnis, dass *regex* schneller ist als *split*; **Julius** für seine ungewöhnliche Denk- und Herangehensweise, die meinen Horizont ziemlich erweitert hat; **Matthias** für seine administrative Kompetenz und die artgerechte Zubereitung und Haltung zahlreicher Mettigel; **Flo** für seine Unermüdlichkeit beim Kreieren von Memes und somit der konstanten Arbeitskreisbespaßung; **Thomas** und **Franzi** für unzählige Brews, ohne die ein gesunder Theoretikeralltag unmöglich gewesen wäre; **Martin** für die Kollegialität und Kompetenz in den Matlab-Kursen; **Sebastian** für seine ausgezeichnete Arbeit am Uracil-Projekt, in dem sich unsere unterschiedlichen Kompetenzen und Eigenschaften perfekt ergänzt haben; **Viviana** für das Einbringen von Südtalientischem Flair in unseren ansonsten tief bayerisch gefärbten Arbeitskreis; **Vitus**, dessen Bachelorarbeit das DNA-self-repair Projekt ein gutes Stück vorangetrieben hat.

Ich danke meinen Kollaborationspartnern für das Durchführen zahlreicher Experimente, für das Einführen und die wertvollen Einsichten in experimentelle Setups, und für die Geduld und Aufgeschlossenheit die es braucht um mit einem Theoretiker zusammenzuarbeiten: **Mario, Juri und Alex** aus dem AK Prof. Paul Knochel in München für teilweise lebensgefährliche metallorganische Synthesen, die nur unter stetiger Überwachung mit Feuerlöscher durchgeführt werden konnten; **Nick, Madlen und Elisabeth** aus dem AK Prof. Marcus Motzkus in Heidelberg, wo ich das (ernst gemeinte) Vergnügen hatte, einen sehr langen und aufregenden Abend im Laser-Labor zu verbringen; **Ioachim und Theresa** vom MPQ in Garching, die mir mit ihrem weltweit einzigartigen Setup die Möglichkeit gegeben haben, über ein paar sehr grundlegende physikalische Effekte nachzudenken, und vor allem darüber wie man ihnen auf die Schliche kommen kann.

Meinen Freunden danke ich für die fantastische Zeit in München. Es war mir eine riesen Freude. Insbesondere danke ich: **Ann-Ka** und **Schorsch** für alles was euch zu den besten Freunden macht mit denen ich am liebsten meine Zeit verbringe; **Henning** für die vielen epischen Schlachten in nahen und fernen Galaxien (der stetige Antrieb zu strategischen und taktischen Höchstleistungen trug bestimmt nicht unwesentlich zu meiner Arbeit bei) ; **Judith, Veit und Hannes** für die sehr angenehme Zeit in der Giesing-WG; allen Mitgliedern der **Fußball- und Volleyballgruppen** für den intensiven sportlichen Ausgleich zum wissenschaftlichen Alltag.

Ich danke meiner **Familie** für die uneingeschränkte Freiheit, die ich schon angefangen in der Schule und bis heute bei der Gestaltung meines Weges hatte. Außerdem danke ich euch dafür, dass ich die sehr wertvolle Gewissheit haben durfte, dass wenn es irgendwo mal brennt, immer jemand zur Stelle sein wird.

Zum Schluss danke ich **Janina** für die enge, geduldige und ausgleichende Begleitung in den Jahren dieser Arbeit, der Zeit davor und der Zeit die daran anschließt.